Probing Local Heterogeneity in the Optoelectronic Properties of Organic-Inorganic Perovskites Using Fluorescence Microscopy

Dane W. De Quilettes

A dissertation submitted in partial fulfillment of the requirements for the degree of

Doctor of Philosophy

University of Washington
2017

Reading Committee:
David S. Ginger, Chair
Daniel R. Gamelin
Cody Schlenker

Program Authorized to Offer Degree:
Chemistry

University of Washington

Abstract

Probing Local Heterogeneity in the Optoelectronic Properties of Organic-Inorganic Perovskites Using Fluorescence Microscopy

Dane W. De Quilettes
Chair of the Supervisory Committee:
Professor David S. Ginger
Department of Chemistry

Unregulated emission of carbon dioxide and greenhouse gases into our atmosphere has led to an increase in the average global surface air temperature, to a disruption of weather patterns, and to the acidification of oceans all of which threaten the continued prosperity of our race and our planet. The transition to renewable sources of energy is therefore one of, if not the most, important challenge that the 21st century faces. Solar energy is predicted to play a major role in global energy production in the coming century, as the amount of energy hitting the earth's surface is far greater than the energy demands of industrialized human activity. Many current photovoltaic technologies show promise in contributing to a large fraction of global energy production, but in order to reach terawatt-scale production the photovoltaic modules will need to be scalable, cheap, and efficient. Perovskite-based photovoltaics hold exceptional potential in contributing to solar energy production. Thus far, the unprecedented rise in power conversion efficiencies over the past few years can be primarily attributed to improvements in film processing and device engineering. Although effective, the fundamental photophysical processes that govern charge generation, transport, recombination, and collection in these materials is still in its infancy. Historically in semiconductor technologies, this understanding has been essential in the rational design of optimized materials. This knowledge appears to be even more critical as perovskite thin films are polycrystalline on the microscale, which suggests that the local structure may determine the optoelectronic quality and device performance on a similar length scale.

Prior to these studies, much of the field had focused on bulk spectroscopic measurements to characterize the semiconducting properties of hybrid perovskite thin films. From our contributions as well as many others, microscopy has now given us a window into how this bulk behavior is composed of an ensemble of spatially varying structure and composition, which controls carrier transport and dynamics on the way to carrier extraction and power generation. This understanding has led to some exciting new discoveries on the rational design of materials and is leveraged to deploy chemical passivation techniques to improve the optoelectronic quality of the material, with the ultimate goal of improving photovoltaic power conversion efficiency.

Reducing non-radiative recombination in semiconducting materials is a prerequisite for achieving the highest performance in a host of light-emitting and photovoltaic

applications. In the first study described herein, we used confocal fluorescence microscopy correlated with scanning electron microscopy to spatially resolve the photoluminescence (PL) decay dynamics from films of nonstoichiometric organic-inorganic perovskites, $CH_3NH_3PbI_3(Cl)$. The PL intensities and lifetimes varied between different grains in the same film, even for films that exhibited long bulk lifetimes. The grain boundaries were dimmer and exhibited faster non-radiative decay. Energy-dispersive x-ray spectroscopy showed a positive correlation between chlorine concentration and regions of brighter PL, while PL imaging revealed that chemical treatment with pyridine could activate previously dark grains.

Next, to better elucidate the sources of these loss pathways, we performed a systematic study using confocal and widefield fluorescence microscopy to deconvolve the contributions from diffusion and non-radiative recombination which lead to the observed image heterogeneity. We showed that, in addition to local variations in non-radiative loss, carriers diffuse anisotropically due to heterogeneous intergrain connectivity.

In addition to non-radiative recombination impeding material performance, we also showed that the materials exhibit a range of complex dynamic phenomena under illumination. We used a unique combination of confocal PL microscopy and chemical imaging to correlate the local changes in photophysics with composition in $CH_3NH_3PbI_3$ films under illumination. We demonstrated that the photo-induced "brightening" of the perovskite PL can be attributed to an order-of-magnitude reduction in trap state density. By imaging the same regions with time-of-flight secondary-ion-mass spectrometry (ToF-SIMS), we correlated this photobrightening with a net migration of iodine. This work provides visual evidence for photo-induced halide migration in triiodide perovskites and reveals the complex interplay between charge carrier populations, electronic traps, and mobile halides, which collectively impact optoelectronic performance.

Next, we studied the effects of a series of post-deposition ligand treatments on the PL of polycrystalline methylammonium lead triiodide perovskite thin films. We showed that a variety of Lewis bases can improve the bulk PL quantum efficiency (PLQE) and extend the average PL lifetime $\langle\tau\rangle$, with large enhancements concentrated at grain boundaries. Notably, we demonstrated thin film PLQE as high as $35 \pm 1\%$ and $\langle\tau\rangle$ as long as 8.82 ± 0.03 μs, at solar equivalent carrier densities using tri-n-octylphosphine oxide (TOPO) treated films. Using glow discharge optical emission spectroscopy (GDOES) and nuclear magnetic resonance (NMR) spectroscopy, we showed that the ligands are incorporated primarily at the film surface and are acting as electron donors. These results indicate it is possible to obtain thin film PL lifetime and PLQE values that are comparable to those from single crystals by control over surface chemistry.

Finally, we further characterized these TOPO treated films to show, with respect to material bandgap, these passivated films could demonstrate quasi-Fermi level splittings comparable to the highest performing GaAs solar cells, reaching 96% of the Shockley-Queisser limit. Importantly, we reported internal photoluminescence quantum efficiency values of 92% under one sun illumination intensity, which are the highest values achieved to date. These results suggest that the material optoelectronic quality has been

nearly optimized and further increases in voltage and device efficiency will be obtained by integrating these types of surface passivation schemes into charge carrier selective interfaces.

Table of Contents

List of Figures iv
List of Tables vi
Acknowledgements vii
Preface ix

Chapter 1: Introduction
1.1 Radiative Limit in Photovoltaic Devices 1
1.2 Defects in Semiconductors 4
1.3 Perovskite Thin Films for Photovoltaic Devices 5
1.4 References 7

Chapter 2: Impact of Microstructure on Local Carrier Lifetime
2.1 Overview 9
2.2 Introduction 9
2.3 Photovoltaic Device and Photoluminescence Measurements 10
2.4 Local Time-Resolved Photoluminescence Decay Dynamics 11
2.5 Improvements in Photoluminescence by Pyridine Vapor Treatment 11
2.6 Correlation of High Photoluminescence with Chlorine Content 12
2.7 Conclusions 12
2.8 Appendix A 12
2.9 Acknowledgements 13
2.10 Figures 2.1-2.4 14
2.11 References 18

Chapter 3: Tracking Photo-Excited Carriers on the Microscale: Diffusion Vs Trap-Dominated Behavior
3.1 Overview 21
3.2 Introduction 21
3.3 Confocal Versus Widefield Fluorescence Imaging 22
3.4 Intensity-Dependent Fluorescence Images 22
3.5 Probing Diffusion with Local Excitation and Widefield Detection 23
3.6 Probing Diffusion with Local Excitation and Widefield Detection After Surface Treatment 24
3.7 Kinetic Modelling of Confocal Time-Resolved Kinetics 25
3.8 Conclusions 27
3.9 Appendix B 27
3.10 Acknowledgements 27
3.11 Figures 3.1-3.5 28
3.12 References 32

Chapter 4: Photo-induced Halide Redistribution
4.1 Overview 36
4.2 Introduction 36
4.3 Bulk Changes in Photoluminescence Under Illumination 37
4.4 Local Changes in Photoluminescence Under Illumination 38

4.5 Compositional Changes After Illumination 39
4.6 Proposed Mechanism of Photobrightening 40
4.7 Discussion 42
4.8 Conclusions 43
4.9 Appendix C 43
4.10 Acknowledgements 44
4.11 Figures 4.1-4.6 45
4.12 References 51

Chapter 5: Photoluminescence Lifetimes Exceeding 8 μs and Quantum Yields Exceeding 30% by Ligand Passivation
5.1 Overview 55
5.2 Introduction 55
5.3 General Enhancements in Photoluminescence with Lewis Bases: 57
5.4 Chemical Characterization of Lewis Base Treatments 57
5.5 Champion Improvements in Photoluminescence Lifetime and Quantum Efficiency 58
5.6 Grain Boundaries Exhibit Greatest Improvements Upon Surface Passivation 59
5.7 Discussion 60
5.8 Conclusions 60
5.9 Appendix D 61
5.10 Acknowledgements 61
5.11 Figures 5.1-5.4 62
5.12 References 66

Chapter 6: Near Unity Radiative Efficiencies and Ultra-High Quasi-Fermi Level Splittings by Surface Passivation
6.1 Overview 71
6.2 Introduction 71
6.3 Determination of Quasi-Fermi Level Splitting from Absolute Intensity PL 73
6.4 Determination of Internal Photoluminescence Quantum Efficiency 74
6.5 Impact of Excitation Intensity and Temperature on Internal PLQE 76
6.6 Discussion 77
6.7 Conclusion 78
6.8 Appendix E 79
6.9 Acknowledgements 79
6.10 Figures 6.1-6.4 80
6.11 References 84

Appendix A: (Supporting Information for Chapter 2) 89
A.1 Additional Supporting Information and Figures 89
A.2 Supporting References 109

Appendix B: (Supporting Information for Chapter 3) 112
B.1 Additional Supporting Information and Figures 112
B.2 Supporting References 130

Appendix C: (Supporting Information for Chapter 4) 132
C.1 Additional Supporting Information 132
C.2 Supporting References 160

Appendix D: (Supporting Information for Chapter 5) 163
D.1 Additional Supporting Information and Figures 163
D.2 Supporting References 179

Appendix E: (Supporting Information for Chapter 6) 181
E.1 Additional Supporting Information and Figures 181
E.2 Supporting References 209

Curriculum Vitae 213

List of Figures

1.1. Perovskite unit cell.....5

2.1 Solar cell device measurement, bulk PL lifetime measurement, and correlated images from scanning electron microscopy and fluorescence microscopy experiments.....14
2.2 Fluorescence microscopy of $CH_3NH_3PbI_3(Cl)$ film and local PL measurements 15
2.3 Fluorescence microscopy of $CH_3NH_3PbI_3(Cl)$ film with pyridine vapor treatment.....16
2.4 Correlated images and line scans of $CH_3NH_3PbI_3(Cl)$ film using fluorescence microscopy, scanning electron microscopy, and energy-dispersive x-ray spectroscopy.....17

3.1 Widefield vs confocal fluorescence imaging.....28
3.2 Intensity-dependent fluorescence images 28
3.3 Local excitation and widefield fluorescence detection.....29
3.4 Local excitation and widefield fluorescence detection with surface treatment 30
3.5 Simulated and experimental confocal time-resolved photoluminescence kinetics.....31

4.1 Bulk changes in photoluminescence (PL) over time under illumination.....45
4.2 Local changes in photoluminescence over time under illumination.....46
4.3 Local photoluminescence rises and relaxation after exposure to simulated sunlight 47
4.4 Iodide redistribution after light soaking.....48
4.5 Time-of-flight secondary ion mass spectrometry (ToF-SIMS) depth profiling 49
4.6 Proposed mechanism of photo-induced cleaning by halide redistribution 50

5.1 Photoluminescence studies of films treated with Lewis bases 62
5.2 Evidence that Lewis bases are acting as surface ligands 63
5.3 Photoluminescence measurements of optimized ligand treatment 64
5.4 Fluorescence microscopy of ligand passivated film 65

6.1 Absolute intensity photoluminescence spectra of control and TOPO treated $CH_3NH_3PbI_3$ films deposited on an Au back reflector substrate 80
6.2 Images and schematic diagram of multi-metal back reflector substrates for determining internal photoluminescence quantum efficiency 81
6.3 Loss factor and photoluminescence quantum efficiency maps.....82
6.4 PL spectroscopy measurements to determine the maximum achievable quantum efficiency under high excitation powers and low temperatures.....83

A.1 Schematic of solar cell and stabilized power output.....97
A.2 Atomic force microscopy topography image versus photoluminescence map.....98
A.3 Stability of film under confocal excitation 99
A.4 Photoluminescence images and line scans around grain boundaries.....100
A.5 Schematic of confocal fluorescence microscopy setup.....101
A.6 Local steady-state photoluminescence spectra 102
A.7 Fluorescence image before and after PCBM deposition.....103
A.8 Local steady-state versus time-resolved photoluminescence.....104
A.9 Effect of solvent vapor on local photoluminescence intensity 105

A.10 SEM images of pyridine vapor treated films 106
A.11 EDS and ToF-SIMS analysis of films prepared with Cl precursor.....107

B.1 SEM image.....114
B.2 Correlation plot of widefield versus confocal image 115
B.3-B6 Control experiments for alternate explanations for PL heterogeneity 117
B.7 Fluorescence image histograms 122
B.8 Widefield fluorescence power dependence.....123
B.9 Pulsed laser intensity dependent fluorescence images.....124
B.10 Correlation plot of grain size versus PL intensity at different fluences 125
B.11 Bulk time-resolved PL decays before and after surface passivation.....126
B.12 Kinetic simulation showing diffusion-dominated behavior.....129

C.1 Photoluminescence (PL) rise behavior in different atmospheres and for different processing conditions.....135
C.2 Monitoring PL spectra in time 136
C.3 Monitoring structural changes of films under illumination 137
C.4 Intensity dependent bulk time-resolved PL.....138
C.5 Temperature-dependent PL changes 139
C.6 Temperature-dependent PL rises.....140
C.7 Intensity-dependent PL changes under illumination.....141
C.8 Grain size analysis via scanning electron microscopy (SEM) 142
C.9 PL enhancement compared to laser profile 143
C.10 Local grain emission relaxation 144
C.11 Bulk film relaxation in the dark 145
C.12 Local grain emission and relaxation without light soaking.....146
C.13 ToF-SIMS intensity images 147
C.14 ToF-SIMS and time-resolved PL measurements of $CH_3NH_3PbI_3$ films.....148
C.15 ToF-SIMS depth profile data of an illuminated $CH_3NH_3Pb(I_{1-x}Br_x)_3$ film (x=0.4).....149
C.16 Monitoring iodide content over time via energy dispersive X-ray spectroscopy 150

D.1 Photoluminescence improvements using thiol and amine Lewis bases.....167
D.2 Photoluminescence improvements for films with $PbCl_2$ and PbI_2 as Pb source.....169
D.3 Photoluminescence measurements of samples exposed to treatment solvent.....170
D.4 Reinitialization of photoluminescence properties after solvent wash.....171
D.5 Glow discharge optical emission spectroscopy after thiol treatment.....172
D.6 SEM, absorbance, and XRD characterization of surface treated films.....173
D.7 XRD characterization of control and ligand treated single crystal perovskite powders.174
D.8 Simulation and fits of photoluminescence quantum efficiency vs. carrier density 175
D.9 Streak camera experiment probing photoluminescence spectral shift induced by ligand treatment 176
D.10 Fluorescence image characterization with image masks before and after treatment....177

E.1 Statistics of parameters extracted from sub-gap absorptivity model.....184
E.2 Absorptivity spectra calculated from photoluminescence spectra 185

E.3 Shockley-Queisser and radiative limits for perovskite with 1.6 eV bandgap 186
E.4 Schematic of blackbody calibration 188
E.5 Calibration of integrating sphere with rhodamine.....190
E.6 Cross-calibration of integrating sphere with blackbody calibration.....191
E.7 Summary of reported V_{oc}'s for record performing perovskite solar cells.....193
E.8 Perovskite emission versus LED profile used to calculate loss factor.....194
E.9 Intensity dependent photoluminescence for different back reflector substrates 196
E.10 Atomic force microscope topography images of multi-metal substrates.....197
E.11 Transfer-matrix method to determine outcoupling efficiency.....198
E.12 R-squared values for internal PLQE fits assuming different outcoupling 199
E.13 Ellipsometry to determine TOPO thickness.....201
E.14 Change in outcoupling with thin layer of TOPO.....202
E.15 Photoluminescence enhancements in TOPO solution.....203
E.16 Fit to intensity dependent PL quantum efficiency values for TOPO 204
E.17 Temperature and intensity dependence of emission on linear scale.....204
E.18 Time-resolved photoluminescence decay traces for control and treated films 206
E.19 Temperature-dependent fluorescence images for control and TOPO samples 207
E.20 Carrier transport PL measurement before and after TOPO.....208

List of Tables

Table D.1 Ligand structures and concentration ranges of surface treatments 168
Table E.1 Perovskite material parameters calculated with different methods.....187
Table E.2 Blackbody calibration geometry parameters.....189
Table E.3 Absolute intensity calibration between integrating sphere and blackbody 191
Table E.4 Cross-calibration of integrating sphere and blackbody for perovskite.....192

Acknowledgements

The work presented in this thesis is the culmination of not only the work conducted at the University of Washington, but a reflection of the dedicated teachers and mentors who have invested in my education and life. I have been inspired by Skip Utech, Ken Barnes, Mark Anderson, and Kirk Einspahr who were the teachers that first introduced me to science at a young age and Timothy Lucas, David Green, Joseph Fritsch, and Jane Ganske who fueled my passion for research while at Pepperdine University. At the University of Washington, I want to thank David Ginger for sharing his contagious passion and drive to better understand the world through science and for also showing how a scientist can be an active part of the clean energy revolution. Along with my advisor, my graduate committee members throughout the years: Daniel Gamelin, Brandi Cossairt, Xiaosong Li, Alex Jen, Cody Schlenker, and Peter Pauzauskie have also been critical in my development as a scientist.

Through my graduate studies, I have also had the opportunity to collaborate with many exceptional scientists and want to thank Henry Snaith, Wei Zhang, and Jacob Wang for hosting me at the University of Oxford and sharing their knowledge as well as sending samples, which was fundamental in the completion of many projects. While at Oxford, I also met Sam Stranks who has been a great friend and colleague throughout the years who has extended many invaluable opportunities in the development of my career. Other collaborators include Gerd Bacher and Wolf Quitsch from Duisberg-Essen University in Germany and Eline Hutter and Tom Savenije at Delft University in the Netherlands.

Collaborators and technical staff at the University of Washington such as Ian Braly, Dan Graham, Liam Bradshaw, Rajan Paranji, and Ron Musgrave have willingly shared their expertise, which has significantly improved much of the work presented in this thesis.
I have had the opportunity to mentor and work alongside many excellent students such as Sarthak Jariwala, Sven Burke, Susanne Koch, Alfred Shropshire, Maggie Khu, Jasmine Beverly, and Stephen Hsieh. Their insightful questions have led to many of the research projects that make up the body of this thesis and their hard work and dedication in lab has led to many of the eventual publications.

I would also like to thank many of the current and former members of the Ginger Lab, several graduate students at the University of Washington, and staff at the Clean Energy Institute throughout the years that I have collaborated with, who have trained me on an instrument or technique, or have been a memorable part of my graduate experience. Those individuals include Michael Salvador, Elizabeth Strein, Hiro Nagaoka, Adam Colbert, Sarah Vorpahl, Mark Ziffer, Giles Eperon, Soumya Samai, Lucas Flagg, Zhaoxia Qian, David Moerman, Phu Nguyen, Feizhi Ding, and Shaun Taylor.

The successful completion of this thesis signifies the first doctoral degree awarded in my immediate and extended family and my hope is that it is not the last. The only reason this has been possible is because of the continual support and love that I have received from my Mom, Kim Johnson; fathers, Mark Johnson and Cliff deQuilettes; brothers, Mitch deQuilettes and Hyatt Johnson; grandparents, close relatives, and my friends. I would

also like to dedicate this work to my Uncle Ron, who passed away in the mudslides in Oso, WA on March 23, 2014, as well as my Aunt Margie, who passed away in July of 2017 after battling cancer for many years. I appreciate the conversations we had about my research in solar energy and the many thought-provoking questions and suggestions you both always had, they have led me to the place I am now. Both of you are a constant reminder of the importance of family and hard work, you will forever live in my heart and mind.

Preface

The replacement of finite fossil fuels with renewable sources of energy is one of the largest challenges facing the next century of industrialized human activity and is a necessary transition to ensure global welfare. Not only does the transition to carbon free sources of energy have major implications in the impediment of climate change and keeping our planet habitable, but is critical to continue supporting the systems for generating clean water, maintaining clean cooking facilities, making the fertilizers that grow food, powering the hospitals that provide healthcare, reducing air pollution, and powering the schools and equipment that form the basis of our education system. Although of massive importance now, this will become even more important as the world population increases and the 1.2 billion people worldwide that currently do not have access to electricity will seek the most inexpensive routes to become electrified.[1,2]

To address this global energy challenge, we need to develop a vast infrastructure of renewable energy production, storage, and distribution. Although there are several promising avenues in shifting our society toward renewable sources, prerequisites in the replacement of existing technologies are scalable to terawatts, carbon-free, highly efficient, and low-cost. These types of technologies paired with continued research and investment, resilient energy policies, and effective grid integration are all critical factors that will play into the eventual success and continued prosperity of humankind.

Photovoltaic modules, which convert sunlight directly into electricity, provide a rather elegant solution to contribute to our growing energy demands as they have proven to exhibit long operational lifetimes due to their low maintenance requirements from no moving parts. Apart from this distinct advantage, the solar resource is a widely under-utilized source of energy. For example, by performing a simple calculation taking into account the power density at the surface of the sun (treated as a black body source), the angular range of the sun upon the earth, the attenuation of the radiation by the atmosphere, one can calculate the average integrated irradiance upon the earth's surface. This is often defined as airmass 1.5 (AM1.5), which equates to an integrated irradiance of 1000 W/m^2. To put this value in perspective, the average power consumed globally is 18.3 TW-year per annum, the total amount of power that hits emerged continents on earth is 23,000 TW-year per annum, whereas the total amount of known coal reserves on planet earth is estimated to be only 830 TWy.[3] Using these values, it can be approximated that 13 days worth of energy from the sun is equivalent to the total energy reserves of coal that is currently known to exist.

Our ability to utilize this vast resource has been underwhelming in the last several decades. Currently solar energy only contributes only 272 GW,[4] a small fraction to global power production and consumption (18.3 TW). The hurdles in achieving TW production from solar lies largely in scalability and reducing the dependency on incentive programs and other project finance structures. For example, the success of photovoltaic installation in Germany and Japan is largely attributed to feed-in tariffs and associated policies,[4] although more recently both countries have encountered financial as well as grid constraints which has slowed the continued expansion.

In order to achieve TW scale photovoltaics some of the future directions include 1) improving the performance of modules and 2) reducing the cost and time required to manufacture and install photovoltaics. Currently, silicon dominates ~93% of total PV production, largely due to the rapid drop in module prices over the past few years, and will continue to significantly contribute to energy production in the coming decades. One major drawback for silicon based photovoltaics that will eventually limit its growth and deployment is the high capital expenditure (capex). This term broadly encompasses the upfront cost to build a factory and to fill it with equipment.[5] The capex for c-Si has been approximated to be $1/W-year, which equates to ~$1 billion to build a plant capable of producing 1 GW/year. On the other hand, a solution-processed material has potential to reduce capex to $0.06/W-year, which equates to ~$60 million to build a plant that can generate the same 1 GW/year.[5] Therefore, capex innovation may be one of the most promising avenues, apart from increasing module efficiency, to achieve TW-scale photovoltaics. Therefore, a material that is solution-processable and demonstrates high efficiency may prove to be the disruptive technology that power generations to come.

1.1 Radiative Limit in Photovoltaic Devices

The thermodynamic limit of a photovoltaic device as a function of semiconductor bandgap was derived in Shockley and Queisser's seminal paper.[6] One of the major assumptions made in this derivation is that the only loss pathway is radiative recombination.

One natural question is how the theoretical efficiency changes if this assumption breaks down? For example, if there are additional loss pathways within the material that compete with radiative recombination, how does this affect the device performance? Several studies have analyzed this question in detail, and the reader is encouraged to explore this concept outside the narrow breadth of this thesis. In brief, Shockley and Queisser made use of the thermodynamic concept that materials which absorb light, must also emit light in proportion to their absorptivity.[6] Therefore, a good solar cell material must also be a good radiative emitter. A simple relationship showing that the chemical potential in a broadband photochemical system is dependent on non-radiative recombination and the external luminescence efficiency was derived by Ross.[7] This relationship evaluates the maximum work which can be done by a photochemical system, and is outlined below.

The generation rate (G) within a light absorbing material can be described by equation 1:

$$G = \iint a(E) N_{AM1.5}(E) dE cos\theta d\Omega \tag{1}$$

Where a(E) is the dimensionless absorptivity as a function of energy, $N_{AM1.5}(E)$is the solar radiation spectrum, θ is the polar angle, and Ω is the solid angle of the incoming radiation.

The spontaneous emission rate from band to band transitions within the absorbing material can be described using the generalized Planck equation (equation 2):

$$b(E) = \frac{2n_r^2}{h^3 c^2} \frac{E^2 a(E)}{e^{\left(\frac{E-\mu}{kT}\right)} - 1} \tag{2}$$

Where n_r is the material refractive index, h is Planck's constant, c is the speed of light, k is Boltzmann's constant, T is the temperature, and μ is the quasi-Fermi level splitting.

The total recombination rate then becomes:

$$R_{ext} = \iint b(E) dE cos\theta d\Omega \tag{3}$$

Utilizing the fact that in the detailed balance limit, the generation rate is balanced by the photon emission rate, we equate equation (1) to equation (3) and use the Wien approximation (E-μ>>kT) to solve for μ.

$$\mu_{ideal} = kT \ln\left(\frac{\iint a(E) N_{AM1.5}(E) dE cos\theta d\Omega}{\iint B(E) dE cos\theta d\Omega}\right) \quad (4)$$

Where B(E) = $\frac{2n_r^2}{h^3c^2}\frac{E^2 a(E)}{e^{\left(\frac{E}{kT}\right)}}$

As often the photon emission rate can be modified by non-radiative recombination or other parasitic losses, the resulting emission rate is the ideal emission rate multiplied by the external photoluminescence quantum efficiency (PLQE or η_{ext}). The radiative recombination rate becomes

$$R_{ext}\eta_{ext} = \iint b(E) dE cos\theta d\Omega \, \eta_{ext} \quad (5)$$

By equating equation (1) with (5), making use of the Wien approximation, and the fact that $\mu = qV_{oc}$, we obtain

$$V_{oc} = V_{oc-ideal} - kT \, |\ln(\eta_{ext})| \quad (6)$$

As evident from equation (6), the radiative limit open circuit voltage cannot be achieved when η_{ext} is <1. Therefore, improving η_{ext} is a clear direction for optimizing a material for photovoltaic applications. In addition to this useful metric used to describe single absorber materials, another practical metric for characterizing how close full photovoltaic devices are to the radiative limit is external radiative efficiency (ERE).

Briefly, Green has shown an intricate relationship between ERE and photovoltaic power conversion efficiency,[8] by making use of Rau's reciprocity theorems, which relate electroluminescence spectra to external quantum efficiency (EQE).[9] Here, by simply knowing the open circuit voltage and EQE spectrum of a solar cell, one can determine the ERE according to Green's definition:

$$ERE = \frac{\frac{2\pi q}{h^3c^2} e^{qV_{oc}/kT} \int \frac{\overline{EQE}_{abs} E^2}{e^{E/kT-1}} dE}{J_{sc}} \quad (7)$$

$$= \frac{e^{qV_{oc}/kT} \int \overline{EQE}_{rel} N_{BB}(E) dE}{\int EQE_{rel} N_{AM1.5}(E) dE} \quad (8)$$

Where q is the elementary charge, $\overline{EQE}_{abs}$ and $\overline{EQE}_{rel}$ are the absolute and relative angularly weighted external quantum efficiency values, respectively, and N_{BB} is the black body spectrum.

Equation (8) essentially connects the electrical input of a solar cell to the optical output and vice versa.[9] This relationship has been verified by reporting an ERE value as high as 32.3% for the record single junction GaAs solar cell, which demonstrated a 28.8 % power conversion efficiency. In contrast, some of the best silicon solar cells, which have demonstrated power conversion efficiencies of 25%, exhibit ERE values as low as 0.57%.[8] From these examples, it is clear that improving ERE will allow devices to reach the radiative limit and the highest power conversion efficiencies. These findings are what motivates much of the work in this thesis.

1.2 Defects in Semiconductors

From the previous section, it is clear that the external radiative efficiency is a key parameter to optimize in designing efficient photovoltaic devices. Factors that inhibit photoluminescence quantum efficiency are 1) non-radiative recombination losses and 2) optical losses (i.e. parasitic absorption outside of the active layer or emission that escapes in a different direction other than the front surface).[10] With regards to the first point, non-radiative losses are often attributed to imperfections in the crystal lattice, which are commonly referred to as defects. Physically these could manifest themselves as point defects such as vacancies, interstitials, antisites; line defects such as dislocations; and planar defects such as twin and grain boundaries. These defects can introduce distortions in the uninterrupted translational symmetry of a perfect lattice. These small differences in bond strength and orientation introduce a large distribution of energy levels, often located within the bandgap.

Recombination, which occurs through these defect sites is commonly referred to as Shockley-Read-Hall (SRH) recombination.[11,12] This process typically occurs in two steps:

1) An electron (or hole) is trapped by an energy state within the bandgap.
2) A hole (or electron) populates the same energy state and the charge carrier recombines.

As this process does not result in the emission of a photon, it is considered to be a non-radiative process, where the energy is lost to vibrations in the lattice. This energy-loss mechanism is an avoidable pathway and therefore prevents the material from reaching the radiative limit.

Traps are generally described by a capture rate. In this general formulation, the capture rate is a product of the thermal velocity of the carrier (v_c), the capture cross-section (σ), and the trap density (N). Therefore the capture rate can be written as

$$AN = v_c \sigma N \tag{9}$$

$$= \sqrt{\frac{8kT}{\pi m}} (\pi r_c^2) N = \left(\frac{1}{sec}\right) \tag{10}$$

The terms in (9) can be expanded out as shown in (10), where m is the mass of the particle and r_c is the capture radius. The thermal velocity is described classically in this case, but could be significantly reduced by scattering with phonons and defects. The capture radius can depend on the charge of the defect as well as other thermodynamic factors. Reducing the number of trapped carriers is essential in reaching the radiative limit.

1.3 Perovskite Thin Films for Photovoltaic Devices

Perovskites are the general class of materials that have the generic formula ABX_3. Historically, several different formulations of the perovskite structure have been synthesized and studied in detail,[13] but more recently mixed organic-inorganic halide perovskites have shown exceptional promise as semiconducting layers in a host of electronic and optoelectronic applications.[14,15] In this subclass of perovskites, A is typically an organic or inorganic cation such as methylammonium ($CH_3NH_3^+$), formamidinium ($CH(NH_2)_2^+$), or Cs^+; B is a metal cation such as lead (Pb^{2+}) or tin (Sn^{2+}); and X is a halide such as I^-, Cl^-, or Br^-.

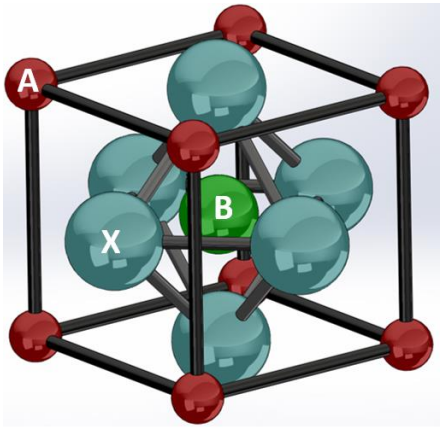

Figure 1.1 Schematic of the tetragonal crystal structure of a perovskite unit cell, where A is typically an organic cation, B is a metal cation, and X is a halide.

An attractive feature of the metal halide perovskites is that thin film semiconducting layers can easily be formed by a range of solution and vapor-phase based deposition techniques at relatively low temperatures (~100 ºC). The resulting films have demonstrated exceptional semiconducting properties, including high absorption coefficients comparable to high-quality GaAs,[16] low exciton binding energies,[17] long-range ambipolar diffusion,[18] and long carrier lifetimes,[18] and fairly high radiative efficiencies.[19]

From a material standpoint, this is quite remarkable as other solution-processed semiconductors, such as those derived from conjugated polymers, typically suffer from low carrier mobilities and poor external radiative efficiencies partly due to device architectures, but also the inevitable formation of defects from the facile processing. On the other hand, purely inorganic semiconductors are fabricated under more stringent conditions, where high temperatures and pressures are commonly deployed. These low-defect materials possess high carrier mobilities, long diffusion lengths, and also ultrahigh radiative efficiencies.[20,21] Mixed organic-inorganic perovskites find a balance between the two, with the processability of organic materials, but the optoelectronic quality approaching that of inorganic materials. This makes these materials highly desirable in the realization of a host of efficient flexible electronics including photovoltaic cells,[14] light-emitting diodes, lasers,[15] and transistors.[22]

Accordingly, the first solar cells demonstrated moderate efficiencies of 3.8%,[23] which have drastically improved over the past few years to values as high as 22.1%.[24] Most of these improvements have been achieved through improved processing conditions, materials design, and device architectures. Despite these unprecedented rises in power conversion efficiencies in the past few years, the fundamental photophysics that govern charge generation, transport, and recombination have not been properly elucidated. This thesis seeks to fill some of the gaps in this understanding in order to not only improve state-of-the-art devices, but also to help form a foundation in the rational design of high-quality, solution-processed semiconductors.

1.4 References

1 Agency, I. E. Energy and Air Pollution, World Energy Outlook 2016 Special Report. (2016).

2 King, D. Global clean energy in 2017. *Science* **355**, 111, doi:10.1126/science.aam7088 (2017).

3 Perez, R. a. P., M. A Fundamental Look at Energy Reserves for the Planet. *IEA-SHCP-Newsletter* **62** (2015).

4 Haegel, N. M. *et al.* Terawatt-scale photovoltaics: Trajectories and challenges. *Science* **356**, 141-143, doi:10.1126/science.aal1288 (2017).

5 Powell, D. M. *et al.* The capital intensity of photovoltaics manufacturing: barrier to scale and opportunity for innovation. *Energy Environ. Sci.* **8**, 3395-3408, doi:10.1039/c5ee01509j (2015).

6 Shockley, W. & Queisser, H. J. Detailed Balance Limit of Efficiency of p-n Junction Solar Cells. *Journal of Applied Physics* **32**, 510-519, doi:10.1063/1.1736034 (1961).

7 Ross, R. T. Some Thermodynamics of Photochemical Systems. *J. Chem. Phys.* **46**, 4590-4593, doi:10.1063/1.1840606 (1967).

8 Green, M. A. Radiative Efficiency of State-of-the-Art Photovoltaic Cells. *Prog. Photovolt: Res. Appl.* **20**, 472-476, doi:10.1002/pip.1147 (2012).

9 Rau, U. Reciprocity relation between photovoltaic quantum efficiency and electroluminescent emission of solar cells. *Phys. Rev. B*, doi:https://doi.org/10.1103/PhysRevB.76.085303 (2007).

10 Miller, O. D., Yablonovitch, E. & Kurtz, S. R. Strong Internal and External Luminescence as Solar Cells Approach the Shockley-Queisser Limit. *IEEE J. Photovolt.* **2**, 303-311, doi:10.1109/jphotov.2012.2198434 (2012).

11 Hall, R. N. Electron-Hole Recombination in Germanium. *Phys. Rev.* **87**, 387-387, doi:Doi 10.1103/Physrev.87.387 (1952).

12 Shockley, W. & Read, W. T. Statistics of the Recombinations of Holes and Electrons. *Phys. Rev.* **87**, 835-842, doi:10.1103/PhysRev.87.835 (1952).

13 Kagan, C. R. M., D.B.; Dimitrakopoulos, C.D. Organic-Inorganic Hybrid Materials as Semiconducting Channels in Thin-Film Field-Effect Transistors. *Science* **286**, 945-947, doi:10.1126/science.286.5441.945 (1999).

14 Zhang, W., Eperon, G. E. & Snaith, H. J. Metal Halide Perovskites for Energy Applications. *Nat. Energy* **1**, 16048, doi:10.1038/nenergy.2016.48 (2016).

15 Stranks, S. D. & Snaith, H. J. Metal-Halide Perovskites for Photovoltaic and Light-Emitting Devices. *Nat. Nanotechnol.* **10**, 391-402, doi:10.1038/nnano.2015.90 (2015).

16 De Wolf, S. *et al.* Organometallic Halide Perovskites: Sharp Optical Absorption Edge and Its Relation to Photovoltaic Performance. *J. Phys. Chem. Lett.* **5**, 1035-1039, doi:10.1021/jz500279b (2014).

17 Miyata, A. *et al.* Direct measurement of the exciton binding energy and effective masses for charge carriers in organic–inorganic tri-halide perovskites. *Nature Physics* **11**, 582-587, doi:10.1038/nphys3357 (2015).

18 Stranks, S. D. *et al.* Electron-Hole Diffusion Lengths Exceeding 1 Micrometer in an Organometal Trihalide Perovskite Absorber. *Science* **342**, 341-344, doi:Doi 10.1126/Science.1243982 (2013).
19 Deschler, F. *et al.* High Photoluminescence Efficiency and Optically Pumped Lasing in Solution-Processed Mixed Halide Perovskite Semiconductors. *J. Phys. Chem. Lett.* **5**, 1421-1426, doi:Doi 10.1021/Jz5005285 (2014).
20 Gmitter, I. S. E. Y. C. C. A. E. T. J. Ultra-high Spontaneous Emission Quantum Efficiency, 99.7% Internally And 72% Externally, From AlGaAs/GaAs/AlGaAs Double Heterostructures. *Appl. Phys. Lett.* **62**, 131-133, doi:10.1109/LEOS.1992.693875 (1993).
21 Cardona, P. Y. a. M. Fundamentals of Semiconductors: Physics and Materials Properties. *Springer-Verlag Berlin Heidelberg* **4** (2010).
22 Mei, Y., Zhang, C., Vardeny, Z. V. & Jurchescu, O. D. Electrostatic Gating of Hybrid Halide Perovskite Field-Effect Transistors: Balanced Ambipolar Transport at Room-Temperature. *MRS Commun.* **5**, 297-301, doi:http://dx.doi.org/10.1557/mrc.2015.21 (2015).
23 Kojima, A., Teshima, K., Shirai, Y. & Miyasaka, T. Organometal halide perovskites as visible-light sensitizers for photovoltaic cells. *J Am Chem Soc* **131**, 6050-6051, doi:10.1021/ja809598r (2009).
24 NCPV at NREL. Research Cell Efficiency Records. http:// www.nrel.gov/ncpv/ (accessed Dec. 11.

Chapter 2: Impact of Microstructure on Local Carrier Lifetime in Perovskite Solar Cells

Authors: Dane W. deQuilettes, Sarah M. Vorpahl, Samuel D. Stranks, Hirokazu Nagaoka, Giles E. Eperon, Mark E. Ziffer, Henry J. Snaith, David S. Ginger

2.1 Overview:

The remarkable performance of hybrid perovskite photovoltaics is attributed to their long carrier lifetimes and high photoluminescence (PL) efficiencies. High-quality films are associated with slower PL decays, and it has been claimed that grain boundaries have a negligible impact on performance. We used confocal fluorescence microscopy correlated with scanning electron microscopy to spatially resolve the PL decay dynamics from films of nonstoichiometric organic-inorganic perovskites, $CH_3NH_3PbI_3(Cl)$. The PL intensities and lifetimes varied between different grains in the same film, even for films that exhibited long bulk lifetimes. The grain boundaries were dimmer and exhibited faster non-radiative decay. Energy-dispersive x-ray spectroscopy showed a positive correlation between chlorine concentration and regions of brighter PL, while PL imaging revealed that chemical treatment with pyridine could activate previously dark grains.

2.2 Introduction:

As active layers in solar cells, organic-inorganic perovskites [25,26] combine the promise of solution processing [27,28] with the ability to tailor the band gap through chemical substitution [29-31], yielding solar-cell power conversion efficiencies as high as 20.1% [24]. Concomitant with their photovoltaic performance, perovskites also exhibit high fractions of radiative recombination with apparent carrier lifetimes of 250ns or longer [18,32], and are challenging the dogma that solution-processed semiconductors inevitably possess high densities of performance-limiting defects. Ensuring all recombination is radiative is critical for approaching the thermodynamic efficiency limits for solar cells and other optoelectronic devices [10].

Carrier recombination lifetimes measured by photoluminescence (PL) are commonly taken as a hallmark of perovskite film quality, with longer decay lifetimes used as indicators of better performing materials [18,32-35]. Carrier recombination kinetics have been described as a combination of trap-assisted, monomolecular (first-order), and bimolecular (second-order) recombination [36]. While most studies agree radiative bimolecular recombination dominates at high initial carrier densities ($n_0>10^{17}cm^{-3}$) [19,36-38], reports of kinetics at lower excitation densities (and relevant to solar cell operation) [39] range from single-exponential [33,40], to biexponential [34,35], to stretched-exponential [18,30] functions with varying levels of fidelity. These distributions have in turn been explained in terms of unintentional doping [41] or charge trapping [42]. The perovskite growth conditions [27,28,32] and post-deposition treatments [33,43] can greatly alter film morphology, carrier lifetime, and device performance, yet the underlying relations between these parameters are important open questions. For instance, perovskite films grown from nonstoichiometric mixed halide (Cl/I) precursor solutions have exhibited lifetimes of

hundreds of nanoseconds, but PL lifetimes in films grown from chloride-free precursors are generally much shorter [18,40].

Correlated confocal PL and scanning electron microscopy (SEM) has been a powerful tool to reveal structure/function relationships in biology [44]. Here we applied similar techniques to study structure/function relationships in perovskite films. We found substantial local PL heterogeneity even for $CH_3NH_3PbI_3(Cl)$ films with average lifetimes of ~1μs (comparable to the longest lifetimes reported) [18,32], which suggests considerable scope remains for reducing non-radiative recombination in these films. In addition to observing entire grains which appear dark, we also observed that grain boundaries are associated with PL quenching, indicating they are not as benign as has been suggested previously [45,46]. We further used PL microscopy to show post-deposition chemical treatments can activate previously "dark" regions in the film, and we correlated local energy-dispersive x-ray spectroscopy (EDS) with confocal fluorescence maps, finding brighter grains with longer lifetimes were associated with local spikes in Cl concentration.

2.3 Photovoltaic Device and Photoluminescence Measurements:

We studied $CH_3NH_3PbI_3(Cl)$ films prepared on glass slides by spin-coating a nonstoichiometric mixed halide precursor solution comprised of CH_3NH_3I and $PbCl_2$ (3:1) in *N*,*N*-dimethylformamide [39,47]. Films prepared under identical conditions and incorporated into standard solar cell device architectures (Fig. S1) [39] exhibit power conversion efficiencies (η) up to 14.5% (Fig. 1A), which is comparable to other reports using this architecture [26,48]. Importantly, Fig. 1B shows that our PL lifetimes are as long as those reported for films used in the best devices to date [32]. These films exhibited average carrier lifetimes >1000ns when excited at low intensity ($30nJ/cm^2$, $n_0 \sim 10^{15} cm^{-3}$). At short times (Fig. 1B inset), the PL decay could appear nearly single-exponential, but at longer times, the decay deviated from a single-exponential [18,30,36]. We fit the decay in Fig. 1B with a stretched-exponential function of characteristic lifetime, τ_c=431ns, and distribution parameter, β=0.57, which we interpret as arising from a superposition of exponential relaxation functions (see below) with an average lifetime of $<\tau>$=1005ns [39,49].

Green and co-workers recently examined microscopic PL quenching of discontinuous perovskite islands with *n*- and *p*-type capping layers [50]. Here, we used fluorescence microscopy to probe the inherent decay properties of neat semiconducting films. Figure 1 shows a correlated SEM micrograph (Fig. 1C), confocal PL image (Fig. 1D), and an overlaid SEM/PL microscopy image (Fig. 1E) of a high-performing perovskite film on a glass substrate. Although this film appears contiguous (Fig. 1C) and exhibits $<\tau>$=1005ns, Fig. 1D shows a large distribution in local PL intensity across the film. We observed these large distributions in films prepared in different research labs (Fig. S2D) [39], and we exclude variations in film thickness (Fig. S2) [39] and photodegradation during imaging (Fig. S3) [39] as primary causes. The PL intensity not only varied from grain to grain, with roughly 30% of grains imaged in Fig. 1C consisting of dark grains *(19)*, but we also observed ~65% lower PL intensity at grain boundaries (Fig. S4, A-C) [39], after

deconvolution of the microscope point spread function (Fig. S5) [39]. These results are surprising because, through considerations of detailed balance [10,51], one expects high performance films to have minimal non-radiative decay.

2.4 Local Time-Resolved Photoluminescence Decay Dynamics:

Instead, the spatial variations in PL intensity in the polycrystalline perovskite films are suggestive of variations in local non-radiative decay rates. By taking local steady-state and time-resolved PL data, we confirmed darker regions have greater non-radiative loss. Figure 2 shows a confocal PL image (Fig. 2A) along with local PL spectra (Fig. 2B) and lifetime data (Fig. 2C-E) from a film with a long average bulk lifetime ($<\tau>$=1010ns). Figure 2B shows the steady-state spectra of a bright (red square) and dark (blue circle) region. The PL spectrum collected at the dark region is both red-shifted (~2nm) and slightly broader than the bright region (Fig. S6) [39]. These trends suggest a less sharp band-edge [52], likely caused by the presence of defect states or shallow trapping levels in the darker regions. In Figs. 2C-2E, we show local PL decays of the indicated dark and bright regions at low ($1\mu J/cm^2$), medium ($2.1\mu J/cm^2$), and high ($3.4\mu J/cm^2$) excitation intensities. Several studies have reported a transition from trap-assisted monomolecular recombination to free-carrier bimolecular recombination over this fluence range [36,38]. Consistent with the picture that bright regions have fewer non-radiative pathways, bright regions show a slower decay, a transition to bimolecular recombination kinetics at a lower excitation fluence, and more efficient PL quenching when contacted by fullerene (Fig. S7) [39] in comparison to dim regions. We modeled the PL dynamics (black lines in Fig. 2C-E) as a combination of trapping, monomolecular, and bimolecular recombination *(19)*. We report a higher deep trap state density in the dark region ($4x10^{16}cm^{-3}$) compared to the bright region ($<1x10^{15}cm^{-3}$). In addition, we extracted the trapping, monomolecular, and bimolecular decay rates in both regions to be $1x10^{-8}cm^3s^{-1}$, $1x10^6s^{-1}$, and $2.3\text{-}7.8x10^{-11}cm^3s^{-1}$, respectively. We also report consistent ratios of PL intensity measured across the steady state and integrated time-resolved PL measurements (Fig. S8) for bright and dark regions *(19)*.

Importantly, the local PL lifetimes are also shorter at grain boundaries (Fig. S4E) [39]. Grain boundaries frequently serve as non-radiative recombination centers in polycrystalline semiconductor films [53]. Studies have suggested that grain boundaries in perovskites are less detrimental than in other semiconductors [45,46], or even beneficial [54]. Other results suggest that single crystal perovskites exhibit even higher performance [55-57], and some describe improvements in carrier lifetime and device performance from post-growth treatments, such as exposure of the film to pyridine (C5H5N), in the context of surface passivation [33,43].

2.5 Improvements in Photoluminescence by Pyridine Vapor Treatment:

In this context, we next show pyridine vapor exposure can brighten dark domains. In Fig. 3, A and B, we show the PL from a $CH_3NH_3PbI_3(Cl)$ film before and after exposure to pyridine vapor. The entire film was both brighter (~8X integrated over the entire image) and more uniform after pyridine exposure (no enhancement without pyridine, Fig. S9) [39]. For instance, the relative increase of a dark domain (squares in Fig. 3A and 3B), was 180% larger than the relative increase of a bright domain (circles). Interestingly, the PL

emission also blue-shifted (by ~3nm) and narrowed slightly (Fig. 3C) after pyridine exposure, which could be caused by a reduction in shallow trap density. Finally, Fig. 3D shows that the grain boundary brightness, relative to the surrounding grains, increased by 11% and the width decreased by 25% after pyridine exposure (see Fig. S10 for other examples) *(19).* Both trends are consistent with passivation, albeit incomplete, of defects at grain boundaries. Although pyridine treatment can also result in some restructuring of film morphology (Fig. S10) [39], these data suggest pyridine was indeed remediating non-radiative defects in the perovskite film.

2.6 Correlation of High Photoluminescence with Chlorine Content

Finally, we explored the role of Cl in perovskite films by comparing SEM/EDS elemental composition traces with local PL intensity traces. Figure 4A shows an overlaid SEM/PL microscopy image of a $CH_3NH_3PbI_3$(Cl) film on glass. We tracked the changes in PL intensity with Cl content (Fig. 4B) and showed bright regions correlate with areas of higher relative Cl content (Cl/Cl+I) (trace Cl in $CH_3NH_3PbI_3$ control films, Fig. S11) [39]. Although films prepared from Cl/I mixed halide precursors stoichiometrically resemble triiodides [58], there is evidence for residual Cl at levels of ~2wt% or less [34,59]. The lifetime enhancement in the presence of Cl is consistent with recent findings that Cl-rich nucleation sites lead to better crystal coalescence [60,61] and helps explain why films grown in the presence of Cl have slower recombination rates [18,37]. We hypothesize Cl could be present at the surface or within the crystals, interstitially or substitutionally, or simply at the substrate surface as a residual but unincorporated component leftover from the seeding of low-defect crystallites. We performed time-of-flight secondary ion mass spectrometry (Fig. S11F) [39], and found higher Cl content in $CH_3NH_3PbI_3$(Cl) films compared to $CH_3NH_3PbI_3$ films without Cl. This data probes the top 2nm of the film.

2.7 Conclusions:

Although perovskite solar cells have better radiative efficiencies than many technologies such as dye-sensitized solar cells, organic solar cells, or even CdTe, they still suffer from greater non-radiative losses than inorganic materials such as GaAs, and are only at present approaching CIGS [51]. Our results identify a subpopulation of dark grains and grain boundaries as specific targets for perovskite growth and passivation studies, and show that local fluorescence lifetime imaging provides a route by which changes in film processing can be evaluated to assess their influence on carrier recombination in films. By removing these non-radiative pathways to obtain uniform brightness with high emissivity across all grains, it is likely that we will see the performance of perovskite devices approach the thermodynamic limits for solar cells and other light-emitting devices.

2.8 Appendix A:

Materials and methods and supplementary text

2.9 Acknowledgments:

This material is based in part upon work supported by the State of Washington through the University of Washington Clean Energy Institute. DWD acknowledges support from a National Science Foundation Graduate Research Fellowship (DGE-1256082). SMV acknowledges support from a National Defense Science and Engineering Graduate Fellowship. The research leading to these results has received funding from the European Union Seventh Framework Program [FP7/2007-2013] under Grant Agreement No. 604032 of the MESO project. GE is supported by the EPSRC and Oxford Photovoltaics Ltd. through a Nanotechnology KTN CASE award. The authors gratefully acknowledge funding from the National Institute for Biomedical Imaging and Bioengineering (NIH grant EB-002027) supporting NESAC/BIO and ToF-SIMS instrumentation. D.W.D thanks Ian Braly, David Moerman, and Brigit Miller for valuable assistance. S.M.V. gratefully acknowledges Dan Graham for assistance with ToF-SIMS. Additional data, including materials, methods, and key controls are available online as Supplementary Material *(19)*.

2.10 Figures:

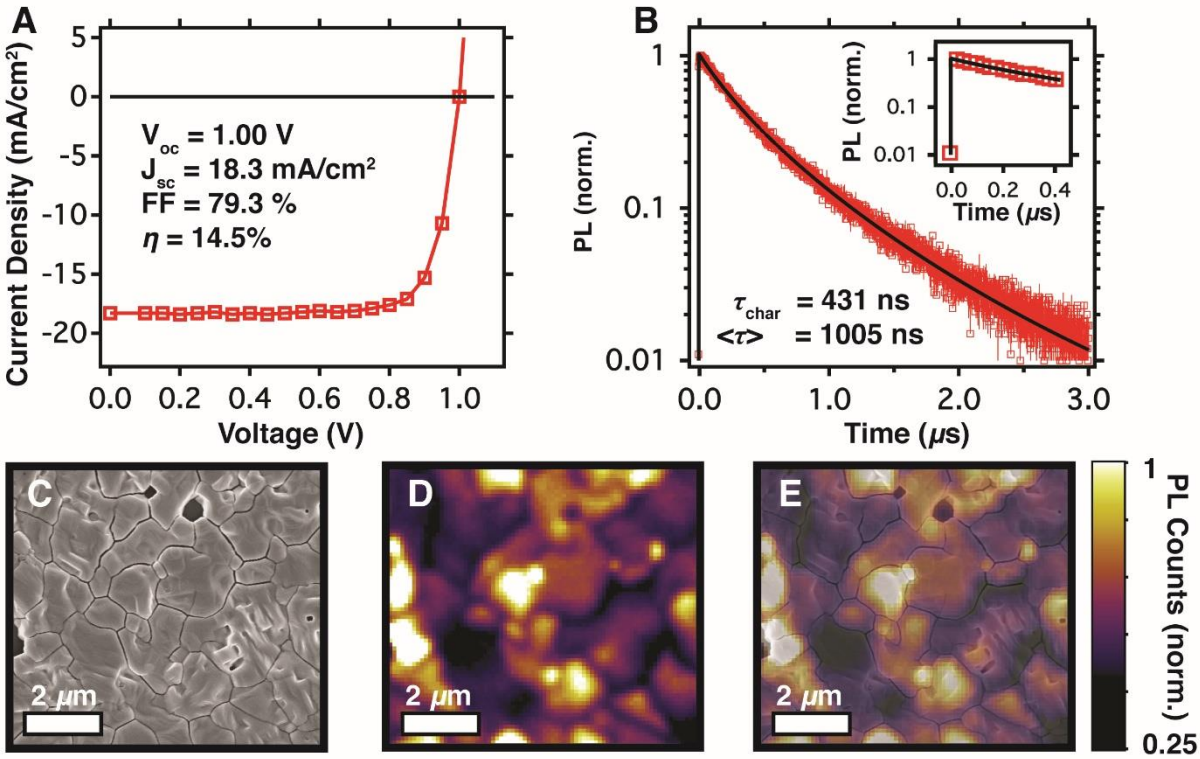

Figure 2.1. Solar cell device measurement, bulk PL lifetime measurement, and correlated images from scanning electron microscopy (SEM) and fluorescence microscopy experiments. (**A)** Light current-voltage **(**J-V) characteristics of a high-performing mixed halide perovskite solar cell. (**B)** Bulk time-resolved PL decay trace of $CH_3NH_3PbI_3(Cl)$ perovskite film on glass after excitation at 470nm, 125kHz, 30nJ/cm^2 (n_0~10^{15}cm^{-3}), and fitted to a stretched-exponential function with $<\tau>$=1005ns, (τ_c=431ns, β=0.57), with nearly single-exponential dynamics at short times (inset). **(C)** Correlated SEM micrograph, **(D)** fluorescence image, and **(E)** composite image showing significant variations in PL intensity across different grains and grain boundaries.

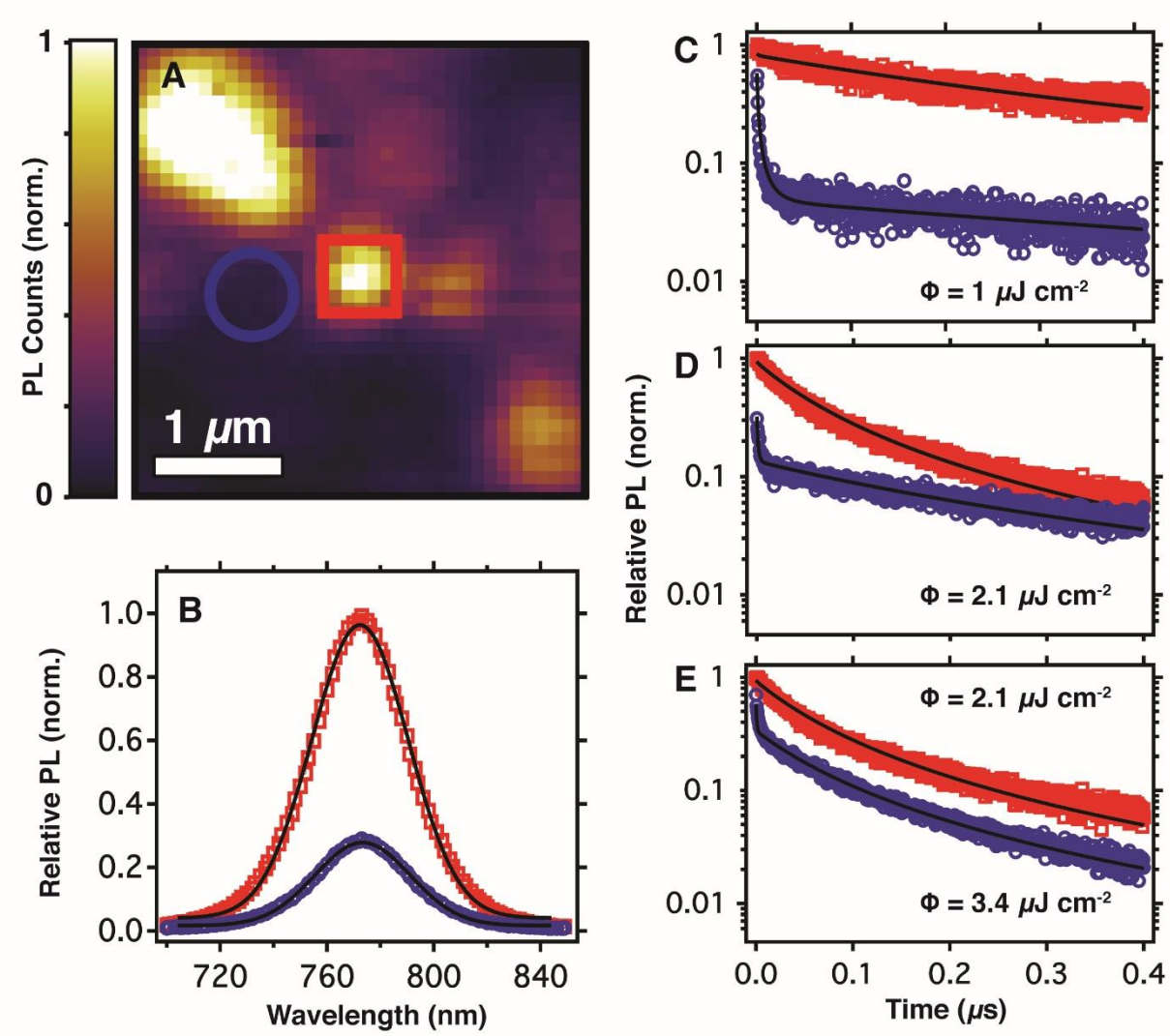

Figure 2.2. Fluorescence microscopy of $CH_3NH_3PbI_3(Cl)$ film and local PL measurements. (A) A 3μm by 3μm fluorescence image of the perovskite film with bulk lifetime $<\tau>$=1010ns (τc =433ns, β =0.57). **(B)** Relative steady state PL spectra of bright (red square) and dark (blue circle) regions. **(C)** Time-resolved PL decay curves of bright (red square) and dark (blue circle) regions after excitation at 470nm, 125kHz, φ=1μJ/cm^2 (n_0 ~5x10^{16}cm^{-3}), **(D)** φ=2.1μJ/cm^2 (n_0~1x10^{17}cm^{-3}) and **(E)** bright region measured at φ=2.1μJ/cm^2 vs. dark region measured at φ=3.4μJ/cm^2 (n_0~1.6x10^{17}cm^{-3}) showing dark regions require higher initial carrier densities to exhibit kinetics dominated by bimolecular recombination. Black traces are simulations to the data *(19)*.

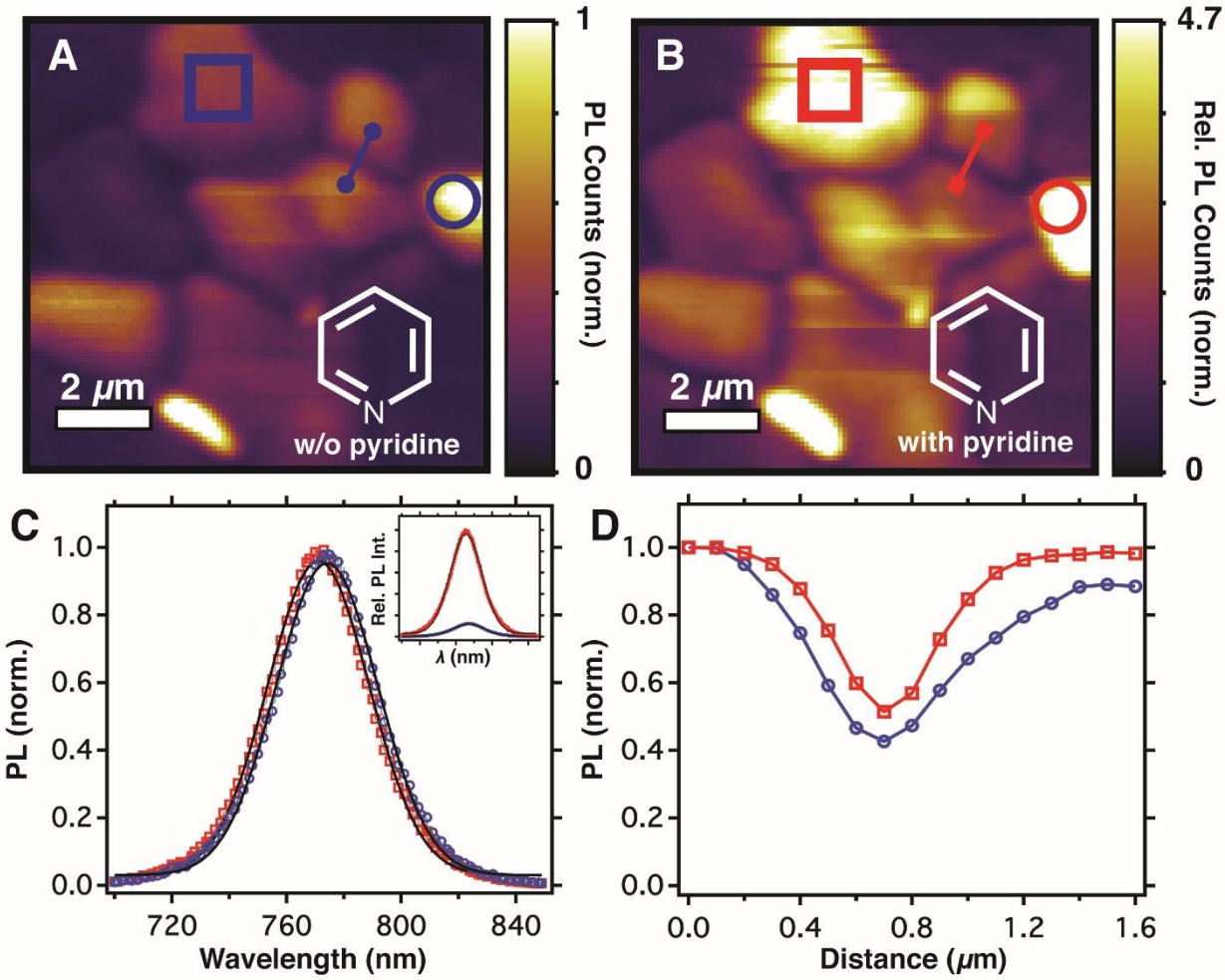

Figure 2.3. Fluorescence microscopy of $CH_3NH_3PbI_3(Cl)$ film with pyridine vapor treatment. (A) Fluorescence image before and **(B)** after treatment showing activation of $CH_3NH_3PbI_3(Cl)$ film. **(C)** Local steady-state PL spectra showing the relative PL intensities before (blue circle) and after (red square) treatment (inset) and normalized spectra showing a slight blue shift and narrowing of FWHM after treatment. **(D)** Grain boundary PL line scan before (blue line in 3A) and after (red line in 3B) treatment showing slight relative reduction in PL quenching across the grain boundary post-treatment.

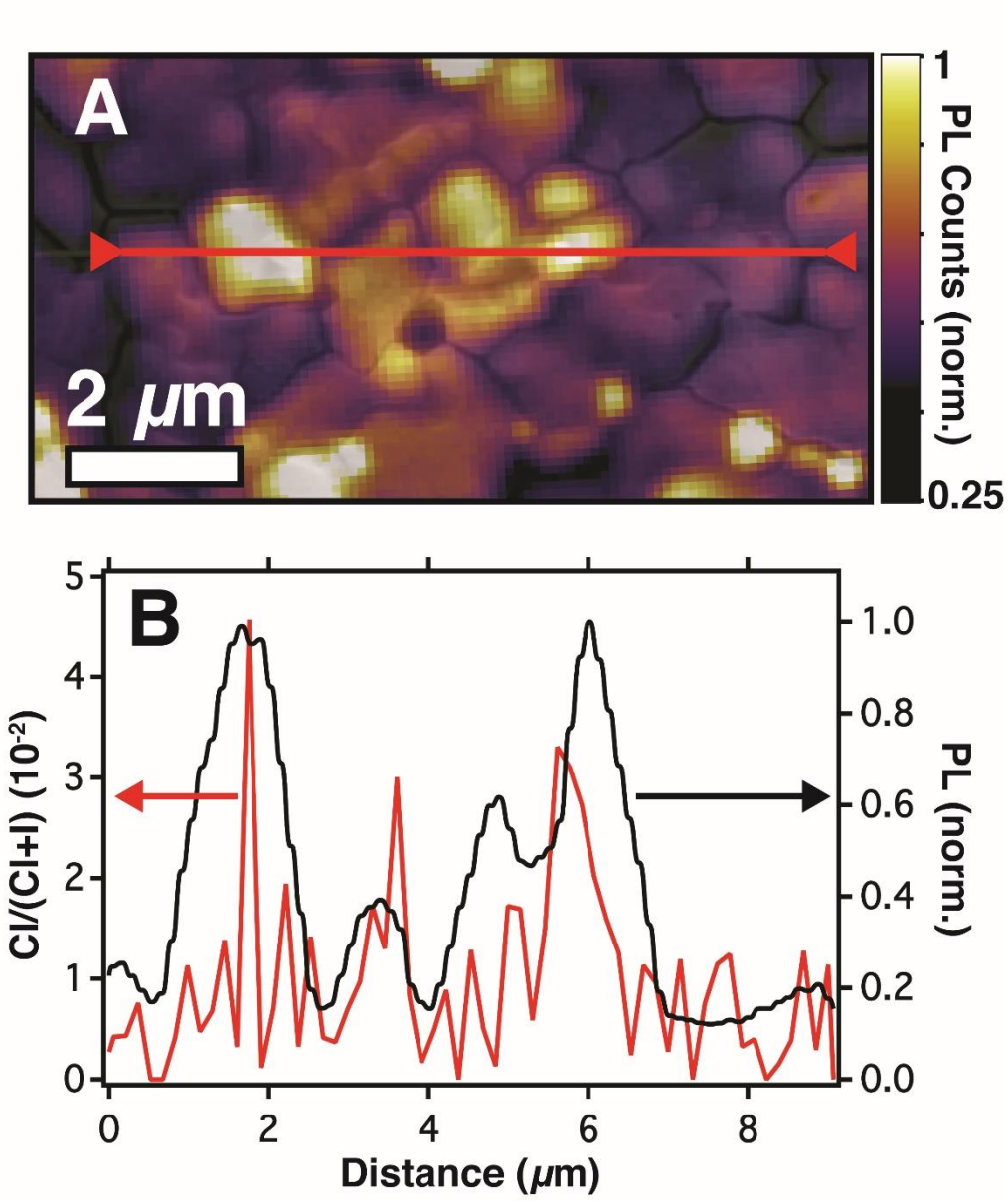

Figure 2.4. Correlated images and line scans of $CH_3NH_3PbI_3(Cl)$ film using fluorescence microscopy, scanning electron microscopy (SEM), and energy-dispersive x-ray spectroscopy (EDS). (A) SEM micrograph overlaid on fluorescence image and **(B)** EDS line scan showing the local elemental weight ratio of Cl/(Cl+I) tracks areas of higher integrated PL intensity indicating Cl is associated with better performing grains.

2.11 References:

1. T. C. Sum, N. Mathews, Advancements in perovskite solar cells: photophysics behind the photovoltaics. *Energ. Environ. Sci.* **7**, 2518-2534 (2014).
2. M. A. Green, A. Ho-Baillie, H. J. Snaith, The emergence of perovskite solar cells. *Nat. Photonics* **8**, 506-514 (2014).
3. J. Burschka *et al.,* Sequential deposition as a route to high-performance perovskite-sensitized solar cells. *Nature* **499**, 316-319 (2013).
4. G. E. Eperon, V. M. Burlakov, P. Docampo, A. Goriely, H. J. Snaith, Morphological control for high performance, solution-processed planar heterojunction perovskite solar cells. *Adv. Funct. Mater.* **24**, 151-157 (2014).
5. G. Xing *et al.,* Low-temperature solution-processed wavelength-tunable perovskites for lasing. *Nat. Mater.* **13**, 476-480 (2014).
6. G. E. Eperon *et al.,* Formamidinium lead trihalide: a broadly tunable perovskite for efficient planar heterojunction solar cells. *Energ. Environ. Sci.* **7**, 982-988 (2014).
7. J. H. Noh, S. H. Im, J. H. Heo, T. N. Mandal, S. I. Seok, Chemical management for colorful, efficient, and stable inorganic-organic hybrid nanostructured solar cells. *Nano Lett.* **13**, 1764-1769 (2013).
8. NCPV at NREL. Research Cell Efficiency Records. http:// www.nrel.gov/ncpv/ (accessed April 11, 2015).
9. S. D. Stranks *et al.,* Electron-hole diffusion lengths exceeding 1 micrometer in an organometal trihalide perovskite absorber. *Science* **342**, 341-344 (2013).
10. H. Zhou *et al.,* Interface engineering of highly efficient perovskite solar cells. *Science* **345**, 542-546 (2014).
11. O. D. Miller, E. Yablonovitch, S. R. Kurtz, Strong internal and external luminescence as solar cells approach the Shockley-Queisser limit. *IEEE J. Photovolt.* **2**, 303-311 (2012).
12. N. K. Noel *et al.,* Enhanced photoluminescence and solar cell performance via Lewis base passivation of organic-inorganic lead halide perovskites. *ACS Nano* **8**, 9815-9821 (2014).
13. J. B. You *et al.,* Low-temperature solution-processed perovskite solar cells with high efficiency and flexibility. *ACS Nano* **8**, 1674-1680 (2014).
14. P. W. Liang *et al.,* Additive enhanced crystallization of solution-processed perovskite for highly efficient planar-heterojunction solar cells. *Adv. Mater.* **26**, 3748-3754 (2014).
15. S. D. Stranks *et al.,* Recombination kinetics in organic-inorganic perovskites: excitons, free charge, and subgap states. *Phys. Rev. Applied* **2**, 034007 (2014).
16. F. Deschler *et al.,* High photoluminescence efficiency and optically pumped lasing in solution-processed mixed halide perovskite semiconductors. *J. Phys. Chem. Lett.* **5**, 1421-1426 (2014).
17. C. Wehrenfennig, M. Z. Liu, H. J. Snaith, M. B. Johnston, L. M. Herz, Charge-carrier dynamics in vapour-deposited films of the organolead halide perovskite $CH_3NH_3PbI_{3-x}Cl_x$. *Energ. Environ. Sci.* **7**, 2269-2275 (2014).

18. J. S. Manser, P. V. Kamat, Band filling with free charge carriers in organometal halide perovskites. *Nat. Photonics* **8**, 737-743 (2014).
19. See Supplementary Materials on Science Online.
20. G. Xing *et al.*, Long-range balanced electron- and hole-transport lengths in organic-inorganic $CH_3NH_3PbI_3$. *Science* **342**, 344-347 (2013).
21. Y. Yamada, T. Nakamura, M. Endo, A. Wakamiya, Y. Kanemitsu, Photocarrier recombination dynamics in perovskite $CH_3NH_3PbI_3$ for solar cell applications. *J. Am. Chem. Soc.* **136**, 11610-11613 (2014).
22. M. Saba *et al.*, Correlated electron-hole plasma in organometal perovskites. *Nature Commun.* **5**, 5049 (2014).
23. A. Abate *et al.*, Supramolecular halogen bond passivation of organic-inorganic halide perovskite solar cells. *Nano Lett.* **14**, 3247-3254 (2014).
24. S. Watanabe *et al.*, Protein localization in electron micrographs using fluorescence nanoscopy. *Nat. Methods* **8**, 80-84 (2011).
25. E. Edri *et al.*, Why lead methylammonium tri-iodide perovskite-based solar cells require a mesoporous electron transporting scaffold (but not necessarily a hole conductor). *Nano Lett.* **14**, 1000-1004 (2014).
26. W. J. Yin, T. Shi, Y. Yan, Unique properties of halide perovskites as possible origins of the superior solar cell performance. *Adv. Mater.* **26**, 4653-4658 (2014).
27. M. M. Lee, J. Teuscher, T. Miyasaka, T. N. Murakami, H. J. Snaith, Efficient hybrid solar cells based on meso-superstructured organometal halide perovskites. *Science* **338**, 643-647 (2012).
28. P. Gao, M. Gratzel, M. K. Nazeeruddin, Organohalide lead perovskites for photovoltaic applications. *Energ. Environ. Sci.* **7**, 2448-2463 (2014).
29. K. Munechika *et al.*, Quantum dot/plasmonic nanoparticle metachromophores with quantum yields that vary with excitation wavelength. *Nano Lett.* **11**, 2725-2730 (2011).
30. X. Wen *et al.*, Morphology and carrier extraction study of organic–inorganic metal halide perovskite by one- and two-photon fluorescence microscopy. *J. Phys. Chem. Lett.* **5**, 3849-3853 (2014).
31. K. Tvingstedt *et al.*, Radiative efficiency of lead iodide based perovskite solar cells. *Sci Rep.* **4**, 6071 (2014).
32. S. De Wolf *et al.*, Organometallic halide perovskites: sharp optical absorption edge and its relation to photovoltaic performance. *J. Phys. Chem. Lett.* **5**, 1035-1039 (2014).
33. C. H. Seager, Grain boundaries in polycrystalline silicon. *Annu. Rev. Mater. Sci.* **15**, 271-302 (1985).
34. J. S. Yun *et al.*, Benefit of grain boundaries in organic–inorganic halide planar perovskite solar cells. *J. Phys. Chem. Lett.* **6**, 875-880 (2015).
35. Q. Dong *et al.*, Electron-hole diffusion lengths > 175 μm in solution-grown $CH_3NH_3PbI_3$ single crystals. *Science* **347**, 967-970 (2015).
36. W. Nie *et al.*, High-efficiency solution-processed perovskite solar cells with millimeter-scale grains. *Science* **347**, 522-525 (2015).
37. D. Shi *et al.*, Low trap-state density and long carrier diffusion in organolead trihalide perovskite single crystals. *Science* **347**, 519-522 (2015).

38. M. Gratzel, The light and shade of perovskite solar cells. *Nat. Mater.* **13**, 838-842 (2014).
39. G. Grancini *et al.,* The impact of the crystallization processes on the structural and optical properties of hybrid perovskite films for photovoltaics. *J. Phys. Chem. Lett.* **5**, 3836-3842 (2014).
40. Y. Tidhar *et al.,* Crystallization of methyl ammonium lead halide perovskites: implications for photovoltaic applications. *J. Am. Chem. Soc.* **136**, 13249-13256 (2014).
41. S. T. Williams *et al.,* Role of chloride in the morphological evolution of organo-lead halide perovskite thin films. *ACS Nano* **8**, 10640-10654 (2014).

Chapter 3: Tracking Photoexcited Carriers in Hybrid Perovskite Semiconductors: Trap-Dominated Spatial Heterogeneity and Diffusion

Authors: Dane W. deQuilettes, Sarthak Jariwala, Sven Burke, Mark E. Ziffer, Jacob T.-W. Wang, Henry J. Snaith, David S. Ginger

3.1 Overview:

We use correlated confocal and widefield fluorescence microscopy to probe the interplay between local variations in charge carrier recombination and carrier transport in methylammonium lead triiodide perovskite thin films. We find that local photoluminescence variations present in confocal imaging are also observed in widefield imaging, while intensity-dependent confocal measurements show that the heterogeneity in non-radiative losses observed at low excitation powers becomes less pronounced at higher excitation powers. Both confocal and widefield images show that carriers undergo anisotropic diffusion due to differences in inter-grain connectivity. These data are all qualitatively consistent with trap-dominated variations in local photoluminescence intensity, and with grain boundaries that exhibit varying degrees of opacity to carrier transport. We use a two-dimensional kinetic model to simulate and compare confocal time-resolved photoluminescence decay traces with experimental data. The simulations further support the assignment of local variations in non-radiative recombination as the primary cause of photoluminescence heterogeneity in the films studied herein. These results point to surface passivation and inter-grain connectivity as areas that could yield improvements in perovskite solar cell and optoelectronic device performance.

3.2 Introduction:

Organic-inorganic perovskites have demonstrated promising semiconducting properties for a range of optoelectronic applications,(*1, 2*) yet many devices are still limited by non-radiative recombination(*3, 4*) and internal photoluminescence quantum efficiencies are still below unity in solution-processed thin films.(*5-7*)

Confocal fluorescence microscopy has served as a powerful tool to probe structure-function relationships in polycrystalline thin films and has provided insight into potential sources of non-radiative loss in perovskites. Our group previously showed that photoluminescence intensities and lifetimes varied between different grains in the same film and furthermore showed that grain boundaries were generally dimmer and exhibited faster photoluminescence decays.(*8*) Several groups have now reported similar local variations in photoluminescence intensity, and have generally interpreted these results as showing variations in non-radiative recombination rates due to heterogeneous distributions of surface traps.(*8-20*) Although many of these reports attribute the contrast in the confocal fluorescence and cathodoluminescence imaging to spatial variation in non-radiative recombination, other reports have ascribed the heterogeneity to the effects of heterogeneous diffusion outside of the excitation volume and collection spot.(*21, 22*). In particular, Tian *et al.* showed that photoexcited carriers generated under a diffraction-limited spot size undergo diffusion outside the spot, affecting the measured photoluminescence.(*22*) Furthermore, Yang *et al.* have attributed confocal photoluminescence contrast exclusively to variations in grain size and diffusion, and

indeed found that photoluminescence intensity was anticorrelated with grain size in their samples.(*21*)

The origins of the photoluminescence heterogeneity in perovskites, and the existence of structural and electronic barriers to lateral carrier diffusion in perovskite film are important topics that not only affect the performance of perovskites in solar cells and other device applications, but also in turn affect the analysis of many other experiments, and even the extraction of fundamental properties like carrier diffusion lengths and recombination rate constants.

To address these important questions head on, we combine confocal and widefield fluorescence microscopy with local modeling to better understand the interplay of local non-radiative recombination and diffusion in explaining the photoluminescence of methylammonium lead triiodide.

3.3 Confocal Versus Widefield Fluorescence Imaging:

We prepared neat perovskite films on glass by spin-coating a precursor solution containing $PbOAc_2 \cdot 3H_20$ and methylammoniumiodide (MAI) in *N*,*N*-dimethylformamide with a hypophosphorous acid (HPA) additive, following previous reports.(*23, 24*) This procedure has been used to form perovskite active layers in high-performing photovoltaic devices with power conversion efficiencies approaching 20%.(*23, 24*) Scanning electron microscopy (SEM) confirmed the formation of large-grain, pin-hole free films without noticeable voids or gaps between grains that might physically impede charge transport (Figure S1).

Next, we used correlated confocal and widefield fluorescence microscopy to study the intrinsic photoluminescence properties of these films. Importantly, we performed both measurements in the same area to serve as a direct comparison of material response under optical excitation. Figure 1a shows a confocal fluorescence image taken at a relatively low excitation fluence of 0.2 μJ/cm^2 per pulse compared to a widefield fluorescence image (Figure 1b) taken at a comparable continuous-wave (cw) excitation density 220 mW/cm^2 (~ 3 suns). Under these experimental conditions, we estimate the initial and steady-state carrier densities to be ~10^{15} cm^{-3}, which is below or comparable with the reported trap state densities (~$1x10^{15}$ - $1x10^{17}$ cm^{-3}) in commonly prepared perovskite thin films.(*8, 10, 25, 26*) Both images show significant contrast in the local photoluminescence intensity, appear similar by eye, and have a strong quantitative linear correlation (R = 0.69, Figure S2). This result suggests that, at least at excitation densities on the order of those encountered in a solar cell, the confocal photoluminescence data collected from a diffraction-limit spot in our samples at least appears qualitatively similar to the data collected when the entire film is illuminated with a large area excitation source.

These similar images suggest that, for the types of perovskite samples studied in this work and under low excitation powers, non-radiative recombination is present and varies locally (see SI and Figures S3-S6 for a complete consideration of alternate explanations). Importantly, we expect diffusion to have less of an impact in the widefield experiment compared to the confocal experiment because the excitation spot size (~50 μm) is much larger than the typical reported diffusion lengths (~ 1-5 μm).(*7, 22, 27, 28*) In other words, since the widefield image excites the entire field of view uniformly, diffusion out

of the excitation spot cannot be the dominant factor in the photoluminescence heterogeneity.

3.4 Intensity-Dependent Fluorescence Images:

On the surface, these results appear quite distinct from those of Zhu and coworkers(*21*) as well as Jin and coworkers.(*22*) One obvious explanation is that we could be studying different perovskite films with different trap distributions. In addition to perovskite properties being notoriously sensitive to growth conditions,(*29, 30*) the conditions under which the films are imaged can also influence the measurement results. For instance, the photoluminescence quantum efficiency of bulk perovskite films is well-known to depend on excitation power, where at higher powers traps become saturated and increasing rates of radiative bimolecular recombination start to outcompete non-radiative channels.(*7, 12, 25, 26, 31, 32*) In the literature, groups have conducted their confocal photoluminescence imaging over a range of more than two orders of magnitude in intensity, ranging from 0.03 to 10 μJ/cm^2 per pulse for pulsed excitation(*8, 10, 12, 15, 21*) and from 10 to 5,000 mW/cm^2 for continuous-wave excitation.(*12, 14, 18-20*) We next consider the effect that using excitation densities much higher than those encountered in a solar cell might have on the resulting photoluminescence data.

Figure 2 explores the dependence of local confocal photoluminescence imaging on perovskite films as a function of continuous-wave excitation power. Figure 2a shows a fluorescence image collected at a low excitation power (180 mW/cm^2, 532 nm), where we observe large variations in the local photoluminescence intensity consistent with previous reports.(*8, 10*) Figure 2b-d show photoluminescence images collected at higher excitation powers, where we observe more uniform photoluminescence images (image histograms are reported in Figure S7). Notably, we observe this same shift to more uniform photoluminescence images for *both* widefield excitation and pulsed excitation, where the local kinetics also converged at higher excitation fluences (Figures S8 and S9). Consistent with these results, we note that studies using higher fluences in the literature also tend to observe less local variation in photoluminescence.(*12, 21*) For example, Zhu and coworkers used a higher excitation fluence (3 μJ/cm^2 per pulse)(*21*) to generate an initial carrier density of ~6x10^{17} cm^{-3} (higher than reported trap state densities, 1x10^{15}-1x10^{17} cm^{-3}) (*8, 10, 25, 26*) and observed diffusion-dominated behavior. Diffusion-dominated behavior is signified by an anticorrelation between grain size and photoluminescence intensity,(*21*) where the carrier population becomes more dilute in larger grains due to diffusion and results in a smaller fraction of radiative recombination as the reduced bimolecular rate is less able to outcompete non-radiative decay.(*21*) At high excitation powers (90,000 mW/cm^2), we observed this same anticorrelation between average grain photoluminescence intensity and grain area (Figure S10), but observed little correlation at lower excitation powers (180 mW/cm^2). These results highlight the importance of performing confocal experiments at lower excitation powers or fluences if the goal is to probe for local variations in non-radiative decay rates.

3.5 Probing Diffusion with Local Excitation and Widefield Detection:

Next, we explicitly consider the extent of diffusion in the sample under low-to-moderate excitation density with a diffraction-limited spot as encountered in the confocal experiment. A number of experiments have reported indirect evidence for the existence of lateral diffusion and diffusion barriers affecting photoluminescence distributions in

perovskite thin films – indeed, the existence of photoluminescence heterogeneity in a variety of local-probe (confocal, cathodoluminescence, and NSOM) experiments is strong evidence for such barriers.(*11-13*) In addition to these imaging studies, lateral carrier diffusion has previously been probed using separate excitation and collection objectives,(*13, 22*) as well as a scanning single-photon detector.(*33*)

Here, we used a simple alternative technique to probe the extent of carrier transport under steady-state conditions. Briefly, we used a diffraction-limited laser spot to photoexcite the sample and then detect the photoluminescence over a large area with a sensitive charge-coupled device (CCD) camera, revealing the extent of the resulting carrier recombination profile. Figure 3a shows a fluorescence image of a perovskite thin film sample with photoluminescence contrast consistent with Figures 1 and 2a. Figures 3b-f show widefield photoluminescence images of a selection of grains that have been locally excited (colored circles represent the laser spot locations, where the diameter of the circle is the measured full-width half-maximum of the focused laser beam). Notably, these images show that carriers diffuse outside of the excitation volume (and therefore outside of the confocal pinhole collection spot). We believe that this anisotropic behavior does not likely result from photon recycling, which we expect would result in a more uniform photoluminescence profile.(*34*) Importantly, these images show that the local excitation is predominantly confined to the excited grain, confirming the existence of a barrier to lateral carrier diffusion at grain boundaries as has previously been proposed.(*21, 35, 36*) Notably, however, figures 3b-f show that carriers do diffuse across grain boundaries, and provide direct evidence that the inter-grain conductivity varies significantly from grain to grain. Factors that govern inter-grain connectivity and diffusivity will be interesting topics of future studies.

3.6 Probing Diffusion with Local Excitation and Widefield Detection After Surface Treatment:

The anisotropic diffusion observed in Figure 3 likely results from poor inter-grain connectivity, which could originate from facet-dependent crystallographic terminations,(*37*) local variations in trap energetics,(*34*) or potential barriers at the grain boundaries.(*21, 35, 38, 39*) Previously, Li *et al.* have proposed that treatments with alkylphosphonic acids result in the cross-linking of grains and an improvement in photovoltaic performance.(*40*) Whether these improvements in device metrics result from enhancements in lateral conductivity (due to the cross-linking) or passivation is still an open question. In this regard, we have previously studied *n*-trioctylphosphine oxide (TOPO) as a surface passivating agent.(*9*) Here, we performed a fluorescence microscopy study to test the influence of this ligand on inter-grain transport. Figure 4a and b show matched-area fluorescence images before and after treatment with TOPO on the same intensity scale. We report a spatially-averaged improvement in photoluminescence emission of ~3x after TOPO treatment, consistent with the enhancement in photoluminescence lifetime (Figure S11). Figure 4c-e show local excitation/widefield detection fluorescence images (similar to that of Figure 3) and normalized profiles of various grains before and after surface treatment with TOPO. We observe a range of behaviors in the grain-to-grain line profiles, where grain transparency appears to increase (Figure 4c), decrease (Figure 4d), and remain relatively unchanged (Figure 4e). We note

that these profiles in emission intensity are likely influenced by changes in inter-grain connectivity, disproportional improvements in grain emission due to local variations in passivation,(*8, 9*) and possibly an increased contribution from photon recycling. Together these considerations complicate a quantitative description of grain transparency and carrier flux in these films as a function of surface treatment, but suggest that future studies could isolate the relative contributions by measuring the spatiotemporal dynamics and pairing this data with a suitable kinetic model.

Currently, there is still a debate in the field on whether grain boundaries are localized regions of non-radiative recombination,(*21, 38*) self-passivating or benign,(*41*) or whether they form a potential barrier for charge transport.(*21, 35, 38, 39*) The fact that they appear dimmer in the widefield image (Figure 1b) and under high excitation power (Figure 2d) suggests that they are possibly static or dynamic quenching centers or local regions that repel carriers towards the grain centers. Both of these ideas are further supported by grain-size-dependent mobility and photoconductivity studies, where charge carrier mobility and photocurrent collection were found to increase as a function of grain size.(*35, 36, 42*) Although this behavior may seem unique to perovskites, silicon and GaAs polycrystalline films have also shown charge accumulation at grain boundaries which has led to carrier repulsion.(*43, 44*) Other potential explanations could be differences in the transport mechanisms between grain interiors and grain boundaries, where defect-mediated hopping at grain boundaries could affect mobility as previously observed in CdTe films.(*34*)

3.7 Kinetic Modelling of Confocal Time-Resolved Photoluminescence Kinetics:

Together figures 1-4 suggest that both non-radiative recombination as well as diffusion are present in these films when measured at low excitation powers, but whether non-radiative recombination or diffusion dominates likely depends on experimental conditions (i.e. excitation power) as well as sample characteristics (trap concentration, diffusion coefficient, inter-grain connectivity, and grain size). To better quantify how these different parameters affect the confocal time-resolved photoluminescence kinetics, we simulated the evolution of the carrier population using a simplified set of coupled, partial differential equations and took into account both diffusion and trap-filling as described in equations 1 and 2:

$$\frac{\partial N_c(x,y,t)}{\partial t} = D\nabla^2 N_c(x,y,t) - k_{DT} N_{DT}(\mathrm{x,y,t}) N_C(\mathrm{x,y,t}) - k_m N_c(x,y,t) - k_b N_c(x,y,t)^2 \quad (1)$$

$$\frac{\partial N_{DT}(x,y,t)}{\partial t} = -k_{DT} N_{DT}(\mathrm{x,y,t}) N_C(\mathrm{x,y,t}) \quad (2)$$

Here $N_c(x,y,t)$ is the carrier density as a function of position (x,y) and time (t), D is the ambipolar diffusion coefficient, ∇^2 is the Laplacian operator, k_{DT} is the deep trap non-radiative recombination rate constant, $N_{DT}(x,y,t)$ is the density of available deep traps, k_m is the radiative monomolecular recombination rate constant, and k_b is the bimolecular rate constant.

Equations for the initial and boundary conditions as well as a complete description of the simulation parameters can be found in the supporting information. Figure 5a shows the simulated photoluminescence intensity as a function of time under the confocal pinhole without the trap-filling term (N_{DT} = 0, diffusion-dominated simulation) and with an initial carrier density of $3x10^{16}$ cm^{-3} (black trace). We observed an order-of-magnitude drop in photoluminescence intensity within the first ~25 ns, which can be attributed to fast diffusion outside of the confocal pinhole, consistent with simulations previously reported by Tian *et al*.(*22*) When we increased the initial carrier density to $8x10^{16}$ cm^{-3} (red trace), the fast drop in intensity was qualitatively unaffected and the kinetics became slightly faster due to the increase in carrier population. Next, we studied the behavior with inclusion of the trap-filling term (N_{DT} = $4x10^{16}$ cm^{-3} and k_{DT} = $1x10^{8}$ s^{-1}). Figure 5b shows the simulated photoluminescence kinetics, where the fast initial drop can be attributed to the depletion in the carrier population due to trapping as well as diffusion outside of the confocal pinhole. We increased the initial carrier density to $8x10^{16}$ cm^{-3} (red trace) and observed the fast initial drop decrease in magnitude, which can be attributed to trap-filling. This behavior is distinct from the trend observed for the diffusion-dominated simulation and serves as a useful reference to experimentally differentiate between diffusion and trap-filling.

With our simulations showing qualitative differences in intensity-dependent photoluminescence kinetics for trap-dominated and diffusion-dominated scenarios, we next turn to test these predications against experimental data. To make this comparison, we measured the trends in time-resolved photoluminescence kinetics as function of excitation fluence for a $CH_3NH_3PbI_3(Cl)$ thin film on glass. Figure 5c shows a confocal fluorescence image measured at 0.2 $\mu J/cm^2$ per pulse (2.5 MHz repetition rate, 470 nm), again demonstrating spatial heterogeneity in the photoluminescence emission. Figure 5d shows the time-resolved photoluminescence kinetics of the dark region marked with a white square as a function of excitation fluence. Initially, we observed a fast initial drop in photoluminescence intensity (black trace), which could result from either diffusion outside of the confocal pinhole or non-radiative recombination. We increased the excitation fluence to yield an initial carrier density of $8x10^{16}$ cm^{-3}, and observed a reduction in the magnitude of the fast initial drop. This trend in the fluence-dependent carrier dynamics is qualitatively consistent with the trap-dominated simulation in Figure 5b, and therefore we conclude that the recombination kinetics in this region of the film are dominated by a trap-mediated mechanism rather than diffusion, consistent with our earlier studies on similar films.(*8*) Previously, we had used a similar kinetic model to extract local trap state densities in a $CH_3NH_3PbI_3(Cl)$ film,(*8*) and while we find here that carrier diffusion out of the confocal excitation spot complicates *quantitative* extraction of local trap density, the assignments of local qualitative variations in non-radiative recombination rates remain intact. Importantly, the trends we observed here and in our previous work,(*8*) are consistent with local variations of non-radiative recombination and a reduction in these pathways at higher excitation fluences (*cf.* Figure 2).

We note that as sample quality improves, and local non-radiative recombination centers are passivated, for example with improved surface termination,(*8, 9, 45, 46*) the reduction in non-radiative recombination will push samples closer to the diffusion-dominated

regime (see Figure S12).

3.8 Conclusions:

In summary, we used confocal and widefield fluorescence microscopy to assess how structural and electronic defects influence carrier recombination and transport in hybrid perovskite thin films. First, we correlated confocal and widefield fluorescence images to show that the images appear qualitatively similar. Importantly, this result suggests that non-radiative recombination is dominating the photoluminescence heterogeneity in our films, as diffusion is negligible in the widefield experiment when the excitation spot size is much greater than the diffusion length. Next, we performed intensity-dependent confocal fluorescence measurements to probe for local changes in the relative fractions of radiative recombination. We found that at higher excitation powers, the local contrast in the photoluminescence images becomes less prevalent as the trap-mediated pathways became saturated and diffusive behavior dominates. Next, we studied carrier diffusion in these samples by locally exciting a grain with a diffraction-limited spot and imaging the photoluminescence emission surrounding the excitation spot. We observed the diffusion of carriers outside of the confocal spot and show that there are extensive variations in inter-grain carrier transport throughout the film that are affected in complicated ways by treatment with surface passivating agents that are known to improve photoluminescence intensity by reducing non-radiative recombination. We hope this work inspires the study of this rich and important phenomena, while providing a relatively facile means to do so using widefield imaging. Finally, we used a detailed kinetic model to simulate time-resolved photoluminescence data and show that trap-filling behavior is prominent in dark regions of prototypical perovskite films that have been widely studied. These findings give deeper insight into the fundamental photophysics of carrier recombination and transport on the microscale, where it is expected that this knowledge will be further leveraged in fabricating optimized optoelectronic devices.

3.9 Appendix B:

Materials and methods and supplementary text

3.10 Acknowledgements:

D. deQuilettes and D. Ginger acknowledge DOE (DE-SC0013957) for supporting correlative microscopy work. D. deQuilettes. acknowledges support from an NSF Graduate Research Fellowship (DGE-1256082). Part of this work was conducted at the Molecular Analysis Facility, a National Nanotechnology Coordinated Infrastructure site at the University of Washington, which is supported in part by the National Science Foundation (grant ECC-1542101), the University of Washington, the Molecular Engineering & Sciences Institute, the Clean Energy Institute, and the National Institutes of Health.

3.11 Figures:

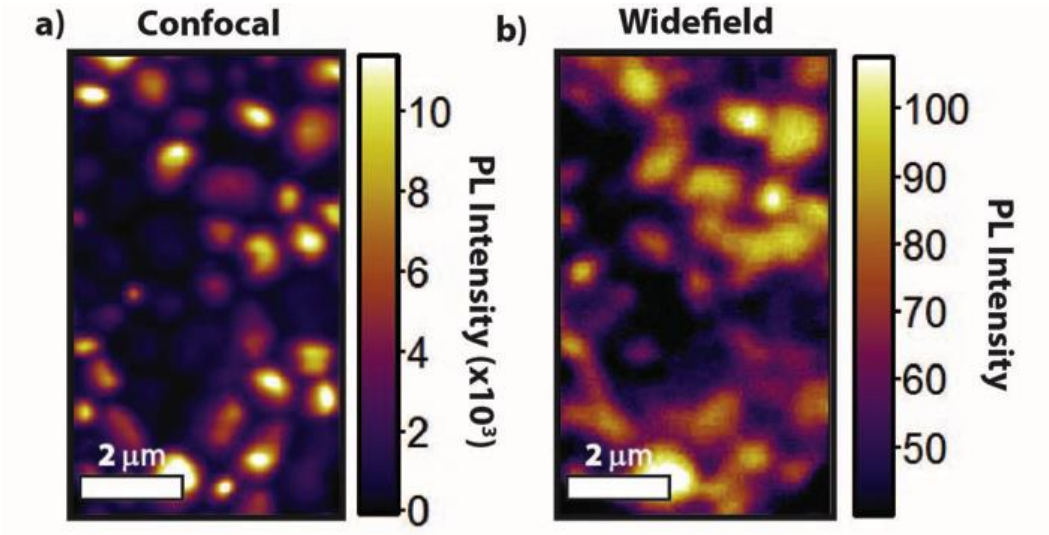

Figure 3.1: Comparison of confocal and widefield photoluminescence images of a $CH_3NH_3PbI_3$ perovskite film on glass showing similar spatial variation, thus ruling out diffusion out of the confocal spot as the primary source of intensity variation for these samples images when measured at low excitation power. a) Confocal fluorescence image (470 nm, 2.5 MHz, 0.2 μJ/cm^2) and b) widefield fluorescence image of the same area (532 nm, 220 mW/cm^2), where both images show variations in PL intensity across different grains and grain boundaries.

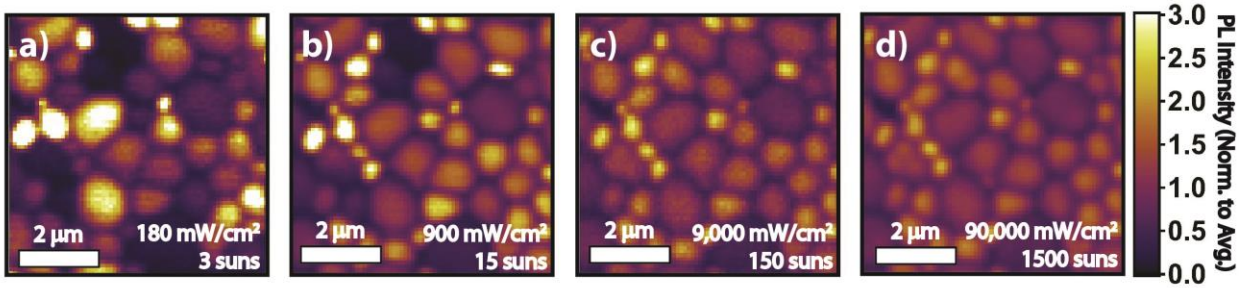

Figure 3.2: Intensity dependent confocal photoluminescence (PL) images of a $CH_3NH_3PbI_3$ perovskite film on glass showing that the images become more uniform at higher fluence. a) Confocal fluorescence image measured at 180 mW/cm^2 (~3 suns), b) 900 mW/cm^2 (~15 suns), c) 9,000 mW/cm^2 (~150 suns), and d) 90,000 mW/cm^2 (~1500 suns) showing a reduction in grain-to-grain contrast.

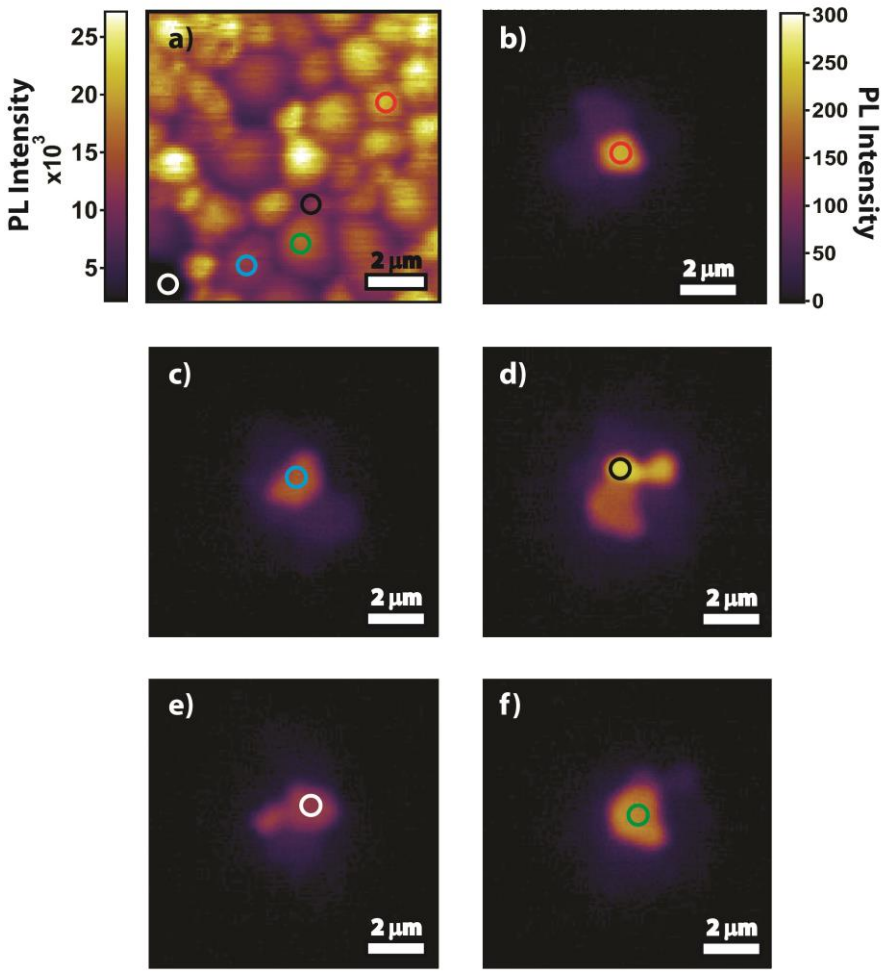

Figure 3.3: Confocal excitation and widefield detection reveal inter-grain diffusion and inter-grain diffusion barriers in perovskite films. a) Confocal fluorescence image of a $CH_3NH_3PbI_3$ perovskite film on glass (532 nm, 300 mW/cm^2) and b-f) widefield images of various grains which were locally excited with a diffraction-limited spot in the grain centers (colored circles represent the photoexcitation areas, where the circle diameter is the measured FWHM of the laser excitation spot).

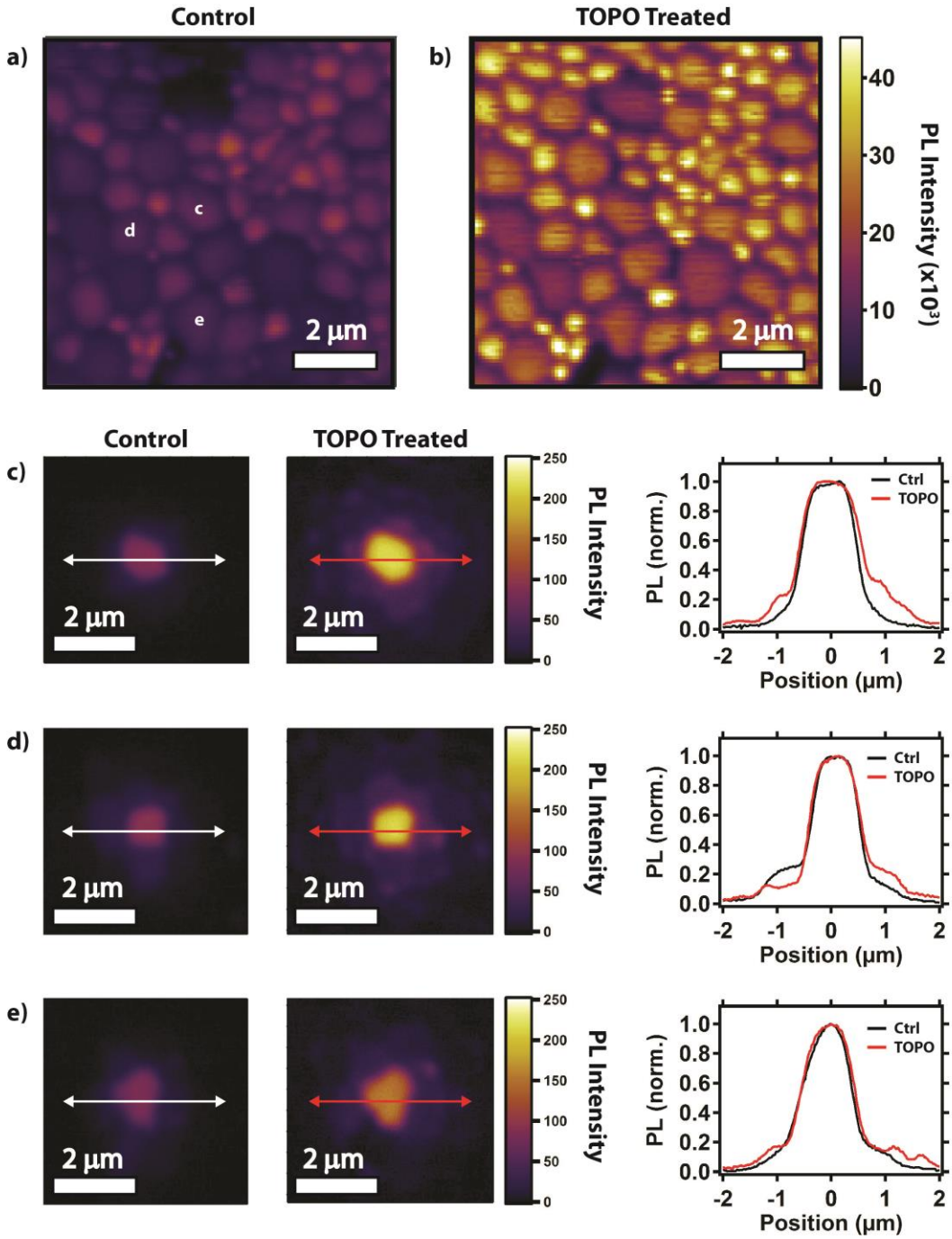

Figure 3.4: Effects of *n*-trioctylphosphine oxide (TOPO) treatment on grain-connectivity. Photoluminescence (PL) images of a $CH_3NH_3PbI_3$ perovskite film on glass (532 nm, 180 mW/cm^2) before a) and after b) TOPO treatment, c-e) local excitation/widefield detection images and photoluminescence line scans, showing c) an increase, d) decrease, and e) neutral effect on carrier transport.

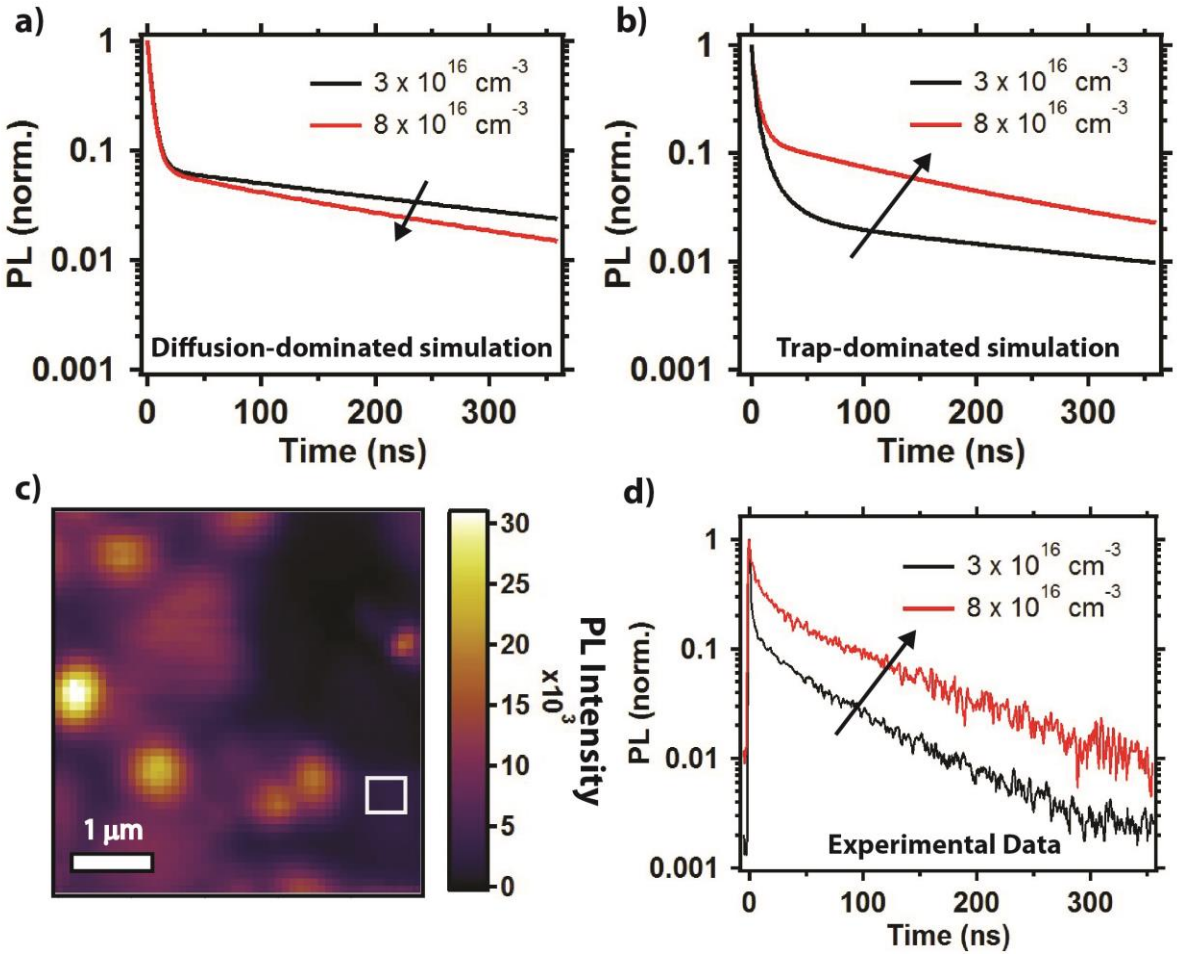

Figure 3.5: Comparison of simulated and experimental time-resolved photoluminescence (PL) decays shows evidence for trap-dominated photoluminescence decays. Simulated time-resolved photoluminescence integrated under the confocal pinhole at low ($3x10^{16}$ cm^{-3}, black) and high ($8x10^{16}$ cm^{-3}, red) initial carrier densities with a) no trap-filling (N_{DT} = 0) term, b) with a trap-filling term (N_{DT} = $4x10^{16}$ cm^{-3}, k_{DT} = $1x10^{8}$ s^{-1}), (c) fluorescence image of a $CH_3NH_3PbI_3(Cl)$ film on glass, and d) experimental data showing intensity-dependent, time-resolved photoluminescence kinetics of the region designated by a white box in (c), showing the trend is qualitatively similar to the trap-dominated simulation. In both simulations, D = 0.17 cm^2s^{-1}, k_m = $1x10^{6}$ s^{-1}, and k_b = $8x10^{-11}$ cm^{-3}.

3.12 References:

1. Stranks, S. D.; Snaith, H. J. Metal-halide perovskites for photovoltaic and light-emitting devices. *Nat. Nanotechnol.* **2015**, 10, 391-402.
2. Sutherland, B. R.; Sargent, E. H. Perovskite photonic sources. *Nat. Photonics* **2016**, 10, 295-302.
3. Miller, O. D.; Yablonovitch, E.; Kurtz, S. R. Strong internal and external luminescence as solar cells approach the shockley-queisser limit. *IEEE J. Photovolt.* **2012**, 2, 303-311.
4. Ball, J. M.; Petrozza, A. Defects in perovskite-halides and their effects in solar cells. *Nat. Energy* **2016**, 1, 16149.
5. Richter, J. M.; Abdi-Jalebi, M.; Sadhanala, A.; Tabachnyk, M.; Rivett, J. P.; Pazos-Outon, L. M.; Godel, K. C.; Price, M.; Deschler, F.; Friend, R. H. Enhancing photoluminescence yields in lead halide perovskites by photon recycling and light out-coupling. *Nat Commun* **2016**, 7, 13941.
6. Pazos-Outon, L. M.; Szumilo, M.; Lamboll, R.; Richter, J. M.; Crespo-Quesada, M.; Abdi-Jalebi, M.; Beeson, H. J.; Vrucinic, M.; Alsari, M.; Snaith, H. J. *et al.* Photon recycling in lead iodide perovskite solar cells. *Science* **2016**, 351, 1430-1433.
7. Johnston, M. B.; Herz, L. M. Hybrid perovskites for photovoltaics: Charge-carrier recombination, diffusion, and radiative efficiencies. *Acc. Chem. Res.* **2016**, 49, 146-154.
8. deQuilettes, D. W.; Vorpahl, S. M.; Stranks, S. D.; Nagaoka, H.; Eperon, G. E.; Ziffer, M. E.; Snaith, H. J.; Ginger, D. S. Impact of microstructure on local carrier lifetime in perovskite solar cells. *Science* **2015**, 348, 683-686.
9. deQuilettes, D. W.; Koch, S.; Burke, S.; Paranji, R. K.; Shropshire, A. J.; Ziffer, M. E.; Ginger, D. S. Photoluminescence lifetimes exceeding 8 μs and quantum yields exceeding 30% in hybrid perovskite thin films by ligand passivation. *ACS Energy Letters* **2016**, 438-444.
10. deQuilettes, D. W.; Zhang, W.; Burlakov, V. M.; Graham, D. J.; Leijtens, T.; Osherov, A.; Bulovic, V.; Snaith, H. J.; Ginger, D. S.; Stranks, S. D. Photo-induced halide redistribution in organic-inorganic perovskite films. *Nat. Commun.* **2016**, 7, 11683.
11. Bischak, C. G.; Sanehira, E. M.; Precht, J. T.; Luther, J. M.; Ginsberg, N. S. Heterogeneous charge carrier dynamics in organic-inorganic hybrid materials: Nanoscale lateral and depth-dependent variation of recombination rates in methylammonium lead halide perovskite thin films. *Nano Lett.* **2015**, 15, 4799-4807.
12. Draguta, S.; Thakur, S.; Morozov, Y. V.; Wang, Y.; Manser, J. S.; Kamat, P. V.; Kuno, M. Spatially non-uniform trap state densities in solution-processed hybrid perovskite thin films. *J. Phys. Chem. Lett.* **2016**, 7, 715-721.
13. Vrućinić, M.; Matthiesen, C.; Sadhanala, A.; Divitini, G.; Cacovich, S.; Dutton, S. E.; Ducati, C.; Atatüre, M.; Snaith, H.; Friend, R. H. *et al.* Local versus long-range diffusion effects of photoexcited states on radiative recombination in organic-inorganic lead halide perovskites. *Adv. Sci.* **2015**, 2, 1500136.

14. Merdasa, A.; Tian, Y.; Camacho, R.; Dobrovolsky, A.; Debroye, E.; Unger, E. L.; Hofkens, J.; Sundstrom, V.; Scheblykin, I. G. "Supertrap" at work: Extremely efficient nonradiative recombination channels in mapbi3 perovskites revealed by luminescence super-resolution imaging and spectroscopy. *ACS nano* **2017**, 11, 5391-5404.
15. Simpson, M. J.; Doughty, B.; Das, S.; Xiao, K.; Ma, Y. Z. Separating bulk and surface contributions to electronic excited-state processes in hybrid mixed perovskite thin films via multimodal all-optical imaging. *J Phys Chem Lett* **2017**, 8, 3299-3305.
16. Yamashita, D.; Handa, T.; Ihara, T.; Tahara, H.; Shimazaki, A.; Wakamiya, A.; Kanemitsu, Y. Charge injection at the heterointerface in perovskite ch3nh3pbi3 solar cells studied by simultaneous microscopic photoluminescence and photocurrent imaging spectroscopy. *J Phys Chem Lett* **2016**, 7, 3186-3191.
17. De Marco, N.; Zhou, H.; Chen, Q.; Sun, P.; Liu, Z.; Meng, L.; Yao, E. P.; Liu, Y.; Schiffer, A.; Yang, Y. Guanidinium: A route to enhanced carrier lifetime and open-circuit voltage in hybrid perovskite solar cells. *Nano Lett.* **2016**, 16, 1009-1016.
18. Galkowski, K.; Mitioglu, A. A.; Surrente, A.; Yang, Z.; Maude, D. K.; Kossacki, P.; Eperon, G. E.; Wang, J. T.; Snaith, H. J.; Plochocka, P. *et al.* Spatially resolved studies of the phases and morphology of methylammonium and formamidinium lead tri-halide perovskites. *Nanoscale* **2017**, 9, 3222-3230.
19. Mastroianni, S.; Heinz, F. D.; Im, J. H.; Veurman, W.; Padilla, M.; Schubert, M. C.; Wurfel, U.; Gratzel, M.; Park, N. G.; Hinsch, A. Analysing the effect of crystal size and structure in highly efficient $CH_3NH_3PbI_3$ perovskite solar cells by spatially resolved photo- and electroluminescence imaging. *Nanoscale* **2015**, 7, 19653-19662.
20. Mamun, A. A.; Ava, T. T.; Jeong, H. J.; Jeong, M. S.; Namkoong, G. A deconvoluted pl approach to probe the charge carrier dynamics of the grain interior and grain boundary of a perovskite film for perovskite solar cell applications. *Phys. Chem. Chem. Phys.* **2017**, 19, 9143-9148.
21. Yang, M.; Zeng, Y.; Li, Z.; Kim, D. H.; Jiang, C. S.; van de Lagemaat, J.; Zhu, K. Do grain boundaries dominate non-radiative recombination in ch3nh3pbi3 perovskite thin films? *Phys. Chem. Chem. Phys.* **2017**, 19, 5043-5050.
22. Tian, W.; Cui, R.; Leng, J.; Liu, J.; Li, Y.; Zhao, C.; Zhang, J.; Deng, W.; Lian, T.; Jin, S. Limiting perovskite solar cell performance by heterogeneous carrier extraction. *Angew Chem Int Ed Engl* **2016**, 55, 13067-13071.
23. Zhang, W.; Pathak, S.; Sakai, N.; Stergiopoulos, T.; Nayak, P. K.; Noel, N. K.; Haghighirad, A. A.; Burlakov, V. M.; deQuilettes, D. W.; Sadhanala, A. *et al.* Enhanced optoelectronic quality of perovskite thin films with hypophosphorous acid for planar heterojunction solar cells. *Nat Commun* **2015**, 6, 10030.
24. Jacob Tse-Wei Wang, Z. W., Sandeep K Pathak, Wei Zhang, D.W. deQuilettes, Florencia Wisnivesky, Jian Huang, Pabitra Nayak, Jay Patel, Yana Vaynzof, Rui Zhu, Ivan Ramirez, Jin Zhang, Caterina Ducati, Chris Grovenor, Michael

Johnston, David S Ginger, Robin Nicholas, Henry Snaith. Efficient perovskite solar cells by metal ion doping. *Energ. Environ. Sci.* **2016**, 9, 2892-2901.
25. Stranks, S. D.; Burlakov, V. M.; Leijtens, T.; Ball, J. M.; Goriely, A.; Snaith, H. J. Recombination kinetics in organic-inorganic perovskites: Excitons, free charge, and subgap states. *Phys. Rev. Appl.* **2014**, 2, 034007.
26. Herz, L. M. Charge-carrier dynamics in organic-inorganic metal halide perovskites. *Annu Rev Phys Chem* **2016**, 67, 65-89.
27. Stranks, S. D.; Eperon, G. E.; Grancini, G.; Menelaou, C.; Alcocer, M. J. P.; Leijtens, T.; Herz, L. M.; Petrozza, A.; Snaith, H. J. Electron-hole diffusion lengths exceeding 1 micrometer in an organometal trihalide perovskite absorber. *Science* **2013**, 342, 341-344.
28. Stoddard, R. J.; Eickemeyer, F. T.; Katahara, J. K.; Hillhouse, H. W. Correlation between photoluminescence and carrier transport and a simple in-situ passivation method for high-bandgap hybrid perovskites. *J Phys Chem Lett* **2017**.
29. Park, N.-G. Crystal growth engineering for high efficiency perovskite solar cells. *CrystEngComm* **2016**, 18, 5977-5985.
30. Park, N. G. Methodologies for high efficiency perovskite solar cells. *Nano Converg* **2016**, 3, 15.
31. Yamada, Y.; Nakamura, T.; Endo, M.; Wakamiya, A.; Kanemitsu, Y. Photocarrier recombination dynamics in perovskite ch3nh3pbi3 for solar cell applications. *J. Am. Chem. Soc.* **2014**, 136, 11610-11613.
32. Zheng, K.; Žídek, K.; Abdellah, M.; Messing, M. E.; Al-Marri, M. J.; Pullerits, T. Trap states and their dynamics in organometal halide perovskite nanoparticles and bulk crystals. *J. Phys. Chem. C* **2016**, 120, 3077-3084.
33. Akselrod, G. M.; Deotare, P. B.; Thompson, N. J.; Lee, J.; Tisdale, W. A.; Baldo, M. A.; Menon, V. M.; Bulovic, V. Visualization of exciton transport in ordered and disordered molecular solids. *Nat Commun* **2014**, 5, 3646.
34. Alberi, K.; Fluegel, B.; Moutinho, H.; Dhere, R. G.; Li, J. V.; Mascarenhas, A. Measuring long-range carrier diffusion across multiple grains in polycrystalline semiconductors by photoluminescence imaging. *Nat Commun* **2013**, 4, 2699.
35. Reid, O. G.; Yang, M.; Kopidakis, N.; Zhu, K.; Rumbles, G. Grain-size-limited mobility in methylammonium lead iodide perovskite thin films. *ACS Energy Letters* **2016**, 1, 561-565.
36. Oga, H.; Saeki, A.; Ogomi, Y.; Hayase, S.; Seki, S. Improved understanding of the electronic and energetic landscapes of perovskite solar cells: High local charge carrier mobility, reduced recombination, and extremely shallow traps. *J Am Chem Soc* **2014**, 136, 13818-13825.
37. Leblebici, S. Y.; Leppert, L.; Li, Y.; Reyes-Lillo, S. E.; Wickenburg, S.; Wong, E.; Lee, J.; Melli, M.; Ziegler, D.; Angell, D. K. *et al.* Facet-dependent photovoltaic efficiency variations in single grains of hybrid halide perovskite. *Nat. Energy* **2016**, 1, 16093.
38. MacDonald, G. A.; Yang, M.; Berweger, S.; Killgore, J. P.; Kabos, P.; Berry, J. J.; Zhu, K.; DelRio, F. W. Methylammonium lead iodide grain boundaries exhibit

depth-dependent electrical properties. *Energy Environ. Sci.* **2016**, 9, 3642-3649.
39. Edri, E.; Kirmayer, S.; Henning, A.; Mukhopadhyay, S.; Gartsman, K.; Rosenwaks, Y.; Hodes, G.; Cahen, D. Why lead methylammonium tri-iodide perovskite-based solar cells require a mesoporous electron transporting scaffold (but not necessarily a hole conductor). *Nano Lett.* **2014**, 14, 1000-1004.
40. Li, X.; Ibrahim Dar, M.; Yi, C.; Luo, J.; Tschumi, M.; Zakeeruddin, S. M.; Nazeeruddin, M. K.; Han, H.; Gratzel, M. Improved performance and stability of perovskite solar cells by crystal crosslinking with alkylphosphonic acid ω-ammonium chlorides. *Nat. Chem.* **2015**, 7, 703-711.
41. Yin, W. J.; Shi, T.; Yan, Y. Unique properties of halide perovskites as possible origins of the superior solar cell performance. *Adv. Mater.* **2014**, 26, 4653-4658.
42. Lee, B.; Lee, S.; Cho, D.; Kim, J.; Hwang, T.; Kim, K. H.; Hong, S.; Moon, T.; Park, B. Evaluating the optoelectronic quality of hybrid perovskites by conductive atomic force microscopy with noise spectroscopy. *ACS Appl Mater Interfaces* **2016**, 8, 30985-30991.
43. Spencer, M. G.; Schaff, W. J.; Wagner, D. K. Electrical characterization of grain boundaries in gaas. *Journal of Applied Physics* **1983**, 54, 1429-1440.
44. Baccarani, G.; Riccò, B.; Spadini, G. Transport properties of polycrystalline silicon films. *Journal of Applied Physics* **1978**, 49, 5565-5570.
45. Stewart, R. J.; Grieco, C.; Larsen, A. V.; Maier, J. J.; Asbury, J. B. Approaching bulk carrier dynamics in organo-halide perovskite nanocrystalline films by surface passivation. *J. Phys. Chem. Lett.* **2016**, 7, 1148-1153.
46. Noel, N. K.; Abate, A.; Stranks, S. D.; Parrott, E. S.; Burlakov, V. M.; Goriely, A.; Snaith, H. J. Enhanced photoluminescence and solar cell performance via lewis base passivation of organic-inorganic lead halide perovskites. *ACS nano* **2014**, 8, 9815-9821.

Chapter 4: Photo-Induced Halide Redistribution in Organic-Inorganic Perovskite Films

Authors: Dane W. deQuilettes, Wei Zhang,Victor M. Burlakov, Daniel J. Graham, Tomas Leijtens, Anna Osherov, Vladimir Bulović, Henry J. Snaith, David S. Ginger, Samuel D. Stranks

4.1 Overview:

Organic-inorganic perovskites such as $CH_3NH_3PbI_3$ are promising materials for a variety of optoelectronic applications, with certified power conversion efficiencies in solar cells already exceeding 21%. Nevertheless, state-of-the-art films still contain performance-limiting non-radiative recombination sites and exhibit a range of complex dynamic phenomena under illumination that remain poorly understood. Here, we use a unique combination of confocal photoluminescence (PL) microscopy and chemical imaging to correlate the local changes in photophysics with composition in $CH_3NH_3PbI_3$ films under illumination. We demonstrate that the photo-induced "brightening" of the perovskite PL can be attributed to an order-of-magnitude reduction in trap state density. By imaging the same regions with time-of-flight secondary-ion-mass spectrometry (ToF-SIMS), we correlate this photobrightening with a net migration of iodine. Our work provides visual evidence for photo-induced halide migration in triiodide perovskites and reveals the complex interplay between charge carrier populations, electronic traps, and mobile halides which collectively impact optoelectronic performance.

4.2 Introduction:

Organic-inorganic metal halide perovskites such as $CH_3NH_3PbI_3$ are generating a great deal of excitement for their potential applications in a variety of high-performance optoelectronic devices including solar cells, light-emitting diodes, photodetectors, and lasers[1,2]. These applications are enabled by the favorable material properties of these perovskites, which include long charge carrier diffusion lengths[3-5], high absorption coefficients with a sharp absorption edge[6], and a remarkably high photoluminescence quantum efficiency (PLQE)[7,8]. This latter property is particularly important for approaching the highest photovoltaic device performances at the Shockley-Queisser limit, in which all non-radiative recombination is eliminated[9]. Nevertheless, we recently reported that the PL lifetimes and intensities vary substantially between different grains even in high-quality films[10]. These observations are consistent with the presence of trap states that act as non-radiative recombination sites and influence the recombination kinetics[8,10-13]. In addition, the bulk optoelectronic properties such as photoluminescence[8,14], electroluminescence[15,16] and photoconductivity[17] have also been shown to rise slowly over time under illumination or current flow. These observations indicate that, despite their remarkable device efficiencies, the perovskite films are still far from optimized for stabilized optoelectronic device performance.

It has been suggested that ionic migration in these perovskite materials could impact optoelectronic performance and affect device operation[16,18,19]. A substantial amount of recent evidence indicates that the hysteresis effects in current-voltage measurements

originate from a migration of mobile ionic species, where positive and/or negative ionic species migrate to opposite electrodes under an internal field and impact charge collection.[16,18-23] Recent poling experiments on architectures with contacts have revealed evidence for the movement of ions under applied fields[24-28] which can sometimes lead to degradation[24,26]. However, there are no reports presenting visual evidence for ionic migration in perovskite films without contacts and the ensuing impact of migration upon the optoelectronic properties is not well understood.

Here, we use a combination of confocal fluorescence microscopy and chemical imaging through time-of-flight secondary ion mass spectrometry (ToF-SIMS) to study high-quality thin films of the neat perovskite $CH_3NH_3PbI_3$ without any contacts. We show that the PL lifetime and intensity increase significantly over time under illumination, and that these changes correspond to an order-of-magnitude reduction in the bulk trap state density. On the microscale, we find that light-soaking preferentially brightens regions with higher trap state densities and also induces a redistribution in local emission intensities. We use ToF-SIMS depth profiling to show that the rises in PL correlate with a redistribution of iodine in the film, thereby providing strong evidence for a photo-induced halide migration effect. Our results highlight the interplay between free carriers, traps and halide migration and their collective impact on optoelectronic performance.

4.3 Bulk Changes in Photoluminescence Under Illumination:

In Figure 1a we show bulk time-resolved PL decays of a neat $CH_3NH_3PbI_3$ film prepared on glass and corresponding to excellent device performance[29] (see Supplementary Methods), and the time-integrated intensity in Figure 1b, over a time period of 10 minutes under pulsed illumination *in vacuo*. Initially, the PL lifetime is very fast with a significant fraction of non-radiative decay. However, over a period of tens to hundreds of seconds under illumination, the lifetime and total intensity both increase and eventually stabilize after ~10 minutes[8,14]. These observations are consistent with a substantial reduction and stabilization of fast non-radiative decay pathways (herein termed 'cleaning'), and correlate closely with the rise in open-circuit voltage, as we show in the inset of Figure 1b. The extent of the PL enhancements is influenced by different atmospheres[14,30,31], though the effects are still observed in extremely low oxygen level environments including *in vacuo* and nitrogen and also in films made using other fabrication routes (see Supplementary Fig. 1, Note 1), suggesting that the general photo-induced rise behavior is intrinsic to these polycrystalline films. We note that the PL spectrum shape and position appears unchanged (see Supplementary Fig. 2, Note 2), suggesting that we are monitoring the same emissive species over the course of the measurement. We also do not observe any significant changes in X-Ray Diffraction (XRD) patterns of the films acquired while light soaking, indicating that the illumination is not inducing large changes in crystal structure or phase composition (Supplementary Fig. 3)[19].

We have recently developed a model that is able to describe the photoluminescence kinetics in perovskite films in the presence of N_T electronic subgap trap states (see Supplementary Fig. 4, Note 3)[8]. The fits from the model are shown with the gray lines in Figure 1a, and the extracted trap densities are shown in Figure 1b, exhibiting the derived

inverse dependence with PL intensity (see Supplementary Note 4). The initial trap density of the sample just after illumination (t = 4 s) is ~1.7 x 10^{17} cm^{-3} and this slowly reduces to eventually stabilize at ~2.5 x 10^{16} cm^{-3} (t = 862 s, total photon dose of 258 J cm^{-2}). This order-of-magnitude reduction in trap density under illumination also translates to increased emission and device photovoltage. Importantly, the stabilized values (~10^{16} cm^{-3}) are still well above the trap densities reported for single crystals (~10^{10} cm^{-3})[32,33], suggesting that the polycrystalline films still have significant scope for improvement and that light soaking alone may not close the gap in trap state density with their single crystal counterparts. To make the connection between the trap state density and slow photo-induced optoelectronic improvements explicit, we find that the time taken to reach stabilized emission for both cleaved and uncleaved surfaces of single crystal samples is greatly reduced (Supplementary Fig. 1). We note that these results agree with recent theoretical work investigating the effect of different densities of sub-gap states on the open-circuit voltage, where the authors found that the voltage is significantly reduced below its theoretical limit at trap densities of >10^{17} cm^{-3} but not significantly impacted at trap densities of ~5x10^{15} cm^{-3}.[34] These findings are also in agreement with recent reports showing a light-induced increase in electron diffusion length[35] as well as a reduction in the surface potential barrier at the grain boundaries[5].

We show the normalized integrated PL over time at different temperatures in Figure 1c (see Supplementary Fig. 5, Note 5 for decay curves and extracted trap densities at each temperature). At low temperature (190 K), stabilized emission is reached after 10,000 seconds (~3000 J cm^{-2}), whereas at high temperature (340 K), the PL reaches a stable output after just ~100 seconds (~30 J cm^{-2}). This compares to ~1000 seconds (~300 J cm^{-2}) at room temperature (295 K). We determine an activation energy for the process of E_a = 0.19 ± 0.05 eV using an Arrhenius fit to the rises in PL rates (Figure 1c inset, see Supplementary Fig. 6, Note 6). We also find that the time taken to reach stabilized emission varies dramatically with illumination intensity, with higher intensities leading to substantially faster rise times (see Supplementary Fig. 7, Note 7). The very slow time scales, strong dependencies on temperature and intensity, and an activation energy on the order of hundreds of milli-electronvolts are consistent with a photo-induced ion migration phenomenon[18,19,36] and will be discussed further below (also see Supplementary Note 8).

4.4 Local Changes in Photoluminescence Under Illumination:

We now investigate how microstructure impacts the PL rise behavior by considering the correlated scanning electron microscopy (SEM) micrograph (Figure 2a) and photoluminescence image shown in Figure 2b. We observe a heterogeneous distribution of grains with median grain size of ~0.76 μm (see Supplementary Fig. 8, Note 9), where some regions are particularly bright in emission, while other grains and grain boundaries are comparatively dark and correspond to higher trap state densities[10]. In Figure 2c, we monitor the local emission of different spots over time under continuous-wave (CW) 532-nm illumination at an intensity equivalent to ~3 suns (188 mW cm^{-2}) with a waist (w) spot size of ~500 nm. A bright spot (red triangle) starts at a comparatively high emission level but does not substantially increase over time (relative change by a factor of 1.4). In contrast, a dark spot (blue circle) rises in intensity by nearly an order of magnitude after

~3 minutes of illumination (factor of 8.7 relative change). An intermediate spot (green-square), also rises by a factor of ~1.6 over the same period.

These results provide important insight into the bulk measurements presented earlier, which represent an average across the distribution of grains (w ~17 μm). While the bulk PL increases over time under illumination, each individual grain shows dramatically varied rise time behavior depending on the initial trap state density. Dark spots rise significantly but the relative change in bright spots is much less, and the net result is an increase in spatially-averaged PL eventually reaching a stabilized bulk PL, with the enhancements closely following the spatial profile of the laser (see Supplementary Fig. 9, Note 10).

To investigate the transient behavior of the perovskite active layer under solar conditions, we show a fluorescence image in Figure 3a before exposing the entire film to full-simulated sunlight for 60 minutes (100 mW/cm^2, AM 1.5). Following the light soak (yellow shaded area in Figure 3f), we observe PL enhancements consistent with those reported in Figure 2c, then we monitor the local retention by taking fluorescence images over extended time intervals (Figure 3b–d; see Supplementary Fig. 10 for complete series, Note 11), where the sample was kept in the dark in between imaging. In Figure 3f we show the average PL relaxation dynamics of the dark, intermediate, and bright regions of interest (ROIs) defined in Figure 3e (see Supplementary Fig. 10) as well as the average relaxation (dotted black trace) across the fluorescence image. The emission from the dark regions relax and eventually reach a stabilized emission after ~9 hours, maintaining a PL level ~3x higher than their initial value before illumination. In contrast, the emission from the bright regions relax and stabilize at a lower PL level (0.66) relative to their initial value. Although the emission from all regions generally improves while under illumination, these results suggest that the photo-induced cleaning is locally retained (when left in the dark) in dark regions but not in bright regions (see Supplementary Figs. 10 and 11, Note 11). Importantly, the stabilized average PL intensity of the analyzed area after ~9 hrs is approximately the same as the average initial PL intensity before illumination (initial and final points of dotted black trace). These observations are consistent with a new equilibrium corresponding to a redistribution of emission intensities with improved grain-to-grain homogeneity, which is only reached after an extended illumination period and several hours in the dark (see Supplementary Fig. 12).

4.5 Compositional Changes After Illumination:

To ascertain whether the light-induced PL enhancements and redistributions can be directly related to compositional changes, we now investigate the changes in local composition due to illumination by performing ToF-SIMS depth profiling on photo-irradiated films. We first light-soaked a local dark spot for several minutes with pulsed excitation (1.2 kJ cm^{-2}) and recorded the typical slow rises in emission (Figure 4a). Previously, we have reported enhancements in solar cell performance metrics, namely the open circuit voltage (V_{oc}), under similar photon doses used for this experiment[37]. We then performed ToF-SIMS on this same film and report the summed iodide signal through a depth profile at the illuminated region in Figure 4b. Figure 4c shows the iodide

distribution across the linescan (blue arrow) from Figure 4b, along with the measured laser profile (blue line). We see that the regions of highest illumination intensity corresponding to the spatial profile of the laser show depleted levels of iodide, while the immediately-adjacent regions show an enrichment in iodide relative to the background iodide levels (ROI shown in Supplementary Fig. 13). These results suggest a lateral migration of iodine away from the illumination area, which can be attributed to iodine redistribution (see Supplementary Fig. 13, Note 12). The ToF-SIMS counts suggest that the relative changes in iodine-containing fragments are on the order of a few percent, and since we also observe local variations in other lower intensity fragments, we conclude that iodine migration alone does not encompass the complexity of this ionic redistribution effect (see Supplementary Note 12).

To probe the extent of halide redistribution as a function of film depth, we illuminated two different regions, one with a photon dose of 1.2 kJ cm^{-2} (red circle) and another with 2.4 kJ cm^{-2} (green circle), as shown in Figure 5a, and we show the iodide intensity map in Figure 5b. We again observe the typical PL rises and an anti-correlation between the measured excitation laser beam spatial profile and the resulting iodide intensity (see Supplementary Fig. 14). In Figure 5c, we show ToF-SIMS depth profiling data for iodide. To highlight the differences relative to a control area, the data are displayed as the difference between the light soaked regions (red and green lines) and the background iodide level from a region that had not been light soaked (blue line). We also show the carrier generation profile through the film thickness as a guide to the eye. As seen in Figure 5c, the iodide level is lower in the light-soaked areas in comparison to the background region, and this is particularly true for film depths corresponding to high carrier densities. Consistent with this observation, as the carrier generation profile decays through the film, the iodide level increases relative to the background level deeper in the film and at the substrate interface (see Supplementary Fig. 14). We observe a greater fraction of iodide deeper in the film when exposed to a photon dose of 2.4 kJ cm^{-2} (green line) as compared to 1.2 kJ cm^{-2} (red line), suggesting that the magnitude of iodide displacement is dependent on photon dose. Figure 5d shows the depth profiles of regions adjacent to the illuminated areas (pink and gold lines), where the iodide content is higher in the bulk of the film as well as deeper in the film in comparison to the background profile. These data are consistent with iodine migration away from the illuminated region both laterally and vertically. We also observe similar effects in mixed halide (i.e. $CH_3NH_3PbI_{3-x}Br_x$) films[19] (see Supplementary Fig. 15) and also from energy-dispersive X-ray spectroscopy (EDS) measurements (see Supplementary Fig. 16, Note 13).

4.6 Proposed Mechanism of Photobrightening:

Our interpretation of these results is that the illumination induces a redistribution of iodide resulting in a photo-cleaned (brightened) region with net reduced trap densities. The redistribution in iodide intensities alone is larger than the changes in iodine concentration associated with trap annihilation (~ppm). Here, we propose a mechanism in Figure 6 that broadly describes our observations in this study, but it is likely that there are other complex mass transport mechanisms simultaneously occurring. Upon film formation, some regions contain larger densities of electronic traps, which could arise

from iodine vacancies (undercoordinated lead sites, δ+) with associated interstitial iodide ions[8,18,29,38-40], which are numerous at surfaces and grain boundaries (Figure 6a)[10,41,42]. Under illumination, we create a relatively high density of photo-excited electrons and holes, which is highest at the surface and falls off exponentially through the film (Figure 5c). Many of the photo-excited electrons will become trapped in the vacancies particularly near the surface (Figure 6b)[13,29,42]. The trap filling would perturb the system and create electric fields which induce iodide migration and subsequent trap annihilation in several ways: 1) Coulombic repulsion between now-unscreened iodide ions, 2) Spatial charge separation arising from the surface-trapped electrons and diffused holes or 3) A change in band bending at the surface upon illumination[29]. In all cases, this field-induced migration allows the large amount of mobile iodide to fill vacancies and therefore yield a net reduction in the density of vacancies and interstitials which could be responsible for the non-radiative recombination (Figure 6c) [39,43]. By locally illuminating a region we observe both vertical and lateral migration away from the carrier generation profile (cf. Figure 5). If the entire film is illuminated (cf. Figure 3), we expect vertical migration to still be prevalent and annihilation of defects under the illumination spot, leading to a net brightening of all grains, but the lateral migration will be dominated by local iodide and (filled) defect density gradients which will vary within and between grains; thus, some regions will locally brighten more than others due to relatively greater excess iodine removal in those regions. At higher excitation intensity, the time to reach stabilized emission will be faster because more traps will be filled by photo-generated electrons, thereby producing a larger field to drive halide migration. Likewise, at higher temperature the ionic conductivity will increase and the system will again reach stabilized emission in a shorter time. In the dark, the photo-excitation profile is removed and some traps remain, which may allow some iodide ions to slowly migrate back laterally or vertically to establish a new equilibrium (Figure 6d; cf. Figure 3), thereby leading to a partial reversibility. However, new concentration gradients may appear over time as ions cluster or disperse, thus the dynamics may be much more complicated (see Supplementary Fig. 11).

We believe that our mechanism is also consistent with the rapid photo-brightening in perovskite nanocrystals and nanocrystalline domains with few trap sites per crystal, as reported by Tian et al.[44] and Tachikawa et al[31]. Here, traps are efficiently filled and the gradient driving ion migration results in the rapid net removal of the few interstitial-vacancy pairs per crystal. The mechanism we propose here may not be able to explain all photo-brightening phenomena. For example, it has been recently shown that oxygen species could contribute to the photo-brightening process[14,30]. Tian et al. recently proposed a model for the photo-brightening in the presence of oxygen, where photo-generated charge carriers and oxygen-related species interact to deactivate the trapping defects[14]. In their mechanism and in ours, the photo-brightening is limited by the interaction volume of photo-excited carriers in the film. We take means to minimize oxygen in our measurements presented here, suggesting that oxygen may not be essential in the process. Nevertheless, the competition between oxygen and iodine in both diffusion and ability to annihilate traps, and any possible synergy between the two, remains an ongoing question for the community.

4.7 Discussion:

Tian et al. and others also speculate that the photo-induced brightening could be related to ion migration[14,19]. Here, we provide direct strong visual evidence of photo-induced halide redistribution effects. Hoke et al. used PL measurements to calculate a bulk activation energy of 0.27 ± 0.06 eV for halide migration in mixed halide systems ($CH_3NH_3PbI_{3-x}Br_x$)[19], which roughly agrees with the value we extract here of 0.19 ± 0.05 eV for the pure trihalide systems (Figure 1c). Indeed, activation energies for iodide migration in $CH_3NH_3PbI_3$ have been recently estimated to be in the range ~0.1–0.6 eV[18,36]. The differences may in part be due to different local stoichiometry, i.e. iodide-rich or iodide-poor conditions, which has a large influence on the formation energies of iodide interstitials[39,45]. For example, the formation energy of iodide interstitials in iodide-rich conditions is also ~0.2 eV, suggesting that the activation energy we extract here could be related to the interstitial/vacancy-mediated transport of iodide[18,36]. The reversible ion redistribution could also be consistent with the photo-induced structural changes reported elsewhere[46,47].

Finally, we discuss how these slow transient effects and our measurements are relevant to full optoelectronic devices. We have observed a light-induced halide migration in neat films, which we attribute to the formation of local fields created by filling traps under illumination. Others have reported methylammonium migration but only in full devices in the presence of a field across the entire film.[24-26] Since the migration in both cases likely arises from electric fields, we could use the light-induced changes as a proxy to learn about the field-induced changes in the full devices. For instance, the depth profile data (Figure 5) revealed that just by illuminating with light, we can deplete iodine at the top surface and redistribute it to the substrate interface (i.e. contact in a full device), which would strongly affect band bending and charge collection[16]. Furthermore, we learn that the ion migration in full devices is not simply due to defects moving under an applied field, rather that there is a dynamic interplay between carriers, traps and mobile ions which needs to be considered. This has direct relevance to the hysteresis phenomena in full solar cells, which has been proposed to be primarily caused by ion migration[16,21,23] but also necessitates the presence of trap states[22]. The rise times to stabilized efficiency at the maximum power point in full n-i-p solar cells closely match the time scales to reach stabilized emission due to photo-induced cleaning under 1-sun equivalent irradiation[8,23], which is consistent with both phenomena arising from ion migration. Notably, we observe here that the halide migration is related to the passivation, or deactivation of traps, hence the hysteresis observed in solar cells could be amplified by the activation or deactivation of electron traps depending upon whether the mobile iodine is pushed towards, or away from, the n-type charge collection layer. This is consistent with our recent work where we have reduced the perovskite trap density by an order of magnitude by treating the polycrystalline film surface with small molecules such as pyridine and we observe that the rise times to stabilized maximum power output are much faster and hysteresis is reduced[40,48]. In the extreme case of negligibly low trap densities as in single crystals, we show that the emission stabilizes rapidly (see Supplementary Fig. 1), and this is consistent with the minimal hysteresis effects reported for devices comprised of single crystals or millimeter-scale grain thin films[32,33,49]. We can conclude that the rise times to

stabilized maximum power are much faster for solar cells incorporating perovskites with lower trap densities, and a lack of transient behavior strongly suggests that ion migration has been suppressed. It is therefore imperative to reduce the trap density to eliminate unwanted ion migration effects, and future work should concentrate on fabricating perovskites with uniform iodine distributions and low trap densities (by improving growth processes or post-treating samples) to achieve instantaneously-stabilized optoelectronic behavior. It still remains unclear if we require films with a stoichiometric composition, or if in fact halide-deficient regions are more PL active[39]. The finding that potentially large fractions of iodine are moving under illumination without major changes to crystal structure (cf. XRD measurements, Supplementary Fig. 3) needs to be understood and remains an open question for the community.

4.8 Conclusions:

In conclusion, we have investigated $CH_3NH_3PbI_3$ films without contacts and find that the PL lifetime and PL intensity rise substantially over time under illumination corresponding to nearly an order-of-magnitude reduction in trap densities. On the microscale, we find that the changes in PL and trap density are particularly significant for the dimmer spots. There is a strong correlation between the increase in PL over time under illumination and a redistribution of iodine away from the illuminated region, where this redistribution is likely connected to the redistribution of stabilized PL intensities. These results are consistent with a photo-induced iodide migration with an activation energy of 0.19 ± 0.05 eV. This work gives direct visualization of photo-induced halide migration in the neat perovskite materials that is related to slow transient optoelectronic phenomena and lowering of the trap densities through 'cleaning' effects; the precise mechanism of migration and significance of the activation energy remains an open question for the community. The correlations between local photophysical behavior and local composition profiled through the film presented in this work will provide an excellent tool set to further understand the impact of chemical-, photo-, field- and atmospheric-induced effects on these slow transients and ion migration in operating devices.

4.9 Appendix C:

Materials and methods and supplementary text

4.10 Acknowledgements:

The research leading to these results has received funding from the European Union Seventh Framework Programme [FP7/2007-2013] under grant agreement 604032 of the MESO project, and also from the People Programme (Marie Curie Actions) of the European Union's Seventh Framework Programme (FP7/2007-2013) under REA grant agreement number PIOF-GA-2013-622630. D.W.D and D.S.G acknowledge DOE (DE-SC0013957) for supporting the local imaging work. D.W.D. acknowledges support from an NSF Graduate Research Fellowship (DGE-1256082) and thanks M. Ziffer and J. Mohammed for providing single crystal samples. S.D.S also thanks R. H. Friend for additional support and R. Brenes for additional PL measurements. W.Z. thanks the EPSRC Supergen Supersolar project for financial support. This research was performed in part at the Molecular Analysis Facility (MAF) is funded, in part, by the University of Washington, Molecular Engineering and Sciences Institute, and the Clean Energy Institute, as well as infrastructure grants from the National Institutes of Health (NIH) and the National Science Foundation. The argon cluster source used in this research was funded by NIH grant S10 OD010607.

4.11 Figures:

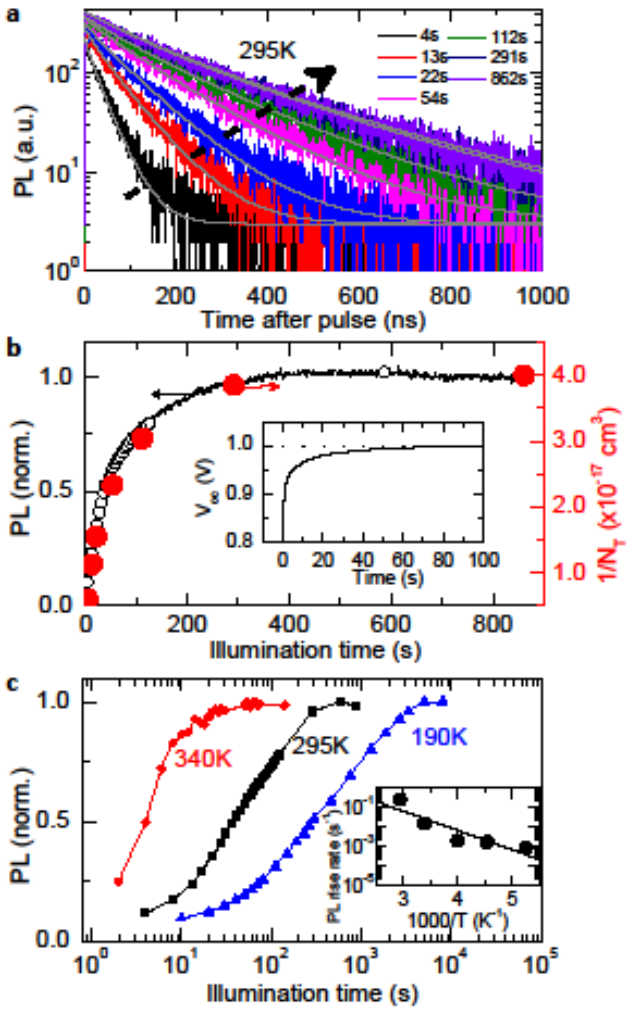

Figure 4.1. **Bulk changes in photoluminescence (PL) over time under illumination.** (a) A series of time-resolved PL decays from a $CH_3NH_3PbI_3$ film measured over time under illumination. The sample was photoexcited with pulsed excitation (507 nm, 1 MHz repetition rate, 0.3 μJ cm^{-2} per pulse) and the emission was detected at 780 nm. (b) The PL over time under initial illumination determined from integrating acquired PL decays (black open symbols) or monitoring the PL count rate (black solid line). The red symbols are inverse trap densities $1/N_T$, where N_T are extracted from the fits to the data in (a) (gray lines). *Inset*: Open circuit voltage (*V*oc) rise of a full solar cell with an illumination intensity comparable to full sunlight (532-nm cw laser, ~60 mW cm^{-2}). (c) The normalized integrated PL over time under illumination at different temperatures. *Inset*: Temperature dependence of the rate of PL rise deduced from exponential fits to the data in the main panel (see Supplementary Notes 5 and 6). The solid line represents a fit to the data using the Arrhenius relation to extract an activation energy (E_a = 0.19 ± 0.05 eV).

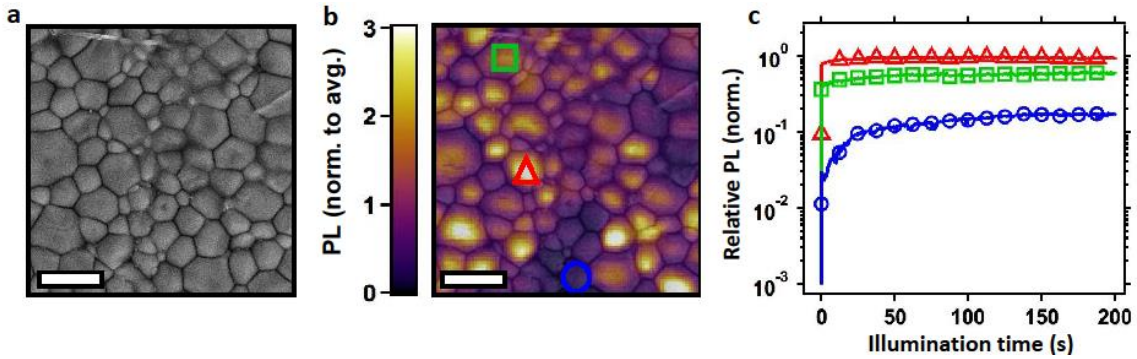

Figure 4.2. Local changes in photoluminescence over time under illumination. (a) correlated scanning electron microscopy (SEM) image and (b) fluorescence image of a perovskite film measured in nitrogen with pulsed photo-excitation (470 nm, 40 MHz repetition rate, 0.03 μJ cm^{-2} per pulse) with semitransparent SEM image overlaid, scale bars are 2 μm. (c) PL intensity over time from a dark spot (blue circles, enhancement of 8.7x), intermediate spot (green squares, enhancement of 1.6x) and a bright spot (red triangles, enhancement of 1.4x) corresponding to the regions highlighted with the same symbols in (b), with photo-excitation at 532 nm (188 mW cm^{-2}, ~3 suns).

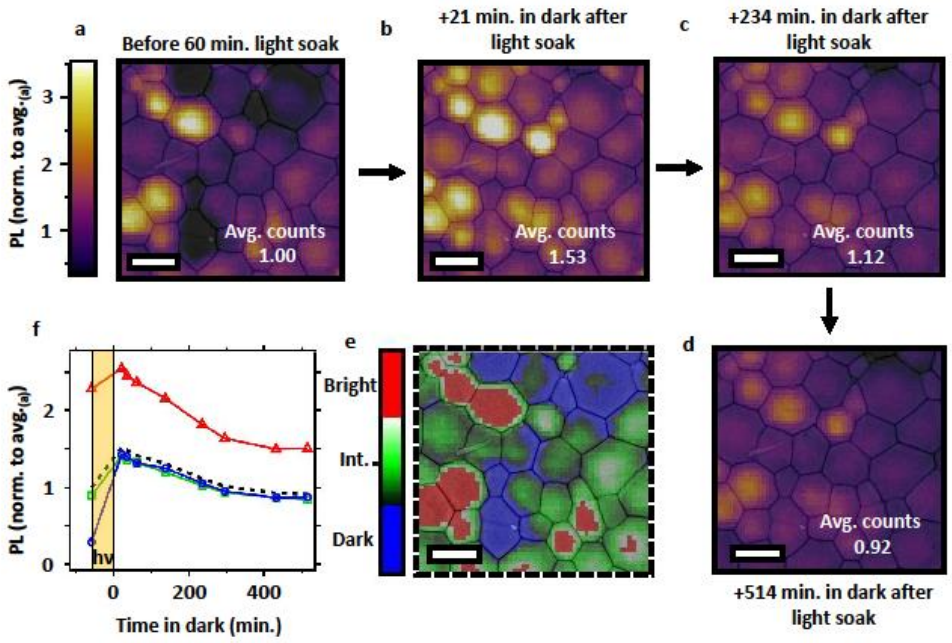

Figure 4.3. Local photoluminescence (PL) rises and relaxation after exposure to simulated sunlight. Fluorescence images under pulsed excitation (470 nm, 40 MHz repetition rate, 0.03 μJ cm^{-2} per pulse) measured in nitrogen with semitransparent scanning electron microscopy (SEM) images overlaid (a) before light soaking, and after exposing the entire film to simulated sunlight (AM 1.5, 100 mW cm^{-2}) for 60 minutes and leaving in the dark for (b) 21 (c) 234 and (d) 514 minutes (all images have the same PL intensity scale normalized to the average PL intensity in a, scale bars are 1 μm). (e) Three-color scale image showing the regions classified as dark, intermediate (Int.) and bright (see Supplementary Note 11). (f) Local PL enhancement and relaxation for dark (blue, enhancement of 4.9x), intermediate (green, enhancement of 1.6x), and bright (red, enhancement of 1.1x) regions, where the time (t) under illumination is highlighted by the yellow shaded region for $-60 \leq t \leq 0$ minutes , and $t > 0$ show the local PL relaxation dynamics over time left in the dark. The dotted black line is the PL relaxation averaged across the whole fluorescence image.

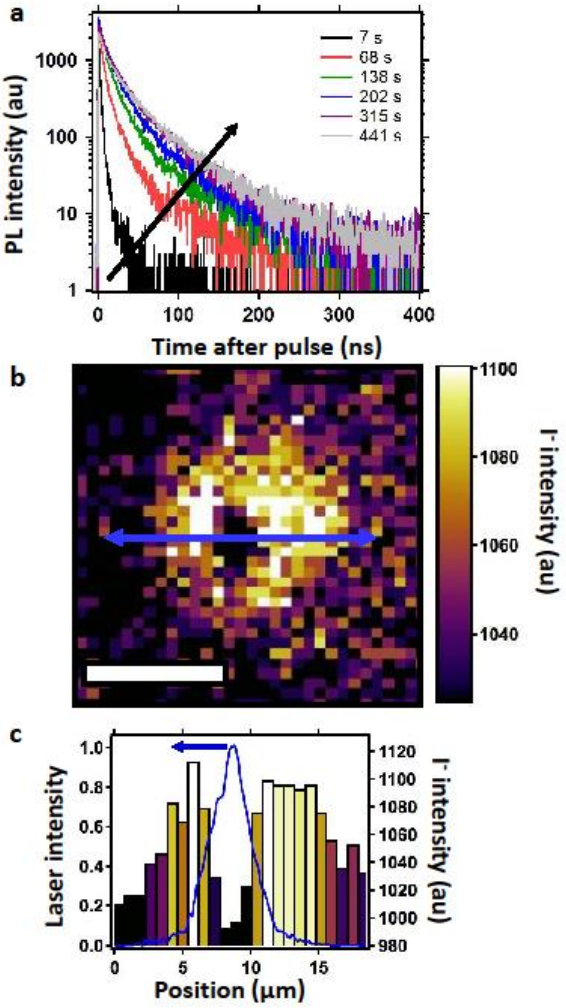

Figure 4.4. Iodide redistribution after light soaking. (a) A series of time-resolved photoluminescence decays from a $CH_3NH_3PbI_3$ film measured over time under illumination before time-of-flight secondary ion mass spectrometry (ToF-SIMS). The sample was photoexcited with pulsed excitation (470 nm, 1.2 kJ cm^{-2}). (b) ToF-SIMS image of the iodide distribution summed through the film depth (the image has been adjusted to show maximum contrast), scale bar is 10 μm. (c) Line scan of the blue arrow in (b) to show the iodide distribution (right axis). The measured spatial profile of the illumination laser (blue) is shown on the left axis.

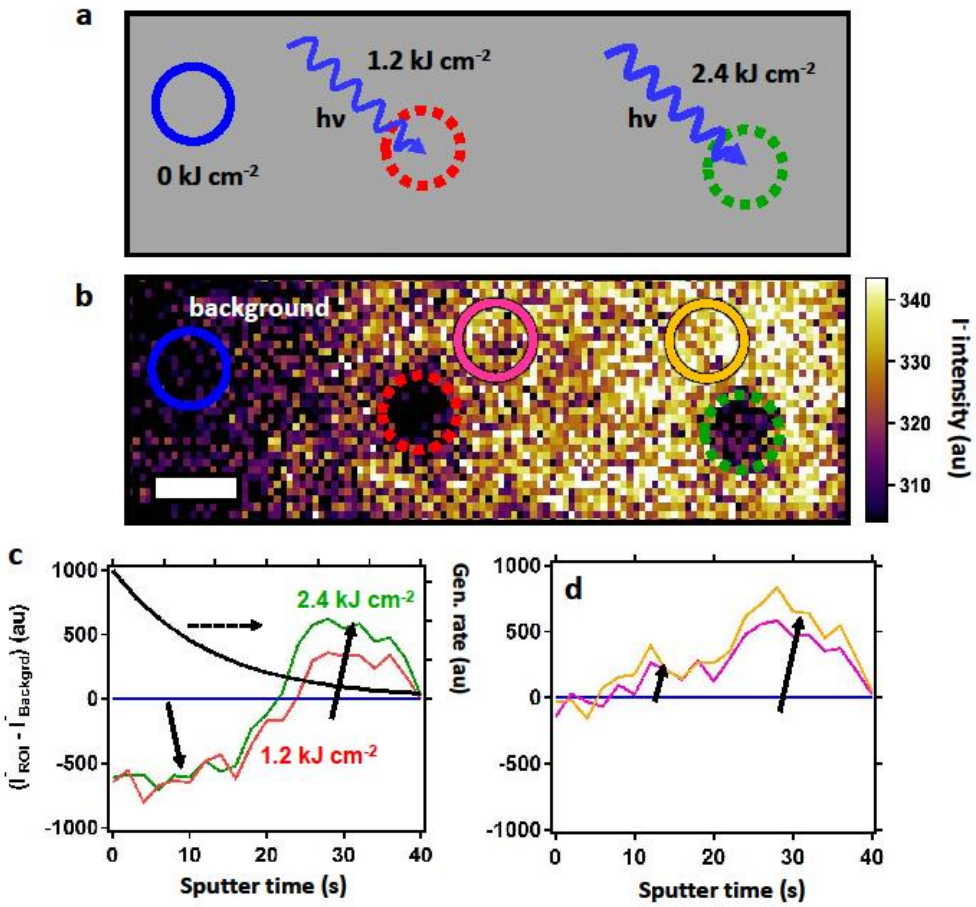

Figure 4.5. Time-of-flight secondary ion mass spectrometry (ToF-SIMS) depth profiling. (a) Schematic of photon dose-dependent experiment indicating the regions exposed to 1.2 kJ cm^{-2} (red dotted circle) and 2.4 kJ cm^{-2} (green dotted circle) (b) ToF-SIMS image of the iodide intensity distribution summed through the film depth (the image has been adjusted to show maximum contrast) after local exposure to the photon doses shown in (a), scale bar is 5 μm. (c) Depth profile data of the iodide intensity in regions of interest (ROI) relative to the background (I^-_{ROI} – $I^-_{background}$) for regions illuminated in (a), with the carrier generation (gen.) rate plotted on the right axis. (d) Depth profile data for ROI's adjacent to 1.2 kJ cm^{-2} (pink) and 2.4 kJ cm^{-2} (gold) illumination areas compared with a background level (blue circle). All selected regions contained the same number of pixels to allow comparison.

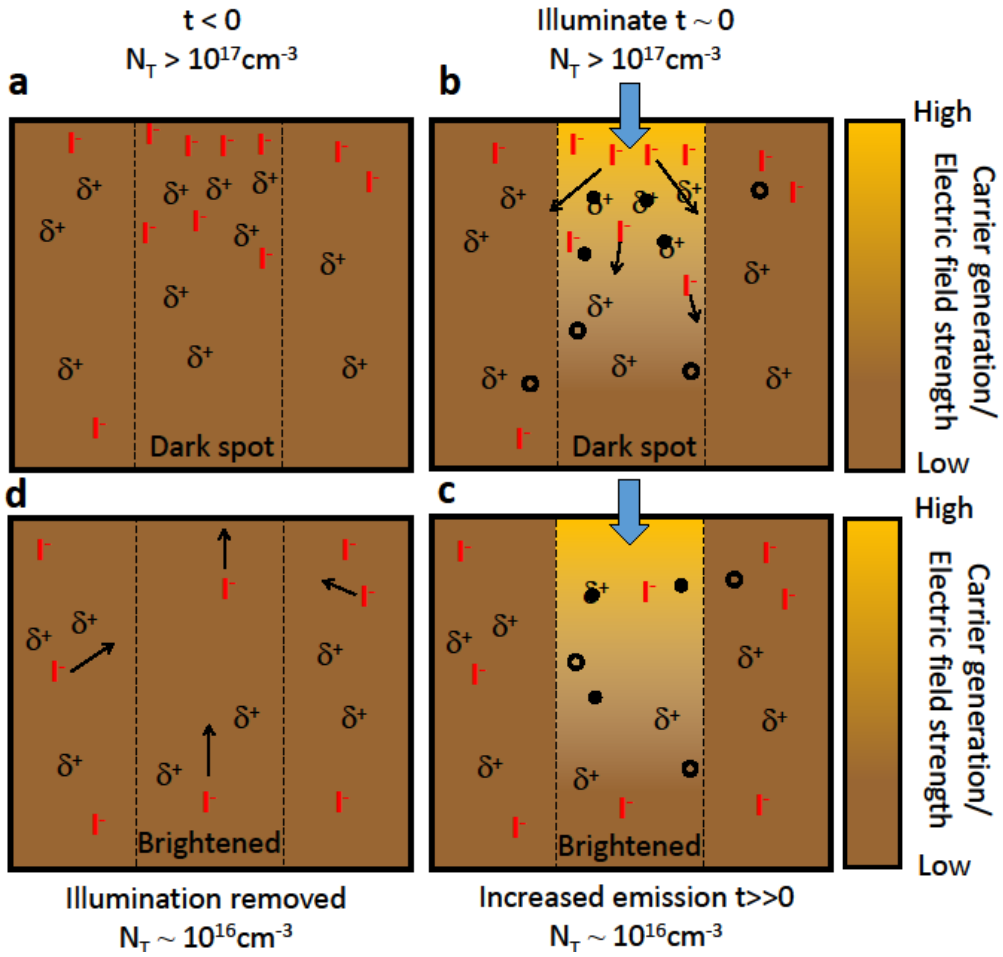

Figure 4.6. Proposed mechanism of photo-induced cleaning by halide redistribution. The cartoon represents a cross-section of the films illuminated through the top surface. (a) The trap density in a 'dark spot' is initially high with a corresponding excess of iodide. (b) Upon illumination, electrons will quickly fill traps, inducing an electric field that causes iodide to migrate away from the illuminated region and fill vacancies. (c) The system eventually reaches a stabilized emission output with a reduced trap density and iodide concentration in the illuminated region. (d) When the illumination is removed, there may be concentration gradients driving some iodide back into the grain before it eventually reaches a new equilibrium with a net redistributed iodide profile. δ^+ are iodide (I^-) vacancies, filled circles are electrons, open circles are holes.

4.12 References:

1 Stranks, S. D. & Snaith, H. J. Metal-halide perovskites for photovoltaic and light-emitting devices. *Nat. Nanotechnol.* **10**, 391-402, doi:10.1038/nnano.2015.90 (2015).

2 Johnston, M. B. Optoelectronics: Colour-selective photodiodes. *Nat Photon* **9**, 634-636, doi:10.1038/nphoton.2015.180 (2015).

3 Stranks, S. D. *et al.* Electron-hole diffusion lengths exceeding 1 micrometer in an organometal trihalide perovskite absorber. *Science* **342**, 341-344, doi:10.1126/science.1243982 (2013).

4 Xing, G. *et al.* Long-range balanced electron- and hole-transport lengths in organic-inorganic CH3NH3PbI3. *Science* **342**, 344-347, doi:10.1126/science.1243167 (2013).

5 Edri, E. *et al.* Why lead methylammonium tri-iodide perovskite-based solar cells require a mesoporous electron transporting scaffold (but not necessarily a hole conductor). *Nano Lett* **14**, 1000-1004, doi:10.1021/nl404454h (2014).

6 De Wolf, S. *et al.* Organometallic Halide Perovskites: Sharp Optical Absorption Edge and Its Relation to Photovoltaic Performance. *J. Phys. Chem. Lett.* **5**, 1035-1039, doi:10.1021/jz500279b (2014).

7 Deschler, F. *et al.* High Photoluminescence Efficiency and Optically Pumped Lasing in Solution-Processed Mixed Halide Perovskite Semiconductors. *J. Phys. Chem. Lett.* **5**, 1421-1426, doi:10.1021/jz5005285 (2014).

8 Stranks, S. D. *et al.* Recombination Kinetics in Organic-Inorganic Perovskites: Excitons, Free Charge, and Subgap States. *Phys Rev Appl* **2**, 034007, doi:10.1103/Physrevapplied.2.034007 (2014).

9 Miller, O. D., Yablonovitch, E. & Kurtz, S. R. Strong Internal and External Luminescence as Solar Cells Approach the Shockley-Queisser Limit. *IEEE Journal of Photovoltaics* **2**, 303-311, doi:10.1109/JPHOTOV.2012.2198434 (2012).

10 deQuilettes, D. W. *et al.* Impact of microstructure on local carrier lifetime in perovskite solar cells. *Science* **348**, 683-686, doi:10.1126/science.aaa5333 (2015).

11 Wetzelaer, G. J. *et al.* Trap-assisted non-radiative recombination in organic-inorganic perovskite solar cells. *Adv Mater* **27**, 1837-1841, doi:10.1002/adma.201405372 (2015).

12 Yamada, Y., Nakamura, T., Endo, M., Wakamiya, A. & Kanemitsu, Y. Photocarrier recombination dynamics in perovskite CH3NH3PbI3 for solar cell applications. *J Am Chem Soc* **136**, 11610-11613, doi:10.1021/ja506624n (2014).

13 Leijtens, T. *et al.* Electronic properties of meso-superstructured and planar organometal halide perovskite films: charge trapping, photodoping, and carrier mobility. *ACS Nano* **8**, 7147-7155, doi:10.1021/nn502115k (2014).

14 Tian, Y. *et al.* Mechanistic insights into perovskite photoluminescence enhancement: light curing with oxygen can boost yield thousandfold. *Phys Chem Chem Phys* **17**, 24978-24987, doi:10.1039/c5cp04410c (2015).
15 Wojciechowski, K. *et al.* Heterojunction modification for highly efficient organic-inorganic perovskite solar cells. *ACS Nano* **8**, 12701-12709, doi:10.1021/nn505723h (2014).
16 Tress, W. *et al.* Understanding the rate-dependent J–V hysteresis, slow time component, and aging in CH3NH3PbI3 perovskite solar cells: the role of a compensated electric field. *Energy Environ. Sci.* **8**, 995-1004, doi:10.1039/c4ee03664f (2015).
17 Gottesman, R. *et al.* Extremely Slow Photoconductivity Response of CH3NH3PbI3 Perovskites Suggesting Structural Changes under Working Conditions. *J. Phys. Chem. Lett.* **5**, 2662-2669, doi:10.1021/Jz501373f (2014).
18 Eames, C. *et al.* Ionic transport in hybrid lead iodide perovskite solar cells. *Nat Commun* **6**, 7497, doi:10.1038/ncomms8497 (2015).
19 Hoke, E. T. *et al.* Reversible photo-induced trap formation in mixed-halide hybrid perovskites for photovoltaics. *Chem. Sci.* **6**, 613-617, doi:10.1039/c4sc03141e (2015).
20 Unger, E. L. *et al.* Hysteresis and transient behavior in current-voltage measurements of hybrid-perovskite absorber solar cells. *Energy Environ. Sci.* **7**, 3690-3698, doi:10.1039/C4ee02465f (2014).
21 Zhang, Y. *et al.* Charge selective contacts, mobile ions and anomalous hysteresis in organic-inorganic perovskite solar cells. *Materials Horizons* **2**, 315-322, doi:10.1039/C4mh00238e (2015).
22 van Reenen, S., Kemerink, M. & Snaith, H. J. Modeling Anomalous Hysteresis in Perovskite Solar Cells. *J. Phys. Chem. Lett.* **6**, 3808-3814, doi:10.1021/acs.jpclett.5b01645 (2015).
23 Snaith, H. J. *et al.* Anomalous Hysteresis in Perovskite Solar Cells. *J. Phys. Chem. Lett.* **5**, 1511-1515, doi:10.1021/Jz500113x (2014).
24 Leijtens, T. *et al.* Mapping Electric Field–Induced Switchable Poling and Structural Degradation in Hybrid Lead Halide Perovskite Thin Films. *Adv. Energy Mater.* **In Press**, doi:10.1002/aenm.201500962 (2015).
25 Yuan, Y. B. *et al.* Photovoltaic Switching Mechanism in Lateral Structure Hybrid Perovskite Solar Cells. *Adv. Energy Mater.* **5**, doi:10.1002/Aenm.201500615 (2015).
26 Xiao, Z. *et al.* Giant switchable photovoltaic effect in organometal trihalide perovskite devices. *Nat Mater* **14**, 193-198, doi:10.1038/nmat4150 (2015).
27 Deng, Y., Xiao, Z. & Huang, J. Light-Induced Self-Poling Effect on Organometal Trihalide Perovskite Solar Cells for Increased Device Efficiency and Stability. *Advanced Energy Materials* **In Press**, doi:10.1002/aenm.201500721 (2015).
28 Yang, T. Y., Gregori, G., Pellet, N., Gratzel, M. & Maier, J. The Significance of Ion Conduction in a Hybrid Organic-Inorganic Lead-Iodide-Based Perovskite Photosensitizer. *Angew. Chem. Int. Ed.* **54**, 7905-7910, doi:10.1002/anie.201500014 (2015).

29 Zhang, W. *et al.* Enhanced optoelectronic quality of perovskite thin films with hypophosphorous acid for planar heterojunction solar cells. *Nat Commun* **6**, 10030, doi:10.1038/ncomms10030 (2015).
30 Galisteo-López, J. F., Anaya, M., Calvo, M. E. & Míguez, H. Environmental Effects on the Photophysics of Organic–Inorganic Halide Perovskites. *J. Phys. Chem. Lett.* **6**, 2200-2205, doi:10.1021/acs.jpclett.5b00785 (2015).
31 Tachikawa, T., Karimata, I. & Kobori, Y. Surface Charge Trapping in Organolead Halide Perovskites Explored by Single-Particle Photoluminescence Imaging. *J. Phys. Chem. Lett.* **6**, 3195-3201, doi:10.1021/acs.jpclett.5b01566 (2015).
32 Dong, Q. *et al.* Electron-hole diffusion lengths > 175 mum in solution-grown CH3NH3PbI3 single crystals. *Science* **347**, 967-970, doi:10.1126/science.aaa5760 (2015).
33 Shi, D. *et al.* Low trap-state density and long carrier diffusion in organolead trihalide perovskite single crystals. *Science* **347**, 519-522, doi:10.1126/science.aaa2725 (2015).
34 Yang, W., Yao, Y. & Wu, C.-Q. Origin of the high open circuit voltage in planar heterojunction perovskite solar cells: Role of the reduced bimolecular recombination. *J. Appl. Phys.* **117**, 095502, doi:10.1063/1.4913519 (2015).
35 Kedem, N. *et al.* Light-Induced Increase of Electron Diffusion Length in a p–n Junction Type CH3NH3PbBr3 Perovskite Solar Cell. *J. Phys. Chem. Lett.* **6**, 2469-2476, doi:10.1021/acs.jpclett.5b00889 (2015).
36 Azpiroz, J. M., Mosconi, E., Bisquert, J. & De Angelis, F. Defect migration in methylammonium lead iodide and its role in perovskite solar cell operation. *Energy Environ. Sci.* **8**, 2118-2127, doi:10.1039/c5ee01265a (2015).
37 Matsumoto, F., Vorpahl, S. M., Banks, J. Q., Sengupta, E. & Ginger, D. S. Photodecomposition and Morphology Evolution of Organometal Halide Perovskite Solar Cells. *J. Phys. Chem. C*, doi:10.1021/acs.jpcc.5b06269 (2015).
38 Walsh, A., Scanlon, D. O., Chen, S., Gong, X. G. & Wei, S. H. Self-regulation mechanism for charged point defects in hybrid halide perovskites. *Angew Chem Int Ed Engl* **54**, 1791-1794, doi:10.1002/anie.201409740 (2015).
39 Buin, A. *et al.* Materials processing routes to trap-free halide perovskites. *Nano Lett* **14**, 6281-6286, doi:10.1021/nl502612m (2014).
40 Noel, N. K. *et al.* Enhanced Photoluminescence and Solar Cell Performance via Lewis Base Passivation of Organic-Inorganic Lead Halide Perovskites. *ACS Nano* **8**, 9815-6821, doi:10.1021/nn5036476 (2014).
41 Verwey, J. F. Time and intensity dependence of the photolysis of lead halides. *J. Phys. Chem. Solids* **31**, 163-168, doi:10.1016/0022-3697(70)90297-0 (1970).
42 Bischak, C. G., Sanehira, E. M., Precht, J. T., Luther, J. M. & Ginsberg, N. S. Heterogeneous Charge Carrier Dynamics in Organic-Inorganic Hybrid Materials: Nanoscale Lateral and Depth-Dependent Variation of Recombination Rates in Methylammonium Lead Halide Perovskite Thin Films. *Nano Lett* **15**, 4799-4807, doi:10.1021/acs.nanolett.5b01917 (2015).

43 Du, M.-H. Density Functional Calculations of Native Defects in CH3NH3PbI3: Effects of Spin–Orbit Coupling and Self-Interaction Error. *J. Phys. Chem. Lett.* **6**, 1461-1466, doi:10.1021/acs.jpclett.5b00199 (2015).

44 Tian, Y. *et al.* Enhanced Organo-Metal Halide Perovskite Photoluminescence from Nanosized Defect-Free Crystallites and Emitting Sites. *The Journal of Physical Chemistry Letters*, 4171-4177, doi:10.1021/acs.jpclett.5b02033 (2015).

45 Yin, W.-J., Shi, T. & Yan, Y. Unusual defect physics in CH3NH3PbI3 perovskite solar cell absorber. *Appl. Phys. Lett.* **104**, 063903, doi:10.1063/1.4864778 (2014).

46 Juarez-Perez, E. J. *et al.* Photoinduced Giant Dielectric Constant in Lead Halide Perovskite Solar Cells. *J. Phys. Chem. Lett.* **5**, 2390-2394, doi:10.1021/jz5011169 (2014).

47 Gottesman, R. *et al.* Photoinduced Reversible Structural Transformations in Free-Standing CH3NH3PbI3 Perovskite Films. *J. Phys. Chem. Lett.* **6**, 2332-2338, doi:10.1021/acs.jpclett.5b00994 (2015).

48 Nagaoka, H. *et al.* Zr Incorporation into TiO2 Electrodes Reduces Hysteresis and Improves Performance in Hybrid Perovskite Solar Cells while Increasing Carrier Lifetimes. *J. Phys. Chem. Lett.* **6**, 669-675, doi:10.1021/jz502694g (2015).

49 Nie, W. *et al.* High-efficiency solution-processed perovskite solar cells with millimeter-scale grains. *Science* **347**, 522-525, doi:10.1126/science.aaa0472 (2015).

50 Vanbellingen, Q. P. *et al.* Time-of-flight secondary ion mass spectrometry imaging of biological samples with delayed extraction for high mass and high spatial resolutions. *Rapid Commun. Mass Spectrom.* **29**, 1187-1195, doi:10.1002/rcm.7210 (2015).

Chapter 5: Photoluminescence Lifetimes Exceeding 8 μs and Quantum Yields Exceeding 30% in Hybrid Perovskite Thin Films by Ligand Passivation

Authors: Dane W. deQuilettes, Susanne Koch, Sven Burke, Rajan Paranji, Alfred J. Shropshire, Mark E. Ziffer, David S. Ginger

5.1 Overview:

We study the effects of a series of post-deposition ligand treatments on the photoluminescence (PL) of polycrystalline methylammonium lead triiodide perovskite thin films. We show that a variety of Lewis bases can improve the bulk PL quantum efficiency (PLQE) and extend the average PL lifetime $<\tau>$, with large enhancements concentrated at grain boundaries. Notably, we demonstrate thin film PLQE as high as 35 ± 1% and $<\tau>$ as long as 8.82 ± 0.03 μs, at solar equivalent carrier densities using tri-n-octylphosphine oxide (TOPO) treated films. Using glow discharge optical emission spectroscopy (GDOES) and nuclear magnetic resonance (NMR) spectroscopy, we show that the ligands are incorporated primarily at the film surface and are acting as electron donors. These results indicate it is possible to obtain thin film PL lifetime and PLQE values that are comparable to those from single crystals by control over surface chemistry.

5.2 Introduction:

Organic-inorganic trihalide perovskites are a family of earth-abundant semiconductors with composition-tunable bandgaps that exhibit promising performance in a range of electronic and optoelectronic devices including solar cells, light-emitting diodes, lasers, and ambipolar transistors.[1-3] Recently, high-quality perovskite single crystals have been grown using a variety of techniques and demonstrate exceptional optoelectronic properties that surpass their polycrystalline counterparts.[4-6] In particular, it has been shown that single crystals possess lower defect concentrations, higher mobilities, longer carrier diffusion lengths, and longer carrier lifetimes,[4-6] suggesting that the surface defects that are more prevalent in polycrystalline films limit performance.[7-9] Despite the quality of single crystals, their growth can be time consuming and their structural properties make them more difficult to incorporate into many devices, particularly those requiring large areas such as solar cells. Therefore, there is still significant interest in processing perovskites rapidly from solution into polycrystalline thin films for device applications. Many studies have highlighted the "defect tolerance" of perovskites, underlining their apparent resistance to defects that would normally plague semiconductors processed at low temperature.[10,11] While the performance of hybrid perovskite devices may be surprisingly good for a low-temperature, solution-processed thin-film technology, polycrystalline perovskite films still operate well below their theoretical performance limits indicating that losses remain. Indeed, we recently used photoluminescence (PL) microscopy to reveal a subset of grain boundaries and "dark" regions in the films that serve as non-radiative centers, highlighting the role of heterogeneity and surface effects.[12,13] Consistent with these studies, it has been shown photoluminescence quantum efficiency (PLQE) and lifetime are limited by traps at carrier densities obtained under typical solar illumination, and only at high carrier densities (when the majority of traps are filled) are the highest PLQEs observed.[14-17]

These observations help explain why the carrier lifetimes and PLQEs of thin films of perovskites remain below those reported for single crystals,[2,7,8,18,19] and suggest that surface defect chemistry remains an important topic of study.[7,9,20,21]

Historically, controlling the surface chemistry in semiconductors such as Si and GaAs has been important in improving material properties for the development of solar cell technologies.[22-24] In II-VI and IV-VI quantum dot systems, a substantial amount of work has focused on ligand passivation to modify surface states to improve PL emission properties as well as solar cell efficiencies.[25-29]

In an effort to increase the photoluminescence quantum efficiency and lifetime in perovskites, several groups have utilized Lewis bases and acids to reduce defect densities and improve solar cell device performance.[14,21,30-33] For example, we recently found that pyridine vapor exposure to as-grown films can improve PL brightness while partially homogenizing the heterogeneous local PL emission.[12] Other reports have incorporated Lewis bases and acids into perovskite precursor solutions before film deposition to improve performance.[30-33] However, it has been difficult to assess whether the additives lead to better crystallization and growth of the films,[30-32] or if their residual presence in the film ameliorates non-radiative recombination.[31,32] Recently Li et al. proposed that alkylphosphonic acid ω-ammonium chlorides can hydrogen bond with iodine atoms at the surface to improve grain cohesivity and device performance, while also noting the beneficial role passivation may have in long term device stability.[32] Chen et al. have controlled the formation of PbI_2 at grain boundaries to reduce recombination at surface states,[34] while Asbury and co-workers showed that small dithiols could remove surface defects.[21]

Herein, we study the effect of post-deposition treatments with a variety of Lewis bases on the photoluminescence behavior of methylammonium lead triiodide perovskite thin films. We find that Lewis bases generally enhance the PL properties, and can boost PL lifetimes nearly an order of magnitude to values as high as 8.82 ± 0.03 μs, the longest PL lifetime measured to date for thin films. Concomitant with improvements in lifetime, treated films also exhibit PLQE values as high as 35 ± 1 % at solar equivalent carrier densities. We use fluorescence imaging to show that these improvements are concentrated at the grain boundaries. Using glow discharge optical emission spectroscopy (GDOES) and nuclear magnetic resonance (NMR) spectroscopy, we confirm that these treatments behave in a fashion consistent with an electron donating surface layer, rather than structure directing agents. This work identifies quick and facile post-deposition methods to improve materials processing and the quality of perovskite films. Further optimization of passivation schemes and a better understanding of perovskite surface chemistry could allow solution-processed polycrystalline films to approach the electronic quality of single crystals.

We prepared neat perovskite films on glass by spincoating a precursor solution containing $PbOAc_2 \bullet 3H_20$ and MAI in N,N-dimethylformamide (DMF) following the work of Zhang et al. (see SI for full details).[35] We then exposed these films to a variety of thiols, amines, phosphines and phosphine oxides, and studied their impact on PL properties. We treated the films with low concentration (0.005M – 0.087M) solutions of different ligands dissolved in chlorobenzene (CB) by spin-coating the ligand solutions onto the perovskite thin films (See SI). To improve reproducibility, as well as exclude the

effects that small amounts of water and oxygen can impart on the PL, we prepared, treated, and measured all samples in dry nitrogen (see SI).[36-38]

5.3 General Enhancements in Photoluminescence with Lewis Bases:

Figure 1a shows typical bulk time-resolved PL decay traces measured at low pump fluence (470 nm, 30 nJ/cm^2 per pulse, corresponding to an excitation density of ~ 10^{15} cm^{-3}) of several samples before and after single chemical treatments with tri-*n*-octylphosphine oxide (TOPO), 1-octadecanethiol (ODT), and triphenylphosphine (PPh_3) measured in nitrogen. These compounds are all expected to behave as monodentate ligands as they possess only one coordinating atom. We also investigated some bidentate ligands as well as various other coordinating atoms, all of which showed general improvements in the PL (See Figure S1 for all treatments explored). Before ligand treatment, the PL lifetimes are typically of the order of a hundred nanoseconds, consistent with high-quality $CH_3NH_3PbI_3$ films reported by a number of authors.[21,39,40] Figure 1 shows that all of the screened treatments extend both the PL lifetime and the integrated PL intensity (Figure 1b) of the perovskite films, suggesting that the treatments are removing non-radiative decay pathways. To determine if this observation extends to different perovskite preparation routes, we performed these same treatments on films prepared using $PbCl_2$ and PbI_2 as Pb sources and observed similar improvements (Figure S2). We note that control films exposed to only neat CB solution do not show improvements in PL (Figure S3) and also that treated films washed with CB or 2-propanol can, depending on the washing procedure, result in a reinitialization of the PL intensity (Figure S4). This data suggests that the ligands are relatively labile and can be removed by rinsing with a suitable solvent.

5.4 Chemical Characterization of Lewis Base Treatments:

Next, we examine the interaction between the potential ligands and the perovskite thin films. First, we used glow discharge optical emission spectroscopy (GDOES) to probe the chemical composition as a function of depth for samples treated with the thiol, ODT. This technique has been employed to detect small dopant concentrations (ppm) in thin films of a-Si:H and other semiconductors, making it capable of probing the small concentrations of molecules introduced onto the perovskite surface.[41,42] Figures 2a and b show the sulfur (S) and lead (Pb) intensities as a function of sputtering time (film depth) for a sample treated with 0.087 M ODT (see SI for sample preparation). We observe a peak in the sulfur signal at the surface (i.e onset of the Pb signal) of the ODT treated film, which is not present in an untreated control film (Figure S5), indicating that ODT is primarily present at the film surface, not the bulk. We note that small concentrations of ODT may have penetrated further into the film (i.e. grain boundaries), but may be below the detection limit (ppm) of the technique.[41,42] We also confirmed that the treatments do not measurably change the optical density of the film or lead to measurable microscopic restructuring of the film morphology as evidenced by scanning electron microscopy and XRD (Figure S6 and S7). The fact that the treatment is applied after film growth, that the ODT is confined to the surface, and that we see no other quantifiable changes in the film structure strongly suggests that the Lewis base is acting as a surface ligand rather than affecting the bulk structure.

To further verify whether the Lewis bases could be interacting with the perovskite surfaces as classic electron donating ligands, we performed ^{31}P solid-state nuclear magnetic resonance (NMR) spectroscopy on PPh_3 treated samples (see SI for sample preparation). NMR spectroscopy gives insight into the local bonding environment of spin-active nuclei and has been widely employed to understand the surface chemistry of quantum dots.[26,43] Figure 2c shows that the phosphorus peak of a PPh_3 treated perovskite sample is shifted downfield when compared to the free ligand control. This downfield shift is consistent with the expected reduction in electron density surrounding the phosphorus nucleus (i.e. deshielding) upon interaction with the perovskite, which we take as confirmation that PPh_3 is indeed acting as an electron donating molecule (Lewis base) and surface ligand.[43,44] Our results from solid-state NMR in conjunction with GDOES build a strong case that surface defects exist and can be passivated with post-deposition ligand treatments. Underscoring this result, we note that the ligands improve the PL while being confined nearly exclusively to the film surface as would be expected from their steric bulk, and experimentally confirmed by GDOES. Furthermore, the NMR data show that the compounds are acting as electron donating ligands.

5.5 Champion Improvements in Photoluminescence Lifetime and Quantum Efficiency:

Having screened a range of different Lewis base treatments with our perovskite thin films, we next consider the PL enhancements that can be achieved with an optimized treatment. Figure 3a shows the champion time-resolved PL decay trace of a control film treated with 0.025 M TOPO dissolved in chlorobenzene and measured at a low fluence (470 nm, 30 nJ/cm^2 per pulse). The fits to the data are stretched exponential curves with a characteristic lifetime, τ_c = 0.92 ± 0.01 μs, and stretching exponent, β = 0.90, for the control and τ_c = 7.60 ± 0.04 μs and β = 0.77 for the TOPO treated film. Error ranges for the PL lifetimes are estimated from the uncertainties in the fit parameters based on photon counting statistics, where the errors in the reported beta values are negligible. This stretched exponential behavior at relatively low excitation power is consistent with literature reports,[12,45,46] and indicative of a distribution of local monomolecular recombination rates resulting from heterogeneity in the local non-radiative decay rates.[12,13,20,47-50] We computed the average lifetime, <τ> of the stretched exponential distribution according to equation 1:[51]

$$\langle\tau\rangle = \frac{\tau_c}{\beta}\Gamma\left(\frac{1}{\beta}\right) \quad (1)$$

where $\Gamma\left(\frac{1}{\beta}\right)$ is defined as the gamma function in equation 2:

$$\Gamma\left(\frac{1}{\beta}\right) = \int_0^\infty x^{(1-\beta)/\beta} e^{-x} dx \quad (2)$$

We obtained <τ> = 0.97 ± 0.01 μs for the control film, which improved to <τ> = 8.82 ± 0.03 μs when treated with TOPO, where error values are the propagated uncertainty in the input fit parameters. Figure 3b plots the PLQE of these same films measured in an integrating sphere as a function of excitation power. The data show that the PLQE

increases roughly an order of magnitude for films treated with TOPO compared to control films across all excitation powers. Importantly, we find at excitation powers which generate carrier densities comparable to 1 sun illumination that the PLQE can be enhanced from ~3% for the control film to values as high as 35 ± 1% for the TOPO treated film. The increase in PLQE as a function of excitation power has been attributed to increasing radiative bimolecular recombination as a result of trap filling.[15,16,52] Following previous reports,[12,52] we modeled the PLQE data using a combination of non-radiative and radiative monomolecular, bimolecular, and Auger recombination terms (see SI and Figure S8). We report small variations in the radiative monomolecular, $k_r = 3.8 \times 10^4$ s^{-1}, bimolecular, $k_b = 4.0 \times 10^{-11}$ cm^3 s^{-1}, and Auger rate constants, $k_A = 4 \times 10^{-28}$ cm^6 s^{-1} for the treated film, compared to the control film, where $k_r = 4.1 \times 10^4$ s^{-1}, $k_b = 3.5 \times 10^{-11}$ cm^3 s^{-1}, and $k_A = 4 \times 10^{-28}$ cm^6 s^{-1}, which are consistent with literature values.[12,53,54] In contrast, we observe a significant difference in the non-radiative monomolecular rate constant, $k_{nr} = 9.1 \times 10^5$ s^{-1} for the TOPO treated film compared to $k_{nr} = 6.6 \times 10^6$ s^{-1} for the control film. This corresponds to a ~7-fold reduction in the non-radiative decay rate for the TOPO treated film, consistent with a comparable reduction in non-radiative recombination centers and nearly an order of magnitude increase in PLQE for the TOPO treated film. We note that these rate constant values are consistent with our fitting of the TRPL data at low carrier densities (~10^{15} cm^{-3}) to a superposition of monomolecular relaxation functions as we find, within this regime, that bimolecular recombination only contributes to ~5% of the total recombination rate in comparison to ~95% from monomolecular recombination.

To better elucidate the mechanism by which non-radiative recombination is reduced, we also performed steady-state PL spectroscopy. Figure 3c shows the PL spectra before and after TOPO treatment. We consistently observe a small red-shift for TOPO treated films in comparison to the control films. Previously, our group has reported an improvement in PL and concomitant blue-shift in the optical features for pyridine-treated films,[12] which suggests treatments may modulate the electronic structure near the band-edge. Interestingly, it has been reported that large grain size polycrystalline films have a red-shifted PL peak compared to small grain polycrystalline films and also that single crystal bulk emission is red-shifted compared to the surface emission.[9,17,55,56] These differences in the measured optical properties have been attributed to compositional changes at the grain boundaries, lattice strain, variations in crystallinity, and photon recycling. [9,17,55-57] Here we report no observable changes in XRD spectra or in average grain size (Figures S6) and minimal shift in the PL spectrum over long time scales (Figure S9), suggesting that the PL emission in our samples may be dominated, in part, by the surface composition.

5.6 Grain Boundaries Exhibit Greatest Improvements Upon Surface Passivation

Previously, we showed that pyridine homogenizes the PL of perovskite thin films.[12] Figure 4 shows a fluorescence intensity image of a control film before (Figure 4a) and after (Figure 4b) treatment with TOPO plotted on the same PL intensity scale. Overall we find that TOPO treatment has a similar effect as pyridine, generally enhancing PL in all regions of film, with grain boundaries still being generally dimmer than grain centers. This ensemble improvement is also evident from the enhancement in the average bulk

lifetime (Figure 4c), where the control film initially exhibited $<\tau> = 0.73 \pm 0.01$ μs which increased to $<\tau> = 2.40 \pm 0.09$ μs after TOPO treatment. The measured bulk improvement can be further partitioned into local improvements. Figure 4d shows an image with the ratio of the PL intensity image for the TOPO treated film to the control film. We find that the relative differential improvement at the grain boundaries (average enhancement factor of ~1.8x) is larger than for the grain centers (~1.6x), suggesting that the TOPO is preferentially active at passivating grain boundary surface states (Figure S10). More generally, we find that the largest improvements in PL are achieved for regions with initially lower PL, which we have previously correlated to regions of higher defect densities (Figure S10).[12,13] The preferential brightening of grain boundaries could result from the three-dimensional topography of grain boundaries, which may have higher defect densities than some of the flatter surfaces of the grain interiors or potentially the selective targeting of facet dependent defect states.[58] Together these results are again broadly consistent with the picture that these treatments are reducing non-radiative recombination associated with surface states.

5.7 Discussion:

Reducing non-radiative recombination so that perovskite thin films can approach 100% photoluminescence quantum efficiency remains an important technological goal.[11,52,59,60] In the case where all non-radiative surface states were effectively passivated, we would expect the carrier lifetimes and PLQEs in polycrystalline films to approach that of single crystals.[2,7,18] Thus far, there has been a wide range of reported single crystal carrier lifetimes spanning from tens of nanoseconds to hundreds of microseconds, depending on the measurement technique.[4-6,8,56] Polycrystalline films, on the other hand, do not typically exhibit microsecond carrier lifetimes, but rather possess lifetimes ranging from tens of nanoseconds to a few hundred nanoseconds.[39,45,52] To the best of our knowledge, Noel et al. previously reported, until now, the longest measured PL lifetime for polycrystalline films, with values reaching ~ 2 μs upon surface treatment with pyridine and thiophene when measured at low fluence.[14] In addition to the long carrier lifetimes measured in this work, we also report PLQEs exceeding 30%. For polycrystalline thin films, PLQEs are typically ~ 10% or lower under excitation powers comparable to one sun illumination,[12,40,52,61,62] and only in single crystal nanowires and nanocrystals are PLQEs in excess of 50% reached.[2,18,19] Our findings here suggest that the surface chemistry of polycrystalline films can be controlled to approach the carrier lifetimes and PLQEs more typical of single crystals.

5.8 Conclusions:

After studying a library of Lewis bases, we have found that optimized treatments have reduced non-radiative recombination in $CH_3NH_3PbI_3$ perovskite films, extended PL lifetimes to values as high as 8.82 ± 0.03 μs, and improved PLQE values to $35 \pm 1\%$ at solar equivalent carrier densities. To further support the idea that these treatments are specifically targeting surface defects, we used glow discharge optical emission spectroscopy (GDOES) to show ligands are confined predominately at the film surface where steric effects likely prevent penetration further into the bulk of the film. With ^{31}P solid-state nuclear magnetic resonance (NMR), we showed that the molecules are behaving as classic surface ligands and Lewis bases. These results highlight the

detrimental effect of perovskite surface states on optoelectronic performance, and here we show a facile and rapid post-deposition method that can alter the surface composition yielding polycrystalline films with improved optoelectronic quality. With further development and characterization of ligand passivation schemes as well as a deeper understanding of their impact on the perovskite electronic structure, it is likely that thin film perovskites will be able to approach their maximum theoretical performance in a wide range of polycrystalline perovskite optoelectronic devices.

5.9 Appendix D:

Materials and methods, supplementary text, photoluminescence measurements of other Lewis bases and precursor preparation routes, solvent wash control experiments, linear absorption spectroscopy, X-ray diffraction (XRD) spectroscopy, scanning electron microscopy (SEM) characterization, streak camera experiments, and fluorescence image analysis.

5.10 Acknowledgements:

D.W.D and D.S.G acknowledge DOE (DE-SC0013957) for supporting the local imaging work. D.W.D. acknowledges support from an NSF Graduate Research Fellowship (DGE-1256082) and thanks J. Mohammed, L. Bradshaw, G. Eperon, N. Li, and A. Marchioro for experimental help. This research was performed in part at the Molecular Analysis Facility (MAF) is funded, in part, by the University of Washington, Molecular Engineering and Sciences Institute, and the Clean Energy Institute, as well as infrastructure grants from the National Institutes of Health (NIH) and the National Science Foundation (ECCS-1542101).

5.11 Figures:

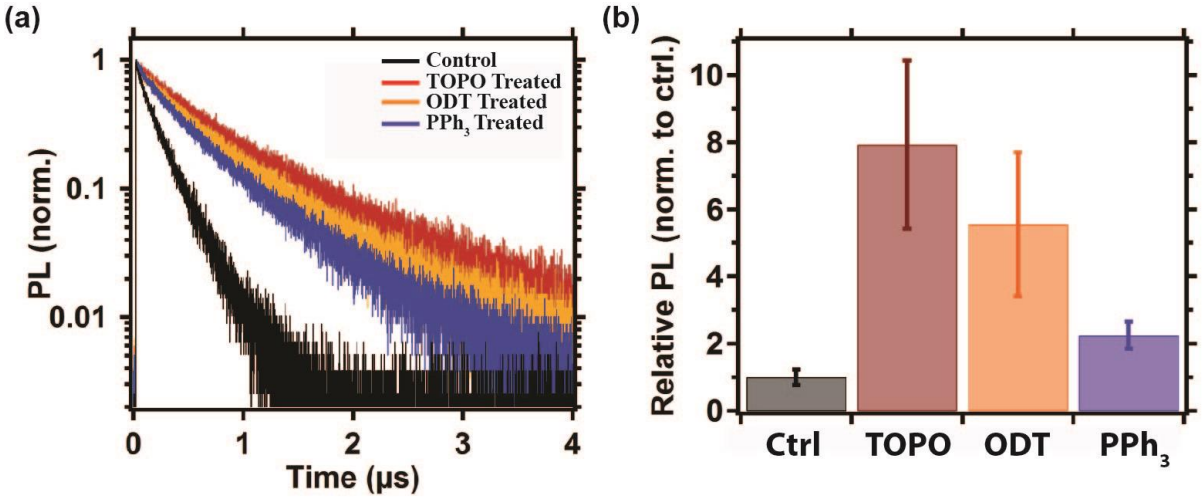

Figure 5.1. Photoluminescence studies of films treated with Lewis bases (a) Bulk time-resolved photoluminescence decay traces of control (black) film treated with trioctylphosphine oxide (TOPO, red), octadecanethiol (ODT, orange), and triphenylphosphine (PPh_3, blue), excited with pulsed excitation (470 nm, 125 kHz repetition rate, 30 nJ/cm^2 per pulse). (b) Integrated PL intensity statistics of control, TOPO, ODT, and PPh_3 treated films, error bars are standard error of the mean for N=20.

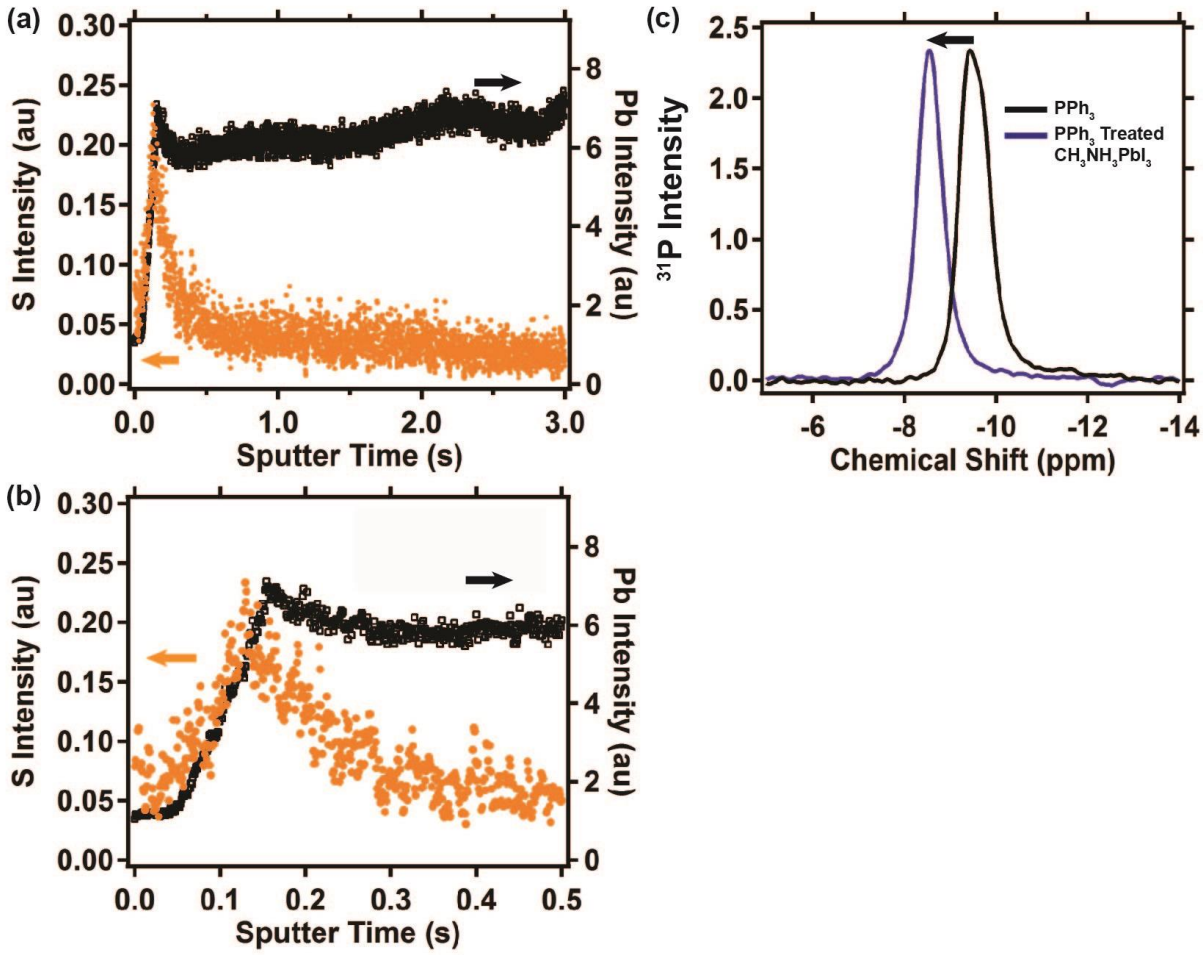

Figure 5.2. Evidence that Lewis bases are acting as surface ligands. (a) Glow discharge optical emission spectroscopy (GDOES) of an octadecanethiol (ODT) treated film monitoring the sulfur (S, orange) and lead (Pb, black) intensities as a function of film depth. (b) Identical plot shown in (a) with a shorter sputter time window, highlighting the composition at the surface. (c) ^{31}P solid state nuclear magnetic resonance (NMR) spectroscopy of the free ligand triphenylphosphine (PPh_3, black) versus a perovskite sample treated with PPh_3 (blue).

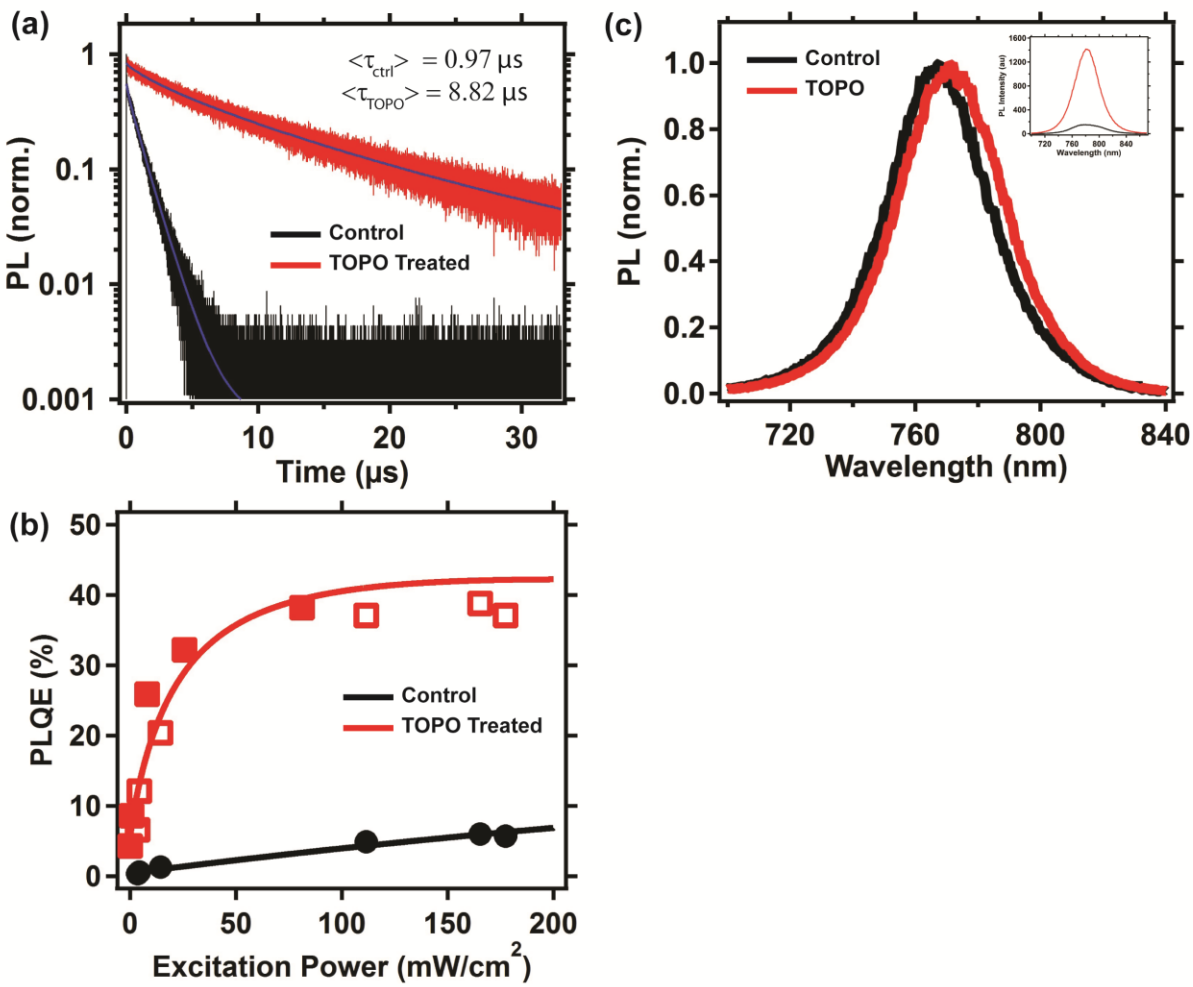

Figure 5.3. Photoluminescence measurements of optimized ligand treatment. (a) Champion bulk time-resolved photoluminescence (PL) decay traces of control (black) and trioctylphosphine oxide (TOPO, red) treated films on glass excited with pulsed excitation (470 nm, 30 kHz repetition rate, 50 nJ/cm^2 per pulse). (b) External PL quantum efficiency (PLQE) of films reported in (a) as a function of excitation power (532 nm, CW laser). Solid red squares are data taken one week prior to data marked with open squares, showing good sample stability. Solid lines are fits to the data taking into consideration monomolecular, bimolecular, and Auger recombination (See SI). (c) Normalized steady-state photoluminescence spectrum of control (black) and TOPO (red) treated film and (inset) raw PL data, showing the relative intensities before and after TOPO treatment.

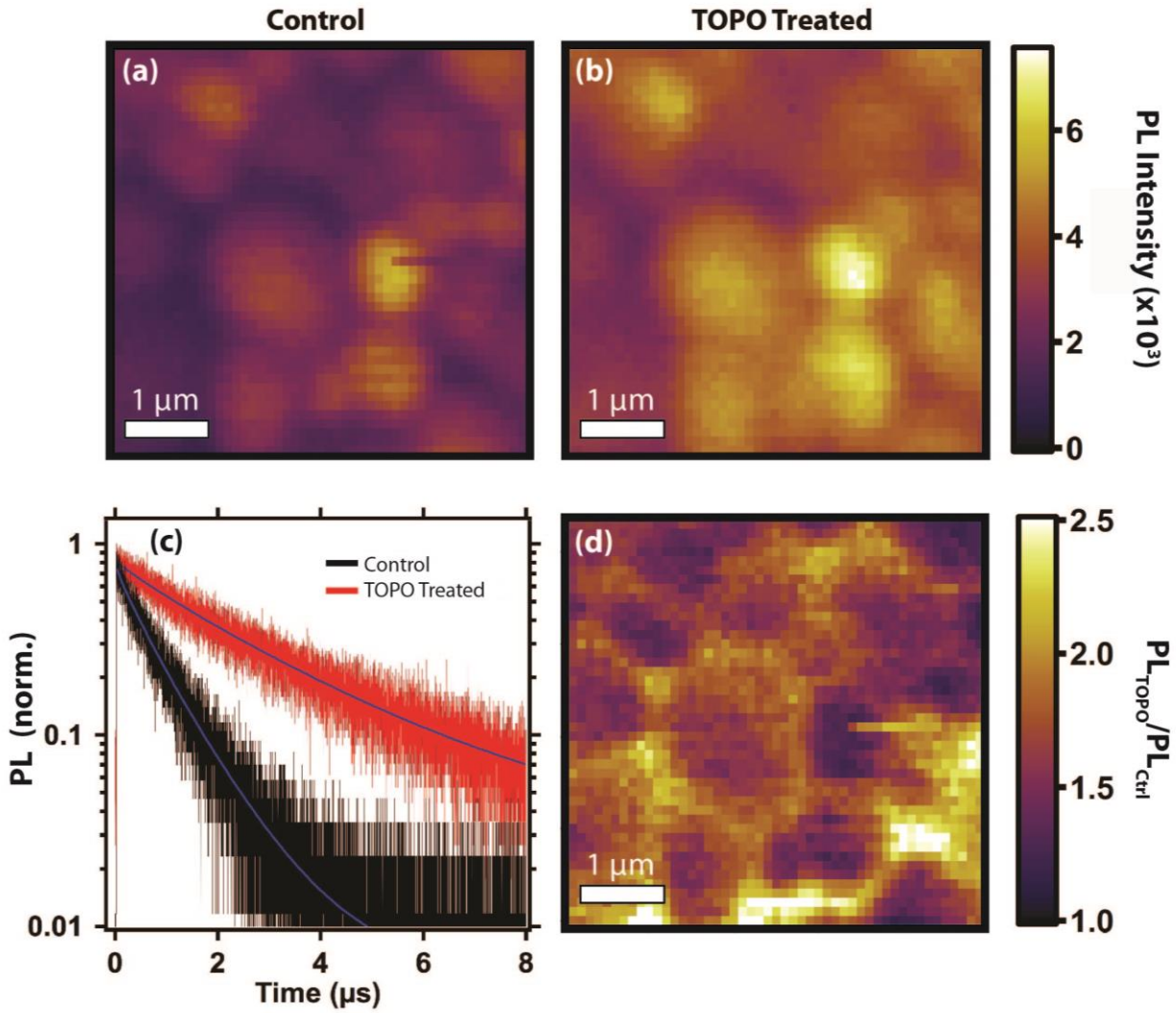

Figure 5.4. **Fluorescence microscopy of ligand passivated film** (a) Fluorescence image of a perovskite film before (a) and after (b) trioctylphosphine oxide (TOPO) treatment plotted on the same PL intensity scale. (c) Bulk time-resolved photoluminescence of the control film (black) with an average lifetime, $\langle\tau\rangle = 0.73 \pm 0.01$ µs, which improved to 2.40 ± 0.09 µs after TOPO (red) treatment (470 nm, 125 kHz, 70 nJ/cm^2 per pulse), solid lines are stretched exponential fits to the data. (d) Image showing the ratio of (b) TOPO treated fluorescence image divided by (a) the control fluorescence image.

5.12 References:

1 Stranks, S. D. & Snaith, H. J. Metal-Halide Perovskites for Photovoltaic and Light-Emitting Devices. *Nat. Nanotechnol.* **10**, 391-402, doi:10.1038/nnano.2015.90 (2015).

2 Zhang, W., Eperon, G. E. & Snaith, H. J. Metal Halide Perovskites for Energy Applications. *Nat. Energy* **1**, 16048, doi:10.1038/nenergy.2016.48 (2016).

3 Mei, Y., Zhang, C., Vardeny, Z. V. & Jurchescu, O. D. Electrostatic Gating of Hybrid Halide Perovskite Field-Effect Transistors: Balanced Ambipolar Transport at Room-Temperature. *MRS Commun.* **5**, 297-301, doi:http://dx.doi.org/10.1557/mrc.2015.21 (2015).

4 Shi, D. *et al.* Low Trap-State Density and Long Carrier Diffusion in Organolead Trihalide Perovskite Single Crystals. *Science* **347**, 519-522, doi:10.1126/science.aaa2725 (2015).

5 Dong, Q. *et al.* Electron-Hole Diffusion Lengths > 175 μm in Solution-Grown $CH_3NH_3PbI_3$ Single Crystals. *Science* **347**, 967-970, doi:10.1126/science.aaa5760 (2015).

6 Saidaminov, M. I. *et al.* High-Quality Bulk Hybrid Perovskite Single Crystals Within Minutes by Inverse Temperature Crystallization. *Nat. Commun.* **6**, 7586, doi:10.1038/ncomms8586 (2015).

7 Yang, Y. *et al.* Low Surface Recombination Velocity in Solution-Grown $CH_3NH_3PbBr_3$ Perovskite Single Crystal. *Nat. Commun.* **6**, 7961, doi:10.1038/ncomms8961 (2015).

8 Bi, Y. *et al.* Charge Carrier Lifetimes Exceeding 15 μs in Methylammonium Lead Iodide Single Crystals. *J. Phys. Chem. Lett.* **7**, 923-928, doi:10.1021/acs.jpclett.6b00269 (2016).

9 Wu, B. *et al.* Discerning the Surface and Bulk Recombination Kinetics of Organic-Inorganic Halide Perovskite Single Crystals. *Adv. Energy Mater.* **1600551**, doi:10.1002/aenm.201600551 (2016).

10 Riley E. Brandt, V. S., David S. Ginley, Tonio Buonassisi. Identifying Defect-Tolerant Semiconductors with High Minority-Carrier Lifetimes: Beyond Hybrid Lead Halide Perovskites. *MRS Commun.* **5**, 265-275, doi:10.1557/mrc.2015.26 (2015).

11 Tvingstedt, K. *et al.* Radiative Efficiency of Lead Iodide Based Perovskite Solar Cells. *Sci. Rep.* **4**, 6071, doi:10.1038/srep06071 (2014).

12 deQuilettes, D. W. *et al.* Impact of Microstructure on Local Carrier Lifetime in Perovskite Solar Cells. *Science* **348**, 683-686, doi:10.1126/science.aaa5333 (2015).

13 deQuilettes, D. W. *et al.* Photo-Induced Halide Redistribution in Organic-Inorganic Perovskite Films. *Nat. Commun.* **7**, 11683, doi:10.1038/ncomms11683 (2016).

14 Noel, N. K. *et al.* Enhanced Photoluminescence and Solar Cell Performance via Lewis Base Passivation of Organic-Inorganic Lead Halide Perovskites. *ACS nano* **8**, 9815-9821, doi:10.1021/nn5036476 (2014).

15 Deschler, F. *et al.* High Photoluminescence Efficiency and Optically Pumped Lasing in Solution-Processed Mixed Halide Perovskite Semiconductors. *J. Phys. Chem. Lett.* **5**, 1421-1426, doi:Doi 10.1021/Jz5005285 (2014).
16 Stranks, S. D. *et al.* Recombination Kinetics in Organic-Inorganic Perovskites: Excitons, Free Charge, and Subgap States. *Phys. Rev. Appl.* **2**, 034007, doi:10.1103/PhysRevApplied.2.034007 (2014).
17 D'Innocenzo, V., Srimath Kandada, A. R., De Bastiani, M., Gandini, M. & Petrozza, A. Tuning the Light Emission Properties by Band Gap Engineering in Hybrid Lead Halide Perovskite. *J. Am. Chem. Soc.* **136**, 17730-17733, doi:10.1021/ja511198f (2014).
18 Zhu, H. *et al.* Lead Halide Perovskite Nanowire Lasers with Low Lasing Thresholds and High Quality Factors. *Nat. Mater.* **14**, 636-642, doi:10.1038/nmat4271 (2015).
19 Protesescu, L. *et al.* Nanocrystals of Cesium Lead Halide Perovskites ($CsPbX_3$, X = Cl, Br, and I): Novel Optoelectronic Materials Showing Bright Emission with Wide Color Gamut. *Nano Lett.* **15**, 3692-3696, doi:10.1021/nl5048779 (2015).
20 Bischak, C. G., Sanehira, E. M., Precht, J. T., Luther, J. M. & Ginsberg, N. S. Heterogeneous Charge Carrier Dynamics in Organic-Inorganic Hybrid Materials: Nanoscale Lateral and Depth-Dependent Variation of Recombination Rates in Methylammonium Lead Halide Perovskite Thin Films. *Nano Lett.* **15**, 4799-4807, doi:10.1021/acs.nanolett.5b01917 (2015).
21 Stewart, R. J., Grieco, C., Larsen, A. V., Maier, J. J. & Asbury, J. B. Approaching Bulk Carrier Dynamics in Organo-Halide Perovskite Nanocrystalline Films by Surface Passivation. *J. Phys. Chem. Lett.* **7**, 1148-1153, doi:10.1021/acs.jpclett.6b00366 (2016).
22 Aberle, A. G. Surface Passivation of Crystalline Silicon Solar Cells: A Review. *Prog. Photovolt: Res. Appl.* **8**, 473-487, doi:10.1002/1099-159x(200009/10)8:5<473::aid-pip337>3.0.co;2-d (2000).
23 Bertness, K. A. *et al.* 29.5%-Efficient GaInP/GaAs Tandem Solar Cells. *Appl. Phys. Lett.* **65**, 989-991, doi:10.1063/1.112171 (1994).
24 Sheldon, M. T., Eisler, C. N. & Atwater, H. A. GaAs Passivation with Trioctylphosphine Sulfide for Enhanced Solar Cell Efficiency and Durability. *Adv. Energy Mater.* **2**, 339-344, doi:10.1002/aenm.201100666 (2012).
25 Tang, J. *et al.* Colloidal-Quantum-Dot Photovoltaics Using Atomic-Ligand Passivation. *Nat. Mater.* **10**, 765-771, doi:10.1038/nmat3118 (2011).
26 Boles, M. A., Ling, D., Hyeon, T. & Talapin, D. V. The Surface Science of Nanocrystals. *Nat. Mater.* **15**, 141-153, doi:10.1038/nmat4526 (2016).
27 Munro, A. M., Jen-La Plante, I., Ng, M. S. & Ginger, D. S. Quantitative Study of the Effects of Surface Ligand Concentration on CdSe Nanocrystal Photoluminescence. *J. Phys. Chem. C* **111**, 6220-6227, doi:10.1021/jp068733e (2007).
28 Colbert, A. E., Wu, W., Janke, E. M., Ma, F. & Ginger, D. S. Effects of Ligands on Charge Generation and Recombination in Hybrid Polymer/Quantum Dot

Solar Cells. *J. Phys. Chem. C* **119**, 24733-24739, doi:10.1021/acs.jpcc.5b07828 (2015).

29 Peterson, M. D. *et al.* The Role of Ligands in Determining the Exciton Relaxation Dynamics in Semiconductor Quantum Dots. *Annu. Rev. Phys. Chem.* **65**, 317-339, doi:10.1146/annurev-physchem-040513-103649 (2014).

30 Lee, J. W., Kim, H. S. & Park, N. G. Lewis Acid-Base Adduct Approach for High Efficiency Perovskite Solar Cells. *Acc. Chem. Res.* **49**, 311-319, doi:10.1021/acs.accounts.5b00440 (2016).

31 De Marco, N. *et al.* Guanidinium: A Route to Enhanced Carrier Lifetime and Open-Circuit Voltage in Hybrid Perovskite Solar Cells. *Nano Lett.* **16**, 1009-1016, doi:10.1021/acs.nanolett.5b04060 (2016).

32 Li, X. *et al.* Improved Performance and Stability of Perovskite Solar Cells by Crystal Crosslinking with Alkylphosphonic Acid ω-Ammonium Chlorides. *Nat. Chem.* **7**, 703-711, doi:10.1038/nchem.2324 (2015).

33 Ahn, N. *et al.* Highly Reproducible Perovskite Solar Cells with Average Efficiency of 18.3% and Best Efficiency of 19.7% Fabricated via Lewis Base Adduct of Lead(II) Iodide. *J. Am. Chem. Soc.* **137**, 8696-8699, doi:10.1021/jacs.5b04930 (2015).

34 Chen, Q. *et al.* Controllable Self-Induced Passivation of Hybrid Lead Iodide Perovskites Toward High Performance Solar Cells. *Nano Lett.* **14**, 4158-4163, doi:10.1021/nl501838y (2014).

35 Zhang, W. *et al.* Ultrasmooth Organic-Inorganic Perovskite Thin-Film Formation and Crystallization for Efficient Planar Heterojunction Solar Cells. *Nat. Commun.* **6**, 6142, doi:10.1038/ncomms7142 (2015).

36 Eperon, G. E. *et al.* The Importance of Moisture in Hybrid Lead Halide Perovskite Thin Film Fabrication. *ACS nano* **9**, 9380-9393, doi:10.1021/acsnano.5b03626 (2015).

37 Tian, Y. *et al.* Mechanistic Insights into Perovskite Photoluminescence Enhancement: Light Curing with Oxygen Can Boost Yield Thousandfold. *Phys. Chem. Chem. Phys.* **17**, 24978-24987, doi:10.1039/c5cp04410c (2015).

38 Galisteo-Lopez, J. F., Anaya, M., Calvo, M. E. & Miguez, H. Environmental Effects on the Photophysics of Organic-Inorganic Halide Perovskites. *J. Phys. Chem. Lett.* **6**, 2200-2205, doi:10.1021/acs.jpclett.5b00785 (2015).

39 Yamada, Y., Nakamura, T., Endo, M., Wakamiya, A. & Kanemitsu, Y. Photocarrier Recombination Dynamics in Perovskite $CH_3NH_3PbI_3$ for Solar Cell Applications. *J. Am. Chem. Soc.* **136**, 11610-11613, doi:10.1021/ja506624n (2014).

40 Sakai, N. *et al.* The Mechanism of Toluene-Assisted Crystallization of Organic–Inorganic Perovskites for Highly Efficient Solar Cells. *J. Mater. Chem. A* **4**, 4464-4471, doi:10.1039/c6ta01087c (2016).

41 Sanchez, P. *et al.* A Path Towards a Better Characterisation of Silicon Thin-Film Solar Cells: Depth Profile Analysis by Pulsed Radiofrequency Glow Discharge Optical Emission Spectrometry. *Prog. Photovolt: Res. Appl.* **22**, 1246-1255, doi:10.1002/pip.2387 (2013).

42 Dharmadasa, I. M., Ives, M., Brooks, J. S., France, G. H. & Brown, S. J. Application of Glow Discharge Optical Emission Spectroscopy to Study Semiconductors and Semiconductor Devices. *Semicond. Sci. Technol.* **10**, 369-372, doi:10.1088/0268-1242/10/3/023 (1995).

43 Anderson, N. C. & Owen, J. S. Soluble, Chloride-Terminated CdSe Nanocrystals: Ligand Exchange Monitored by ^{1}H and ^{31}P NMR Spectroscopy. *Chem. Mater.* **25**, 69-76, doi:10.1021/cm303219a (2013).

44 Kuhl, O. Phosphorus-31 NMR Spectroscopy: A Concise Introduction for the Synthetic Organic and Organometallic Chemist. *Springer,* Verlag Berlin Heidelberg, **2008**.

45 Stranks, S. D. *et al.* Electron-Hole Diffusion Lengths Exceeding 1 Micrometer in an Organometal Trihalide Perovskite Absorber. *Science* **342**, 341-344, doi:Doi 10.1126/Science.1243982 (2013).

46 Eperon, G. E. *et al.* Formamidinium Lead Trihalide: A Broadly Tunable Perovskite for Efficient Planar Heterojunction Solar Cells. *Energ. Environ. Sci.* **7**, 982-988, doi:Doi 10.1039/C3ee43822h (2014).

47 Vrućinić, M. *et al.* Local Versus Long-Range Diffusion Effects of Photoexcited States on Radiative Recombination in Organic-Inorganic Lead Halide Perovskites. *Adv. Sci.* **2**, 1500136, doi:10.1002/advs.201500136 (2015).

48 Draguta, S. *et al.* Spatially Non-uniform Trap State Densities in Solution-Processed Hybrid Perovskite Thin Films. *J. Phys. Chem. Lett.* **7**, 715-721, doi:10.1021/acs.jpclett.5b02888 (2016).

49 Tian, Y. *et al.* Enhanced Organo-Metal Halide Perovskite Photoluminescence from Nanosized Defect-Free Crystallites and Emitting Sites. *J. Phys. Chem. Lett.* **6**, 4171-4177, doi:10.1021/acs.jpclett.5b02033 (2015).

50 Tian, Y. *et al.* Giant Photoluminescence Blinking of Perovskite Nanocrystals Reveals Single-Trap Control of Luminescence. *Nano Lett.* **15**, 1603-1608, doi:10.1021/nl5041397 (2015).

51 Lindsey, C. P. & Patterson, G. D. Detailed Comparison of the Williams–Watts and Cole–Davidson Functions. *J. Chem. Phys.* **73**, 3348-3357, doi:10.1063/1.440530 (1980).

52 Johnston, M. B. & Herz, L. M. Hybrid Perovskites for Photovoltaics: Charge-Carrier Recombination, Diffusion, and Radiative Efficiencies. *Acc. Chem. Res.* **49**, 146-154, doi:10.1021/acs.accounts.5b00411 (2016).

53 Milot, R. L., Eperon, G. E., Snaith, H. J., Johnston, M. B. & Herz, L. M. Temperature-Dependent Charge-Carrier Dynamics in $CH_3NH_3PbI_3$ Perovskite Thin Films. *Adv. Funct. Mater.* **25**, 6218-6227, doi:10.1002/adfm.201502340 (2015).

54 Saba, M. *et al.* Correlated Electron-Hole Plasma in Organometal Perovskites. *Nat. Commun.* **5**, 5049, doi:10.1038/ncomms6049 (2014).

55 Nie, W. *et al.* High-Efficiency Solution-Processed Perovskite Solar Cells with Millimeter-Scale Grains. *Science* **347**, 522-525, doi:10.1126/science.aaa0472 (2015).

56 Yamada, Y. *et al.* Dynamic Optical Properties of $CH_3NH_3PbI_3$ Single Crystals As Revealed by One- and Two-Photon Excited Photoluminescence Measurements. *J. Am. Chem. Soc.* **137**, 10456-10459, doi:10.1021/jacs.5b04503 (2015).
57 Pazos-Outon, L. M. *et al.* Photon Recycling in Lead Iodide Perovskite Solar Cells. *Science* **351**, 1430-1433, doi:10.1126/science.aaf1168 (2016).
58 Leblebici, S. Y. *et al.* Facet-Dependent Photovoltaic Efficiency Variations in Single Grains of Hybrid Halide Perovskite. *Nat. Energy* **1**, 16093, doi:10.1038/nenergy.2016.93 (2016).
59 Green, M. A. Radiative Efficiency of State-of-the-Art Photovoltaic Cells. *Prog. Photovolt: Res. Appl.* **20**, 472-476, doi:10.1002/pip.1147 (2012).
60 Miller, O. D., Yablonovitch, E. & Kurtz, S. R. Strong Internal and External Luminescence as Solar Cells Approach the Shockley-Queisser Limit. *IEEE J. Photovolt.* **2**, 303-311, doi:10.1109/jphotov.2012.2198434 (2012).
61 Braly, I. L. & Hillhouse, H. W. Optoelectronic Quality and Stability of Hybrid Perovskites from $MAPbI_3$ to $MAPbI_2Br$ Using Composition Spread Libraries. *J. Phys. Chem. C* **120**, 893-902, doi:10.1021/acs.jpcc.5b10728 (2016).
62 Sutter-Fella, C. M. *et al.* High Photoluminescence Quantum Yield in Band Gap Tunable Bromide Containing Mixed Halide Perovskites. *Nano Lett.* **16**, 800-806, doi:10.1021/acs.nanolett.5b04884 (2016).

Chapter 6: Hybrid Perovskite Films Approaching the Radiative Limit with Over 90% Internal Photoluminescence Quantum Efficiency

Authors: Ian L. Braly†, Dane W. deQuilettes†, Luis M. Pazos-Outón, Sven Burke, Mark E. Ziffer, David S. Ginger, Hugh W. Hillhouse

† equal contribution

6.1 Overview:

Reducing non-radiative recombination in semiconducting materials is a prerequisite for achieving the highest performance in a host of light emitting and photovoltaic applications. Here we characterize both external and internal photoluminescence quantum efficiency and quasi-Fermi-level splitting of hybrid perovskite ($CH_3NH_3PbI_3$) thin films. With respect to material bandgap, these passivated films exhibit the highest quasi-Fermi level splitting measured to date, reaching 96.5 ± 0.9% of the Shockley-Queisser limit, approaching the highest performing GaAs solar cells. We confirm these values with independent measurements of internal photoluminescence quantum efficiency values of 91.9 ± 2.7% under one Sun illumination intensity, which are also the highest measured to date. These results suggest that the material optoelectronic quality can reach levels unprecedented for solution-processed, band-type semiconductors, which opens new opportunities in optoelectronics, and emphasizes that further increases in voltage and photovoltaic device efficiency for hybrid perovskites will be obtained by combining surface passivation with optimized charge carrier selective interfaces.

6.2 Introduction:

Organic-inorganic lead halide perovskites are promising semiconducting materials for a range of photovoltaic,[1] optoelectronic,[2,3] and electronic applications.[4] Their excellent performance is often attributed to their high absorption coefficents,[5] long charge carrier diffusion lengths, band-like charge carrier transport,[6] slow recombination,[7,8] and high fractions of radiative recombination.[9-11] The latter is particularly important for light-emitting applications as well as photovoltaics, where ideal devices operate in the radiative limit.[12] As this limit is approached, all avoidable charge carrier recombination pathways are eliminated, and only radiative recombination remains.[13] As such, any non-radiative recombination reduces the steady-state non-equilibrium carrier concentrations in the conduction and valence bands, and thus reduces the difference between the quasi-Fermi levels of these two bands ($\Delta\mu = E_F^{CB} - E_F^{VB}$) and the resulting maximum achievable open circuit voltage (V_{OC}).[14,15] Therefore, when assessing the fundamental limitations of a new material, one of the most important considerations is determining whether the material can demonstrate a high fraction of radiative recombination relative to other recombination pathways.[16] For example, although Si has been deployed as a successful commercial technology, it has only demonstrated internal photoluminescence quantum efficiencies (η_{int}) as high as 20%, limiting its open-circuit voltage.[17-19] On the other hand, GaAs, which holds the record power conversion efficiency for a single junction solar cell at 28.8%, has demonstrated η_{int} as high as 99.7%[20].

Although perovskites have shown rapid improvements in device performance over the last seven years, the pace appears to be slowing in single-junction cells,[10] as often happens as technologies mature and approach fundamental limits. A pivotal question now lies in determining the guiding principles to fabricate more efficient devices to approach the theoretical efficiency limit. A similar situation occurred for GaAs, where device efficiencies were static for twenty years and the efficiency jumped by ~2.4% (percentage points) in a very short amount of time. Those improvements have been attributed primarily to improvements in V_{OC}, due to an increased understanding of the importance of luminescence extraction.[19] One might conclude that similar quantum efficiency improvements should be sought in perovskites, as reported short-circuit current densities have been reported to reach 92% of their theoretical maxima in state-of-the-art devices[10,21-23], compared with V_{OC}'s and fill-factors that are more typically only ~87% or less of expected limits[10].

The task of achieving high photoluminescence quantum efficiencies has been challenging for solution-processed semiconductors, due to the formation of both bulk and surface defects, which serve as non-radiative recombination centers[24]. For thin-film perovskite layers, external photoluminescence quantum efficiencies (η_{ext}) at 1-Sun incident photon flux are typically < 15%, which can be increased by changing the outcoupling efficiency.[9,11,25-28] Although outcoupling is one promising avenue, there has been an increasing amount of evidence suggesting that defects at surfaces and surface recombination velocities must be reduced to achieve the highest η_{ext} and therefore allow devices to operate at efficiencies close to the radiative limit.[25,29,30] While surface passivation strategies were essential in the development of leading semiconductor technologies such as Si and GaAs,[31] perovskite surface chemistry remains relatively unexplored by comparison and is expected to be an important consideration in achieving optimized devices[32,33].

In this regard, Lewis bases have been shown to surface passivate $CH_3NH_3PbI_3$.[25] Further, we have recently shown that electron donating molecules such as *n*-trioctylphosphine oxide (TOPO), bind to the surface of $CH_3NH_3PbI_3$ perovskite and reduce non-radiative recombination[8]. These films demonstrated η_{ext} as high as 35% at 1-Sun incident photon flux. This result is extremely encouraging considering the low escape probabilities (in the range of ~5.5 to 12.5% predicted by several groups), implying η_{int} is likely much higher[9,34,35].

Here, we independently measure the quasi-Fermi level splitting ($\Delta\mu$), and the external and internal photoluminescence quantum efficiencies (η_{ext} and η_{int}) for solution-processed $CH_3NH_3PbI_3$ perovskite thin films both before and after chemical surface passivation. We use a photoluminescence spectrometer (calibrated to measure absolute intensity and minimize spectral aberration) to measure a $\Delta\mu$ = 1.280 ± 0.004 eV after surface passivation, which is 96.5 ± 0.8 % of the Shockley-Queisser limit $\Delta\mu$, and which is the highest value reported for a perovskite to date. Further, we use an integrating sphere to measure the external photoluminescence quantum efficiency of a film deposited on a high reflectivity substrate to be η_{ext} = 37.0 ± 1.4%, and we measure η_{int} by fitting experimental data with a detailed ray optics model that predicts external photoluminescence quantum

efficiency as parasitic loss is systematically increased,[20] and obtain a value of η_{int} = 91.9 ± 2.7%.

These improvements relative to the control films are of comparable magnitude to those leading to the record GaAs solar cells[36]. This ultrahigh $\Delta\mu$ suggests that surface passivation implemented with ideal contacts will be useful in overcoming Si efficiency records and in approaching efficiencies only achieved by GaAs.

6.3 Determination of Quasi-Fermi Level Splitting from Absolute Intensity Photoluminescence:

We used confocal photoluminescence spectroscopy to study $CH_3NH_3PbI_3$ films before and after surface passivation. The perovskite precursor solution was prepared by mixing lead acetate and methylammonium iodide in dimethylformamide and spin-coating this solution on a gold back reflector substrate with a SiO_x insulating layer.[37] We note that this type of geometry closely resembles a typical structure for a perovskite based photovoltaic device with Au serving as a back contact.[22] Sister samples were subsequently surface treated with a dilute (0.025 M) solution of n-trioctylphosphine oxide (TOPO) in chlorobenzene. We have previously shown that TOPO treatment reduces non-radiative recombination and is primarily confined to the surface, does not lead to any quantifiable changes in the film structure, and likely forms a new bond upon interaction with the perovskite surface.[8]

To determine the maximum achievable open circuit voltage ($V_{OC} = \Delta\mu/q$), we extract $\Delta\mu$ by non-linear least-squares fitting of the absolute intensity photoluminescence spectrum to an expression based on the generalized Planck Radiation Law developed by Lasher and Stern[38] and Würfel.[39] The equation relates the external spectral flux of radiative emission to the conduction band and valence band quasi-Fermi levels, E_F^{CB} and E_F^{VB}, and the spectral absorptivity, a:

$$I_{PL}(E) = \left\{\frac{2\pi E^2}{h^3c^2}\right\} \cdot \left\{\frac{1}{exp\left(\frac{E-(E_F^{CB}-E_F^{VB})}{kT}\right)-1}\right\} \cdot \{a(E, E_F^{CB}, E_F^{VB}, T)\} \quad (1)$$

Where E is the photon energy in *eV*, and I_{PL} is the spectral photoluminescence emission flux in units of *photons/(m^2·s·eV)*. Importantly, equation (1) is compatible with absorption coefficient models that include sub-gap states (see S.1 for additional details and assumptions). While this is essential for describing the band-band emission peak shape for semiconductors that exhibit potential fluctuations (like CIGS and CZTS), it is also required for fitting the photoluminescence peak shape from near-perfect semiconductors like GaAs that also exhibit Urbach tails.[14,40] The method above, which fits the entire PL emission spectrum, avoids pitfalls associated with other techniques for extracting E_F^{CB} - E_F^{VB} = $\Delta\mu$ from photoluminescence such as the high-energy tail fitting procedure[41], as well as the common approach derived by Ross based on η_{ext} (See S.1)[42]. A distinct advantage of the method detailed here is it can be used to reveal the functional form of

subgap tail-states (see S.2 and S.3 for details of the absorption coefficient model and fitting procedure).

We measured the external photoluminescence quantum efficiency of a representative control sample and TOPO treated film at 1-Sun equivalent illumination intensity (continuous 60 mW/cm^2 at 532 nm, see S.4 for details). We use a NIST-calibrated blackbody source to calibrate (see details in S.5) photoluminescence spectra on an absolute scale of the same films at the same illumination intensity (Fig. 1a) and modeled the spectra using (1). The untreated film exhibited an average external photoluminescence quantum efficiency (η_{ext}) of 0.92 ± 0.50% (Fig. 1b) and spatially averaged $\Delta\mu$ of 1.208 ± 0.008 eV (N = 121, 95% confidence) (Fig. 1c), which is typical for films prepared from the lead acetate route and comparable to values reported for the highest performing devices[10]. Next, we fit the photoluminescence spectrum of a TOPO surface passivated film demonstrating an average η_{ext} of 20.3 ± 5.6% and extracted a $\Delta\mu$ = 1.280 ± 0.004 eV (N = 121, 95% confidence). Because the photoluminescence of polycrystalline solution-processed thin film perovskite films are known to be spatially heterogeneous,[43] we report spatial averages, with the error intervals primarily reflecting the remaining spatial heterogeneity in the film. These fit $\Delta\mu$ data are consistent with the values determined using the relationship derived by Ross based on η_{ext} and the radiative limit $\Delta\mu$; and similar to the method detailed by Bauer, where only the high energy tail of the photoluminescence is fit (See Table S1).

The magnitude of this improvement in $\Delta\mu$ after TOPO treatment is impressive considering the logarithmic dependence of V_{OC} on η_{ext} (See equation (S5)), where enhancements on a similar scale led to record efficiencies for GaAs[36]. Since the V_{OC} deficit for a given material depends on its bandgap, we use the modeled bandgap energy to calculate the Shockley-Queisser limit $\Delta\mu$ in each case and compare to the observed $\Delta\mu$'s. The Shockley-Queisser limit here is defined as the detailed balance limit for a material with a step-function absorptivity, and the radiative limit is defined as the detailed balance limit for a material accounting for its real absorptivity spectrum. Using the extracted band-gap of 1.60 eV, we find that the control film achieved 91.1 ± 1.3% (Fig. 1d) of the Shockley-Queisser limit $\Delta\mu$, again consistent with high quality, untreated films that have been implemented in state-of-the-art devices.[10] The $\Delta\mu$ is enhanced to 96.5 ± 0.9% (Fig. 1d) of the Shockley-Queisser limit $\Delta\mu$ after TOPO surface passivation, which is higher than any device reported to date (See S.6). We calculate this value to be only 39 meV less than the radiative limit $\Delta\mu$ (Fig. S2 and S3 and discussion). To put this in context, if a passivated hybrid perovskite film such as the one studied here can be successfully implemented into a device with appropriate selective contacts, then the resulting device (V_{OC} = 1.280 V) would be comparable to the 1.122 V achieved by the world record GaAs,[44] which is 96.2% of the Shockley-Queisser limit V_{OC} for GaAs.[13,45]

6.4 Determination of Internal Photoluminescence Quantum Efficiency:

The high optoelectronic quality of the TOPO treated $CH_3NH_3PbI_3$ measured in this work could only be obtained from samples with very high internal photoluminescence quantum efficiency (η_{int}). The external photoluminescence quantum efficiency (η_{ext}) of perovskite materials can be significantly lower than the η_{int} as a result of the low outcoupling

efficiencies (~10%), which result from the narrow escape cone from planar films due to the perovskite refractive index (n ~ 2.6, see Fig. S13). Additionally, determining the ratio between radiative and non-radiative recombination can be obscured by reabsorption of emitted photons. For these reasons, and to better gauge the quality of the films prepared in this work, we determine η_{int} by adapting a method previously applied to high-quality GaAs by measuring η_{ext} of the perovskite film with varying back-surface parasitic absorption[20].

Assuming a reflector-independent η_{int} (See Fig. S9), flat interfaces (See Fig. S10), and the outcoupling efficiency is not significantly altered by interference effects, waveguiding, or a thin layer of TOPO (See Fig. S11 through S15), η_{ext} can be related to η_{int} and parasitic losses from non-ideal back-surface reflectivity with equation (2) after Schnitzer et al.[20]:

$$\eta_{ext} = \frac{\eta_{int}/2n^2}{\eta_{int}/2n^2+(1-\eta_{int})+L/4\alpha_0 d_0} \quad (2)$$

In equation (2), n is the average refractive index (2.6, see Fig. S13) over the perovskite emission band,[46] α_0 is the average band-edge absorption coefficient ($1.20\text{x}10^4$ cm^{-1}) over the perovskite emission band,[46] d_0 is the measured absorber thickness (250 nm), and L is the loss factor, defined as L = 100% - Reflectivity%. Using these definitions, we calculate $\alpha_0 d_0$ to be 0.300 and hold this value constant for fitting. Briefly, equation (2) describes the fraction of external radiative recombination over the total recombination. The factors that reduce the photon flux from the front surface include non-radiative recombination within the active layer of the film as well as parasitic absorption outside the active layer. Assuming that waveguiding modes are not present in the back reflector stack (See Fig. S11), photon recycling and total internal reflections at steady state just represent a remission into the pool of trapped luminescent photons and contribute no net gain or loss and are therefore included by default in (2).[20]

Fig. 2 shows the samples used for measuring $\eta_{int,}$ which comprise a thin ~250 nm perovskite active layer spin coated on top of 4 quadrant metal mirror with 4 different metal samples (Fig. 2a). The procedure involves measuring η_{ext} for a number of samples with well-characterized quantities of parasitic absorption outside the active layer,[20] and in our case the varying reflectivity of the back mirrors, Pd, Au, Ti, and Si play the role of the varying parasitic loss terms. A SiOx layer between the mirror and the perovskite layer prevents electronic interaction and near-field quenching with the metals.

To determine the optical losses suffered by the perovskite photoluminescence (780 nm center, 44 nm FWHM) within the stack, we characterize the total optical loss within these substrates before perovskite deposition by measuring the angle-averaged reflectivity across the objective excitation/collection cone using a 790 nm LED (23 nm FWHM) and a calibrated wide-field microscope (See S.7). We measure a loss factor of 3.9 ± 3.6% for Au, 27.8 ± 2.4% for Pd, 49.8 ± 2.1% for Ti, and 78.5 ± 1.7% for Si (95% confidence intervals for N > 1000 within the sample). We also measure the external quantum efficiency (η_{ext}) of our samples independently from the confocal measurements using an integrating sphere. For the sample measured in Fig. 1, we independently determined η_{ext} =

23.5%, which is within the confidence interval of 20.3 ± 5.6% measured using the confocal instrument. Furthermore, when we use the method described by Ross to calculate $\Delta\mu$ (equation (S5)) using the radiative limit $\Delta\mu$, the result is 1.282 eV which is also within the confidence interval of 1.280 ± 0.004 eV determined by the full-peak fit method above.

Fig. 3b shows a representative η_{ext} image of a control film subsequently treated with TOPO (Fig. 3c) on a multimetal back reflector substrate, when measured at 1-Sun incident photon flux (532 nm, 60 mW/cm^2). We find that the regions with the smallest parasitic absorption (lowest L), exhibit the highest η_{ext} and TOPO passivation improves η_{ext} across the entire substrate (Fig. 3c). Fig. 3d and 3e, show the control and champion TOPO passivated films on the multimetal substrates, where the TOPO passivated film demonstrates a maximum η_{ext} of 36.7 ± 1.4%. As opposed to the control sample, the TOPO sample exhibits a strong dependence of η_{ext} with loss factor. This is evidence that the relative rates of loss from parasitic absorption and non-radiative recombination are on a similar scale. We use the progression in η_{ext}'s along with equation (2) to extract the η_{int} values. We report η_{int} = 9.4 ± 3.5% for the control sample and η_{int} = 91.9 ± 2.7% for the TOPO treated film.

The η_{int} of the control is consistent with other reports for unpassivated perovskite thin films measured at 1-Sun incident photon flux[9,34], whereas the surface treated film exhibits an internal quantum efficiency only observed in fluorescent molecules containing no dangling bonds[47], as well as only a few semiconducting materials such as GaAs double heterostructures[20], surface passivated or core/shell quantum dots, and chemically-passivated MoS_2[16].

6.5 Impact of Excitation Intensity and Temperature on Internal Photoluminescence Quantum Efficiency:

To confirm that these TOPO passivated films indeed exhibit η_{int} values approaching unity, we To confirm that these TOPO passivated films indeed exhibit η_{int} values approaching unity, we test whether non-radiative recombination can be further reduced in these films by performing both excitation and temperature dependent measurements. It has previously been shown in perovskite materials that η_{ext} increases as function of excitation power due to the increasing fraction of radiative bimolecular recombination over non-radiative trap-assisted recombination.[11,28,48] In particular, Richter et al. showed that η_{int} as high as 70% could be achieved at carrier densities of ~1x10^{17} cm^{-3} (~ 100 Suns) and others have shown maximum values in excess of 30%.[25,28] In the ideal material, recombination should no longer be limited by traps and η_{int} should be near unity across all carrier densities until non-radiative multi-body effects (i.e. Auger recombination) start to dominate at higher carrier concentrations.[16]

In this regard, we test the excitation-dependent behavior of TOPO passivated films. Fig. 4a shows the η_{ext} of a control and TOPO treated film measured in an integrating sphere as a function of excitation power. For the control film and consistent with literature reports,[9] η_{ext} increases steadily as function of excitation power and reaches a maximum η_{ext} (η_{int}) of 1% (12%) at 738 W/cm^2, where η_{int} is predicted using (2). On the other hand, the

optimized, TOPO-passivated film already demonstrates high η_{ext} even at very low excitation powers (η_{ext} = 36%, 6 mW/cm^2, ~ 0.1 Suns), and only slightly increases from the 1-Sun condition to 43% (94%) at an excitation of 332 mW/cm^2 (~ 5 Suns), whereupon Auger recombination starts to dominate at subsequent excitation powers (See S.9 and S.10). For high-quality perovskite films, the observation that Auger recombination starts to dominate shortly after 1-Sun incident photon flux (60 mW/cm^2) is important as it places these films in a favorable regime where the highest radiative efficiencies are achievable under AM1.5 (in contrast to Si),[49] although we note that this observation may significantly reduce the theoretical performance of the application of perovskites in concentrator photovoltaics[50].

Aside from improving η_{int} by increasing the fraction of radiative recombination by trap-filling, other reports have shown cooling the sample can also achieve a reduction in non-radiative recombination, with maximum η_{ext} values approaching unity at the lowest temperatures.[28,51] Fig. 4b shows the η_{ext} as a function of temperature of the control and TOPO passivated films measured at 60 mW/cm^2 and within the tetragonal phase.[52] This control film started at a modest η_{ext} (η_{int}) of 0.3% (4%) at 300 K, which steadily increased to 2% (22%) at a temperature of 235 K. These improvements correspond to a 5-fold enhancement in η_{ext}, which is consistent with other unpassivated films in the literature.[28] The TOPO treated film, on the other hand, only demonstrates moderate improvements in η_{ext} and η_{int} ranging from 42% (93%) at 300 K to 70% (99%) at 235 K, an improvement factor below 2 for η_{ext}, which is consistent with extremely low levels of non-radiative recombination at room temperature under a generation rate comparable to 1 Sun illumination. We note that at temperatures below 235 K, we begin to observe reversible changes in film morphology (See S.11), which suggests that the outcoupling efficiency may be changing and that our calculation of η_{int} may not be reliable below these temperatures. The comparatively small improvements in TOPO treated film as temperature decreases suggests that some thermally activated nonradiative recombination still exists, but whether these recombination centers reside at the surface or are concentrated within the bulk remains an open question.

6.6 Discussion:

Considering the history of the development of other successful photovoltaic technologies such as Si and GaAs, surface passivation appears to be a prerequisite in achieving the highest quality materials[31,53]. For example, untreated GaAs, Si, and CdTe all exhibit high surface recombination velocities due to the presence of dangling bonds and surface oxide, and these surface recombination centers must be passivated to realize high efficiency devices. Interestingly, initial passivating strategies for GaAs also utilized Lewis bases to significantly reduce the surface recombination velocity.[54,55] Similarly, the passivation of the front and back surfaces of silicon took decades to master,[31] and these foundational studies of tailoring the surface chemistry have allowed silicon to be successful in a wide range of applications. In this study, we show from purely a materials standpoint that surface passivated perovskites can achieve $\Delta\mu$'s higher than any perovskite films or devices we are aware of to date. Notably, these values are beginning to approach high quality passivated GaAs. As a proof of concept, these results are promising, but we note that the successful incorporation of surface passivating agents into device architectures

will likely require careful deposition of a monolayer of non-labile passivating molecules, a detailed understanding of the impact of surface modifiers on band bending and work function,[56,57] and treatments that either maintain or improve conductivity.[58] For example, we have recently shown that while many passivating molecules improve photoluminescence quantum efficiency, some treatment procedures result in the impediment of lateral charge transport[59]. Here, we find that the TOPO surface passivation in this study qualitatively improves the transport length (See S.12), whether this results from better diffusion through improvements in intergrain connectivity or more efficient photon recycling is a topic for further study.

As highlighted earlier, it is remarkable that these perovskite films demonstrate optoelectronic quality comparable to high quality, direct-gap GaAs and possibly suggests that the contribution of the proposed indirect gap of perovskites may have a negligible effect on the radiative efficiency. For example, the indirect nature of the bandgap and Auger recombination in Si limits the internal photoluminescence quantum efficiency to about 20%.[17] This is often attributed to the optical transitions requiring phonons, and thus loss of some energy to lattice vibrations.[17] It has been reported by several groups that photoexcitation in perovskites occurs via a direct transition and recombination occurs via an indirect transition ~25-75 meV below the direct transition.[60-62] This band structure has been predicted to reduce the maximum achievable internal photoluminescence quantum efficiency by 50%[60] and reduce the average bimolecular recombination rate which reduces V_{OC}.[63] More recently, Herz and coworkers have proposed that the indirect gap does not significantly contribute to carrier recombination in perovskite films, and instead suggest that recombination is dominated by a tail of radiative band states due to disorder.[64] We note that despite the possibility of an indirect transition for recombination in $CH_3NH_3PbI_3$, the internal quantum yield approaches unity under one Sun conditions and the $\Delta\mu$ approaches its radiative limit, as predicted by the absorption coefficient (see Fig. S2). This suggests that with significant reductions in non-radiative recombination, perovskite materials are not limited in reaching the radiative efficiencies of direct-gap semiconductors such as GaAs.

6.7 Conclusions:

In summary, we provide the first experimental evidence that polycrystalline, solution processed perovskite ($CH_3NH_3PbI_3$) thin films can achieve internal photoluminescence quantum efficiencies over 90%, and $\Delta\mu$ as high as 1.280 ± 0.01 eV with careful control of the non-radiative losses that dominate at the surfaces. These values are approaching the theoretical open circuit voltages predicted by the Shockley-Queisser limit (1.326 V) of a material with a bandgap of 1.60 eV and are highly encouraging, considering state-of-the-art devices only exhibit V_{OC}'s ~1.15 V. As these high of $\Delta\mu$ are only possible with ultra-high external and internal photoluminescence quantum efficiencies, we confirmed our measured values by both directly measuring η_{ext} and implementing a straightforward strategy for determining the η_{int}. We believe this method will be highly useful for future studies where only η_{ext} and the loss factors of the substrates will need to be measured. Using this method, we report the highest η_{int}'s (91.9 ± 2.7%) achieved to date in perovskite thin films with 1-Sun incident photon flux. This observation places these films amongst the most emissive semiconducting materials ever fabricated, including GaAs

heterostructures and well passivated quantum dots. Importantly, these findings suggest that there should be no limitations preventing perovskites from approaching the radiative under 1-Sun illumination conditions and that these types of surface passivation protocols can be widely implemented in the fabrication of highly efficient light emitting diodes, low-power optically and electrically driven lasing, and potentially in optical refrigeration applications. By careful control over surface chemistry and the use of charge selective contacts, it is expected that we will see the desired improvements in the next generation of high open circuit voltages devices with record power conversion efficiencies.

6.8 Appendix E:

Materials and methods and supplementary text

6.9 Acknowledgements:

D.W.D. and D.S.G. acknowledge DOE (DE-SC0013957) for supporting the microscopy work. D.W.D. acknowledges support from an NSF Graduate Research Fellowship (DGE-1256082) and thanks Lucas Flagg for experimental help. I.L.B. and H.W.H. acknowledge financial support from the U.S. Department of Energy Sunshot Initiative, Next Generation Photovoltaics 3 program, Award DE-EE0006710. Part of this work was conducted at the Molecular Analysis Facility and at the Washington Nanofabrication Facility, two National Nanotechnology Coordinated Infrastructure sites at the University of Washington, which are supported in part by the National Science Foundation (grant ECC-1542101), the University of Washington, the Molecular Engineering & Sciences Institute, the Clean Energy Institute, and the National Institutes of Health.

6.10 Figures:

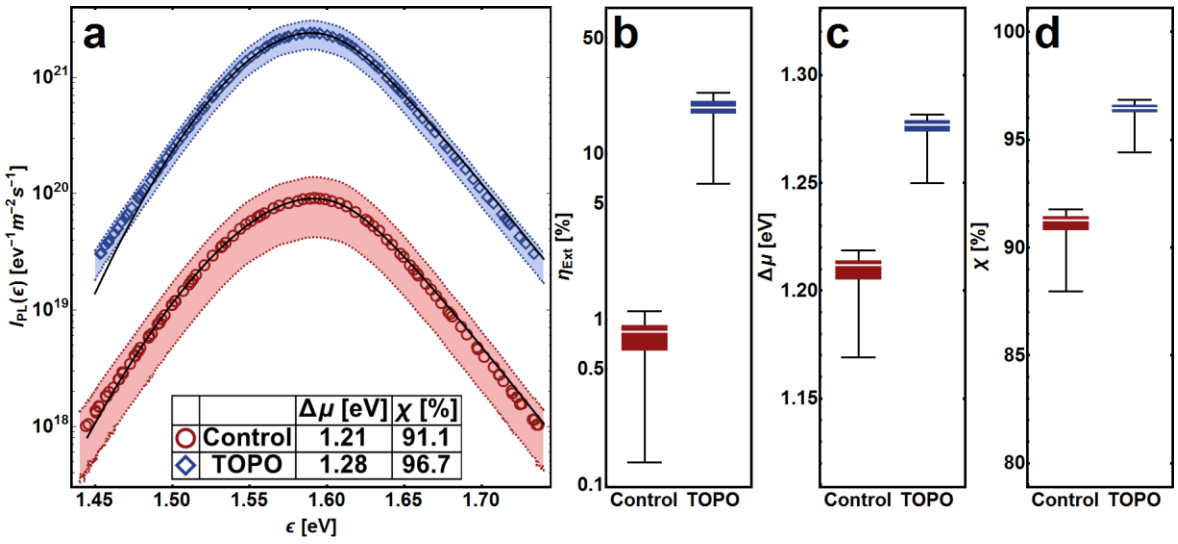

Figure 6.1: Absolute intensity photoluminescence spectra of control (red circles) and TOPO treated (blue diamonds) $CH_3NH_3PbI_3$ films deposited on an Au back reflector substrate measured in air. **a**, Log-scale photoluminescence spectra with generalized Planck model shown as black lines and shaded regions representing 95% confidence intervals for the spatial variation within the sample (N = 121). Quasi Fermi-level splitting ($\Delta\mu$) and percent of Shockley-Queisser limit quasi Fermi-level splitting (χ) are shown in the inset table. **b-d,** Parameter spatial statistics (min, first quartile, median, third quartile, and max. N = 121) of the control film and the TOPO treated film obtained from fits of spectra in **a**, showing external photoluminescence quantum efficiency (η_{ext}), $\Delta\mu$ and χ, respectively. Other fit parameters are reported in the SI (see Fig. S1).

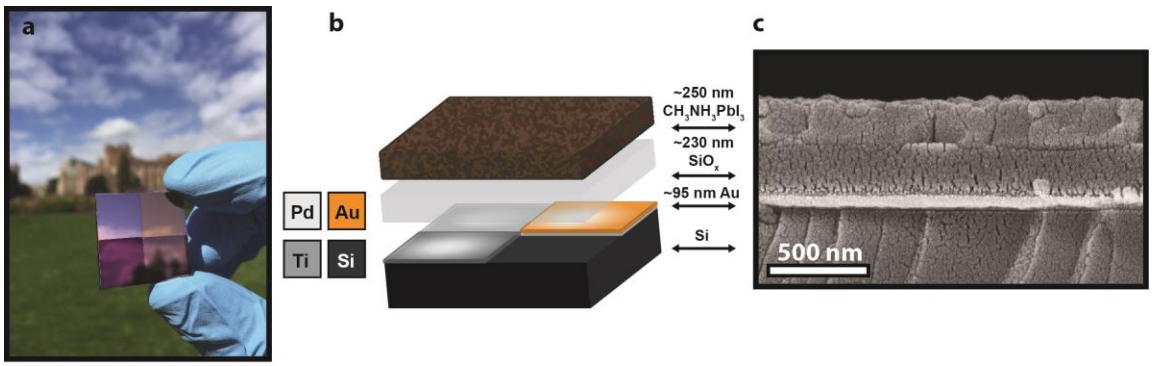

Figure 6.2: Image and schematic diagram of multi-metal back reflector substrates for determining internal photoluminescence quantum efficiency. **a**, A photograph of the multi-metal back reflector substrate before perovskite deposition. **b**, Schematic showing a multi-metal back reflector substrate configuration. ~100 nm of Au, Pd, and Ti were evaporated in separate quadrants on a Si wafer, a 230 nm insulating SiO_x layer was evaporated on top of the metals, then a 250 nm layer of perovskite was spin-coated to complete the sample. **c**, A cross-sectional SEM image of the Si/Au/SiO_x/perovskite back reflector sample.

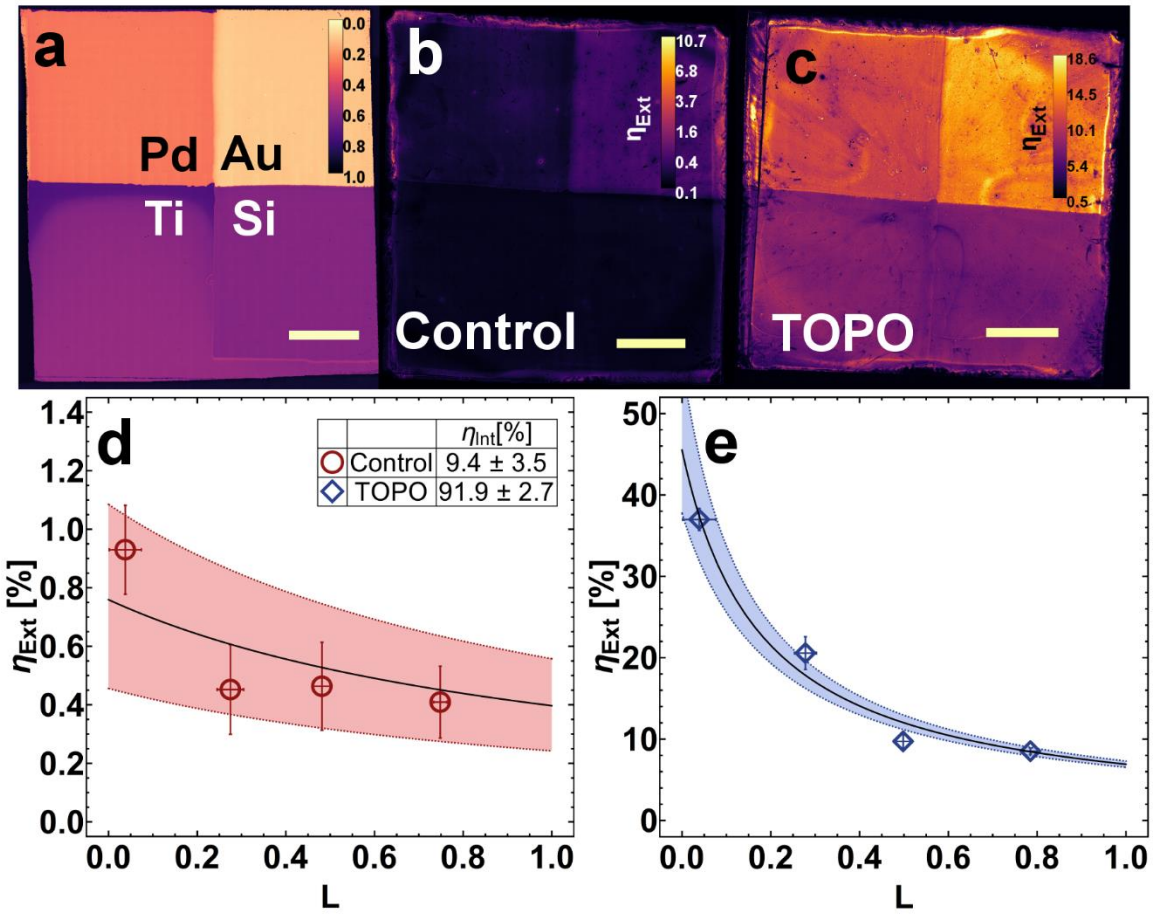

Figure 6.3: a, Spatial map showing the measured optical loss factors, $L = 1 - R$, of the Au, Pd, Ti, and Si quadrants of the metal back reflector substrate before perovskite deposition. **b and** c, Spatial map showing external photoluminescence quantum efficiency (η_{ext}) for a typical, control and TOPO treated film deposited on the multi-metal back reflector substrate, respectively. All scale bars are 5 mm. **d and e**, The η_{ext} data as a function of L for a control film and champion TOPO treated film, respectively. The error bars, shaded areas, and black lines are the 95% confidence intervals over the spatial heterogeneity in the data points, 95% confidence intervals of the nonlinear regression, and the nonlinear regression fits, respectively.

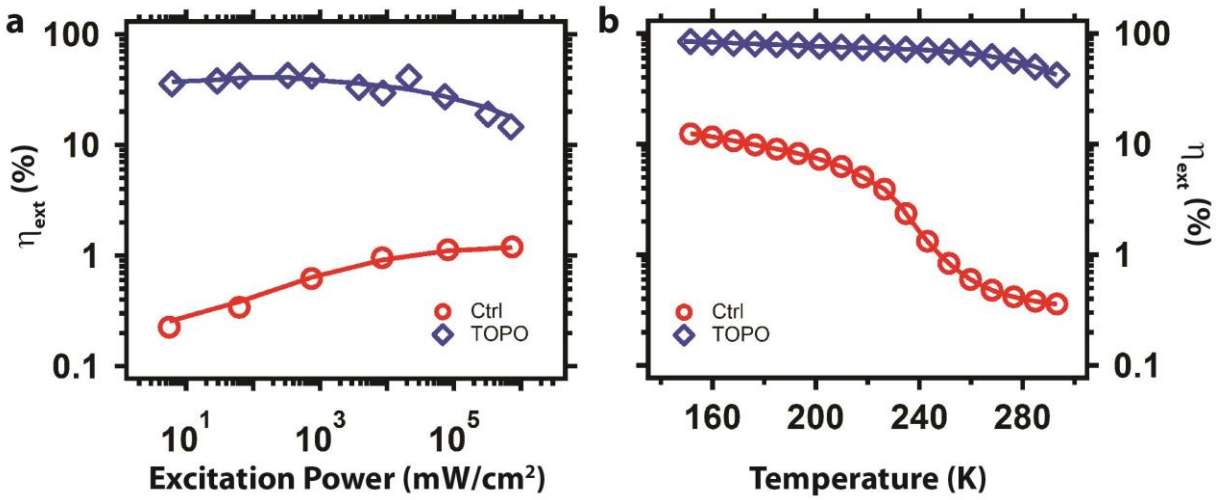

Figure 6.4: Photoluminescence spectroscopy measurements to determine the maximum achievable quantum efficiency under high excitation powers and low temperatures. **a**, Log-log plot of intensity dependent η_{ext} for a control and TOPO treated film at room temperature, showing a maximum η_{ext} of 1.2% and 43%, respectively. **b**, Semi-log plot of temperature dependent η_{ext} for the same control and TOPO treated films. Linear plots of the data are reported in Fig. S17.

6.11 References:

1. Green, M.A. & Ho-Baillie, A. Perovskite solar cells: The birth of a new era in photovoltaics. *ACS Energy Lett.* **2,** 822-830 (2017).

2. Veldhuis, S. A. *et al.* Perovskite materials for light-emitting diodes and lasers. *Adv. Mater.* **28**, 6804-6834 (2016).

3. Stranks, S. D. & Snaith, H. J. Metal-halide perovskites for photovoltaic and light-emitting devices. *Nat. Nanotechnol.* **10**, 391-402 (2015).

4. Li, F. *et al.* Ambipolar solution-processed hybrid perovskite phototransistors. *Nat. Commun.* **6**, 8238 (2015).

5. De Wolf, S. *et al.* Organometallic halide perovskites: Sharp optical absorption edge and its relation to photovoltaic performance. *J. Phys. Chem. Lett.* **5**, 1035-1039 (2014).

6. Oga, H., Saeki, A., Ogomi, Y., Hayase, S. & Seki, S. Improved understanding of the electronic and energetic landscapes of perovskite solar cells: High local charge Carrier mobility, reduced recombination, and extremely shallow traps. *J. Am. Chem. Soc.* **136**, 13818-13825 (2014).

7. Stranks, S. D. *et al.* Electron-hole diffusion lengths exceeding 1 micrometer in an organometal trihalide perovskite absorber. *Science* **342**, 341-344 (2013).

8. deQuilettes, D. W. *et al.* Photoluminescence lifetimes exceeding 8 μs and quantum yields exceeding 30% in hybrid perovskite thin films by ligand passivation. *ACS Energy Lett.* 438-444 **1,** (2016).

9. Richter, J. M. *et al.* Enhancing photoluminescence yields in lead halide perovskites by photon recycling and light out-coupling. *Nat. Commun.* **7**, 13941 (2016).

10. Tress, W. Perovskite solar cells on the way to their radiative efficiency limit – insights into a success story of high open-circuit voltage and low recombination. *Adv. Energy Mater.* **7,** 1602358 (2017).

11. Deschler, F. *et al.* High photoluminescence efficiency and optically pumped lasing in solution-processed mixed halide perovskite semiconductors. *J. Phys. Chem. Lett.* **5**, 1421-1426 (2014).

12. Tvingstedt, K. *et al.* Radiative efficiency of lead iodide based perovskite solar cells. *Sci. Rep.* **4**, 6071 (2014).

13. Shockley, W. & Queisser, H. J. Detailed balance limit of efficiency of p-n junction solar cells. *J. Appl. Phys.* **32**, 510-519 (1961).

14. Katahara, J. K. & Hillhouse, H. W. Quasi-fermi level splitting and sub-bandgap absorptivity from semiconductor photoluminescence. *J. Appl. Phys.* **116**, 173504 (2014).

15. Rau, U. Reciprocity relation between photovoltaic quantum efficiency and electroluminescent emission of solar cells. *Phys. Rev. B*, **76,** 085305 (2007).

16. Amani, M. *et al.* Near-unity photoluminescence quantum yield in MoS_2. *Science* **350**, 1065-1068 (2015).

17. Trupke, T., Zhao, J., Wang, A., Corkish, R. & Green, M. A. Very efficient light emission from bulk crystalline silicon. *Appl. Phys. Lett.* **82**, 2996-2998 (2003).

18. Yao, J. *et al.* Quantifying losses in open-circuit voltage in solution-processable solar cells. *Phys. Rev. Appl.* **4** (2015).

19. Miller, O. D., Yablonovitch, E. & Kurtz, S. R. Strong internal and external luminescence as solar cells approach the Shockley-Queisser limit. *IEEE J. Photovolt.* **2**, 303-311 (2012).

20. Schnitzer, I., Yablonovitch, E., Caneau, C. & Gmitter, T.J. Ultra-high spontaneous emission quantum efficiency, 99.7% internally and 72% externally, from AlGaAs/GaAs/AlGaAs double heterostructures. *Appl. Phys. Lett.* **62**, 131-133 (1993).

21. Correa-Baena, J.-P. *et al.* Identifying and suppressing interfacial recombination to achieve high open-circuit voltage in perovskite solar cells. *Energy Environ. Sci.*, **10,** 1207-1212 (2017).

22. Saliba, M. *et al.* Incorporation of rubidium cations into perovskite solar cells improves photovoltaic performance. *Science* **354**, 206-209, (2016).

23. Bi, D. *et al.* Efficient luminescent solar cells based on tailored mixed-cation perovskites. *Sci. Adv.* **2**, e1501170 (2016).

24. Voznyy, O., Sutherland, B. R., Ip, A. H., Zhitomirsky, D. & Sargent, E. H. Engineering charge transport by heterostructuring solution-processed semiconductors. *Nat. Rev. Mater.* **2**, 17026 (2017).

25. Noel, N. K. *et al.* Enhanced Photoluminescence and Solar Cell Performance via Lewis Base Passivation of Organic-Inorganic Lead Halide Perovskites. *ACS Nano* **8**, 9815-9821 (2014).

26. Sakai, N. *et al.* The mechanism of toluene-assisted crystallization of organic–inorganic perovskites for highly efficient solar cells. *J. Mater. Chem. A* **4**, 4464-4471 (2016).

27. Braly, I. L. & Hillhouse, H. W. Optoelectronic quality and stability of hybrid perovskites from $MAPbI_3$ to $MAPbI_2Br$ using composition spread libraries. *J. Phys. Chem. C* **120**, 893-902 (2016).

28. Stranks, S. D. *et al.* Recombination kinetics in organic-inorganic perovskites: Excitons, free charge, and subgap states. *Phys. Rev. Appl.* **2**, 034007 (2014).

29. Beard, M. C. Top and bottom surfaces limit carrier lifetime in lead iodide perovskite films, **2,** 16207 (2017).

30. Stewart, R. J., Grieco, C., Larsen, A. V., Maier, J. J. & Asbury, J. B. Approaching bulk carrier dynamics in organo-halide perovskite nanocrystalline films by surface passivation. *J. Phys. Chem. Lett.* **7**, 1148-1153 (2016).

31. Aberle, A. G. Surface passivation of crystalline silicon solar cells: A review. *Prog. Photovolt: Res. Appl.* **8**, 473-487 (2000).

32. Zheng, X. *et al.* Defect passivation in hybrid perovskite solar cells using quaternary ammonium halide anions and cations. **2**, 17102 (2017).

33. Yang, W. S. *et al.* Iodide management in formamidinium-lead-halide–based perovskite layers for efficient solar cells. *Science* **356**, 1376 (2017).

34. Pazos-Outon, L. M. *et al.* Photon recycling in lead iodide perovskite solar cells. *Science* **351**, 1430-1433 (2016).

35. Staub, F. *et al.* Beyond bulk lifetimes: Insights into lead halide perovskite films from time-resolved photoluminescence. *Phys. Rev. Appl.* **6**, 044017 (2016).

36. Yablonovitch, E., Miller, O. D. & Kurtz, S. R. The opto-electronic physics that broke the efficiency limit in solar cells. *IEEE Photovoltaic Spec. Conf.* **38,** 001556-001559 (2012).

37. Zhang, W. *et al.* Ultrasmooth organic-inorganic perovskite thin-film formation and crystallization for efficient planar heterojunction solar cells. *Nat. Commun.* **6**, 6142 (2015).

38. Lasher, G. & Stern, F. Spontaneous and stimulated recombination radiation in semiconductors. *Phys. Rev.* **133**, A553-A563 (1964).

39. Würfel, P. The chemical potential of radiation. *J. Phys. C: Solid State Phys.* **15**, 3967-3985, (1982).

40. Katahara, J. K. & Hillhouse, H. W. Erratum: "Quasi-fermi level splitting and sub-bandgap absorptivity from semiconductor photoluminescence" *J. Appl. Phys.* **119**, 239901 (2016).

41. Bauer, G. H., Bruggemann, R., Tardon, S., Vignoli, S. & Kniese, R. Quasi-Fermi level splitting and identification of recombination losses from room temperature

luminescence in $Cu(In_{1-x},Ga_x)Se_2$ thin films versus optical band gap. *Thin Solid Films* **480**, 410-414 (2005).

42. Ross, R. T. Some thermodynamics of photochemical systems. *J. Chem. Phys.* **46**, 4590-4593 (1967).

43. deQuilettes, D. W. *et al.* Impact of microstructure on local carrier lifetime in perovskite solar cells. *Science* **348**, 683-686 (2015).

44. Kayes, B. M. *et al.* in 27.6% conversion efficiency, a new record for single-junction solar cells under 1 sun illumination. *IEEE Photovoltaic Spec. Conf.* **37,** 000004-000008 (2011).

45. Rühle, S. Tabulated values of the Shockley-Queisser limit for single junction solar cells. *Solar Energy* **130**, 139-147 (2016).

46. Ziffer, M. E., Mohammed, J. C. & Ginger, D. S. electroabsorption spectroscopy measurements of the exciton binding energy, electron–hole reduced effective mass, and band gap in the perovskite $CH_3NH_3PbI_3$. *ACS Photonics* **3**, 1060-1068 (2016).

47. Drexhage, K. H. Fluorescence efficiency of laser dyes. *J. Res. Natl. Bur. Stand., Sect. A* **80A**, 421 (1976).

48. Johnston, M. B. & Herz, L. M. Hybrid perovskites for photovoltaics: Charge-carrier recombination, diffusion, and radiative efficiencies. *Acc. Chem. Res.* **49**, 146-154, (2016).

49. Kerr, M. J. & Cuevas, A. General parameterization of Auger recombination in crystalline silicon. *J. Appl. Phys.* **91**, 2473-2480 (2002).

50. Tiedje, T., Yablonovitch, E., Cody, G. D. & Brooks, B. G. Limiting efficiency of silicon solar cells. *IEEE Trans. Electron Devices* **31**, 711-716 (1984).

51. deQuilettes, D. W. *et al.* Photo-induced halide redistribution in organic-inorganic perovskite films. *Nat. Commun.* **7**, 11683 (2016).

52. Stoumpos, C. C., Malliakas, C. D. & Kanatzidis, M. G. Semiconducting tin and lead iodide perovskites with organic cations: phase transitions, high mobilities, and near-infrared photoluminescent properties. *Inorg. Chem.* **52**, 9019-9038 (2013).

53. Bertness, K. A. *et al.* 29.5%-efficient GaInP/GaAs tandem solar cells. *Appl. Phys. Lett.* **65**, 989-991 (1994).

54. Sandroff, C. J., Nottenburg, R. N., Bischoff, J. C. & Bhat, R. Dramatic enhancement in the gain of a GaAs/AlGaAs heterostructure bipolar transistor by surface chemical passivation. *Appl. Phys. Lett.* **51**, 33-35 (1987).

55. Yablonovitch, E., Sandroff, C. J., Bhat, R. & Gmitter, T. Nearly ideal electronic properties of sulfide coated GaAs surfaces. *Appl. Phys. Lett.* **51**, 439-441 (1987).

56. Knesting, K. M. *et al.* ITO interface modifiers can improve V_{OC} in polymer solar cells and suppress surface recombination. *J. Phys. Chem. Lett.* **4**, 4038-4044 (2013).

57. Cho, A.-N. & Park, N.-G. Impact of Interfacial Layers in Perovskite Solar Cells. *ChemSusChem* Accepted Author Manuscript. doi: 10.1002/cssc.201701095 (2017).

58. Tang, J. *et al.* Colloidal-quantum-dot photovoltaics using atomic-ligand passivation. *Nat. Mater.* **10**, 765-771 (2011).

59. Stoddard, R. J., Eickemeyer, F. T., Katahara, J. K. & Hillhouse, H. W. Correlation between photoluminescence and carrier transport and a simple in-situ passivation method for high-bandgap hybrid perovskites. *J. Phys. Chem. Lett*. **8,** 3289-3298 (2017).

60. Wang, T. *et al.* Indirect to direct bandgap transition in methylammonium lead halide perovskite. *Energy Environ. Sci.* **10**, 509-515 (2017).

61. Motta, C. *et al.* Revealing the role of organic cations in hybrid halide perovskite $CH_3NH_3PbI_3$. *Nat. Commun.* **6**, 7026 (2015).

62. Hutter, E. M. *et al.* Direct-indirect character of the bandgap in methylammonium lead iodide perovskite. *Nat. Mater.* **16**, 115-120 (2017).

63. Kirchartz, T. & Rau, U. Decreasing radiative recombination coefficients via an indirect band gap in lead halide perovskites. *J. Phys. Chem. Lett.* **8**, 1265-1271 (2017).

64. Wright, A. D. *et al.* Band-tail recombination in hybrid lead iodide perovskite. *Adv. Funct. Mater.* **27,** 1700860 (2017).

65. de Mello, J. C., Wittmann, H. F. & Friend, R. H. An improved experimental determination of external photoluminescence quantum efficiency. *Adv. Mater.* **9**, 230-232 (1997).

66. Edelstein, A. D. *et al.* Advanced methods of microscope control using μManager software. *J. Biol. Methods* **1,** e10 (2014).

67. Blattner, T. *et al.* A hybrid CPU-GPU system for stitching large scale optical microscopy images. *Int. Conf. Parallel Processing.* **43,** 1-9 (2014).

68. Schindelin, J. *et al.* Fiji: An open-source platform for biological-image analysis. *Nat. Methods* **9**, 676-682 (2012).

Appendix A: Supporting Information for Chapter 2

Materials and Methods

Perovskite Precursor Preparation

Methylammonium iodide (MAI) was prepared by reacting methylamine, 33 wt% in ethanol (Sigma-Aldrich), with hydroiodic acid (HI) 57 wt% in water (Sigma-Aldrich), at room temperature. HI was added dropwise while stirring. MAI was precipitated out of solution by heating the solution at 100 °C overnight to drive off the solvent. The crude MAI was either used without further purification or recrystallized in a mixed solvent of ethanol and ether. To form the non-stoichiometric $CH_3NH_3PbI_3(Cl)$ precursor solution, MAI and lead (II) chloride (99.999%, Sigma-Aldrich) were dissolved in anhydrous *N*,*N*-dimethylformamide (DMF) at a 3:1 molar ratio of MAI to $PbCl_2$, with final concentrations 0.88M lead chloride and 2.64M MAI. This solution was stored under a dry nitrogen atmosphere. The $CH_3NH_3PbI_3$ precursor solution (for control experiments) was prepared by dissolving MAI and PbI_2 at a 1:1 molar ratio in DMF.

Substrate Preparation

Devices were fabricated on fluorine-doped tin oxide (FTO) coated glass (Pilkington, 7Ω). FTO was removed from regions under the anode contact, to prevent shunting upon contact with measurement pins, by etching the FTO with 4M HCl and zinc powder. Substrates were then cleaned sequentially in 2% Micro-90 detergent, acetone, propan-2-ol and air plasma. An electron-accepting layer of compact TiO_2 was deposited by spin-coating a TiO_2 sol-gel, and annealed at 500 °C for 1 hr. Spin-coating was carried out at 2000 rpm for 60 s.

Perovskite Deposition

To form the perovskite layer for spectroscopy measurements and complete devices, the $CH_3NH_3PbI_3(Cl)$ or $CH_3NH_3PbI_3$ precursor solution was spin-coated on a plasma-cleaned substrate in a nitrogen-filled glovebox, at 2000 rpm for 60 s. After spin-coating, $CH_3NH_3PbI_3(Cl)$ films were left to dry at ambient temperature in the glovebox for 30 minutes and then annealed on a hotplate in the glovebox at 90 °C for 150 minutes. $CH_3NH_3PbI_3$ films were annealed directly after spincoating at 100 °C for 10 minutes. Films were then encapsulated in a nitrogen atmosphere for spectroscopy measurements. For devices, a hole transporting layer was then deposited in a nitrogen-filled glovebox via spin-coating a 0.079M solution of 2,2',7,7'-tetrakis-(*N*,*N*-di-*p*-methoxyphenylamine)9,9'spirobifluorene (spiro-OMeTAD) in chlorobenzene (CB), with additives of lithium bis(trifluoromethanesulfonyl)imide and 4-tert-butylpyridine. Spin-coating was carried out at 2000 rpm for 60 s. Finally, 100 nm gold electrodes were thermally evaporated under vacuum of 10^{-7} Torr, at a rate of 0.1 nm s^{-1}, to complete the devices (Fig. S1A).

Solar Cell Characterization

Current density–voltage (J-V) curves were measured using a source meter (Keithley, 2400 Series) under AM 1.5 G light illumination from a solar simulator (Solar Light Co. model 16S-300) with intensity calibrated to 100 mW/cm^2 using a Si reference cell. The solar cells were masked with a metal aperture to define the active area, typically 0.013 cm^{-2}, and measured in a light-tight sample holder to minimize edge effects. Scanning rates of 0.15 V/s or 0.025 V/s were used to assess the hysteretic behavior of devices (Fig. S1B).

Pyridine Vapor Treatment and PCBM Electron Extraction Studies

For pyridine vapor treatment studies, $CH_3NH_3PbI_3(Cl)$ films were suspended above a dilute solution of pyridine (Sigma, anhydrous, 99.8%) in chlorobenzene (CB). Specifically, the solution was prepared by mixing 0.1 mL pyridine with 1 mL CB (9.09% by volume). This solution was then transferred to small Petri dish above which the film was mounted. Vapor treatment was carried out in a fume hood under ambient conditions and was concluded upon successful evaporation of the entire solution (~1 hr). We observed no PL enhancement when films were only exposed to 1 mL of CB (no pyridine) under identical experimental conditions (Fig. S9). Films with [6,6]-Phenyl C_{61} butyric acid methyl ester (PCBM) electron extracting layers were prepared by spincoating a solution of PCBM in anhydrous chlorobenzene (3 mg/mL) at 2000 rpm for 60 s in a nitrogen glovebox.

Atomic Force Microscopy (AFM)

AFM topography images were obtained in intermittent contact mode and carried out on an MFP-3DBIO-based (Asylum Research) AFM using 300 kHz cantilevers (BudgetSensor Tap300-G).

Scanning Electron Microscopy (SEM) and Energy Dispersive Spectroscopy (EDS)

SEM images were taken using a FEI Sirion SEM at 5 kV accelerating voltage. To prevent charging effects, samples for SEM/EDS were imaged after sputtering approximately 7 nm of Au/Pd using a SPI-Module Sputter Coater with argon flow. EDS compositional profiles were also taken on the Sirion SEM using a 20 kV accelerating voltage and the data was analyzed using AZtecEnergy EDS software package (Ver. 2.1).

Time of Flight Secondary Ion Mass Spectrometry (ToF-SIMS)

ToF-SIMS spectra were acquired on an IonToF ToF-SIMS 5 instrument using a 25 keV Bi_1^+ ion source in the pulsed mode. Spectra were acquired for negative ion secondary ions from 100 μm x 100 μm areas using a current of 0.05 pA. Secondary ions were detected using a time-of-flight mass analyzer. The negative ion spectra were calibrated using the CH^-, OH^- and C_2H^- peaks. Calibration errors were kept below 3.1

ppm. Mass resolution (m/Δm) for a typical spectrum was between 4000 and 6000 for m/z 25. The penetration depth of the Bi_1^+ ion source was ~ 2 nm from the top surface of the film.

External Photoluminescence Quantum Yield (PLQY) Measurement

Bulk external PLQY measurements were collected using a modified Horiba LabRAM HR-800 and an upright microscope fitted with a 10x objective (Olympus M Plan achromat, NA 0.25). The adjustable confocal hole before the monochromator was set at 800 μm. A 150 gr/mm Czerny-Turner monochromator blazed at 1200 nm was used, and the emitted light was collected with a silicon CCD array detector. The PL signal was calibrated using a black body source (IR-301, Infrared Systems Development Corporation) at a temperature of 1323.15 K. A 100 μm diameter pin-hole was used to fix the spectral photon black body flux to the detector and allow an absolute photons per count calibration factor to be measured. A 532 nm CW laser was used for excitation. Oriel optical power meter was used to measure the illumination intensity and excitation diameter. An excitation power of 75.8 mW/cm^2 was used, equivalent to intensity at 1.1 sun illumination for a 1.57 eV bandgap material (*6*). The calculated bulk external PLQY (6.4%) was partitioned to each pixel in Fig. S2B based on the weighted raw PL counts. The weighted average PLQY across the 10 μm x 10 μm fluorescence image matches the bulk external PLQY (Fig. S2B).

Fluorescence Lifetime Imaging Microscopy (FLIM)

Optical microscopy and spectroscopy were performed using a custom sample scanning confocal microscope built around a Nikon TE-2000 inverted microscope fitted with an infinity corrected 50x dry objective (Nikon L Plan, NA 0.7, CC 0-1.2) (Figure S5A). We measured the point spread function of our system (Fig. S5B) to be 348 nm FWHM. A 470 nm pulsed diode laser (PDL-800 LDH-P-C-470B, 300 ps pulse width) was used for excitation with repetition rates between 125-500 kHz. Samples were either encapsulated in nitrogen prior to measurements or under continuous nitrogen flow and excited face-on (not through the substrate). The emission was filtered through a 50/50 dichroic beamsplitter and a 700-850 nm bandpass filter (700 LP and 850 SP). Photoluminescence from the sample was directed to a Micro Photon Devices (MPD) PDM Series single photon avalanche photodiode with a 50 μm active area for TRPL measurements or a portable charge coupled device spectrometer (USB2000, Ocean Optics) for steady state PL measurements. The sample stage was controlled using a piezo controller (Physik Instrumente E-710). For collecting fluorescence images, the pixel size was 100 nm with a pixel dwell time (integration time) of 100 ms – 5 s. For excitation intensity dependent measurements, the laser was attenuated with neutral density filters to ensure the instrument response function (IRF) was consistent across measurements. Before measurements, the system was calibrated using 200 nm fluorescent microspheres (Lifetechnologies FluoSpheres® Polystyrene Microspheres, 200 nm, red fluorescent, 580/605). To correlate fluorescence images with SEM and AFM micrographs, we made fiducial markers on the sample and used these markers along with local microstructure to match areas across the separate measurements. Here, we also define bright and dark

perovskite grains. We define "bright" grains as grains with PL counts greater than +σ (one standard deviation from average PL). We define "dark" grains as ones with PL counts < 50% of the onset of bright grains. According to this definition, ~30% of grains imaged in Fig. 1C were dark.

Photoluminescence Decay Fitting

Bulk lifetime measurements at low fluence (<50 nJ/cm^2/pulse)

PL decay traces obtained at low fluences were fit using a stretched-exponential decay function of the form,

$$I(t) = I_0 e^{-(t/t_c)^b} \tag{S1},$$

where I(t) is the time dependent PL intensity, I_0 is the initial PL intensity, t is time, τ_c is the characteristic lifetime defined as the time taken after excitation for the PL intensity to drop to 1/e of its initial intensity (I_0), and β is distribution coefficient. This decay law is typically encountered in systems with a distribution of local decay rates and the β factor can give information pertaining to a random distribution of site energies or a time dependent rate constant *(29)*. When β = 1 the decay function reduces to a single exponential and heterogeneity is negligible. When β is closer to 0, this represents a larger distribution (e.g. decay rates) and therefore more significant heterogeneity. Using the experimentally measured characteristic lifetime and β values, we calculate the total distribution and obtain the average lifetime, $\langle\tau\rangle$, using the following relationship *(29)*:

$$\langle t \rangle = \frac{t_c}{b}\Gamma\left(\frac{1}{b}\right) \tag{S2},$$

where $\Gamma\left(\frac{1}{\beta}\right)$ is defined as the gamma function:

$$\Gamma\left(\frac{1}{b}\right) = \int_0^\infty x^{(1-b)/b} e^{-x}\, dx \tag{S3},$$

Bulk lifetime measurements at medium-high fluences (>1μJ/cm^2/pulse)

PL decay traces for the dark and bright regions in Fig. 2C, D, and E (blue and red traces) were simulated by solving the set of coupled differential equations.

$$\frac{dN_C(t)}{dt} = -k_{DT}N_{DT}(t)N_C(t) - k_mN_C(t) - k_bN_C(t)^2 \quad \text{(S4)},$$

$$\frac{dN_{DT}(t)}{dt} = -k_{DT}N_{DT}(t)N_C(t) \quad \text{(S5)},$$

where $N_c(t)$ is the time dependent carrier population, k_{DT} is the deep trapping rate, $N_{DT}(t)$ is the number of deep traps as a function of time, k_m is the monomolecular rate constant, and k_b is the bimolecular rate constant. Carriers were assumed not to detrap from the deep traps on the timescale of the PL transient *(15)*. Initial carrier concentrations were calculated based on the measured laser power and focal spot size and used as fixed input parameters, not as fitting parameters.

We used the solutions from equations S4 and S5 to model the time evolution of the PL and assumed that the deep traps are non-radiative (no PL) centers (S6).

$$PL(t) = k_mN_C(t) + k_bN_C(t)^2 \quad \text{(S6)},$$

In the dark region, we extracted the deep trap state density, trapping, monomolecular, bimolecular decay rates to be 4 x 10^{16} cm^{-3}, 1 x 10^{-8} cm^3s^{-1}, 1 x 10^6 s^{-1}, and 3.5-5.5 x 10^{-11} cm^3s^{-1}, respectively. In the bright region, we extracted the deep trap state density, trapping, monomolecular, bimolecular decay rates to be 1 x 10^{15} cm^{-3}, 1 x 10^{-8} cm^3s^{-1}, 1 x 10^6 s^{-1}, and 2.3-7.8 x 10^{-11} cm^3s^{-1}, respectively. We ascribe the small range in the bimolecular rate constant to differences in carrier mobility as more traps are filled at higher initial carrier densities. These values are consistent with other reports of trap densities in $CH_3NH_3PbI_3$ and $CH_3NH_3PbI_3$(Cl) films (*5, 15*) and monomolecular (*10*) and bimolecular decay rates (*16, 17*) for $CH_3NH_3PbI_3$(Cl) reported from bulk measurements. We specifically note the presence of a fast non-radiative component in the PL decay trace in the dark region, which is absent in the bright region (Fig. 2C). In our simulation, this component is well described by fast trapping into a population of non-radiative deep traps.

Supplementary Text

Carrier Density Estimates

We use the following equation to approximate the carrier densities relevant to solar cell operation under AM 1.5 sun illumination.

$$N = \frac{(\sum_{\lambda} E_{\lambda} / [1 - 10^{-2OD_{\lambda}}]) < t >}{hcD} \quad \text{(S7)},$$

where E_λ is the spectral irradiance value at a given wavelength (λ), OD_λ is the optical density at λ, $<\tau>$ is the average lifetime as described in the "Photoluminescence Decay Fitting" subhead, h is Planck's constant, c is the speed of light, and D is the measured film thickness (~440 nm). In this approximation, we assume (1) light reflects of the back contact and therefore passes twice ($2OD_\lambda$) through the solar cell with negligible optical interference and (2) that the carrier lifetime is independent of excitation wavelength. To obtain the upper and lower carrier density bounds, we balanced the generation rate with the recombination rate at the two extremes of device operation (namely, open circuit and short circuit). At open circuit and using $<\tau>$ from our experiments, we calculate a carrier density of ~2 x 10^{15} cm^{-3}. At short circuit using the reported lifetime (5 ns) when $CH_3NH_3PbI_3(Cl)$ is interfaced with quencher PCBM (*9*), we calculate a carrier density of ~ 2 x 10^{13} cm^{-3}.

Film Thickness Impact on PL Intensity

The average film thicknesses (~440 nm) were obtained using an atomic force microscope. The absorption depth of 470 nm excitation was calculated to be ~85 nm (much smaller than the film thickness) based on reported absorption coefficients (*20*, *2*). Figure S2 shows the PL intensity is not correlated with perovskite height.

Grain Boundary (GB) Impact on Photoluminescence (PL) Decay

To confirm that the PL is being quenched at the GB's and these dimmer regions do not arise from the broadening of the GB's due to the PSF, we locally probed different regions at and around ground boundaries (Fig. S4D and E) and also performed a Gaussian convolution analysis. Figure S4E shows time-resolved PL traces at a grain boundary (blue circle), on a bright grain (red square) and on a dimmer grain (green triangle). Consistent with the lower PL counts at grain boundaries, these dimmer regions also contain a fast non-radiative component that would not arise from having less material in these areas. We used a convolution analysis to further support this conclusion by assuming that the widest region of any GB observed in SEM is a void that penetrates entirely to the substrate and contributes no PL (black lines in Fig. S4B). We then convolved the PSF with the known width of the GB's (via SEM) and compare the expected values (□ red squares) with the experimental values (□ blue circles) and find

that even under the assumption that the GB's have no perovskite material, the half width at half maximum (HWHM) of the experimental PL line trace is larger than the HWHM of the predicted line trace (red squares in Fig. S4B). This result indicates that there are non-radiative recombination centers near the grain boundaries. To determine the absolute magnitude and spatial extent of PL quenching we deconvolved the apparent grain boundary quenching (blue circles in Fig. S4C) with the point spread function of the confocal setup and have found that carriers are quenching ~210 nm (HWHM) from the grain boundaries with a ~65% reduction in the PL brightness in comparison to the surrounding grains.

Energy Dispersive X-ray Spectroscopy (EDS) Analysis

To confirm the peak at 2.622 keV (Fig. S11B) is indeed detectable Cl in $CH_3NH_3PbI_3(Cl)$ films and not an artifact stemming from the Pb Mγ peak (2.658 keV), we studied a $CH_3NH_3PbI_3$ film as a control. Figure S11 shows 9 μm line scans across separate neat $CH_3NH_3PbI_3(Cl)$ and $CH_3NH_3PbI_3$ films. Figures S11A (Fig. 4 in the main text) shows bright regions are associated with local spikes in Cl/(Cl+I) ratios in the $CH_3NH_3PbI_3(Cl)$ film and, on the contrary, Fig. S11D shows no Cl outside the detection limit of the technique (> 0.1 weight percentage (% wt)) in the $CH_3NH_3PbI_3$ film. Figure S11B and S11D show the point spectra along the two different scans (black arrows in Fig. S11B and S11D). The measured Cl % wt at the point identified in the $CH_3NH_3PbI_3(Cl)$ film is 1.0 ± 0.2 % wt, a statistically significant Cl % wt above the detection limit of this technique (*39, 41*). We further confirm that this peak in indeed the Cl Kα and is not the Pb Mγ transition by first plotting the expected Cl spectra (brown spectra in Fig. S11B and S11D) from a NaCl standard and also showing in the $CH_3NH_3PbI_3$ control film, which should theoretically have a more dominant Pb Mγ peak because of its slightly higher content of Pb (37.1 % wt in $CH_3NH_3PbI_3$ versus 24.2 % wt in $CH_3NH_3PbI_3(Cl)$), that neither the Cl Kα or Pb Mγ peaks can be identified. We further report a statistical analysis of point spectra collected in a bright versus dark domain in Fig. S11E. The bright domain (green square) had Cl/(Cl+I) = 0.026 ± 0.013 for N=4 and the dark domain (black square) had Cl/(Cl+I) = 0.004 ± 0.002 for N=12. Consistent with our findings from Fig. 4 in the main text, regions with higher PL have a greater content of Cl.

Photostability

To verify films did not undergo significant photoinduced degradation during measurements, we measured the exact same area before and after 25 minutes of continuous laser exposure (1 $\mu J/cm^2$) and compared the fluorescence images from one data collection cycle to the next (Figure S3).

Fluorescence Microscopy of a $CH_3NH_3PbI_3(Cl)$ Film With and Without a PCBM Layer and Grain Boundary Analysis Before and After Pyridine Treatments

We compared the fluorescence images (FI) before and after spincoating PCBM on a $CH_3NH_3PbI_3(Cl)$ film (Fig. S7, A and B). Figure S7C shows the local steady state PL spectra of a grain before (red square) and after (blue square) contacting with PCBM. Consistent with our local PL lifetime data, and with our hypothesis that dark grains suffer from more fast non-radiative recombination, we found that grains with high PLQY (Fig. S2B and Fig. 7A and D) were quenched more efficiently than grains with low PLQY (Fig. S2B and Fig. 7A and D). In the presence of the additional fast non-radiative decay channels introduced by the PCBM, we observed less contrast among grains and between grains and grain boundaries (GB's) as evidenced by the image histogram data in Fig. S7, E and F. The average magnitude of quenching (~71%) is somewhat less than previously reported at lower fluence (*9*), which we attribute to the higher initial carrier densities necessary to collect an FI with good signal-to-noise (and hence more emission from fast bimolecular recombination of free carriers competing with quenching via PCBM in our samples). To further understand the impact pyridine has on the PL properties at GB's, we examined several GB's PL profiles before and after pyridine treatment. In Fig. 10 E-H we show four representative PL line traces. We note there is not a single "standard" grain boundary profile, and variations in grain size, shape, PL intensity, and response to pyridine all contribute to distribution observed. Nevertheless, the majority (~ 80%) show a reduction in the PL quenching and narrowing of the PL width at the GB's upon pyridine treatment.

Supplementary Figures

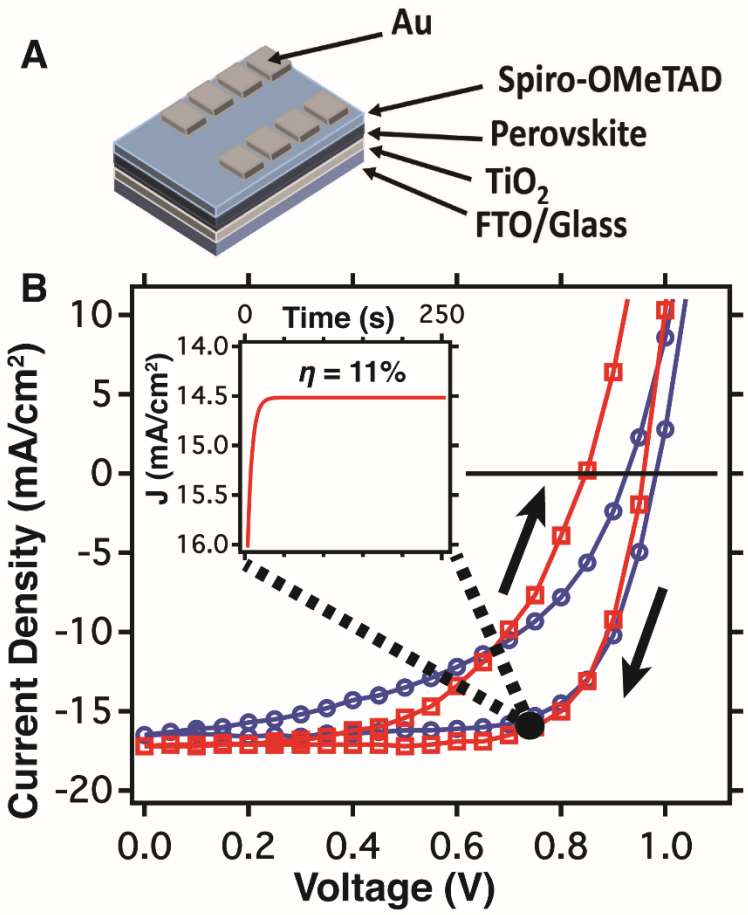

Figure S1. (A) Schematic of device architecture **(B)** J-V characteristics of forward and reverse scans of a typical solar cell fabricated in our lab and measured at a fast scan rate (red squares, 0.15 V/s) and slow scan rate (blue circles, 0.025 V/s). (Inset) Stabilized power output measured close to the max power point (0.75 V) for 250 seconds.

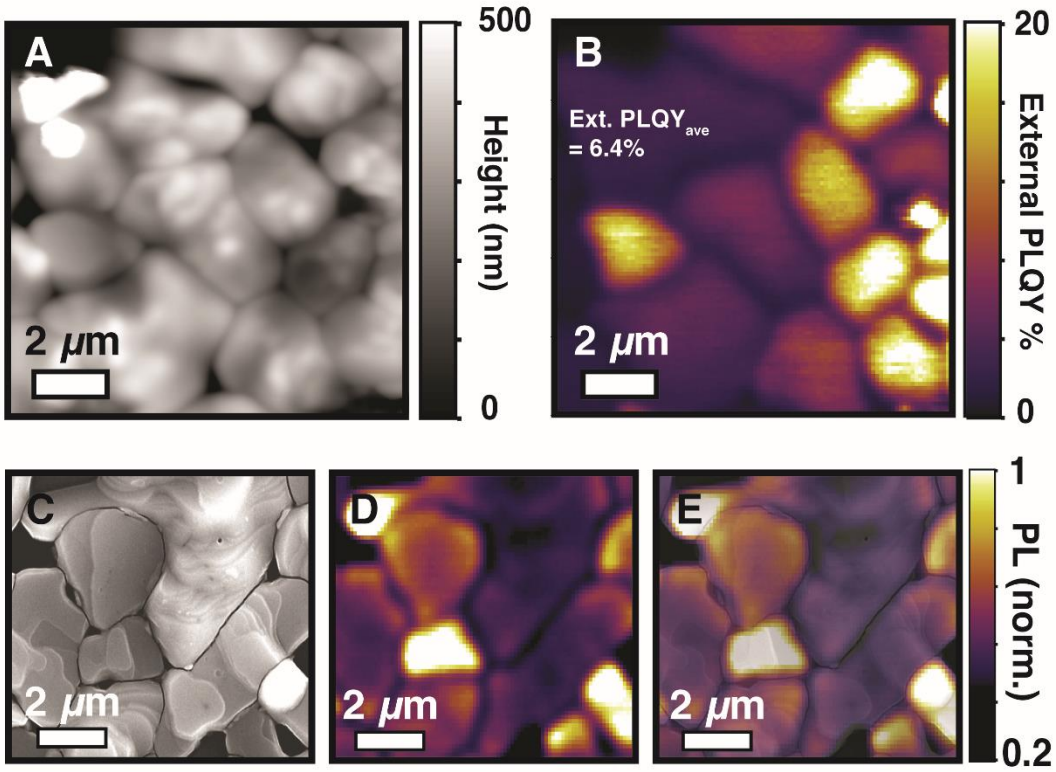

Figure S2. (A) Correlated AFM topography micrograph and **(B)** fluorescence image (FI) of a $CH_3NH_3PbI_3(Cl)$ film on glass with photoluminescence quantum yield (PLQY) distributed locally from the measured bulk PLQY (6.4%) showing PLQY is not correlated with film height. **(C)** Correlated SEM micrograph, **(D)** FI, and **(E)** composite image of SEM overlaid on FI of a $CH_3NH_3PbI_3(Cl)$ film on glass prepared in Oxford by the Snaith group showing variations in photoluminescence intensity across different grains and grain boundaries, consistent with observations in this report for samples prepared in Seattle.

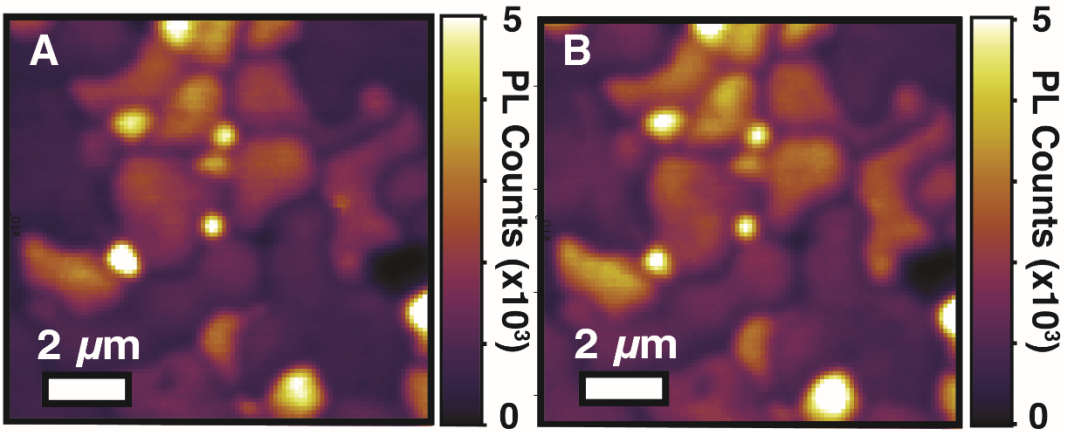

Figure S3. Stability study showing **(A)** fluorescence image obtained at excitation fluence of 1μJ/cm^2. **(B)** A second fluorescence image of the same area collected directly after the first image was acquired. The images are substantially similar when plotted on the same raw scales, showing the film does not undergo any significant photoinduced degradation during data collection. Image collection times were ~ 25 minutes.

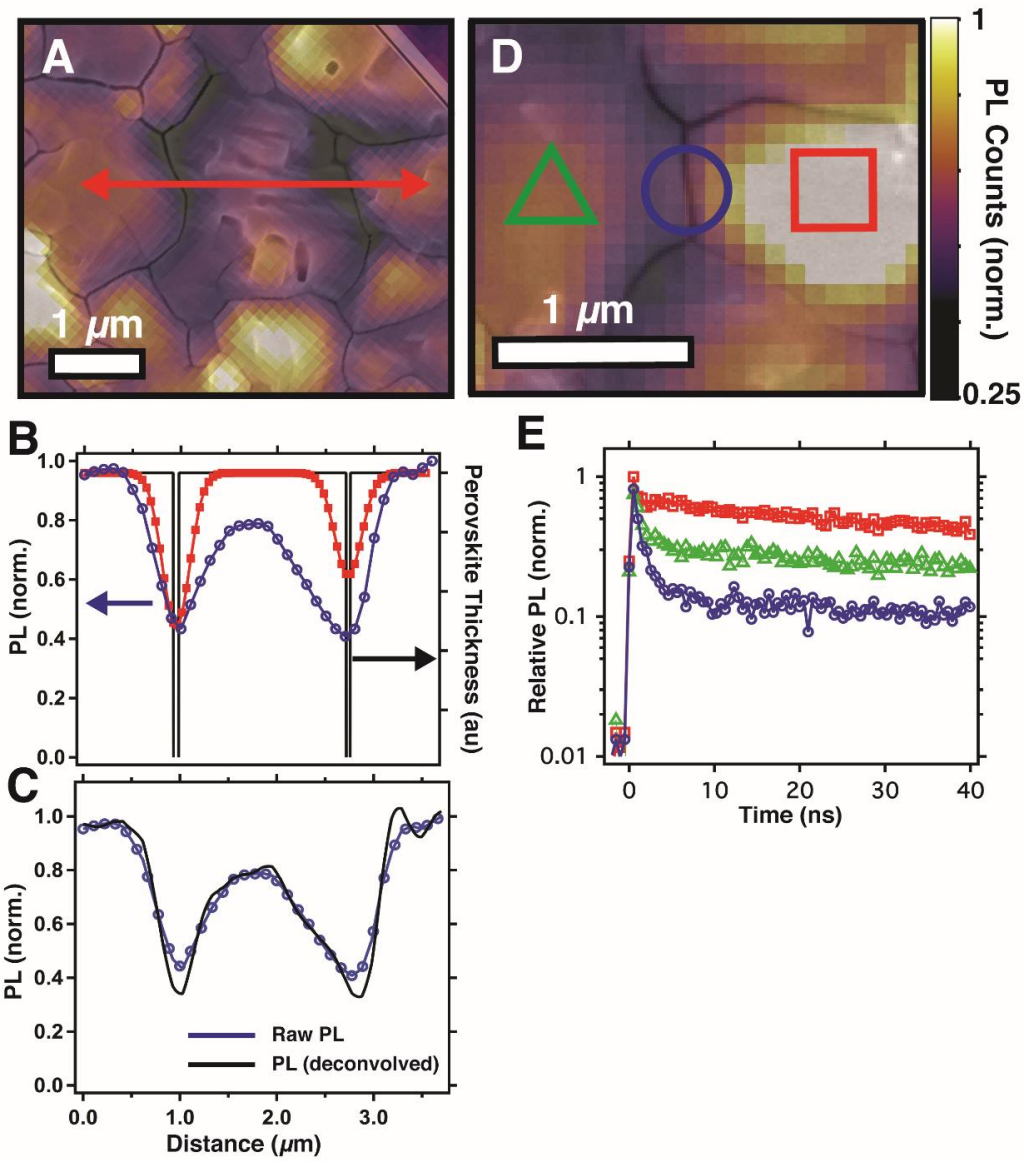

Figure S4. (A) Fluorescence image with semi-transparent SEM overlay showing a line scan (red arrow) across two distinct grain boundaries (GBs). **(B)** Convolution data analysis showing at GBs the half width at half max (HWHM) of the measured PL quenching trace (blue circles) is larger than the HWHM of the point spread function (PSF, red squares) convolved with the grain boundary width (black line). **(C)** We deconvolved the PSF from the raw PL quenching at the GB to determine the spatial extent (~210 nm) and absolute magnitude (~65%) of PL quenching. **(D)** Fluorescence image of $CH_3NH_3PbI_3(Cl)$ film on glass showing PL intensity variations at a bright grain (red square), grain boundary (blue circle), and dark grain (green triangle). **(E)** Time resolved photoluminescence traces showing grain boundaries (blue circle) quench PL significantly more than dark (green triangle) and bright regions (red square).

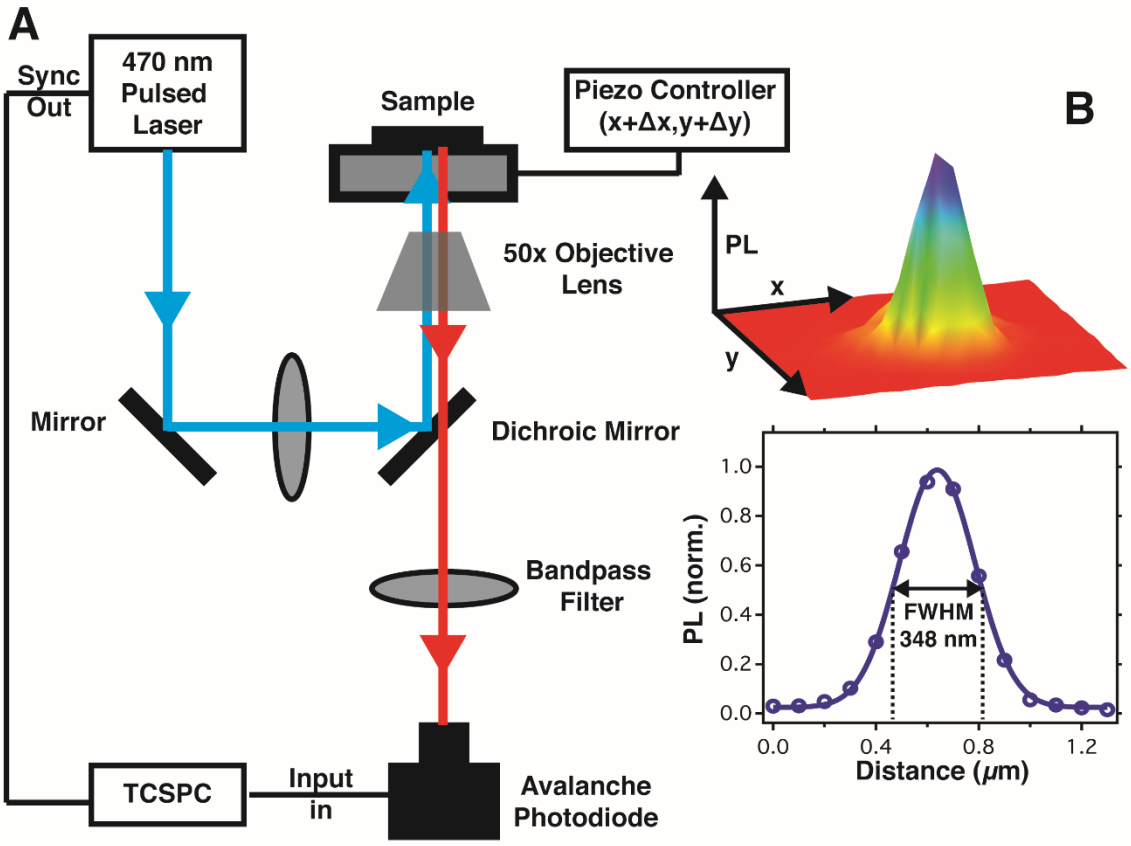

Figure S5. (A) Confocal fluorescence lifetime imaging microscopy schematic **(B)** (**top**) 3-D surface plot of 200 nm fluorescent microsphere used to determine the point-spread function (PSF) of the confocal setup (**bottom**) line scan across fluorescent microsphere showing a PSF of 348 nm at FWHM.

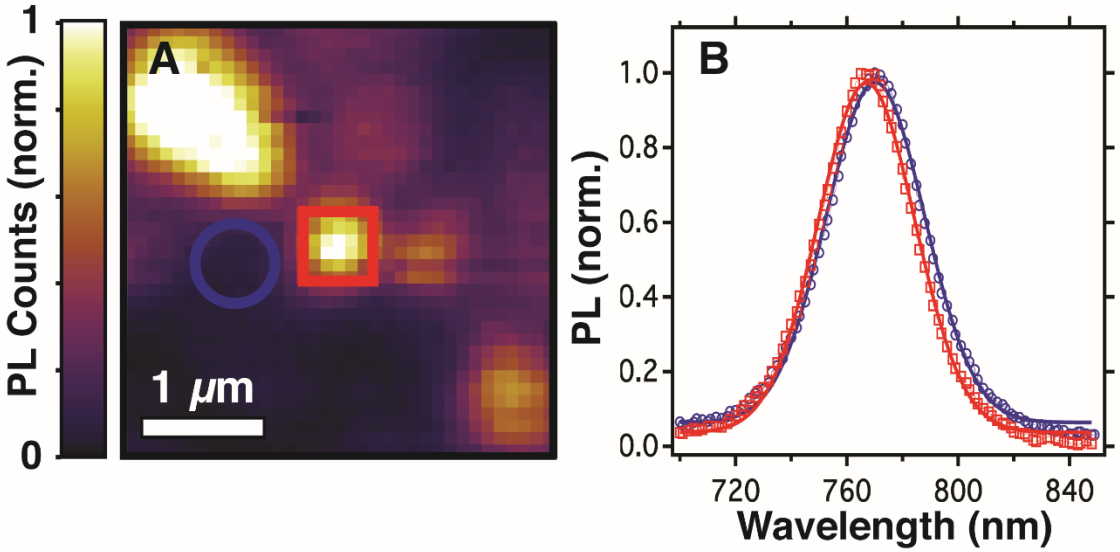

Figure S6. (A) Fluorescence image of the $CH_3NH_3PbI_3(Cl)$ film reported in the main text (Fig. 2A). **(B)** Local normalized steady-state photoluminescence spectra of bright (red squares) and dark regions (blue circles) identified in **(A)**, the dark region is both red shifted and slightly broader than the PL spectrum collected at the bright region.

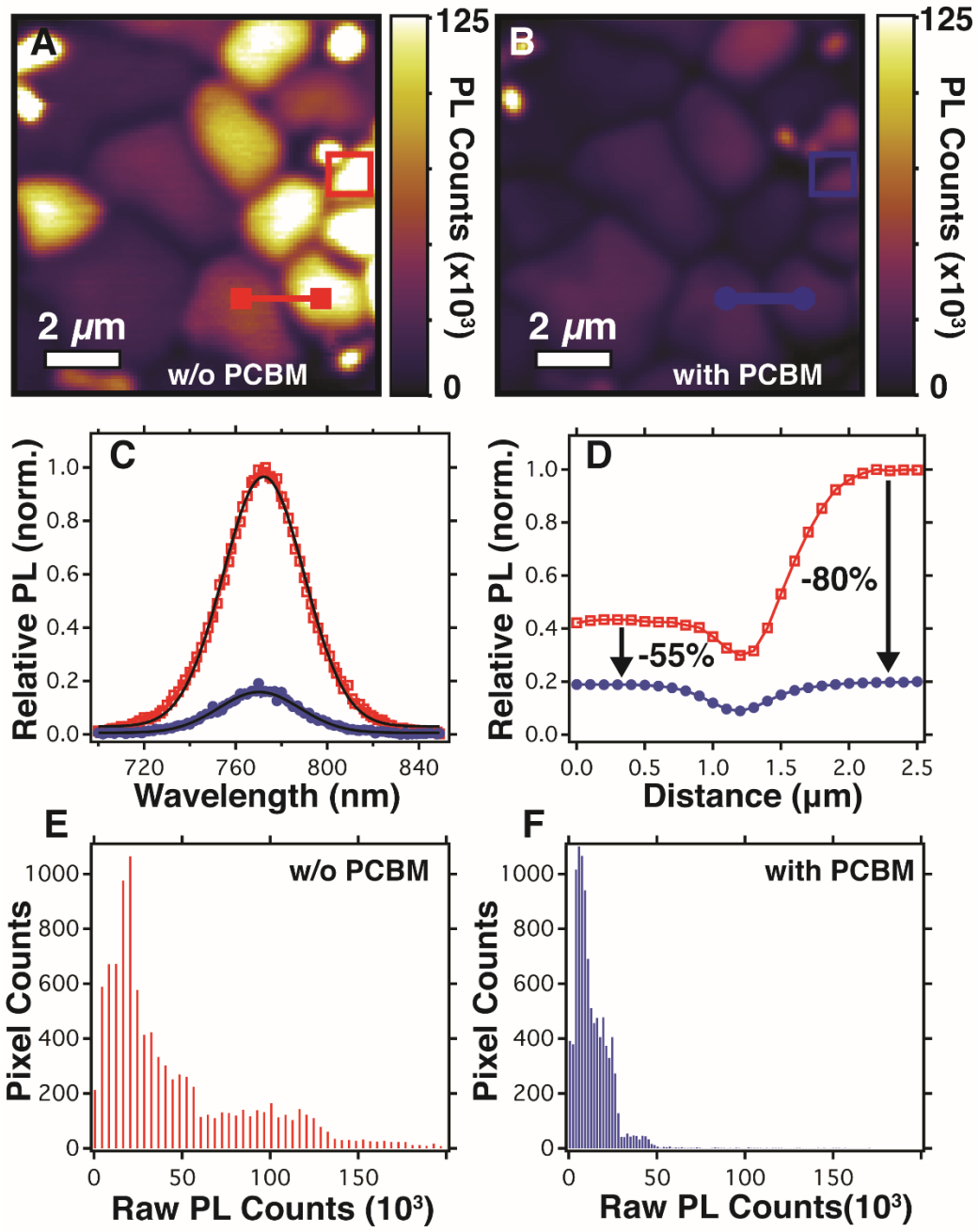

Figure S7. Fluorescence image of $CH_3NH_3PbI_3(Cl)$ film on glass before **(A)** and after **(B)** PCBM deposition. **(C)** Local steady state PL spectra before (red square in **A**) and after (blue square in **B)** PCBM deposition. **(D)** Grain boundary PL line scan before (red line in **A**) and after (blue line in **B**) PCBM showing bright regions are quenched more efficiently by PCBM (-80%) than dark regions (-55%). **(E and F)** Histograms of fluorescence images **(A and B)** with 10,000 total pixels, showing the additional fast non-radiative decay channels introduced by the PCBM result in less contrast among grains and grain boundaries.

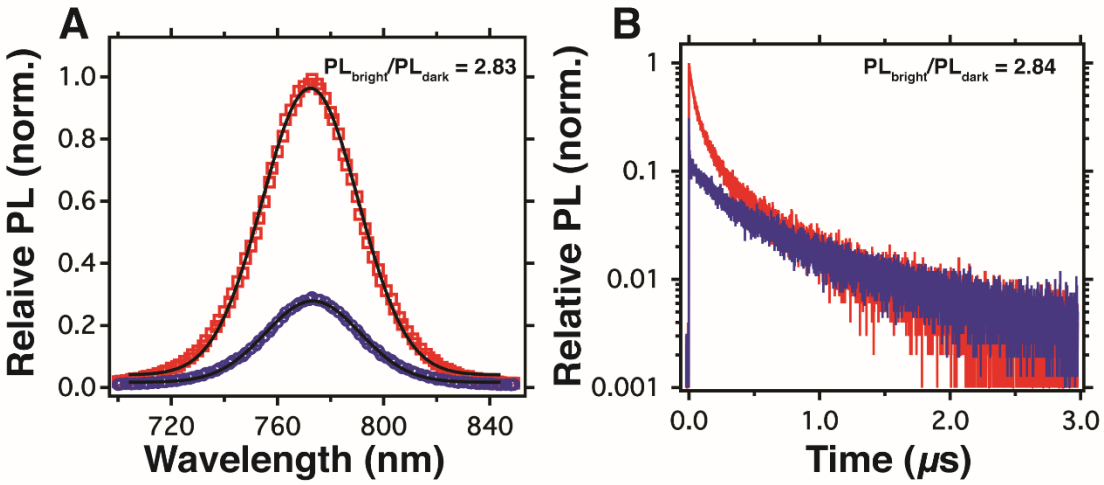

Figure S8. (A) Relative steady-state photoluminescence (PL) spectra of bright (red squares) and dark regions (blue circles) identified in the fluorescence image of the $CH_3NH_3PbI_3(Cl)$ film reported in the main text (Fig. 2), with an integrated PL intensity ratio (PL_{bright}/PL_{dark}) of 2.83. **(B)** Relative time-resolved PL decay traces measured at the same local areas and power density as the steady state spectra in **(A)**, with PL_{bright}/PL_{dark} = 2.84, calculated by integrating over the entire time window of the decay (8 μs for 125 kHz repetition rate). The consistent ratios between the steady state and time resolved PL measurements indicate that we are capturing the important radiative and non-radiative recombination components across both measurements.

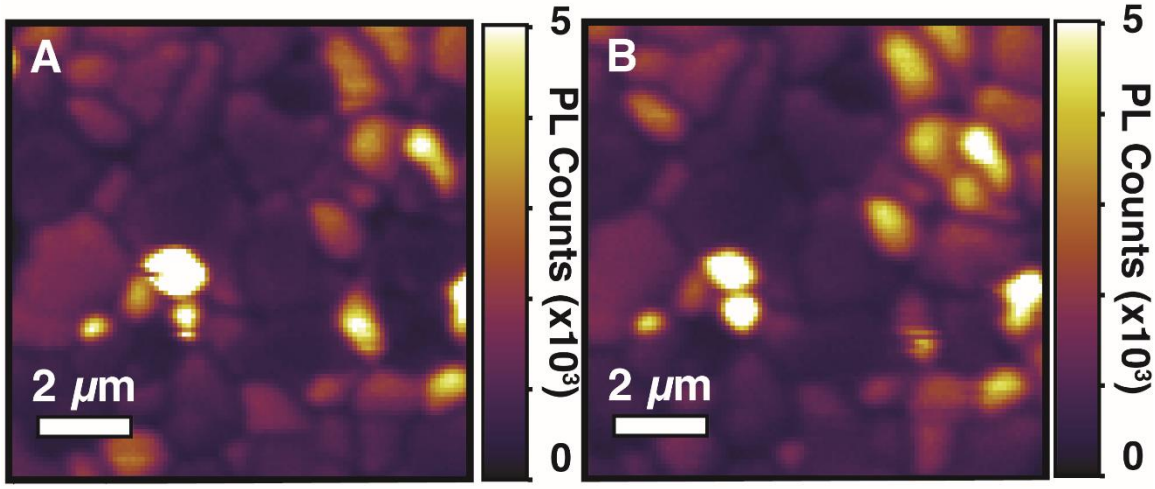

Figure S9. (A) Fluorescence image of $CH_3NH_3PbI_3$ (Cl) film obtained with 470 nm pulsed excitation, 1μJ/cm^2, 125 kHz and **(B)** Control experiment: a second fluorescence image of the same area obtained after chlorobenzene (pyridine solvent) vapor treatment in air. The images appear nearly identical, showing the PL is not enhanced over time in the absence of pyridine.

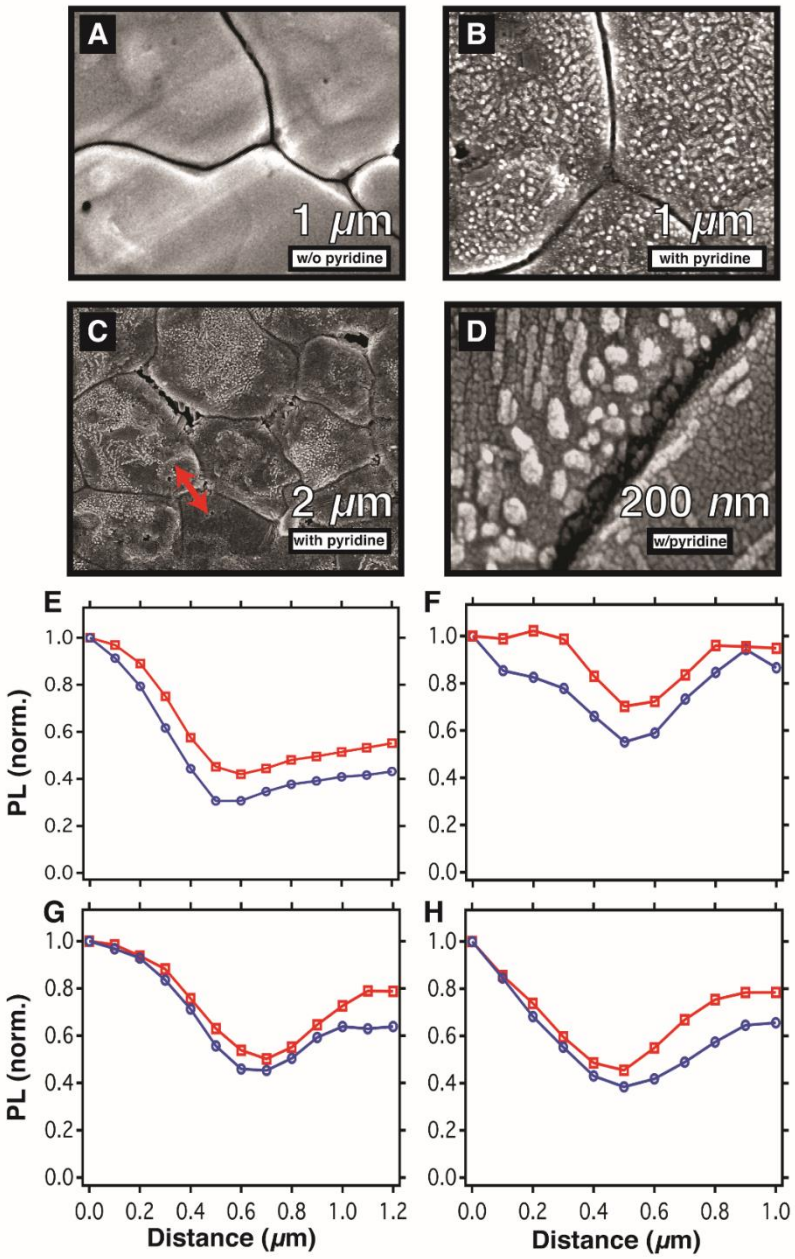

Figure S10. **(A)** SEM micrograph of a $CH_3NH_3PbI_3(Cl)$ film on glass before and **(B)** after pyridine vapor treatment. **(C)** Correlated SEM of area imaged in the PL microscope and reported in Fig. 3. **(D)** High resolution image of grain boundary (GB) after treatment. **(E)** PL linescan across a GB (red arrow in C) before (blue circles) and after (red squares) treatment. (F-H) PL linescans across GB's from separate films before (blue circles) and after (red squares) pyridine treatment, supporting our finding in the main text that pyridine surface treatment generally reduces the magnitude and spatial extent of PL quenching at GB's. The restructuring of the film surface is only observed after pyridine exposure and is characteristic for films where the PL properties were enhanced.

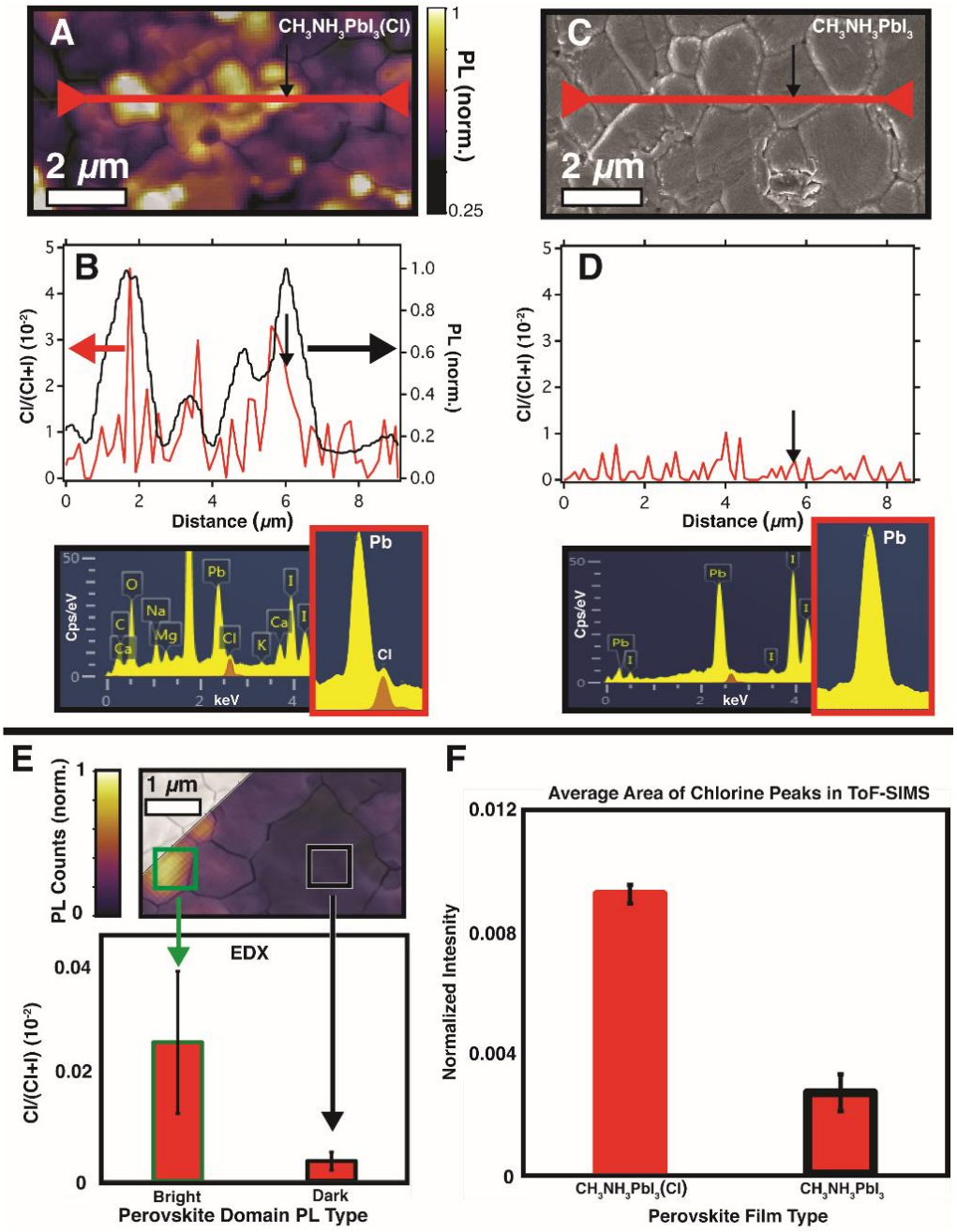

Figure S11. **(A)** SEM micrograph overlaid on fluorescence image of $CH_3NH_3PbI_3(Cl)$ film and (**B, top)** EDS linescan showing the local elemental weight ratio of Cl/(Cl+I) tracks areas of higher integrated photoluminescence intensity indicating that Cl is associated with the better performing grains. (**B, bottom**) Point spectra of area indicated by black arrow in (**B)**, showing detectable Cl. **(C)** SEM micrograph of $CH_3NH_3PbI_3$ film and (**D, top**) EDS linescan showing the local elemental weight ratio of Cl/(Cl+I) is within the baseline noise of the technique for films without intentional Cl. (**D, bottom**) Point spectra of area indicated by black arrow in (**D)**, showing no detectable concentration of Cl. **(E, top)** SEM micrograph overlaid on fluorescence image of $CH_3NH_3PbI_3(Cl)$ film

and **(E, bottom)** EDX statistical analysis of point spectra collected in the bright domain (green square, Cl/(Cl+I) = 0.026 ± 0.013, N=4) versus the dark domain (black square, Cl/(Cl+I) = 0.004 ± 0.002, N=12). **(F)** ToF-SIMS data collected from 100 μm x 100 μm areas for two types of perovskite thin films on glass, $CH_3NH_3PbI_3(Cl)$ (red outline, Cl^- average intensity = 0.0092 ± 0.0003, N=6) and $CH_3NH_3PbI_3$ (black outline, Cl^- average intensity = 0.0027 ± 0.0006, N=5). In both samples, the Cl^- peak was normalized to the total counts. The ToF-SIMs sampling volume is confined to the top ~2 nm of the surface under the imaging conditions used, suggesting that Cl is present at least in the top layer.

Supplementary References

1. T. C. Sum, N. Mathews, Advancements in perovskite solar cells: photophysics behind the photovoltaics. *Energ. Environ. Sci.* **7**, 2518-2534 (2014).

2. M. A. Green, A. Ho-Baillie, H. J. Snaith, The emergence of perovskite solar cells. *Nat. Photonics* **8**, 506-514 (2014).

3. J. Burschka *et al.*, Sequential deposition as a route to high-performance perovskite-sensitized solar cells. *Nature* **499**, 316-319 (2013).

4. G. E. Eperon, V. M. Burlakov, P. Docampo, A. Goriely, H. J. Snaith, Morphological control for high performance, solution-processed planar heterojunction perovskite solar cells. *Adv. Funct. Mater.* **24**, 151-157 (2014).

5. G. Xing *et al.*, Low-temperature solution-processed wavelength-tunable perovskites for lasing. *Nat. Mater.* **13**, 476-480 (2014).

6. G. E. Eperon *et al.*, Formamidinium lead trihalide: a broadly tunable perovskite for efficient planar heterojunction solar cells. *Energ. Environ. Sci.* **7**, 982-988 (2014).

7. J. H. Noh, S. H. Im, J. H. Heo, T. N. Mandal, S. I. Seok, Chemical management for colorful, efficient, and stable inorganic-organic hybrid nanostructured solar cells. *Nano Lett.* **13**, 1764-1769 (2013).

8. NCPV at NREL. Research Cell Efficiency Records. http:// www.nrel.gov/ncpv/ (accessed April 11, 2015).

9. S. D. Stranks *et al.*, Electron-hole diffusion lengths exceeding 1 micrometer in an organometal trihalide perovskite absorber. *Science* **342**, 341-344 (2013).

10. H. Zhou *et al.*, Interface engineering of highly efficient perovskite solar cells. *Science* **345**, 542-546 (2014).

11. O. D. Miller, E. Yablonovitch, S. R. Kurtz, Strong internal and external luminescence as solar cells approach the Shockley-Queisser limit. *IEEE J. Photovolt.* **2**, 303-311 (2012).

12. N. K. Noel *et al.*, Enhanced photoluminescence and solar cell performance via Lewis base passivation of organic-inorganic lead halide perovskites. *ACS Nano* **8**, 9815-9821 (2014).

13. J. B. You *et al.*, Low-temperature solution-processed perovskite solar cells with high efficiency and flexibility. *ACS Nano* **8**, 1674-1680 (2014).

14. P. W. Liang *et al.*, Additive enhanced crystallization of solution-processed perovskite for highly efficient planar-heterojunction solar cells. *Adv. Mater.* **26**, 3748-3754 (2014).

15. S. D. Stranks *et al.*, Recombination kinetics in organic-inorganic perovskites: excitons, free charge, and subgap states. *Phys. Rev. Applied* **2**, 034007 (2014).

16. F. Deschler *et al.*, High photoluminescence efficiency and optically pumped lasing in solution-processed mixed halide perovskite semiconductors. *J. Phys. Chem. Lett.* **5**, 1421-1426 (2014).

17. C. Wehrenfennig, M. Z. Liu, H. J. Snaith, M. B. Johnston, L. M. Herz, Charge-carrier dynamics in vapour-deposited films of the organolead halide perovskite $CH_3NH_3PbI_{3-x}Cl_x$. *Energ. Environ. Sci.* **7**, 2269-2275 (2014).

18. J. S. Manser, P. V. Kamat, Band filling with free charge carriers in organometal halide perovskites. *Nat. Photonics* **8**, 737-743 (2014).

19. See Supplementary Materials on Science Online.

20. G. Xing *et al.*, Long-range balanced electron- and hole-transport lengths in organic-inorganic $CH_3NH_3PbI_3$. *Science* **342**, 344-347 (2013).

21. Y. Yamada, T. Nakamura, M. Endo, A. Wakamiya, Y. Kanemitsu, Photocarrier recombination dynamics in perovskite $CH_3NH_3PbI_3$ for solar cell applications. *J. Am. Chem. Soc.* **136**, 11610-11613 (2014).

22. M. Saba *et al.*, Correlated electron-hole plasma in organometal perovskites. *Nature Commun.* **5**, 5049 (2014).

23. A. Abate *et al.*, Supramolecular halogen bond passivation of organic-inorganic halide perovskite solar cells. *Nano Lett.* **14**, 3247-3254 (2014).

24. S. Watanabe *et al.*, Protein localization in electron micrographs using fluorescence nanoscopy. *Nat. Methods* **8**, 80-84 (2011).

25. E. Edri *et al.*, Why lead methylammonium tri-iodide perovskite-based solar cells require a mesoporous electron transporting scaffold (but not necessarily a hole conductor). *Nano Lett.* **14**, 1000-1004 (2014).

26. W. J. Yin, T. Shi, Y. Yan, Unique properties of halide perovskites as possible origins of the superior solar cell performance. *Adv. Mater.* **26**, 4653-4658 (2014).

27. M. M. Lee, J. Teuscher, T. Miyasaka, T. N. Murakami, H. J. Snaith, Efficient hybrid solar cells based on meso-superstructured organometal halide perovskites. *Science* **338**, 643-647 (2012).

28. P. Gao, M. Gratzel, M. K. Nazeeruddin, Organohalide lead perovskites for photovoltaic applications. *Energ. Environ. Sci.* **7**, 2448-2463 (2014).

29. K. Munechika *et al.*, Quantum dot/plasmonic nanoparticle metachromophores with quantum yields that vary with excitation wavelength. *Nano Lett.* **11**, 2725-2730 (2011).

30. X. Wen *et al.*, Morphology and carrier extraction study of organic–inorganic metal halide perovskite by one- and two-photon fluorescence microscopy. *J. Phys. Chem. Lett.* **5**, 3849-3853 (2014).

31. K. Tvingstedt *et al.*, Radiative efficiency of lead iodide based perovskite solar cells. *Sci Rep.* **4**, 6071 (2014).

32. S. De Wolf *et al.*, Organometallic halide perovskites: sharp optical absorption edge and its relation to photovoltaic performance. *J. Phys. Chem. Lett.* **5**, 1035-1039 (2014).

33. C. H. Seager, Grain boundaries in polycrystalline silicon. *Annu. Rev. Mater. Sci.* **15**, 271-302 (1985).

34. J. S. Yun *et al.*, Benefit of grain boundaries in organic–inorganic halide planar perovskite solar cells. *J. Phys. Chem. Lett.* **6**, 875-880 (2015).

35. Q. Dong *et al.*, Electron-hole diffusion lengths > 175 μm in solution-grown $CH_3NH_3PbI_3$ single crystals. *Science* **347**, 967-970 (2015).

36. W. Nie *et al.*, High-efficiency solution-processed perovskite solar cells with millimeter-scale grains. *Science* **347**, 522-525 (2015).

37. D. Shi *et al.*, Low trap-state density and long carrier diffusion in organolead trihalide perovskite single crystals. *Science* **347**, 519-522 (2015).

38. M. Gratzel, The light and shade of perovskite solar cells. *Nat. Mater.* **13**, 838-842 (2014).

39. G. Grancini *et al.*, The impact of the crystallization processes on the structural and optical properties of hybrid perovskite films for photovoltaics. *J. Phys. Chem. Lett.* **5**, 3836-3842 (2014).

40. Y. Tidhar *et al.*, Crystallization of methyl ammonium lead halide perovskites: implications for photovoltaic applications. *J. Am. Chem. Soc.* **136**, 13249-13256 (2014).

41. S. T. Williams *et al.*, Role of chloride in the morphological evolution of organo-lead halide perovskite thin films. *ACS Nano* **8**, 10640-10654 (2014).

Appendix B: Supporting Information for Chapter 3

Materials and Methods

Perovskite Precursor Preparation

A methylammonium iodide (MAI) stock solution was made by dissolving MAI (Dyesol, CAS:14965-49-2) in anhydrous *N*,*N*- dimethylformamide (DMF) at a concentration of 1.78 M. Then lead acetate trihydrate (99.999%, Sigma-Aldrich, CAS:6080-56-4) was added to obtain a 3:1 molar ratio of MAI to $PbOAc_2 \cdot 3\ H_2O$ (0.59 M).[47] An HPA solution was added to the precursor solution with a molar ratio HPA/$PbOAc_2 \bullet 3H_2O$ of 8%. All solutions were made in a nitrogen filled glovebox.

$PbCl_2$ as a Pb Source

Methylammonium iodide (MAI) was prepared by reacting methylamine, 33 wt% in ethanol (Sigma-Aldrich), with hydroiodic acid (HI) 57 wt% in water (Sigma-Aldrich), at room temperature. HI was added dropwise while stirring. MAI was precipitated out of solution by heating the solution at 100 °C overnight to drive off the solvent. The crude MAI was either used without further purification or recrystallized in a mixed solvent of ethanol and ether.

To form the non-stoichiometric $CH_3NH_3PbI_3(Cl)$ precursor solution, MAI and lead (II) chloride (99.999%, Sigma-Aldrich) were dissolved in DMF at a 3:1 molar ratio of MAI to PbCl2, with final concentrations 0.88 M lead chloride and 2.64 M methylammonium iodide.[48] This solution was stored under a dry nitrogen atmosphere.

Perovskite Deposition

Glass substrates were cleaned sequentially in 2% Micro-90 detergent, acetone, then propan-2-ol. To form the perovskite layer for spectroscopy measurements, the precursor solutions were spin-coated on plasma-cleaned substrates in a nitrogen-filled glovebox, at 2000 rpm for 60 s.

Films prepared from the $PbOAc_2$ precursor were left to dry at room temperature in the glovebox for 10 minutes and then annealed on a hotplate at 100 °C for 5 minutes.

Films prepared from the $PbCl_2$ precursor were left at room temperature in the glovebox for 30 minutes and then annealed on a hotplate in the glovebox at 90 °C for 150 minutes.

Surface Treatment Deposition

n-trioctylphosphine oxide (TOPO, Sigma, CAS: 78-50-2) treatment solutions were prepared in anhydrous chlorobenzene (Sigma-Aldrich, CAS: 108-90-7) with a concentration of 0.025 M. Treatments were carried out by depositing ~200 µl of the treatment solution on the film then immediately spincoating at 2000 rpm for 60 s. Multiple treatments (i.e. ~3) were often performed without a washing step to achieve the largest enhancements.

Characterization

Fluorescence Lifetime Imaging Microscopy (FLIM)

Optical microscopy and spectroscopy were performed using a custom sample scanning confocal microscope built around a Nikon TE-2000 inverted microscope fitted with an infinity corrected 100x dry objective (Nikon LU Plan Fluor, NA 0.9). Either a 470 nm pulsed diode laser (PDL-800 LDH-P-C-470B, 2.5 MHz, ~300 ps pulse width) or a 532 nm continuous-wave (CrystaLaser, GCL532-025-L) were used for excitation and neutral density filters were used to attenuate the laser for intensity-dependent measurements. The emission was filtered through a 50/50 dichroic beamsplitter and a pair of 700 nm longpass filters. Photoluminescence from the sample was directed to a Micro Photon Devices (MPD) PDM Series single-photon avalanche photodiode with a 50 μm active area for TRPL measurements or a CCD camera for widefield measurements (Pixera, Penguin 150CLM) equipped with a 600 nm longpass filter. The sample stage was controlled using a piezo controller (Physik Instrumente E-710) and the pixel size was 100 nm with a pixel dwell time (integration time) of 50 ms. Before measurements, the system was calibrated using 200 nm fluorescent microspheres (Lifetechnologies FluoSpheres® Polystyrene Microspheres, 200 nm, red fluorescent, 580/605).

Supplementary Figures and Text

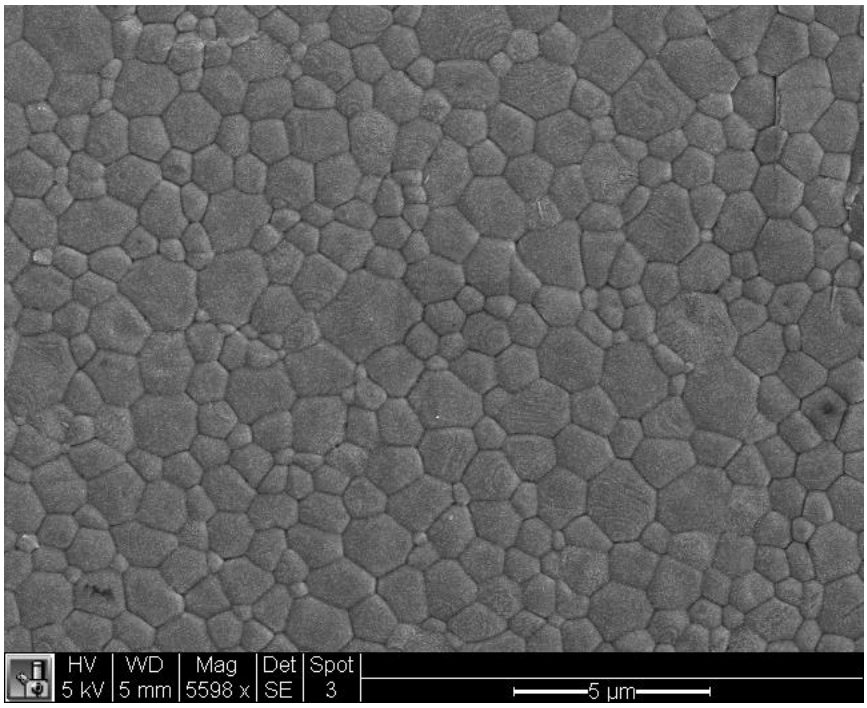

Figure S1. a) A representative top-view scanning electron microscopy (SEM) image of a $CH_3NH_3PbI_3$ film on glass that was studied in this report. We determined the average grain size to be 0.91 µm using the particle analysis function in ImageJ.

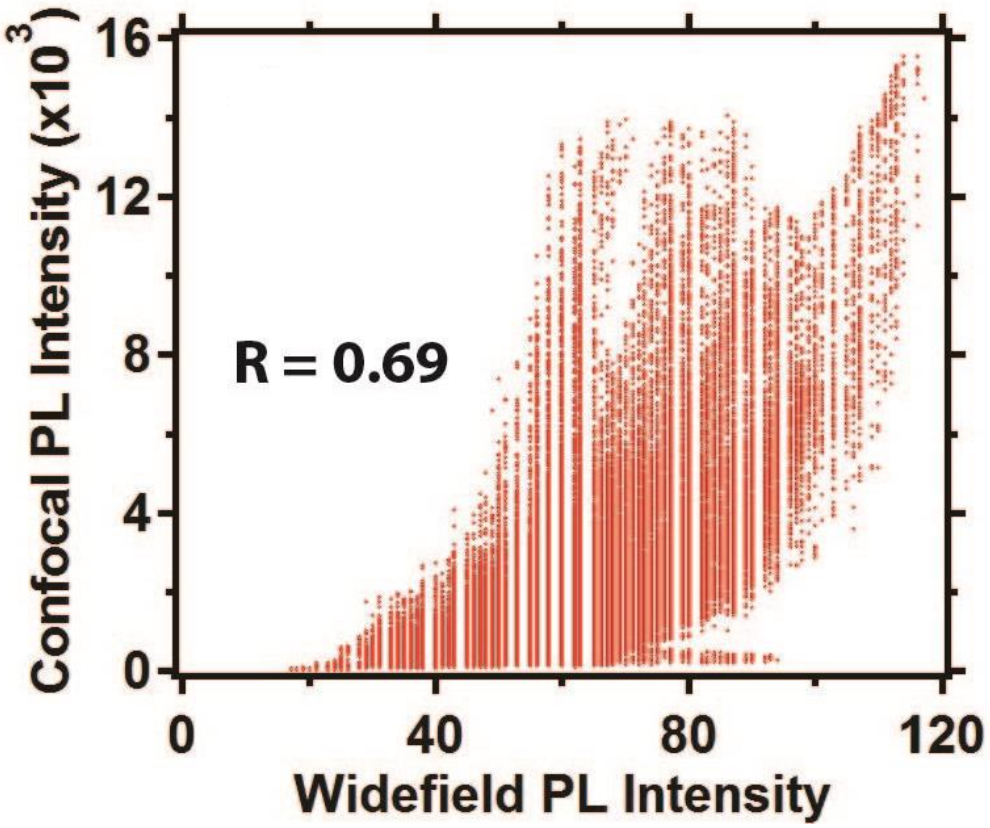

Figure S2. Linear correlation plot of confocal versus widefield photoluminescence (PL) data (from Figure 1 in the main article) with a Pearson coefficient (R) of 0.69, indicating a strong positive correlation.

S.1: Alternate Explanations of Contrast in Fluorescence Images

Other possible explanations for the contrast in the confocal and widefield images could result from 1) differences in the absorption cross-section, 2) variations in local outcoupling efficiency and scattering, 3) the diffusion of carriers to local "hot spots",[1] and/or 4) the reduction of PL quantum efficiency due to dilution of carrier density in larger grains and for grains with good inter-grain connectivity.

Several groups have studied each of these behaviors for different perovskite samples,[1-3] primarily concluding that the variations stem from local differences in non-radiative recombination. For thoroughness, we performed similar studies on our samples to evaluate whether this interpretation holds true.

1) *Differences in absorption:* Figure S3a shows a widefield PL intensity image in transmission mode when excited with a tungsten halogen lamp with a 550 nm shortpass filter and detecting the PL at wavelengths longer than 600 nm (600 nm longpass filter). Figure S3b shows the transmission map of the same area (longpass filter removed in front of CCD camera). Figure S3c shows a correlation plot of the transmission intensity versus the PL intensity, where we report a statistically insignificant Pearson coefficient (R) of 0.07 consistent with previous reports.[1-3] This suggests that regions of low(high) PL intensity do not correlate with regions of low(high) absorption.

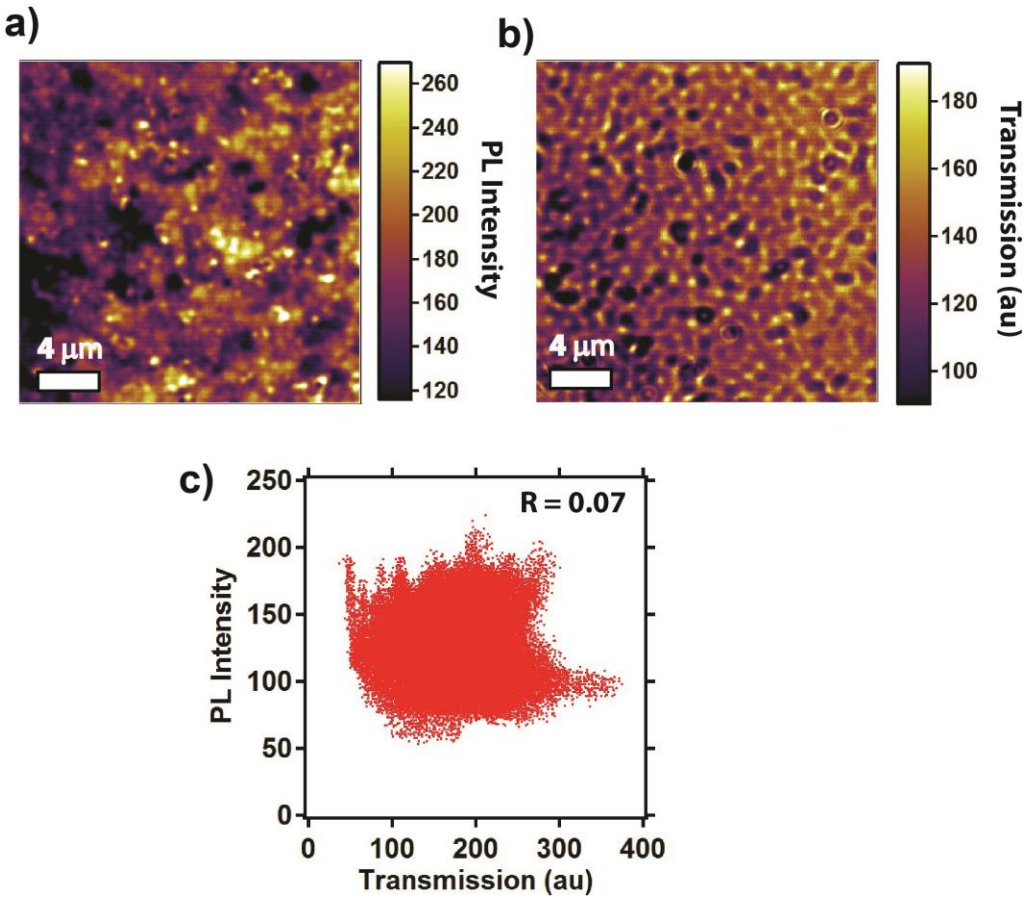

Figure S3. a) Widefield PL intensity image measured at a low excitation power (70 mW/cm^2), b) transmission image of halogen lamp with <550 nm SP filter, and c) linear correlation plot showing a negligible correlation (R=0.07) between transmission and PL intensity.

2) *Differences in photon outcoupling efficiency and scattering:* Figure S4 shows a widefield PL intensity image when excited with a tungsten halogen lamp with a 550 nm shortpass filter and detecting the PL at wavelengths longer than 600 nm (600 nm longpass filter). Figure S4b shows the transmitted darkfield scattering intensity image of the same area. Figure S4c shows a correlation plot of the scattering intensity versus the PL intensity, where we report a statistically insignificant Pearson coefficient (R) of -0.005. This suggests that regions of low(high) PL intensity do not correlate with regions of low(high) scattering (i.e. outcoupling). In addition, Figure S9 shows that regions of high PL intensity also have longer lifetimes, suggesting that photon outcoupling does not significantly contribute differences in PL intensity. If photon outcoupling affected the PL heterogeneity, we would expect regions high in PL intensity to correspond to more efficient outcoupling. More efficient outcoupling would translate to photons spending less time within the film and therefore we would expect regions of higher PL intensity to exhibit faster PL decays (less photon recycling),[4] which is the opposite of what we observe.

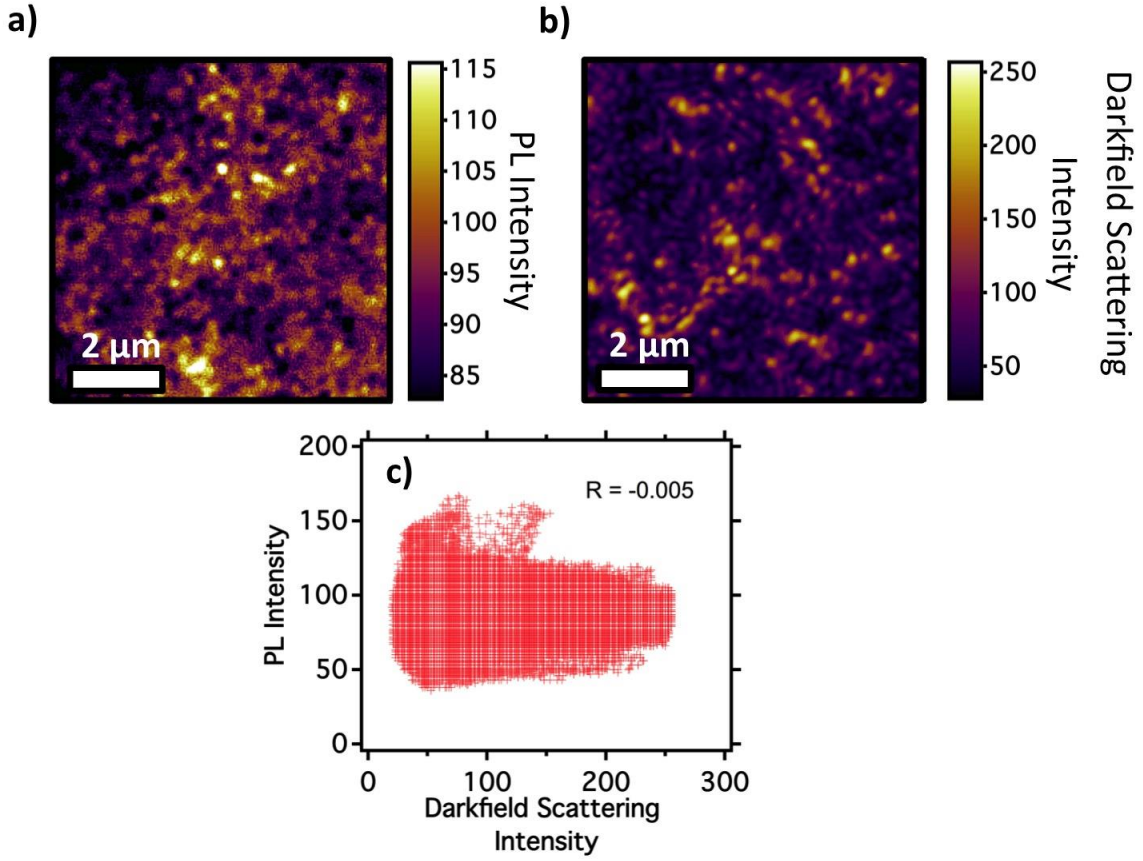

Figure S4. a) Widefield PL intensity image measured at a low excitation power (50 mW/cm^2), b) Transmitted darkfield scattering intensity image of halogen lamp with <700 nm SP filter, and c) linear correlation plot showing a negligible correlation (R=-0.005) between scattering intensity and PL intensity.

3) *Anisotropic diffusion of carriers to "hot spots"*: Regions bright in intensity in the fluorescence images could result from long-range migration of carriers into "hot spots". This hypothesis has previously been tested by Deschler and coworkers,[1] where they tune the collection geometry to probe the extent of diffusion. Here we perform a similar experiment, but image the diffusion in all directions using a local excitation/widefield detection setup. Figure S5a shows a large area confocal fluorescence image (which again is qualitatively consistent with the widefield measurement, *cf.* Figure 1 and S2), with the typical grain-to-grain heterogeneity. Figure S5b shows a selection of Figure S5a, where a bright grain and dark grain of similar size are adjacent to one another. To determine if the bright grain in the center is potentially a "hot spot" where carriers concentrate, we locally excite the grain (indicated by red circle in Figure S5b) and probe the emission using widefield detection (Figure S5c).

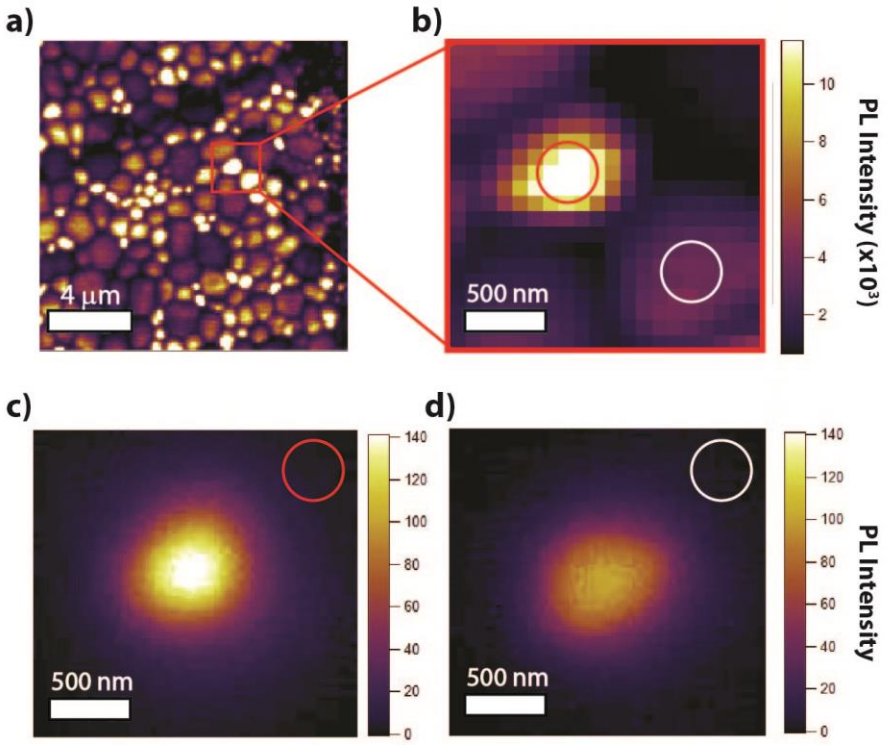

Figure S5. a) Large area confocal fluorescence image taken at 0.2 µJ/cm^2 per pulse, b) selected area of a), showing a bright grain next to a dark grain. c) widefield image of a bright grain that was locally excited (red circle in b), d) widefield image of a dark grain that was locally excited (white circle in b) showing that in both cases, carriers are primarily confined to the grain they were generated in.

Figure S5c and S5d show that even though these grains are similar in size, they exhibit different integrated emission intensities. Importantly, the grain under the

red circle (Figure S5b) is brighter than the grain under the white circle in both the confocal experiment as well as the widefield experiment. If the grain in Figure S5b was a local “hot spot”, we would expect carriers to funnel from the surrounding grains to this region. To test this hypothesis, we locally excited the darker adjacent grain (white circle in Figure S5b) and found that carriers actually remain in the photoexcited grain. This finding indicates that carriers are primarily confined to the grains where they were generated and the contrast observed in both the confocal and widefield images is likely attributed to local variations in non-radiative recombination.

4) *Reduction of PL quantum efficiency due to dilution of carrier density in larger grains and grains with good inter-grain connectivity:* As PL quantum efficiency is known to strongly depend on carrier density,[5,6] we test whether the dilution in the carrier density could potentially explain the contrast in the confocal images. We expect that larger grains should exhibit lower PL intensities, as diffusion of carriers to fill the grain volume results in a lower steady state carrier density and therefore smaller fractions of radiative bimolecular recombination.[4] To test this hypothesis, we performed a local excitation/widefield detection experiment on fourteen different grains that primarily exhibit poor intergrain connectivity (similar to Figures 3 and 4 in the main article). This allowed us to determine the

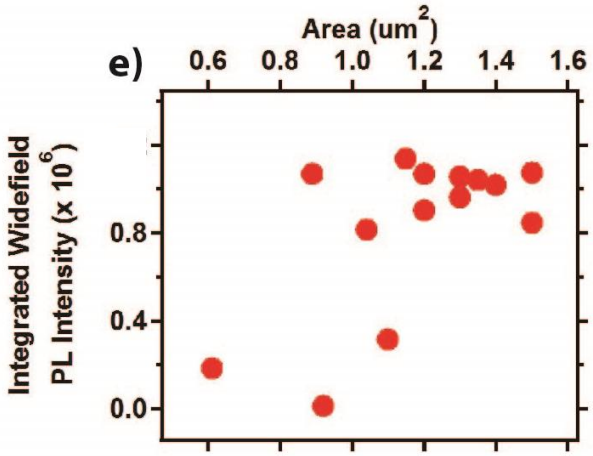

Figure S6. Plot of the integrated widefield intensity for grains that were locally excited versus the grain areas.

grain area and measure the total widefield PL intensity from locally exciting the center of the grain. Figure S6 shows a plot of the integrated widefield PL intensity versus the grain area. We report little correlation between grain area and widefield PL intensity and also note that (out of the grains analyzed in this study) some smaller grains actually exhibit lower PL intensity, which is surprising considering (in the absence of non-radiative recombination and the fact that photogenerated carriers are primarily confined to grains) smaller grains would maintain higher steady-state carrier populations which would result in higher PL.

Considering the results from 1-4 above as well as the observations that the confocal and widefield PL images are strongly correlated (Figures 1 and S2), that the film PL emission become more homogeneous at higher excitation powers and fluences (Figure 2), and that dark regions exhibit greater improvements in PL intensity in comparison to bright regions when light-soaked or treated with a surface ligand,[7,8] we conclude that the variations in PL intensity observed in the confocal experiment are dominated by variations in local non-radiative decay rates when excited at low fluence or excitation powers. These observations are consistent for the films analyzed in this and previous studies.[9]

Here, we also highlight that local changes in the diffusion coefficient, outcoupling efficiency, and absorption cross-section are not predicted to change as a function of excitation power (see Figure 2), but that this behavior is expected for non-radiative recombination.

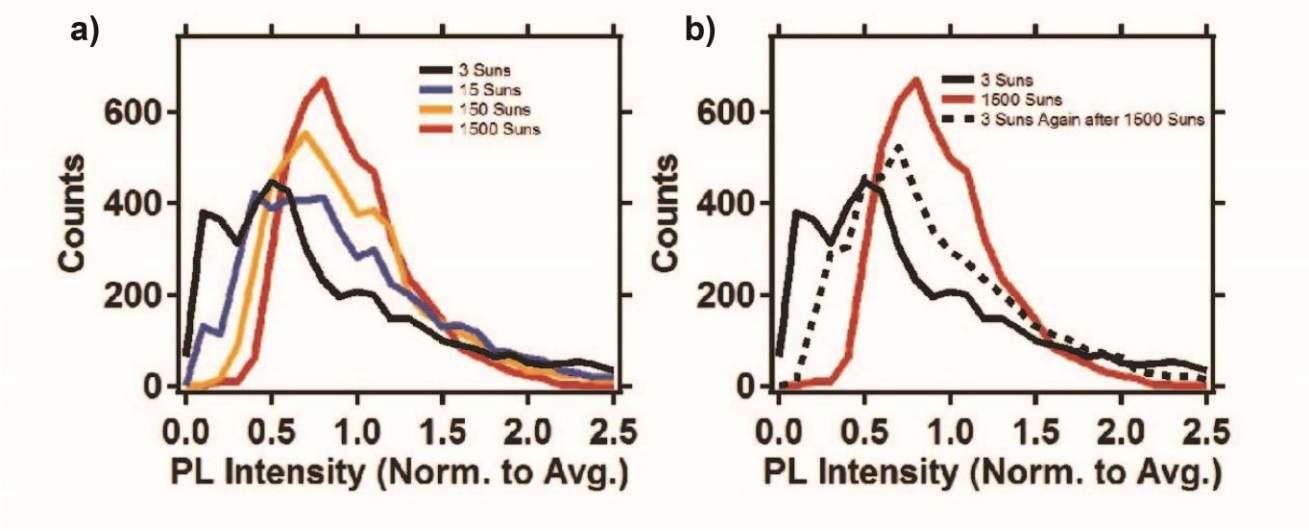

Figure S7. a) Image histograms of Figure 2a-d in the main article measured at 180 mW/cm^2 (~3 suns, black), 900 mW/cm^2 (~15 suns, blue), 9,000 mW/cm^2 (~150 suns, orange), and 90,000 mW/cm^2 (~1500 suns, red). b) histograms of fluorescence images taken at 3 suns, then 1500 suns, then 3 suns again (dotted black trace), showing the partial reversibility of intensity-dependent experiment. Incomplete reversibility can likely be attributed to photobrightening effects observed in similar films.[8]

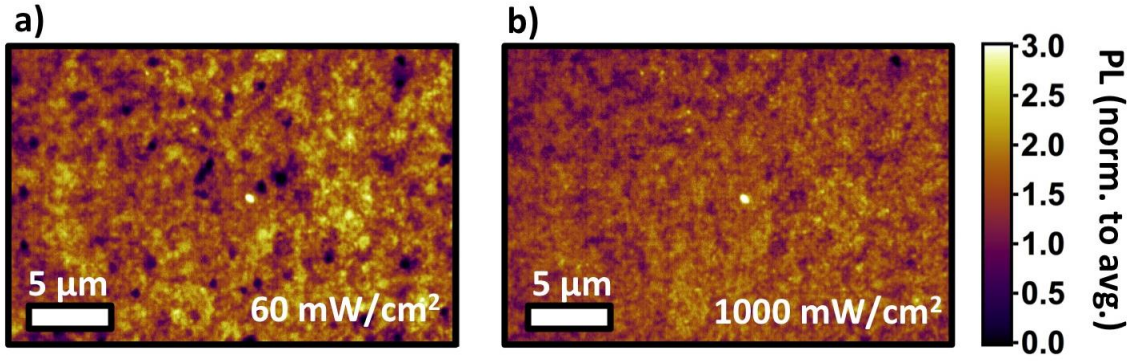

Figure S8. a) Widefield fluorescence image measured at a low excitation power (532 nm, 60 mW/cm^2) and b) at a higher power (532 nm, 1000 mW/cm^2) on the same intensity scale (normalized to the average pixel values of each image) and showing a reduction in spatial heterogeneity.

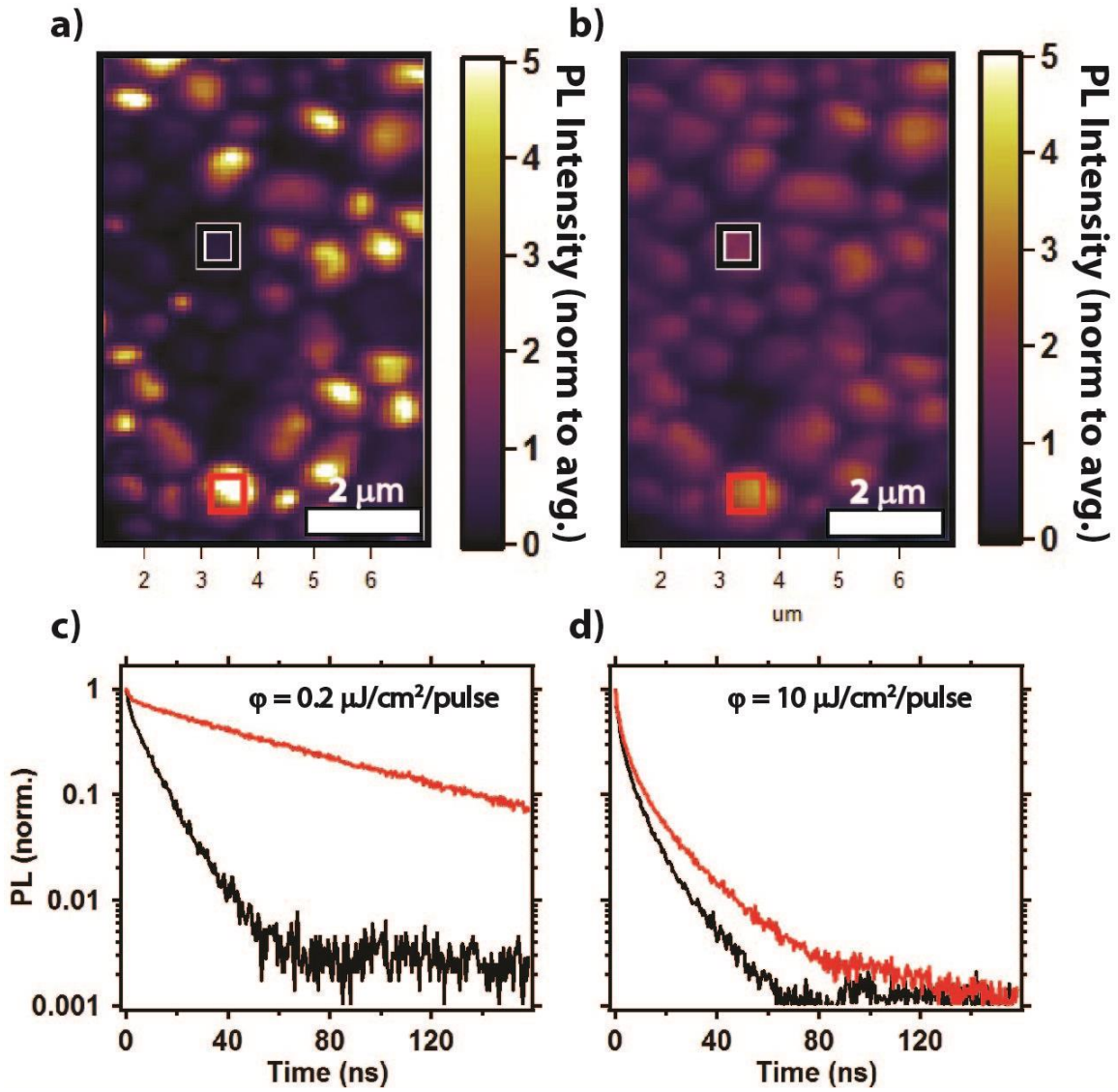

Figure S9. a) Confocal fluorescence image measured at a low excitation fluence (φ = 0.2 $\mu J/cm^2$ per pulse) and b) fluorescence image taken at a higher fluence (φ = 10 $\mu J/cm^2$ per pulse). c) Time-resolved PL decay traces measured at low fluence of a region that appears dark in the confocal region (black square, Figure S9a) versus a region that appears bright (red square, Figure S9a), showing significant contrast in PL kinetics. d) Time-resolved PL decay traces measured at high fluence of a region that appears dark in the confocal image (black square, Figure S9b) versus a region that appears bright (red square, Figure S9b), showing similar PL kinetics, which is consistent with the small contrast observed in the fluorescence image.

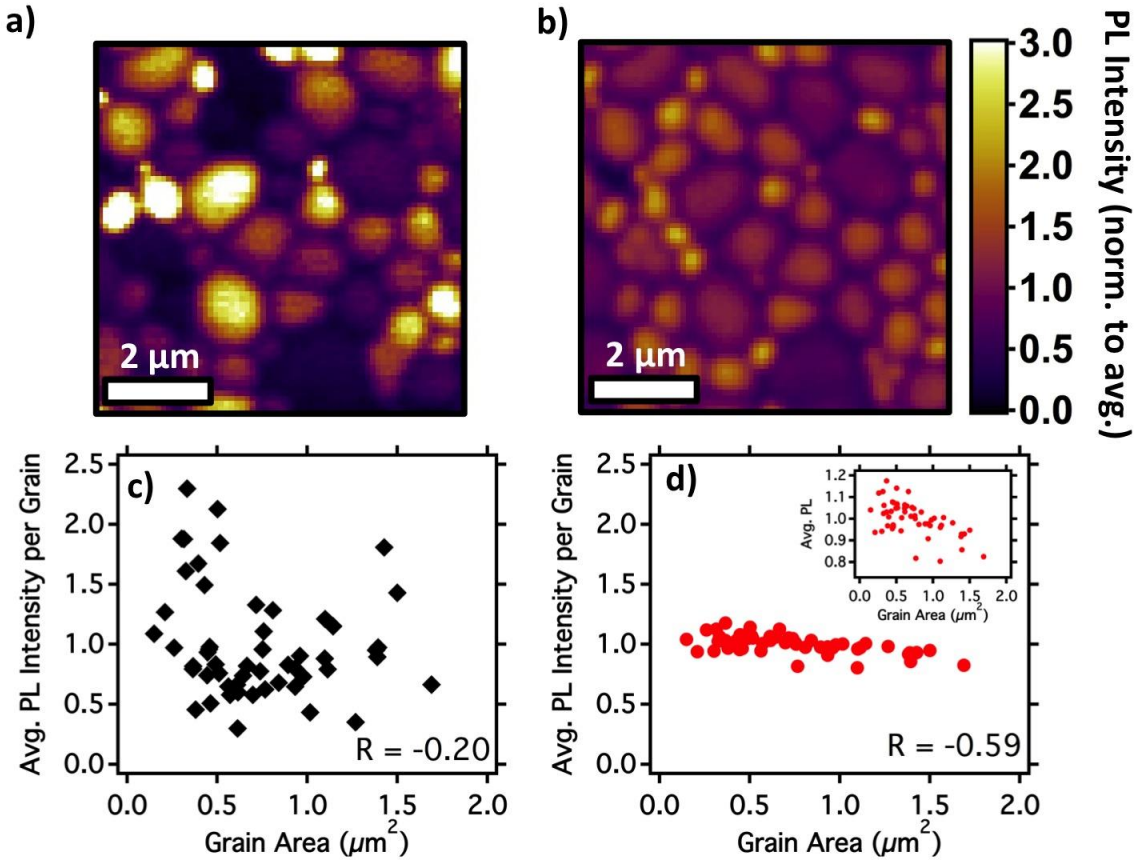

Figure S10. a) Confocal fluorescence image of a $CH_3NH_3PbI_3$ perovskite film on glass measured at 180 mW/cm^2 (~3 suns) and b) 90,000 mW/cm^2 (~1500 suns) showing a reduction in grain-to-grain contrast. c) Linear correlation plot of the average grain photoluminescence (PL) intensity versus the grain area for the image data in a), where (R = -0.20). d) Linear correlation plot of the average grain photoluminescence (PL) intensity versus the grain area for image data in b), (R = -0.59). Inset of d) is an identical data set, but with zoomed y-axis.

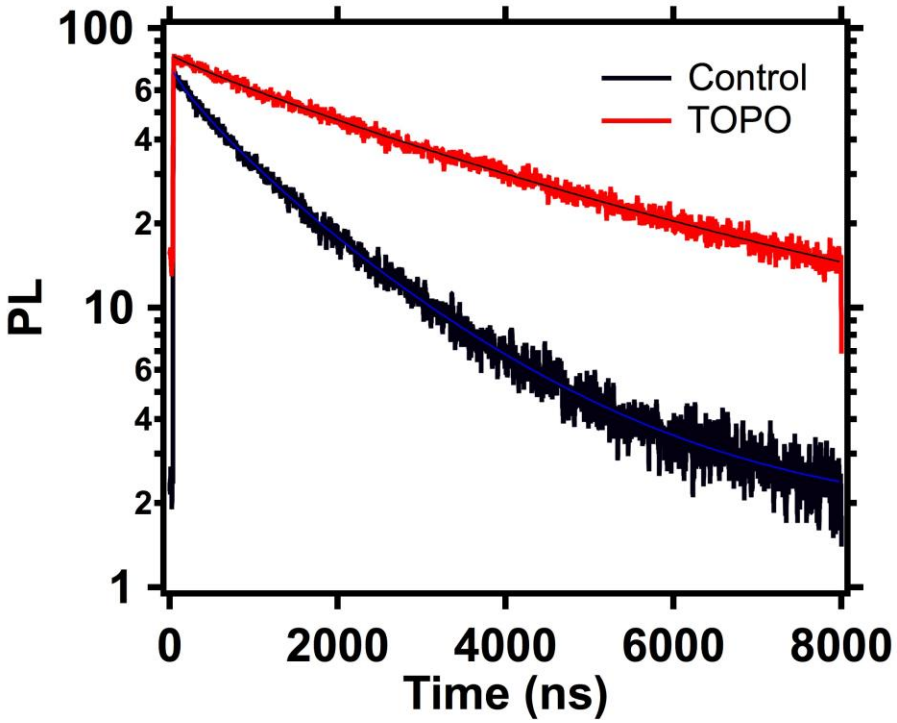

Figure S11. Time-resolved PL decay before (control, black) and after (red) surface treatment with TOPO. Solid lines are stretched exponential fits to the data with the average lifetime,[7] $<\tau_{ctrl}>$ = 1.22 μs and $<\tau_{TOPO}>$ = 3.62 μs.

S.2: Recombination/Diffusion Model

To quantify how non-radiative recombination and diffusion affect the confocal time-resolved PL results, we used a set of coupled partial differential equations to model and simulate the evolution of the carrier population. Briefly, we use a two-dimensional model taking into account both diffusion and trapping as described in equations S1 and S2:

$$\frac{\partial N_c(x,y,t)}{\partial t} = D\nabla^2 N_c(x,y,t) - k_{DT}N_{DT}(\mathrm{x,y,t})N_C(\mathrm{x,y,t}) - k_m N_c(x,y,t) - k_b N_c(x,y,t)^2 \quad \text{(S1)}$$

$$\frac{\partial N_{DT}(x,y,t)}{\partial t} = -k_{DT}N_{DT}(\mathrm{x,y,t})N_C(\mathrm{x,y,t}) \quad \text{(S2)}$$

Where N_c(x,y,t) is the carrier density as a function of space (x,y) and time (t), D is the ambipolar diffusion coefficient, ∇^2 is the Laplacian operator, k_{DT} is the deep trap non-radiative recombination rate constant, N_{DT}(x,y,t) is the density of available deep traps, k_m is the radiative monomolecular recombination rate constant, and k_b is the bimolecular rate constant. We ignored contribution from many body interactions (i.e. Auger) as these processes are negligible at the excitation powers used in our experiments.[10] For our simulations, D = 0.17 cm^2s^{-1}, k_m = 1x10^6 s^{-1}, and k_b = 8x10^{-11} cm^{-3},[5,10,11] and trapping parameters are N_{DT} = 4x10^{16} cm^{-3}, k_{DT} = 1x10^8 s^{-1}.[9,12]

In comparison to the timescale of diffusion, the pulsed carrier generation is assumed to be instantaneous and therefore we define the initial condition as (S3):

$$N_c(x,y,0) = \frac{N_0}{2\pi\sigma^2}\exp\left(-\frac{(x^2+y^2)}{2\sigma^2}\right) \quad \text{(S3)}$$

where N_0 is the initial carrier density, and σ is the measured width (212 nm) of the Gaussian excitation beam. Initial carrier concentrations were calculated based on the measured laser fluences and focal spot size and used as fixed input parameters. For the simulation, we assume that the laser excitation profile is symmetric (x = y), and we also center the excitation source at the origin (x=0, y=0). The prefactor in front of the exponent is a weighting factor that sets the integrated carrier density equal to the initial carrier density (N_0).

For simulating the time-resolved PL kinetics we assume no flux boundary conditions (S4) for simplicity,[11,13] where we verified this assumption by performing a local excitation/widefield detection experiment showing that the intergrain connectivity was weak. We also note that this assumption has negligible impact on the carrier population within the confocal pinhole for the simulated grain area of 2 μm.

$$\left.\frac{\partial N_c(x,y,t)}{\partial x}_{\gamma}\right| = \left.\frac{\partial N_c(x,y,t)}{\partial y}_{\gamma}\right| = 0 \quad \text{(S4)}$$

where γ denotes the spatial coordinates of the grain boundaries.

The solutions to these equations are evaluated using a time-domain, finite-element analysis in Matlab. The PL is then the sum of the radiative recombination constants multiplied by the time-dependent carrier population integrated under the confocal area (set to the width, σ, of the excitation spot as described in S5).

$$PL(t) = \iint (k_m N_c(x,y,t) + k_b N_c(x,y,t)^2)\, dxdy \quad \text{(S5)}$$

Figure S12 shows the PL intensity as a function of time under the confocal pinhole when we do not include a trap-filling term (N_{DT} = 0, diffusion-dominated simulation) for an initial carrier density of $3x10^{16}$ cm^{-3} (black trace), which is the same as Figure 5a in the main article. Again, the initial order-of-magnitude drop in PL intensity within the first ~25 ns can be attributed to fast diffusion outside of the confocal pinhole and is consistent with simulations previously reported by Tian *et al*.[13] When we increased the initial carrier density to $8x10^{16}$ cm^{-3} (red trace), we found that the fast drop in intensity was relatively unaffected. In the main article, we reported the time-resolved PL kinetics for the dark region outline in the white box and found that the trends could only be described if we included a trap filling term. Figure S12c shows the experimentally measured time-resolved PL kinetics for a grain approximately 1.5 μm in diameter, exhibiting a moderate emission intensity, and under the red square. In contrast to the dark region outlined by white, we observed the fast initial drop stay relatively unaffected and the overall kinetics become slightly faster due to an increase in carrier population. This result is qualitatively similar to the diffusion-dominated simulation and therefore we conclude that this region is dominated by diffusion in the confocal experiment.

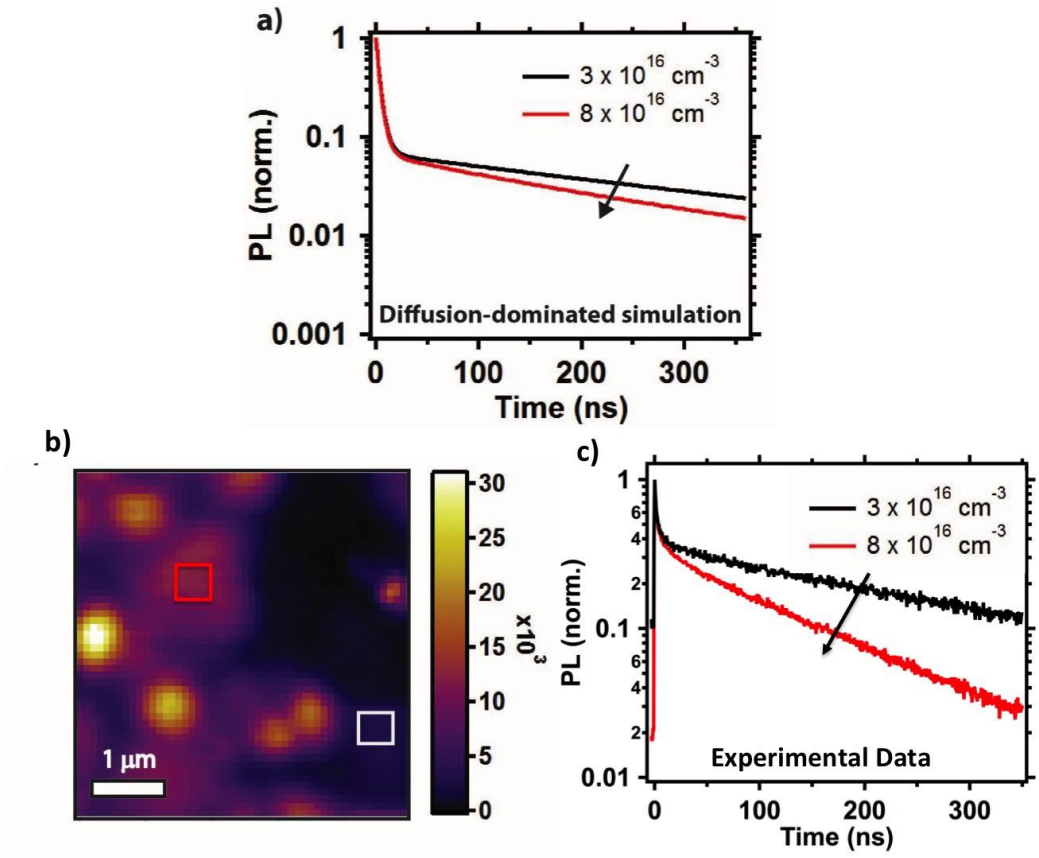

Figure S12. Simulated TRPL integrated under the confocal pinhole at low ($3x10^{16}$ cm^{-3}, black) and high ($8x10^{16}$ cm^{-3}, red) initial carrier densities with a) no trap-filling (N_{DT} = 0) term, b) fluorescence image of a $CH_3NH_3PbI_3(Cl)$ film on glass, and d) experimental data showing intensity-dependent time-resolved PL kinetics of the region designated by a red box in (b), showing the trend is qualitatively similar to the diffusion-dominated simulation. In the simulation, D = 0.17 cm^2s^{-1}, $k_m = 1x10^6$ s^{-1}, and $k_b = 8x10^{-11}$ cm^{-3}.

Supplementary References

1. Vrućinić, M.; Matthiesen, C.; Sadhanala, A.; Divitini, G.; Cacovich, S.; Dutton, S. E.; Ducati, C.; Atatüre, M.; Snaith, H.; Friend, R. H. *et al.* Local versus long-range diffusion effects of photoexcited states on radiative recombination in organic-inorganic lead halide perovskites. *Adv. Sci.* **2015**, 2, 1500136.

2. Draguta, S.; Thakur, S.; Morozov, Y. V.; Wang, Y.; Manser, J. S.; Kamat, P. V.; Kuno, M. Spatially non-uniform trap state densities in solution-processed hybrid perovskite thin films. *J. Phys. Chem. Lett.* **2016**, 7, 715-721.

3. Simpson, M. J.; Doughty, B.; Das, S.; Xiao, K.; Ma, Y. Z. Separating bulk and surface contributions to electronic excited-state processes in hybrid mixed perovskite thin films via multimodal all-optical imaging. *J Phys Chem Lett* **2017**, 8, 3299-3305.

4. Yang, M.; Zeng, Y.; Li, Z.; Kim, D. H.; Jiang, C. S.; van de Lagemaat, J.; Zhu, K. Do grain boundaries dominate non-radiative recombination in ch3nh3pbi3 perovskite thin films? *Phys. Chem. Chem. Phys.* **2017**, 19, 5043-5050.

5. Johnston, M. B.; Herz, L. M. Hybrid perovskites for photovoltaics: Charge-carrier recombination, diffusion, and radiative efficiencies. *Acc. Chem. Res.* **2016**, 49, 146-154.

6. Richter, J. M.; Abdi-Jalebi, M.; Sadhanala, A.; Tabachnyk, M.; Rivett, J. P.; Pazos-Outon, L. M.; Godel, K. C.; Price, M.; Deschler, F.; Friend, R. H. Enhancing photoluminescence yields in lead halide perovskites by photon recycling and light out-coupling. *Nat Commun* **2016**, 7, 13941.

7. deQuilettes, D. W.; Koch, S.; Burke, S.; Paranji, R. K.; Shropshire, A. J.; Ziffer, M. E.; Ginger, D. S. Photoluminescence lifetimes exceeding 8 μs and quantum yields exceeding 30% in hybrid perovskite thin films by ligand passivation. *ACS Energy Letters* **2016**, 438-444.

8. deQuilettes, D. W.; Zhang, W.; Burlakov, V. M.; Graham, D. J.; Leijtens, T.; Osherov, A.; Bulovic, V.; Snaith, H. J.; Ginger, D. S.; Stranks, S. D. Photo-induced halide redistribution in organic-inorganic perovskite films. *Nat. Commun.* **2016**, 7, 11683.

9. deQuilettes, D. W.; Vorpahl, S. M.; Stranks, S. D.; Nagaoka, H.; Eperon, G. E.; Ziffer, M. E.; Snaith, H. J.; Ginger, D. S. Impact of microstructure on local carrier lifetime in perovskite solar cells. *Science* **2015**, 348, 683-686.

10. Herz, L. M. Charge-carrier dynamics in organic-inorganic metal halide perovskites. *Annu Rev Phys Chem* **2016**, 67, 65-89.

11. Beard, M. C. Top and bottom surfaces limit carrier lifetime in lead iodide perovskite films. **2017**.

12. Stranks, S. D.; Burlakov, V. M.; Leijtens, T.; Ball, J. M.; Goriely, A.; Snaith, H. J. Recombination kinetics in organic-inorganic perovskites: Excitons, free charge, and subgap states. *Phys. Rev. Appl.* **2014**, 2, 034007.

13. Tian, W.; Cui, R.; Leng, J.; Liu, J.; Li, Y.; Zhao, C.; Zhang, J.; Deng, W.; Lian, T.; Jin, S. Limiting perovskite solar cell performance by heterogeneous carrier extraction. *Angew Chem Int Ed Engl* **2016**, 55, 13067-13071.

Appendix C: Supporting Information for Chapter 4

Methods

Sample Fabrication

Perovskites were prepared using a method described elsewhere where a methylammonium iodide (CH_3NH_3I) and lead acetate $Pb(Ac)_2{\cdot}3H_2O$ precursor mixture was employed[29]. To generate the perovskite solution, CH_3NH_3I (Dyesol) and $Pb(Ac)_2{\cdot}3H_2O$ were dissolved in anhydrous *N*,*N*-dimethylformamide at a 3:1 molar ratio with final concentration of ~30 wt%, and the stabilizer hypophosphorous acid (HPA) was added at a molar ratio of 7.5% with respect to $Pb(Ac)_2{\cdot}3H_2O$. $Pb(Ac)_2{\cdot}3H_2O$ (316512) and HPA (214906) were purchased from Sigma Aldrich. Microscope slides and coverslips were washed sequentially with soap (2% vol. Hellmanex in water), de-ionized water, isopropanol, acetone and finally treated under oxygen plasma for 10 minutes. The precursor solution was spin-coated at 2000 rpm for 45 seconds in a nitrogen-filled glovebox, and the substrates were then dried at room temperature for 10 minutes before annealing at 100°C for 5 minutes. The samples were then stored in a nitrogen-filled glovebox until used.

Photoluminescence Measurements

Bulk time-resolved PL (TRPL) decays were acquired using a time-correlated single photon counting (TCSPC) setup (FluoTime 300, PicoQuant GmbH). Temperature-dependent measurements were carried out *in vacuo* using an Oxford Instruments OptistatDN cryostat with a specialized fitting for the TCSPC setup. Samples were photoexcited using a 507 nm laser head (LDH-P-C-510, PicoQuant GmbH) with pulse duration of 117 ps, fluences of ~0.03–3 μJ cm^{-2} per pulse, and a repetition rate of 1 MHz. To acquire PL decays over time under illumination, integration times were kept short (2-10 seconds). The stated times in the legends are time stamps at the end of each integration window for each curve.

Confocal Fluorescence Imaging

Optical microscopy and spectroscopy were performed under nitrogen (flow cell) using a custom sample scanning confocal microscope built around a Nikon TE-2000 inverted microscope fitted with an infinity corrected 50x dry objective (Nikon L Plan, NA 0.7, CC 0-1.2). A 470 nm pulsed diode laser (PDL-800 LDH-P-C-470B, 350 ps pulse width) was used for excitation with a repetition rate of 1 MHz for time-resolved PL measurements and 40 MHz for collecting fluorescence images. A 532 nm CW laser (CrystaLaser, GCL532-005-L) was used to excite local regions and monitor the PL rises over time. Samples were excited face-on through the flow cell's coverslip and the emission was filtered through a 700 nm longpass filter then directed to a Micro Photon Devices (MPD) PDM Series single photon avalanche photodiode with a 50 μm active area. The sample stage was controlled using a piezo controller (Physik Instrumente E-710) with custom software. For collecting fluorescence images, the pixel size was 100 nm with a short pixel dwell time (integration time) of 50 ms, in order to minimize the extent of photoinduced cleaning prior to collecting longer exposure local measurements. For wide area light

soaking experiments, the entire film was exposed to AM 1.5 G light illumination from a solar simulator (Solar Light Co. model 16S-300) with intensity calibrated to 100 mW cm^{-2} using a Si reference cell and source meter (Keithley, 2400 Series). Before collecting fluorescence images, the system was calibrated using 200 nm fluorescent microspheres (Lifetechnologies FluoSpheres® Polystyrene Microspheres, 200 nm, red fluorescent, 580/605) to yield a point-spread function of ~350 nm at FWHM. To correlate fluorescence images with SEM micrographs and ToF-SIMS, we made fiducial markers on the sample and used these markers along with local microstructure to match areas across the separate measurements.

Scanning Electron Microscopy (SEM)

SEM images were taken using a FEI Sirion SEM at 5-10 kV accelerating voltage. To prevent charging effects, samples for SEM were imaged after sputtering approximately 7 nm of Au/Pd using a SPI-Module Sputter Coater with argon flow.

Time of Flight Secondary Ion Mass Spectrometry (ToF-SIMS)

ToF-SIMS depth profiles were carried out using an IonToF ToF-SIMS 5 instrument. Dual beam depth profiles were acquired using a 25 keV Bi_3^+ ion source in delayed extraction mode for images and a 20 keV argon 1000 gas cluster ion source for sputtering. Sputtering was carried out over a 600 micron x 600 micron area at 3.3 nA current for 2 seconds for a dose of $1.1x10^{13}$ ions cm^{-2} per sputter cycle. Images were acquired over a 50 micron x 50 micron area within the center of the sputter crater with a current of ~0.03 pA for a dose per cycle of $5.7x10^{11}$ ions cm^{-2}. Secondary ions were detected using a time-of-flight mass analyzer. Due to non-linearity in the mass axis introduced when using delayed extraction[50], peak identities were determined from spectra acquired using the standard spectroscopy mode of the IonToF instrument using similar settings as described above. The negative ion spectra were calibrated using the CH^-, OH^- and I^- peaks. Calibration errors were kept below 30 ppm. Mass resolution ($m/\Delta m$) for a typical spectrum was between 4000 and 6000 for m/z 25.

Open-Circuit Voltage Rises.

Solar cells were fabricated on FTO-coated glass (Pilkington, 7 Ω sq^{-1}). Initially, FTO was removed from regions under the anode contact by etching the FTO with 2 M HCl and zinc powder. Substrates were then cleaned as for the microscope slides. A hole-blocking layer of compact TiO_2 was deposited by spin-coating a mildly acidic solution of titanium isopropoxide in ethanol, and annealed at 500°C for 30 min. The perovskite precursor solution was spin-coated and the substrates annealed as for the microscope slides. After cooling, the spiro-OMeTAD hole-transporting layer was then deposited from a 66-mM chlorobenzene solution containing additives of lithium bis(trifluoromethanesulfonyl)imide and 4-tert-butylpyridine. Finally, 120-nm-gold electrodes were thermally evaporated under vacuum of $\sim10^{-6}$ Torr, at a rate of ~0.1 nm s^{-1}, to complete the devices.

For the transient open-circuit voltage rises, the devices were illuminated with a continuous-wave laser source at a wavelength of 532 nm and an intensity of 60 mW cm^{-2}, giving an approximately equivalent photoexcitation density to the 100 mWcm^{-2} AM 1.5

spectrum. The data were acquired using a sourcemeter (Keithley 2400, USA) coupled to a customized Labview program.

Preparation of Single Crystal $CH_3NH_3PbI_3$

Lead iodide (98%) and anhydrous γ-butyrolactone (> 99%) were purchased from Sigma Aldrich and used without further purification. Methylammonium iodide (MAI) was synthesized by reacting methylamine (33 wt% in EtOH, Sigma) with equimolar hydriodic acid (57 wt%, Sigma) in an ice bath. The reaction mixture was stirred for 60 minutes and the liquid was removed with a rotary evaporator. The crude MAI solid was redissolved with EtOH (> 99.5%, Sigma), then precipitated and washed with diethyl ether (> 99%, Sigma). The MAI was dried and transferred to a nitrogen atmosphere. Our procedure for single crystal growth was based off of the inverse temperature crystallization (ITC) method of Saidaminov et al[6]. A 1.2 M solution of both PbI_2 and MAI (1:1 molar ratio) was prepared in anhydrous γ-butyrolactone. The solution, exposed to ambient conditions, was preheated to 60 °C. Approximately 2 mL of this solution was filtered using a 0.2 μm PTFE filter. The filtrate was added to a 4 mL vial which was sealed shut before submerging in an oil bath heated to 80 °C. Over the course of two days, the temperature of the oil bath was gradually increased to 110 °C. After the two days, a ~1 cm^3 $CH_3NH_3PbI_3$ single crystal was removed from the growth solution and washed with two 2 mL aliquots of acetophenone. The crystal was then dried and transferred into a N_2 filled glovebox. The crystal was cleaved in the glovebox using a razor blade and the PL was measured under nitrogen flow.

Preparation of $CH_3NH_3PbI_3$ ($PbCl_2$ precursor)

Thin films of $CH_3NH_3PbI_{3-x}Cl_x$ ($PbCl_2$ method) were formed by first preparing a 40% weight precursor solution consisting of 2.64 M MAI (Lumtec) and 0.88 M $PbCl_2$ (Sigma-Aldrich 99.99% purity) dissolved in DMF[4,5]. The solutions were spin-coated onto oxygen-plasma-etched glass at 2500 rpm for 60 s in a nitrogen filled glovebox and the substrates subsequently dried at room temperature for 20 mins and then annealed at 90°C for 2 hours.

Preparation of $CH_3NH_3PbI_3$ (Dripping Method)

Thin films of $CH_3NH_3PbI_3$ were also prepared using the solvent engineering ('dripping') method described in detail elsewhere[33,34]. In brief, MAI was synthesized and purified as described above. Equimolar (0.75 M) solutions of MAI and PbI_2 (Alfa Aesar, 99.9985% purity) were prepared in DMF and spin-coated onto oxygen-plasma-etched glass at 5000 rpm for 35 s. After 6 s, 150 μL chlorobenzene was deposited on the spinning sample in order to induce rapid crystallization. After spinning, the samples were immediately heated at 100 °C for 10 minutes.

X-Ray Diffraction (XRD) Measurements.

X-ray diffraction (XRD) patterns of the films deposited on boron-doped Si substrates were collected using a Bruker D8 diffractometer equipped with a Cu Kα radiation source and operated at 40 mV and 40 mA. The patterns were collected while illuminating in-situ with a 532-nm CW laser. Further details, including photon doses, are included in the figure caption (Supplementary Fig. 3).

Energy-Dispersive X-ray Spectroscopy (EDS).

EDS compositional data was taken on a FEI Sirion SEM using a 10 kV accelerating voltage on samples with approximately 7 nm of Au/Pd sputtered using a SPI-Module Sputter Coater with argon flow. The data was analyzed using AZtecEnergy EDS software package (Ver. 2.1). The EDS compositional dynamics were monitored using a video recording device; wt% values were updated by the AZtec software every 500 ms.

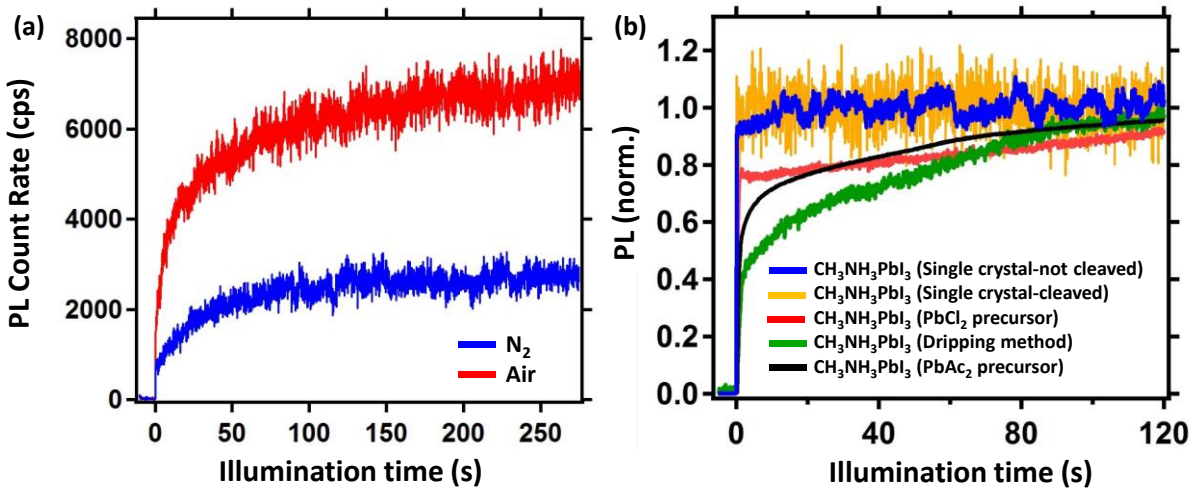

Supplementary Figure 1. **Photoluminescence (PL) rise behaviour in different atmospheres and for different processing conditions. (**a) PL rises over time under illumination (532 nm CW, 60 mW cm^{-2}) of a sample first measured in air and then in nitrogen, demonstrating that the atmosphere can affect the magnitude of PL enhancement but the rise is present in both conditions[1-3]. (b) PL rises over time under illumination of several perovskite samples prepared with various processing techniques and measured in nitrogen, showing that the rises are generally observed in polycrystalline films, but not in single crystals. The films[4,5] and single crystals[6] were processed as described in the Supplementary Methods. The HPA/acetate[7] films were used throughout the remainder of the work. The polycrystalline films and single crystals were excited with a 532 nm CW laser with intensities of 160 mW cm^{-2} and 300 mW cm^{-2}, respectively.

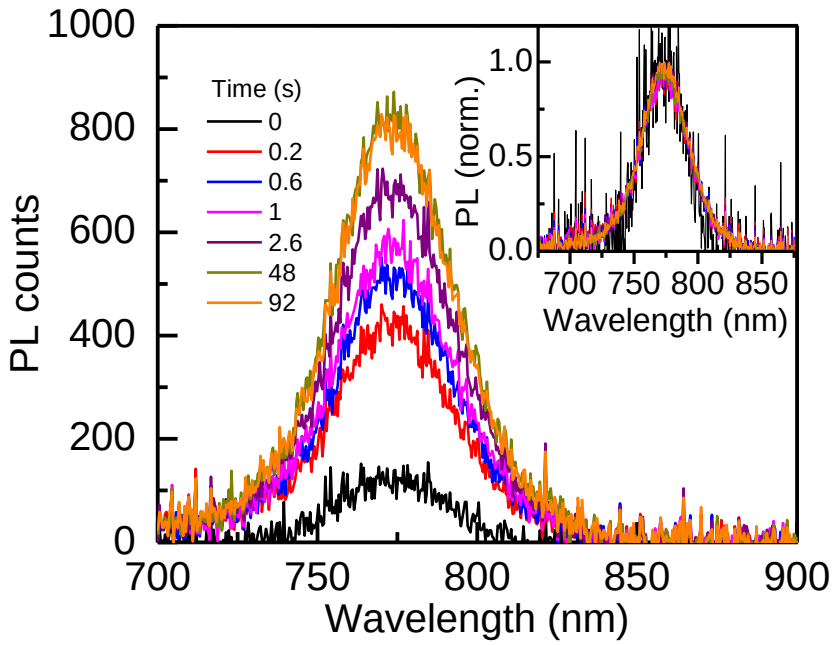

Supplementary Figure 2. Monitoring photoluminescence (PL) spectra in time. PL spectra from a $CH_3NH_3PbI_3$ film over time under illumination with a continuous wave (CW) laser at a wavelength of 532 nm, with an intensity of ~60 mW cm^{-2}, producing photo-excitation densities comparable to 1-sun AM 1.5 illumination. The emission was collected using a fiber-coupled Ocean Optics Mayapro spectrometer with integration times of 200 ms. The inset shows the normalized spectra, indicating that the PL spectral shape and position do not significantly change over time.

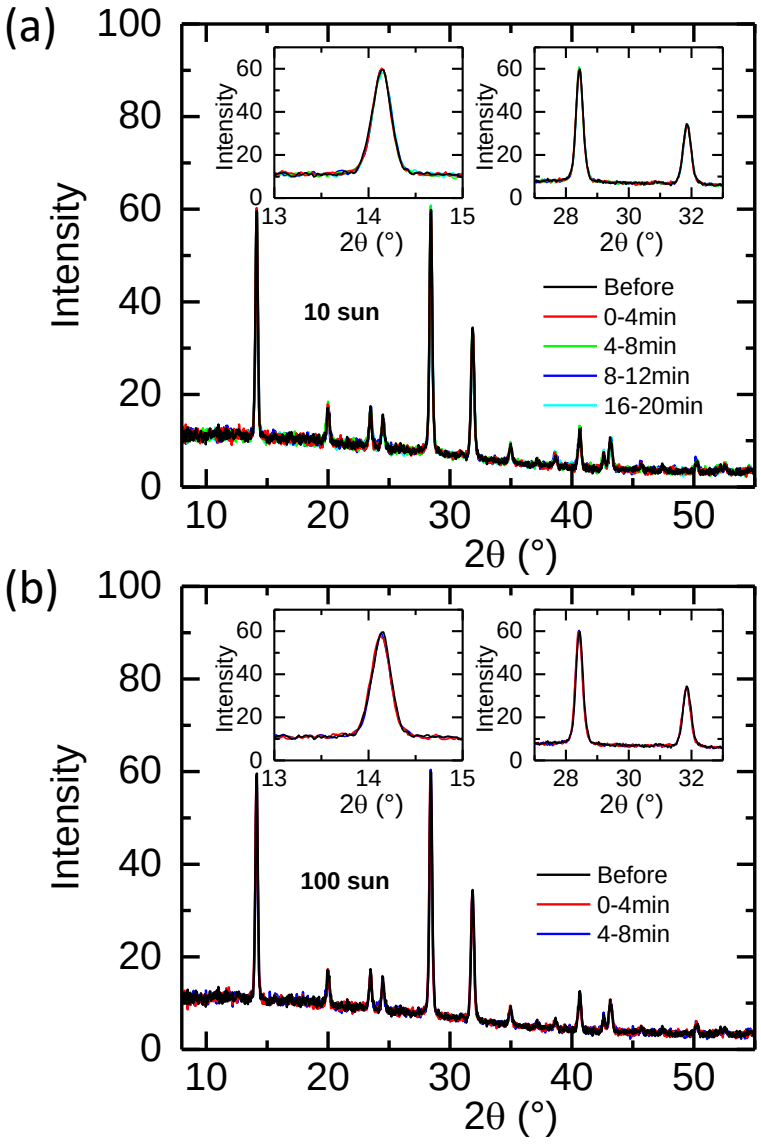

Supplementary Figure 3. Monitoring structural changes of films under illumination. X-Ray Diffraction (XRD) patterns of a $CH_3NH_3PbI_3$ film acquired (4 minute integration time) before illumination and during various windows while under constant illumination with a laser at a wavelength of 532 nm, with an intensity of (a) ~600 mW cm^{-2} (~10 sun equivalent, total photon dose of ~0.7 kJ cm^{-2}) and (b) ~6000 mW cm^{-2} (~100 sun equivalent, total photon dose of ~3 kJ cm^{-2}). No significant changes were observed.

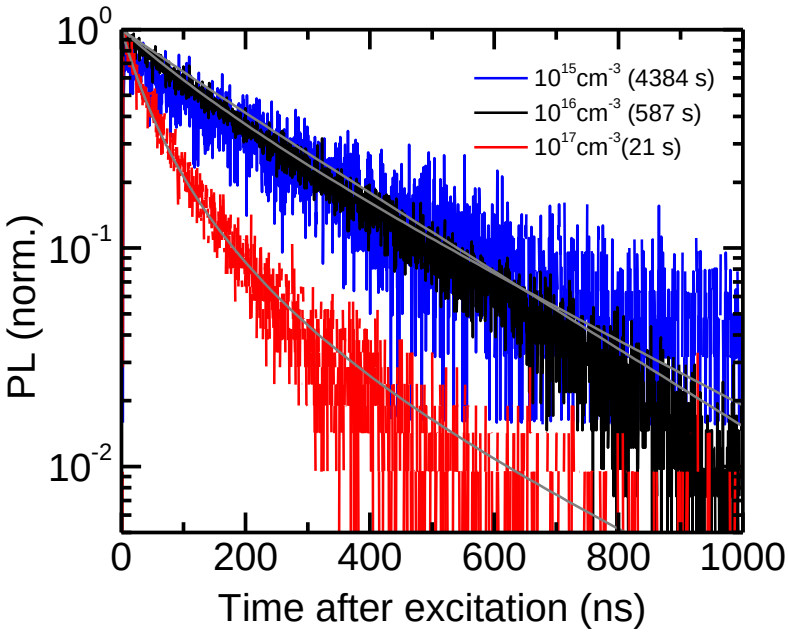

Supplementary Figure 4. **Intensity dependent bulk time-resolved photoluminescence (PL).** Stabilized PL decays detected at 780 nm from the $CH_3NH_3PbI_3$ sample following pulsed excitation (507 nm, 1 MHz repetition rate) with different initial photoexcitation densities $N(0)$. The bracketed numbers indicate the times (in seconds) taken to reach stabilized emission. Solid gray lines are fits from the model.

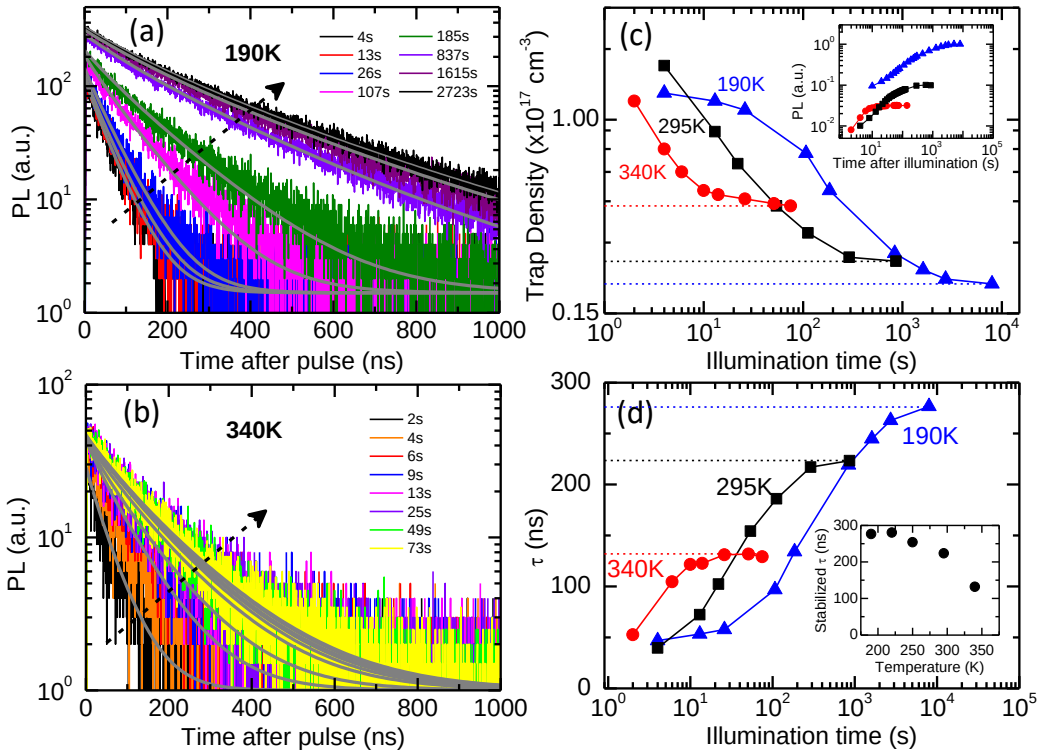

Supplementary Figure 5. **Temperature-dependent PL changes.** A selection of time-resolved PL decays from a thin $CH_3NH_3PbI_3$ film measured over time under illumination at low temperature (190 K) (a) and high temperature (340 K) (b). The stated times in the legend are time stamps at the end of the integration window for each curve. The sample was photoexcited with pulsed excitation (507 nm, 1 MHz repetition rate, 117 ps pulse length and 0.3 μJ cm^{-2} per pulse, which creates a photo-excited species density of ~10^{16} cm^{-3}) and the emission was detected at 780 nm. The gray lines represent fits to the data from the model described in the text. (c) Trap densities extracted from the fits to the data in (a), (b) and Figure 1a (main text). The dashed lines represent the stabilized trap densities. *Inset*: The unnormalized integrated PL over time under initial illumination determined from integrating acquired PL decays at each temperature. (d) Monomolecular lifetimes τ extracted from mono-exponential fits to the PL data over time under illumination at each temperature. *Inset*: The stabilized lifetimes as a function of temperature.

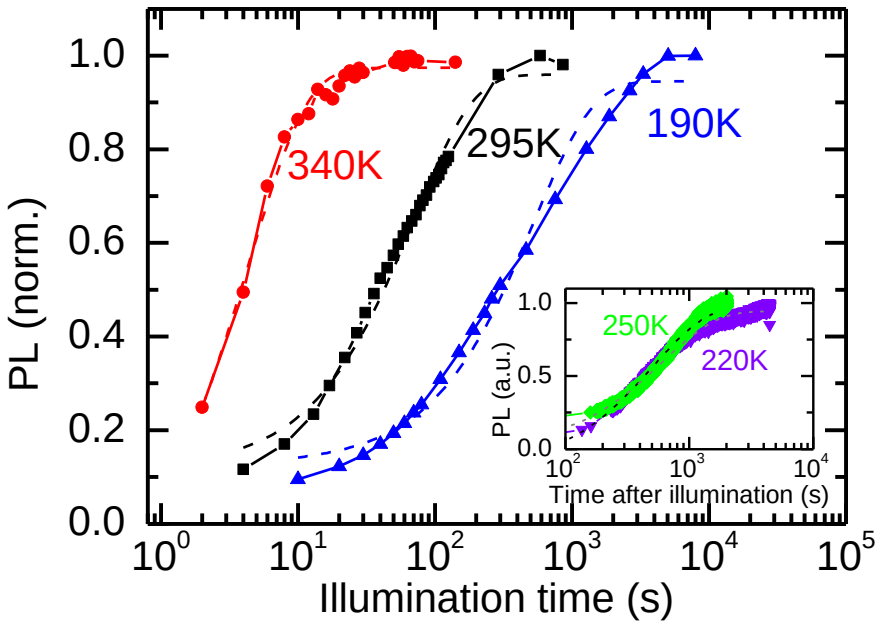

Supplementary Figure 6. Temperature-dependent PL rises. The normalized integrated PL over time under initial illumination determined from integrating acquired PL decays at each temperature, where the time corresponds to the end of the integration window. *Inset*: The integrated PL data over time at 250 K and 220 K. The dashed lines are single exponential fits to the rises to extract approximate time constants τ for the Arrhenius fits in Figure 1c inset (main text).

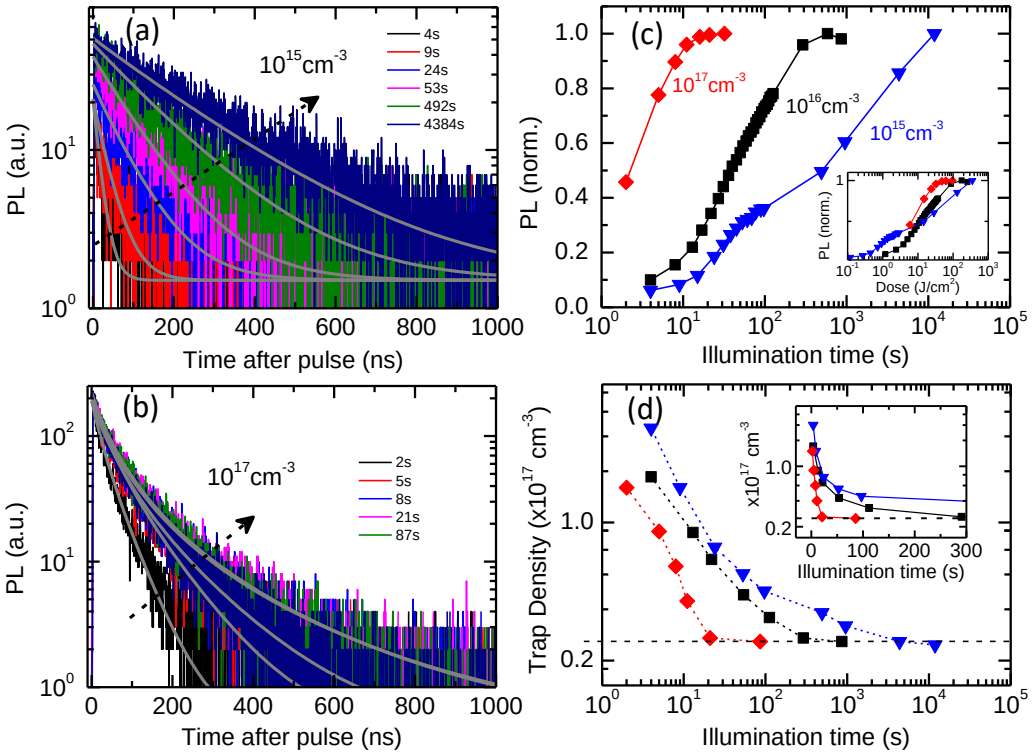

Supplementary Figure 7. **Intensity-dependent PL changes under illumination**. A selection of time-resolved PL decays from a thin $CH_3NH_3PbI_3$ film measured over time under illumination at (a) low excitation fluence (0.03 μJ cm^{-2} per pulse, N_0 ~10^{15}cm^{-3}) and (b) high excitation fluence (3 μJ cm^{-2} per pulse, N_0 ~10^{17}cm^{-3}). The samples were excited at 507 nm, 1 MHz repetition rate, 117 ps pulse length at room temperature, and the PL detected at 780 nm. The stated times in the legend are time stamps at the end of the integration window for each curve. The gray lines represent fits to the data from the model described in Supplementary Note 3. (c) The normalized integrated PL over time under initial illumination determined from integrating acquired PL decays at each fluence. Inset: The same data plotted with total light-soaking dose as the x-axis. (d) Trap densities extracted from the fits to the data in (a), (b) and Figure 1a (main text). The dashed lines represent the stabilized trap densities, as represented by the trap densities extracted from the fits in Supplementary Fig. 4. *Inset*: The same data but on a linear time scale over the first 300s.

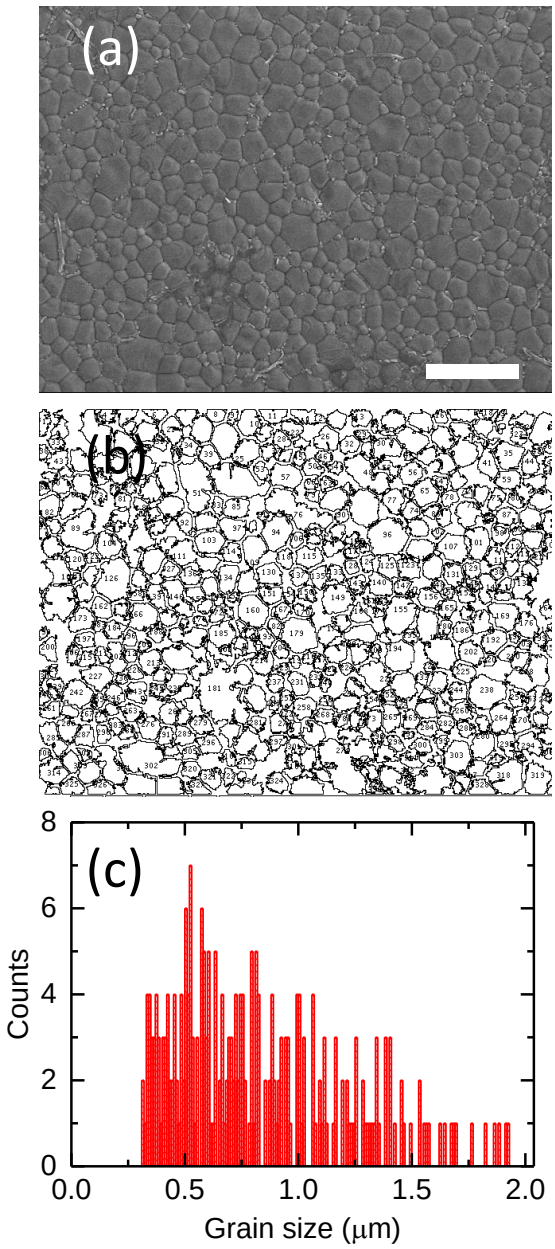

Supplementary Figure 8. Grain size analysis via scanning electron microscopy (SEM) (a) SEM image of the perovskite films, scale bar is 5 μm. (b) Processed SEM image using ImageJ software employing a built-in Gaussian Blue filter, Enhance Contrast and Find Edges operations with grains smaller than 100 nm filtered out to avoid incorrect assignments of grains. (c) Histogram of grain sizes from (b) calculated from the measured grain surface areas.

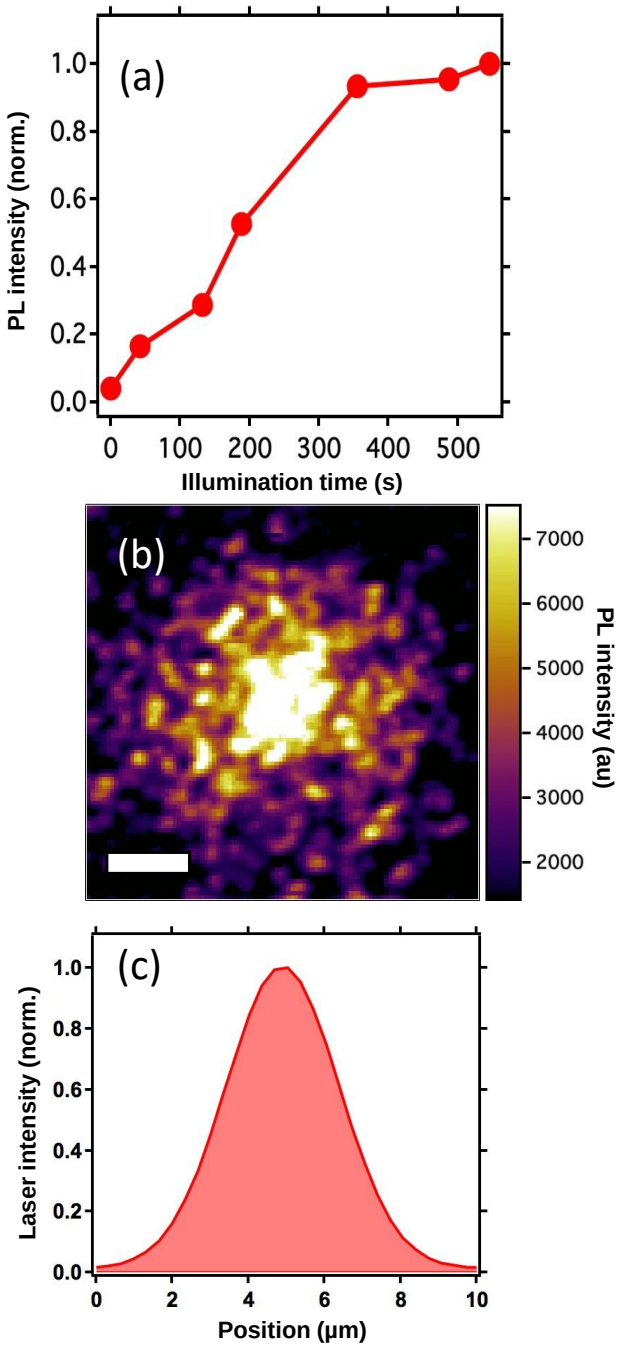

Supplementary Figure 9. PL enhancement compared to laser profile (a) PL rise over time under illumination (470 nm, 40 MHz repetition rate, 0.1 µJ cm^{-2} per pulse). (b) PL map of a wider area showing that the brightening closely follows the laser excitation spatial profile in (c), scale bar is 2 µm.

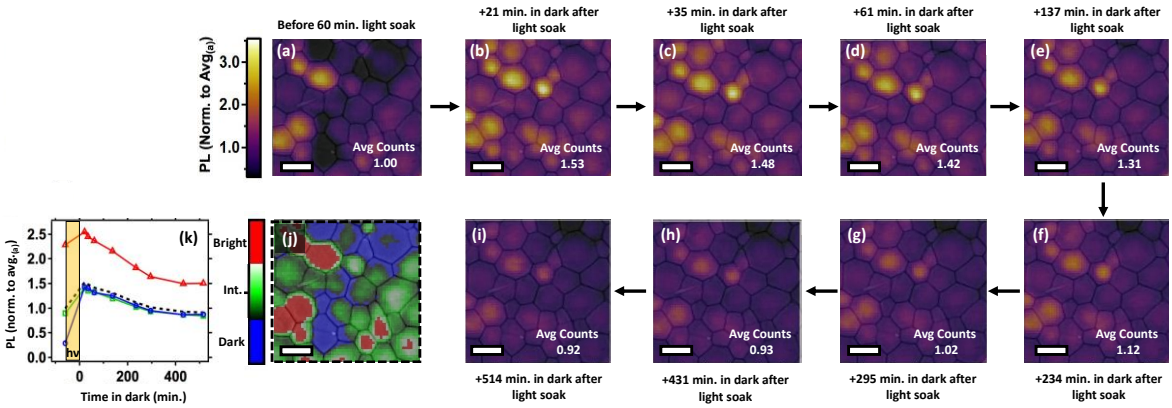

Supplementary Figure 10. Local grain emission relaxation. Fluorescence images under pulsed excitation (470 nm, 40 MHz repetition rate, 350 ps pulse length and 0.03 µJ cm^{-2} per pulse) in nitrogen with semitransparent SEM images overlaid (a) before light soaking, and after exposing the entire film to simulated sunlight (AM 1.5, 100 mW cm^{-2}) for 60 minutes and leaving in the dark for (b) 21, (c) 35, (d) 61, (e) 137, (f) 234, (g) 295, (h) 431, and (i) 514 minutes, scale bar is 1 µm. (j) Three-colour scale image showing the regions classified as dark (blue < -σ from avg. in (a)), intermediate (-σ from avg. ≤ green ≤ +σ from avg.) and bright (red > +σ from avg.). (k) Local PL enhancements for a dark (blue), intermediate (green), and bright regions as indicated in (j), where the time under illumination is highlighted by the yellow shaded region for $t < 0$, and the times $t \geq 21$ show the local PL relaxation dynamics over time left in the dark. The dotted black line is the PL relaxation averaged across the whole fluorescence image.

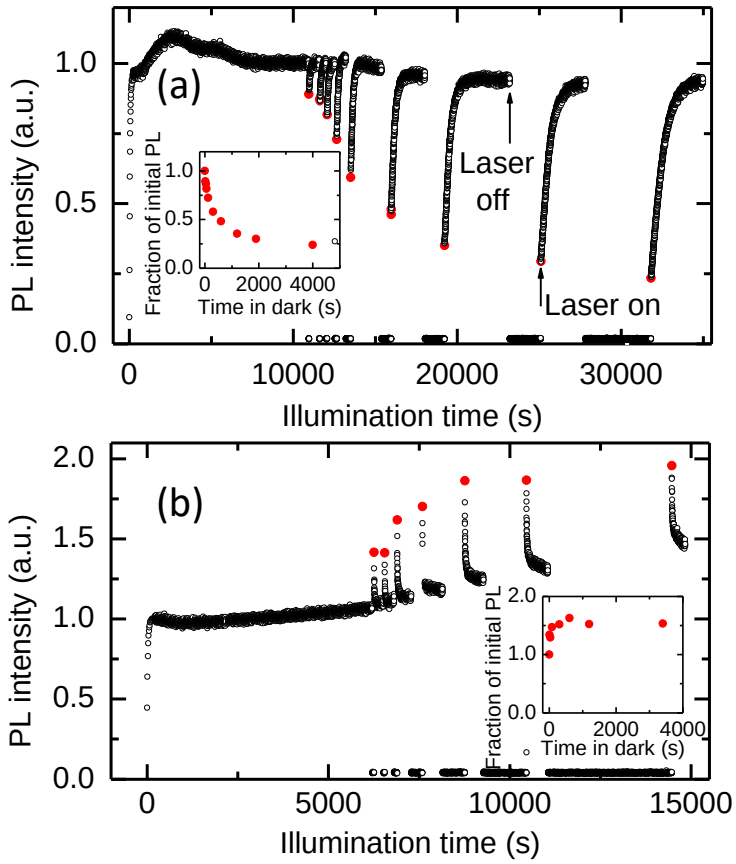

Supplementary Figure 11. Bulk film relaxation in the dark. PL intensity after leaving films in the dark (no illumination) for varying times. In each case, the PL is first allowed to reach a stabilized emission under illumination, then the laser switched off for a fixed length of time and then switched back on, with the PL continually monitored. The red closed circles represent the value of the PL intensity immediately after switching on the laser. The inset shows the PL intensity, relative to the stabilized emission before switching the laser off, for different times in the dark. (a) and (b) are two different scenarios observed in identical (duplicate) films measured under identical conditions. The samples were photoexcited with pulsed excitation (w ~ 17 μm, 507 nm, 1 MHz repetition rate, 117 ps pulse length and 0.3 μJ cm^{-2} per pulse, which creates a photo-excited species density of ~$10^{16}cm^{-3}$) and the emission at 780 nm is time-integrated.

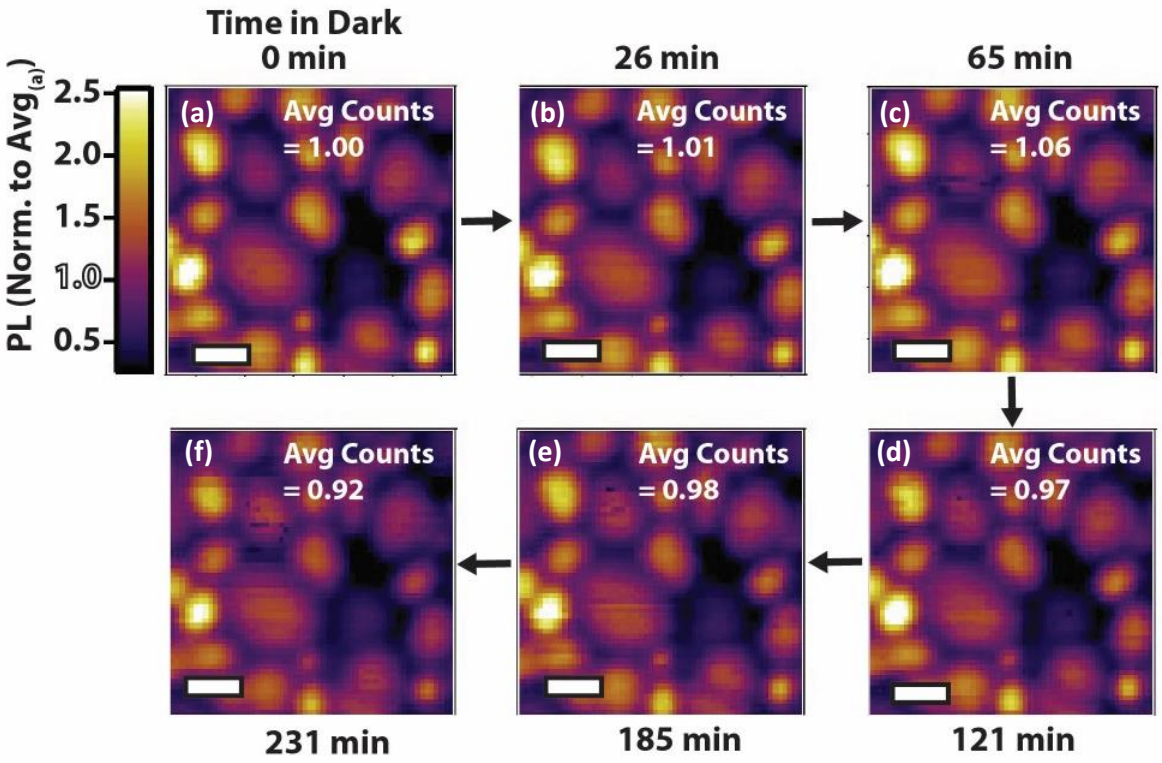

Supplementary Figure 12. Local grain emission and relaxation without light soaking. Fluorescence images under pulsed excitation (470 nm, 40 MHz repetition rate, 350 ps pulse length and 0.03 μJ cm^{-2} per pulse) in nitrogen taken at (a) 0 (b) 26, (c) 65, (d) 121, (e) 185, and (f) 231 minutes showing that a long light soak is required to redistribute the emission intensities, scale bar is 1 μm.

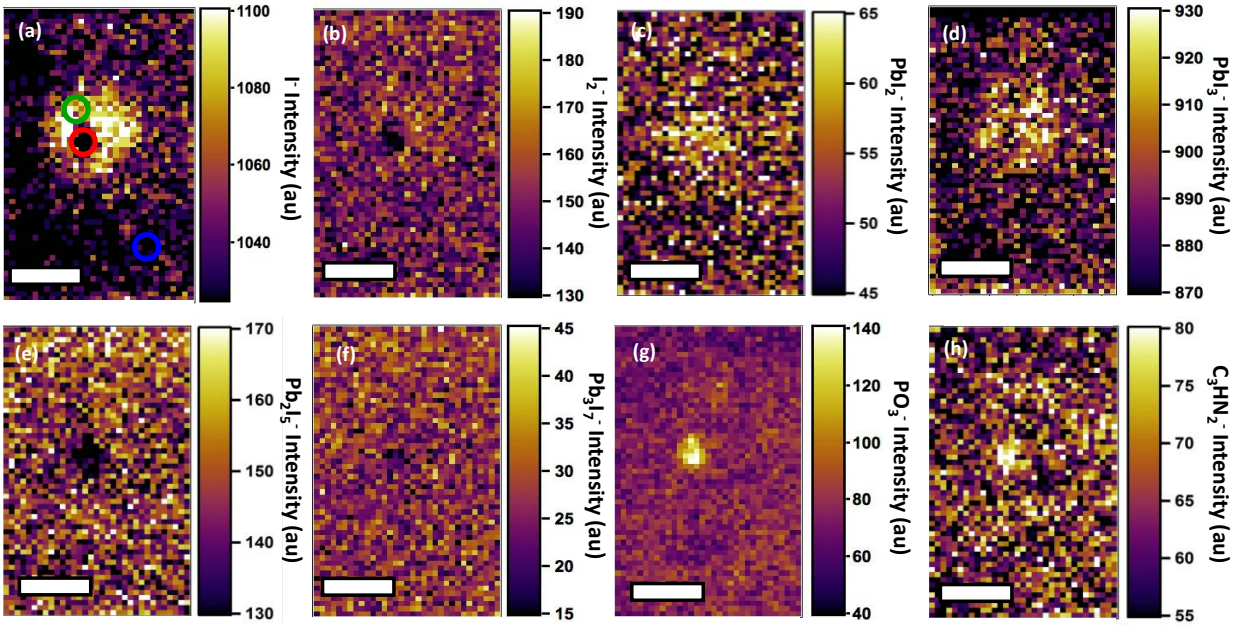

Supplementary Figure 13. **ToF-SIMS intensity images**. (a) ToF-SIMS image of the I^-, (b) I_2^-, (c) PbI_2^-, (d) PbI_3^-, (e) $Pb_2I_5^-$, (f) $Pb_3I_7^-$, (g) PO_3^{3-}, and (h) $C_3HN_2^-$ fragments and their distribution summed through several layers of the entire film, scale bar is 10 µm. The red spot shows where the sample has been light soaked, the green spot an immediately adjacent spot, and the blue spot represents a background region that has not been illuminated.

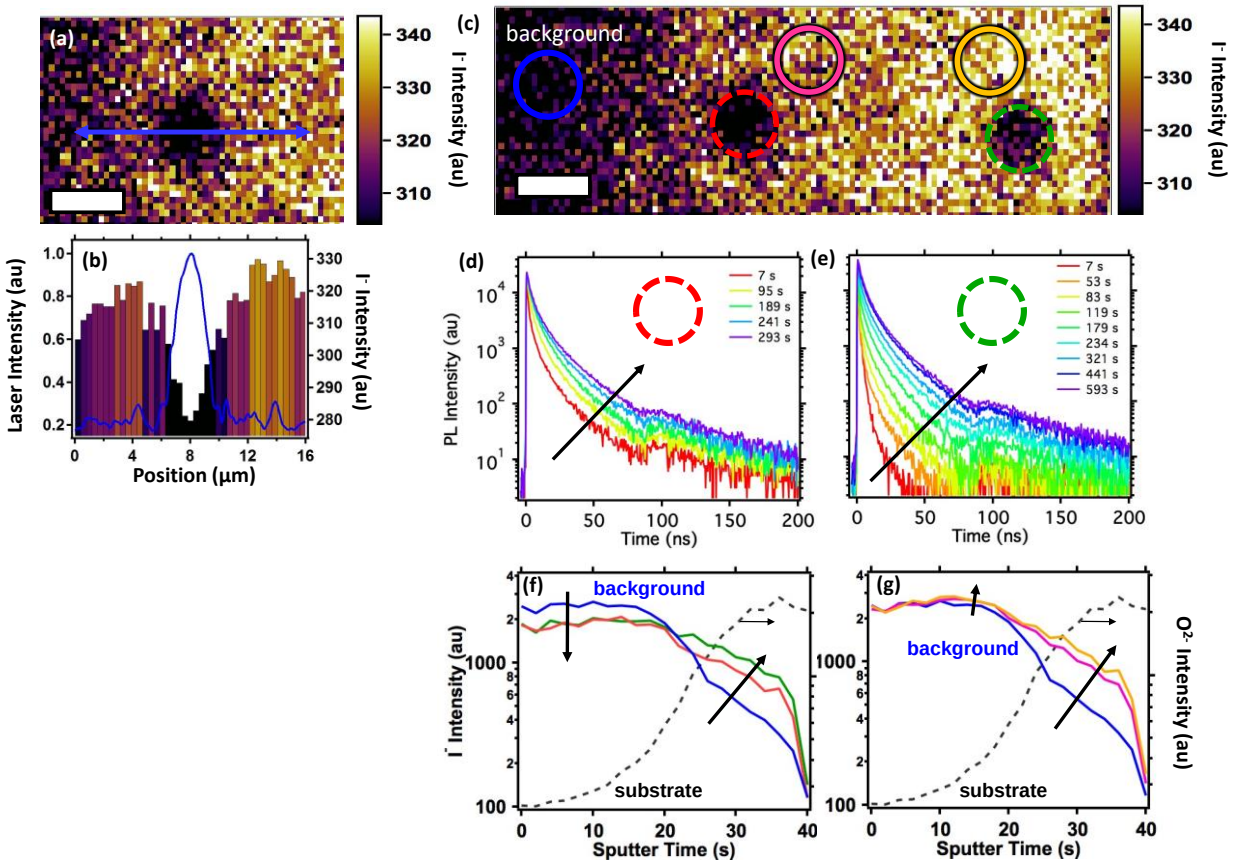

Supplementary Figure 14. ToF-SIMS and time-resolved PL measurements of $CH_3NH_3PbI_3$ films. (a) ToF-SIMS image of region exposed to 1.2 kJ cm^{-2} in the main text (Figure 5a) and the measured laser profile (b) across the line scan in (a), scale bar is 5 µm. (c) ToF-SIMS image of the iodide distribution (the image has been adjusted to show maximum contrast) indicating five regions of interest, where the blue circle represents a background region without any illumination, the red region has been exposed to 1.2 kJ cm^{-2}, and the green region to 2.4 kJ cm^{-2}, and the pink and gold circles are adjacent regions. The corresponding PL decays over time are shown for the (d) red region and (e) green region from (c). (f and g) Raw intensity depth profiles of the various regions of interest with the oxygen intensity (from substrate) indicated by dashed black lines. All selected regions contained the same number of pixels to allow comparisons.

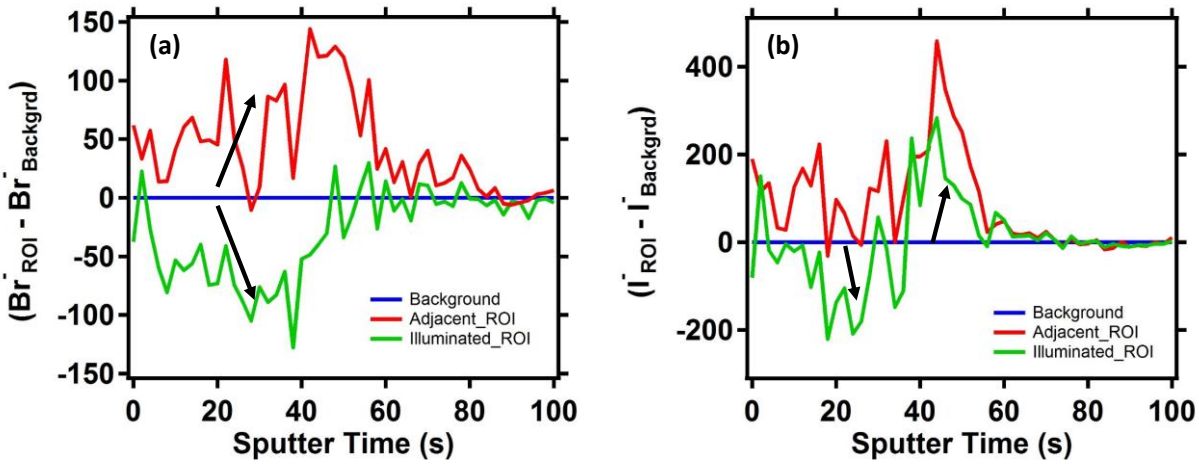

Supplementary Figure 15. **ToF-SIMS depth profile data of an illuminated $CH_3NH_3Pb(I_{1-x}Br_x)_3$ film (x=0.4).** (a) ToF-SIMS depth profile data of the bromide content relative to the background ($Br^-_{ROI} - Br^-_{background}$) for an illuminated (green) and adjacent (red) region. (b) Depth profile data of the iodide content relative to the background ($I^-_{ROI} - I^-_{background}$) for an illuminated and adjacent region.

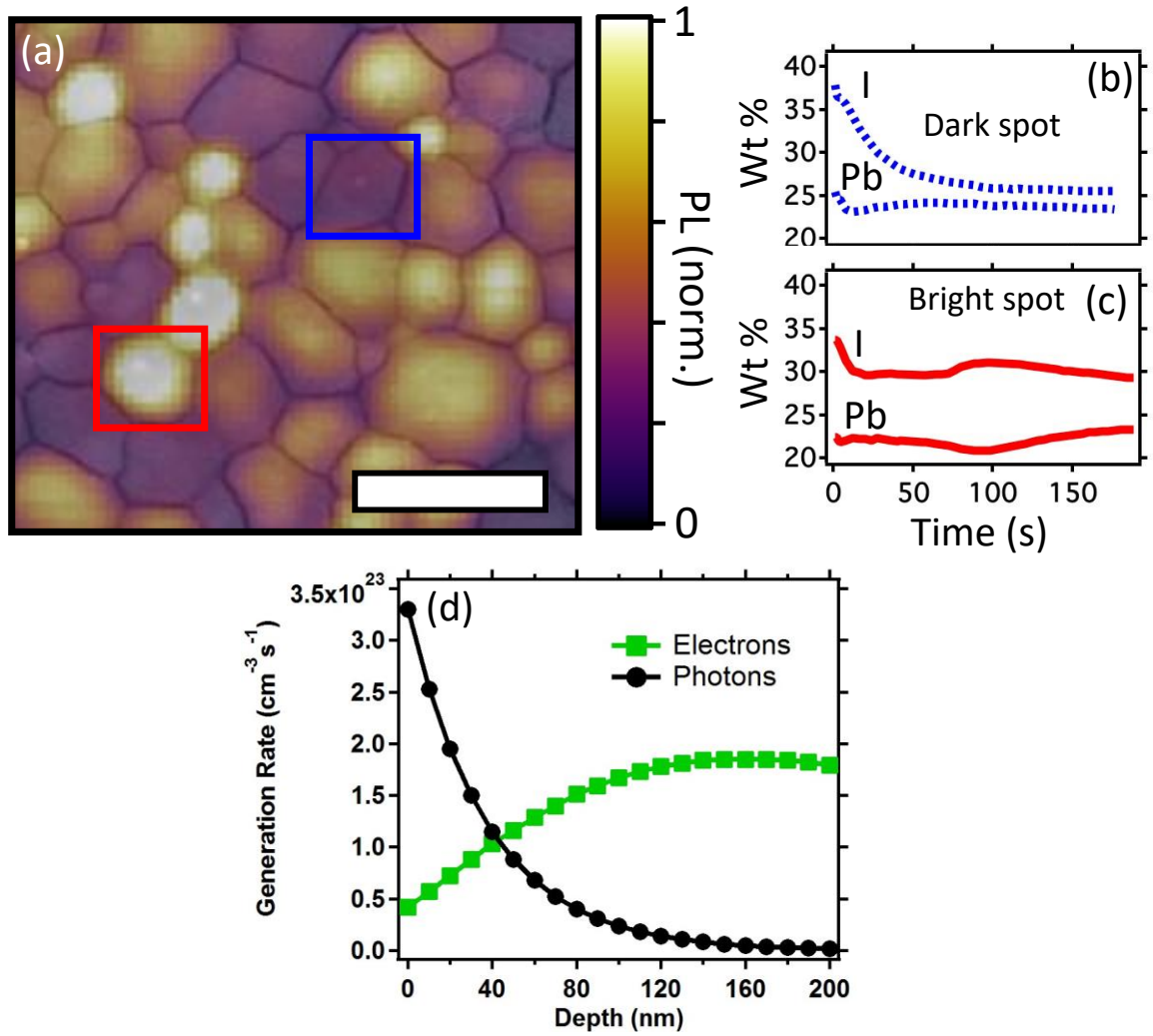

Supplementary Figure 16. **Monitoring iodide content over time via energy dispersive X-ray spectroscopy (EDS).** (a) Composite image of semitransparent SEM micrograph of a perovskite film overlaid on a PL image, scale bar is 2 μm. EDS measurements following lead and iodide weight fractions over time under illumination with a 10 keV electron beam at a (b) dark emission spot (blue) and (c) bright emission spot (blue). (d) Calculated electron-hole generation rates under the optical or electron beam excitation used for PL and EDS measurements, respectively.

Supplementary Note 1. Effect of Atmosphere and Film Preparation on Photoluminescence Transients

Unlike some recent reports[1,2], we do not believe that our observations can be attributed solely to atmospheric effects because we see the transient rise behavior when measuring under vacuum, in nitrogen or in air (Supplementary Fig. 1), although we note that atmospheric conditions such as humidity and oxygen can also influence the film and emission properties, particularly over long time scales (such as storage under these conditions) or when processing under uncontrolled atmospheric conditions[3,8,9].

Supplementary Note 2. Monitoring Bulk Film Properties Over Time Under Illumination

We monitor in time the bulk photoluminescence (PL) spectra (Supplementary Fig. 2) and any structural changes via X-Ray Diffraction (XRD) (Supplementary Fig. 3) over time under illumination.

Supplementary Note 3. Model to Describe Recombination Kinetics

The model to describe the recombination kinetics in the presence of subgap states is derived in detail in our recent work[10], but we summarize the salient points here with some additional modifications. Here, we consider only electronic (subgap) traps, though the same formalism holds for hole traps.

Under pulsed illumination, an optical pulse excitation generates an electron-hole pair density of $N(0)$. There are N_T electron traps, n_T of which are filled leaving n_T free "photo-doped" holes in the valence band such that the total concentration of holes at each point in time is $n_h = n_e + n_T$, where n_e is the concentration of free photogenerated electrons. The total concentration of photo-generated species $N = n_e+n_x$ is thus comprised of concentrations of free electrons and excitons n_x, but excludes trapped electrons and corresponding photo-doped holes. We note that we include excitons here for completeness but due to the low exciton binding energy in these materials, their presence does not significantly affect the results.

In Supplementary Fig. 4 we show transient PL decays at room temperature over a range of pulse fluences, where the sample was first illuminated at each fluence until a steady transient emission was achieved. The shape of the decays is nearly mono-exponential at relatively low excitation fluence, but deviates significantly from mono-exponential at higher fluence. In the steady state, there are many holes already present in the system as 'background' or 'photo-doped' charges because some of the electronic traps are filled. When the sample is photo-excited with a low fluence, the concentration of photo-induced electrons is much lower than the total concentration of free holes (since $n_h(t) = n_e(t) + n_T(t)$, $n_e << n_T$), and the recombination of electrons is almost mono-molecular since the additional photo-excited charge does not noticeably change the concentration of holes. If the excitation fluence is high enough, such that the concentrations of photo-excited electrons and holes from the laser pulse become comparable to the photo-doped hole density ($n_e(0) > n_T \sim N_T$), then the electron-hole recombination is bimolecular resulting in

a power law decay until the free electron concentration drops below the photo-doped hole density, after which the decay again becomes pseudo mono-exponential.

A generic kinetic model, accounting for exciton formation, dissociation into free charges and trapping of free electrons, is given by the rate equations

$$\frac{dn_e}{dt} = \frac{I}{d} + R_d n_x - R_f n_e n_h - R_{eh0} n_e n_h - R_{eh1} n_e n_h \left(N_T - n_T\right) - R_{pop} n_e \left(N_T - n_T\right) \quad (1)$$

$$\frac{dn_x}{dt} = R_f n_e n_h - R_d n_x - R_x n_x \quad (2)$$

$$\frac{dn_T}{dt} = R_{pop} \left(N_T - n_T\right) \cdot n_e - R_{dep} \cdot (n_T^2 + n_T \cdot n_e) \quad (3)$$

The parameters R_f, R_d, and R_x are the rates of exciton formation, dissociation and decay, respectively. R_{eh0} and R_{eh1} describe electron recombination through band-to-band and trap-assisted (Shockley-Read-Hall), respectively, R_{pop} and R_{dep} determine trap population and depopulation by electrons, respectively, where depopulation is exclusively by recombination with either free (photo-generated) or photo-doped holes and we assume the traps are deep enough to inhibit thermal detrapping to the conduction band; I is the excitation intensity ($I = 0$ for pulsed excitation), d is the film thickness, and N_T is the total trap concentration.

Before solving this model we make two further simplifications: 1) the accumulation of charges in traps and their depopulation take place on a time scale of milliseconds to seconds, suggesting that the trap concentration n_T can be taken constant when we consider PL decays on time scales of microseconds. Therefore on the time scales for the evolution of n_e or n_x we set $n_T = Const$, 2) Due to the very fast exciton formation and dissociation, the free carriers and excitons can be assumed to be in thermal equilibrium throughout the entire PL decay.

We can then analytically solve (1)-(3). For consistency with our previous work, we ignore the term involving R_{eh1}, which also effectively takes into account trap-assisted electron recombination in a simplified way avoiding a highly nonlinear equation for n_T. This gives the following expression for the normalized PL:

$$\frac{I_{eh}(t)}{I_{eh}(0)} = \frac{I_{ex}(t)}{I_{ex}(0)} = \frac{n_e(t) \cdot n_h(t)}{n_e(0) \cdot n_h(0)}$$

$$= \frac{1}{\left(n_T + Ax_0\right) \cdot Ax_0} \cdot \left(n_T + \frac{AC_1 x_0 \exp\left[-\gamma \cdot t\right]}{C_1 + x_0 \left(1 - \exp\left[-\gamma \cdot t\right]\right)} \right) \cdot \frac{AC_1 x_0 \exp\left[-\gamma \cdot t\right]}{C_1 + x_0 \left(1 - \exp\left[-\gamma \cdot t\right]\right)} \quad (4)$$

where $A = \frac{\nu_x}{\nu_h \nu_e} \exp\left[-E_b / k_B T\right]$ and $\nu_i = \lambda_i^3$, λ_i is the thermal wavelength of the species *i* (we set E_b = 5 meV [11]), $x_0 = N(t=0)/(A+n_T)$, $\gamma_0 = AR_{eh} + R_x$ is the total rate of electronic decay not involving traps, and

$$\gamma = \frac{n_T \cdot \gamma_0}{A+n_T} + \frac{AR_{pop} \cdot (N_T - n_T)}{A+n_T}, C_1 = \frac{n_T}{A} + \frac{R_{pop} \cdot (N_T - n_T)}{\gamma_0}$$

$$n_T = -\frac{1}{2}\alpha + \frac{1}{2}\sqrt{\alpha^2 + 4\beta N_T}, \alpha = \frac{\left(A + \frac{R_{pop}}{R_{dep}}(A - N_T)\right)}{\left(1 + \frac{1}{K} + \frac{R_{pop}}{R_{dep}}\right)}, \beta = \frac{R_{pop} \cdot A}{R_{dep} \cdot \left(1 + \frac{1}{K} + \frac{R_{pop}}{R_{dep}}\right)} \quad (5)$$

with $K = \frac{1}{\gamma_0 t_0} \ln\left[1 + \frac{AN(0)}{N_T \cdot (A + N_T)}\right]$.

We set the following parameters to be the same as our previous work: $R_{pop} = 2\text{x}10^{-10}\text{cm}^3\text{s}^{-1}$, $R_{dep} = 8\text{x}10^{-12}\text{cm}^3\text{s}^{-1}$, and fix $\gamma_0 = 1.6\text{x}10^7\text{s}^{-1}$. This leaves the only fitting parameter to be the trap density N_T. We globally fit the data across three orders of magnitude in Supplementary Fig. 4 (gray lines) to extract a common stabilized trap density of N_T = 2.5 x 10^{16} cm^{-3} at 300 K. The PL decays over time under illumination are then fit with the same parameters at all temperatures but by varying N_T. We note that the solution including the R_{eh1} term will be presented in a forthcoming publication, but excluding it here is acceptable given we are primarily concerned with the relative changes in trap density under illumination.

Supplementary Note 4. Relation Between Photoluminescence Intensity and Trap Density

To illustrate the relationship between average PL intensity and the trap density, we rewrite the equation (1) for electronic density in a more generic and rigorous form (as we are not interested here in obtaining an analytical expression for n_T):

$$\frac{dn_e}{dt} = -\gamma \cdot n_e \cdot (n_e + n_T), \quad (6)$$

with the effective recombination rate containing the contributions from both the direct band-to-band electron-hole recombination and the trap-assisted (Shockley-Reed-Hall) recombination according to

$$\gamma = \gamma_0 + \beta \cdot (N_T - n_T), \quad (7)$$

where we used the notations $\gamma_0 = R_{eh0} + R_x / A$ for direct band-to-band recombination (radiative and non-radiative), and $\beta = R_{eh1}$ for trap-assisted recombination constant possibly dependent on temperature. Both N_T and n_T are constants on the time scale of PL decay. With this in mind the solution to Eq. (6) is found in the form

$$n_e = \frac{n_T \cdot n_e(0) \cdot \exp(-\gamma n_T \cdot t)}{n_T + n_e(0) \cdot (1 - \exp(-\gamma n_T \cdot t))} \tag{8}$$

Assuming low exciton concentration relative to $n_e(0)$ the latter can be taken as the concentration of all absorbed photons from the excitation pulse and is typically in the range 10^{15} – 10^{17} cm^{-3}. The expression above has a clear physical meaning. At low excitation fluence $n_e(0) << n_T$ and $n_e(t) \approx n_e(0) \cdot \exp(-\gamma n_T \cdot t)$, i.e. the decay of photo-excited electrons is mono-exponential due to monomolecular-type recombination. In the extreme opposite case $n_e(0) >> n_T$ and short times $\gamma \cdot n_T << 1$ the decay is hyperbolic $n_e(t) \approx n_e(0) \cdot (1 + n_e(0) \cdot \gamma \cdot t)^{-1}$ due to nearly-bimolecular recombination. At longer times the recombination becomes monomolecular again with the corresponding decay regime of the photoexcited electrons.

The time-in integrated PL (over the pulse period of duration t_0) calculated using Eq. (8) is

$$\langle I_{PL} \rangle \propto \langle n_e n_h \rangle = \frac{\gamma_{rad}}{t_0} \int_0^{t_0} \left(\frac{n_T \cdot n_e(0) \cdot \exp(-\gamma n_T \cdot t)}{n_T + n_e(0) \cdot (1 - \exp(-\gamma n_T \cdot t))} \right) \cdot \left(\frac{n_T \cdot n_e(0) \cdot \exp(-\gamma n_T \cdot t)}{n_T + n_e(0) \cdot (1 - \exp(-\gamma n_T \cdot t))} + n_T \right) dt \approx \frac{\gamma_{rad} n_e(0)}{\gamma t_0},$$

$$\gamma n_T t_0 >> 1 \tag{9}$$

Substituting here Eq. (7) we obtain

$$\langle I_{PL} \rangle \approx \frac{\gamma_{rad} n_e(0)}{\gamma t_0} = \frac{\gamma_{rad} n_e(0)}{(\gamma_0 + \beta \cdot (N_T - n_T)) t_0} \tag{10}$$

If we compare the samples under constant pulse fluence then most likely $n_T \approx C \cdot N_T$, where the constant $C<1$, and we may write

$$\langle I_{PL} \rangle \approx \frac{\gamma_{rad} n_e(0)}{(\gamma_0 + \beta \cdot N_T \cdot (1 - C)) t_0}. \tag{11}$$

Finally, the second term in the denominator will dominate over the first because the trap densities N_T are large, such that:

$$\langle I_{PL} \rangle \propto \frac{1}{N_T} \tag{12}$$

The inverse relationship given by Eq. (12) is shown in Figure 1b of the main text.

Supplementary Note 5. Temperature-Dependence of Photoluminescence Rises

We show the time-resolved PL decays measured *in vacuo* at low temperature (190 K) in Supplementary Fig. 5a and at high temperature (340 K) in Supplementary Fig. 5b. We note here that the temperature range is chosen to avoid the phase transition in the perovskite at ~160K from a tetragonal to orthorhombic phase, and to avoid high temperatures (>350 K) where degradation will likely occur[12,13]. We fit the time-resolved PL decays measured over time under illumination for each temperature, and the extracted trap densities as a function of time under illumination are shown in Supplementary Fig. 5c. After reaching stabilized emission levels, the trap densities reach temperature-dependent values, with lower trap densities at low temperature (N_T ~ 2 x 10^{16} cm^{-3} at 190 K) compared to those at high temperature (N_T ~ 2.5 x 10^{16} cm^{-3} and 4.3 x 10^{16} cm^{-3} at 295 K and 340 K, respectively). We note that this temperature-dependence of the trap density is consistent with the longer stabilized monomolecular lifetimes (Supplementary Fig. 5d inset) and higher PL intensities (Supplementary Fig. 5c inset) at lower temperature (τ = 280 ns at 190 K) than at high temperature (τ = 132 ns at 340 K). These observations are also consistent with our earlier report where we showed that the PLQE approaches 100% at 190 K[10].

Supplementary Note 6. Arrhenius Fits

We fit single exponential functions to the rise in PL over time (Supplementary Fig. 6) to extract a time constant τ for each temperature. We then plot the rate constants k=1/ τ versus 1/T and fit the data to the Arrhenius relation k = Aexp(-E_a/RT) (where A is a prefactor, R is the ideal gas constant) to extract an estimate for the activation energy E_a, as shown in Figure 1c (main text). We note that we can also fit the PL rise curves using two exponential functions corresponding to a short and long time scale[14,15], but Arrhenius fits for each component separately yield similar activation energies. It is likely that the curves follow much more complicated functions and will need a more detailed analysis, but we simply use exponential functions to give estimates for the time scales involved.

Supplementary Note 7. Excitation Intensity-Dependence of Photoluminescence Changes

We present the results for different excitation intensities in Supplementary Fig. 7, where we observe that the trap densities and the time taken to reach stabilized emission varies dramatically with intensity, but ultimately similar total photon dose to reach stabilization for each case (e.g. ~200-300 J cm^{-2} at room temperature). At low excitation fluences, corresponding to photo-excited densities of ~$10^{15}$$cm^{-3}$ per pulse (1 MHz repetition rate), stabilized emission is reached only at times >10,000 s (~3 hours). This compares to thousands of seconds (~10 minutes) at the intermediate fluences (~$10^{16}$$cm^{-3}$ per pulse, 1

MHz repetition rate) also shown in Figure 1a of the main text, and only ~20 seconds for the highest fluences (~10^{17}cm^{-3} per pulse, 1 MHz repetition rate). Consistent with previous reports[10,16,17], we see a transition at an excitation density of ~10^{17}cm^{-3} from the trap-limited monomolecular kinetics (as seen in Figure 1a) to bimolecular-dominating kinetics, in which the traps are predominantly filled.

Supplementary Note 8. Relation Between Trap Filling and Rise Times

We have previously reported steady state photoconductivity values of 10^{-3}–10^{-2} S cm^{-1} at excitation fluences approximately similar to solar insolation (~10^{17} cm^{-2} s^{-1})[18]. Assuming a carrier mobility of ~1-10 cm^2 V^{-1} s^{-1},[18-20] this requires charge densities of ~10^{15}-10^{17} cm^{-3}. To obtain such charge densities at fluences of ~10^{17} cm^{-2} s^{-1} (~10^{21} cm^{-3} s^{-1}), carrier lifetimes of 10-100 μs are required. Since it is commonly accepted that one of the free carriers (likely the electron) is trapped within 100 ns - 1 μs[10,18,21,22], this long lifetime must be that of the residual (non-trapped) carriers and is likely an underestimate because not all carriers will be trapped (some recombine radiatively). By solving simplified rate equations for the two processes of trap filling (100-ns time scale with typical trap densities of ~10^{16}cm^{-3} [10]) and trap depopulation (100 μs as a conservatively slow estimate[10]), it will not take longer than a few 100s of microseconds for the system to reach equilibrium. This implies that the slow (minutes) transient phenomena observed in this work are not primarily attributed to simple trap filling effects.

Supplementary Note 9. Scanning Electron Microscopy (SEM) Grain Analysis

We show a grain size analysis via scanning electron microscopy (SEM) in Supplementary Fig. 8.

Supplementary Note 10. Local Photo-induced Cleaning

We show how the PL enhancement closely follows the laser profile in Supplementary Fig. 9.

Supplementary Note 11. Film Excitation and Relaxation in the Dark

Supplementary Fig. 11 shows the changes of the bulk PL intensity after varying lengths of time in the dark. Here, the films are illuminated (spot size waist w ~ 17 μm) until they reach a stabilized emission, then the laser is switched off for a fixed length of time and then switched back on, and the PL (at the same spot) continually monitored. Supplementary Fig. 11a shows the situation where the PL is reducing over time in the dark, where the inset shows the PL recovery value as a function of time left in the dark. This suggests that the photo-induced changes can be at least in part reversible and the films can eventually recover to lower stabilized emission levels over a time scale of hours, which is consistent with the microscale PL measurements (Supplementary Fig. 10). In contrast, Supplementary Fig. 11b shows a situation in an identical film measured under identical conditions, and in this case the PL continues increasing over time in the dark although eventually does seem to decrease over very long time scales. These results suggest that the changes that the illumination triggers can continue even while the film is kept in the dark. More generally, we see that the PL moves through long-term ‘phases’,

i.e. over very long time scales (1000s of seconds), we see periods where the emission rises and other periods where it decreases even for the same film and spot. The rises or drops we see in the emission over time in the dark tend to follow the phase of the long term transient. This suggests that there are changes in the film that are instigated by illumination that are partly reversible but that will continue even without illumination. Similar long-term phenomena (long-term phases and associated rises or drops over time) were also reported in these perovskites by Gottesman et al. from photo-conductivity measurements[23], and they are also reminiscent of the photocurrent behavior under different bias conditions in solar cells[24]. We emphasize that here we are studying neat films with no contacts or applied bias. We also note that we cannot exclude the possible contributions of atmospheric effects such as adsorbed oxygen or water species that remain in films even kept under vacuum for long periods of time[1-3].

We note that the photon dose used for collecting a fluorescence image (7 J cm^{-2}) is only ~2% of the photon dose the film was exposed to under simulated sunlight (360 J cm^{-2}) suggesting that the changes observed in Figure 3 (main text) are induced by the long light soak and not by the laser excitation required to collect a fluorescence image. This idea is further supported by the negligible changes in PL observed for a control film that had not been exposed to simulated AM 1.5 sunlight (Supplementary Fig. 12).

Supplementary Note 12. Time-of-flight Second Ion Mass Spectrometry (ToF-SIMS)

For the ToF-SIMS measurements, we first light soak the spot to be analyzed (indicated by the red circle in Supplementary Fig. 13a) and then immediately transfer the film in the dark to the ToF-SIMS instrument and put the sample under ultra-high vacuum (~ 40 minutes). Instrument calibration takes an additional 20 minutes, so in total the film is in the dark for ~ 60 minutes before being depth profiled. We believe the local changes in PL are still retained based on the results reported in Supplementary Figs. 11 and 12 (~9 hrs until stabilization) and therefore any changes in composition should also be retained. ToF-SIMS is a surface-sensitive technique with typical molecular ion escape depths of a few nanometers[25]. For depth profiling, the signal intensity is proportional to the composition at the top surface of the film after each sputter cycle. We identified and analyzed several different negative ion fragments and report the depth-summed ToF-SIMS images most representative of the data set (Supplementary Fig. 13), including I^-, I_2^-, PbI_2^-, PbI_3^-, $Pb_2I_5^-$, $Pb_3I_7^-$, PO_3^-, and $C_3HN_2^-$ (a fragment of methylammonium). In Supplementary Fig. 13a, we show the iodide counts summed through the film depth and also define regions of interest for the illuminated region (red circle), an adjacent region (green circle) and a background region far from illumination (blue circle). As ToF-SIMS is primarily a qualitative technique, obtaining absolute changes in iodine content is not possible without careful calibration, and is therefore beyond the scope of this work. In order to extract an approximate relative change in intensity of iodine-containing fragments (R) between light-soaked, adjacent, and background regions, we used the following equation:

$$R = \sum_i^N \left(\frac{M_i^-(ROI) - M_i^-(Backgrd)}{M_i^-(Backgrd)} \right) \times 100\% \quad (13),$$

where $M_i^-(\dots)$ denotes the intensity of the iodine-containing fragment in the region of interest. To a first-order approximation, we estimate R= -1.2% in the illuminated region and R= +1.4% in the adjacent region, indicating that iodine has been partially redistributed. These values are significant given we only observe ~0.5% variations in several background regions, though we emphasize again here that there is likely a large error without proper calibration.

We briefly consider whether illumination could induce local variations in sputtering rates and ion extraction leading to artifacts in the intensity maps. In this possible scenario, we would expect the adjacent region (red circle in Supplementary Fig. 13a) to have a similar depth profile and intensity as the background region (blue circle in Supplementary Fig. 13a) – both of which have not been illuminated. In contrast, we still observe distinct profiles and intensities in the adjacent and background regions (Supplementary Fig. 14). This strongly suggests that material is moving laterally outside the illumination region. In addition, there are no other high-yield iodine-containing fragments with similar intensity maps as iodide. If illumination was changing the sputtering rate and probability of ion extraction, we would expect a systematic artifact in at least some of the other fragment intensity maps.

Supplementary Note 13. Energy-Dispersive X-Ray Spectroscopy (EDS)

We show a semitransparent scanning electron microscope (SEM) image of the film in Supplementary Figure 16a overlaid on a PL map, again highlighting bright and dark spots. We show energy dispersive X-Ray spectroscopy (EDS) measurements at a dark (Supplementary Fig. 16b) and a bright (Supplementary Fig. 16c) spot to monitor the weight fractions of lead and iodide. Here, we use a high energy 10 keV electron beam to generate electron-hole pairs via inelastic scattering within the material; this same mechanism is exploited in order to detect electron beam-induced current (EBIC) measurements in photovoltaic devices[26,27] and cathodoluminescence measurements[28]. We estimate a peak electron-hole generation rate of 2×10^{23} $cm^{-3}s^{-1}$ (see below), hence we are probing the samples under carrier densities similar to the PL measurements and ~10 sun solar illumination conditions (~3×10^{23} $cm^{-3}s^{-1}$). We note that carriers generated from the electron beam are distributed further in the bulk compared to carriers generated by photoexcitation (Supplementary Fig. 16d). We find that for the dark spot, which is associated with a rise in PL over time under illumination, the iodide content reduces on a time scale consistent with the rise times in PL and device open-circuit voltage at 1-sun equivalent optical irradiation (Figure 1b inset, main text)[10]. In contrast, the bright spot has very little change in iodide content over time under electron excitation. As a reference point, the lead content remains essentially unchanged in both cases. We note that the weight fraction values are dependent on the local interaction volume and include all detected elements including those in the substrate, and therefore the absolute weight fractions should not be compared. We also cannot rule out local differences in volatization of iodide-containing species under high-energy electron excitation. Nevertheless, these EDS results suggest that the dark regions with high trap densities

correspond to regions with excess mobile iodide, in agreement with the ToF-SIMS measurements.

We estimate that the pulsed excitation for PL measurements (~1 MHz, 0.5 μJ cm^{-2} per pulse), gives a peak charge density at t=0 of ~10^{16} cm^{-3} and an average density over the decay of ~10^{15} cm^{-3}. This is roughly equivalent to the charge density arising from 1-sun equivalent irradiation (upper bound charge density of ~10^{15} cm^{-3})[10,12,17]. We approximate the electron-hole generation rate under optical excitation using the average power output of the laser and by using the absorption coefficient reported elsewhere[29], and we plot the resulting profile in Supplementary Fig. 16d (black circles). We estimate the electron beam generation rate as a function of depth using established cathodoluminescence equations[30] taking into consideration the measured beam current (53.5 pA), perovskite density (4.286 g cm^{-3})[31], and perovskite bandgap (1.55 eV)[32]; we also plot this in Supplementary Fig. 16d (green squares).

The maximum generation rate is quite similar for both photon and electron-beam excitations. For the PL experiments, we obtain a maximum rate of ~$3x10^{23}$ $cm^{-3}s^{-1}$ compared to ~$2x10^{23}$ $cm^{-3}s^{-1}$ for the electron beam measurements. However, the spatial generation profiles are quite different. The optical excitation generation rate peaks at the surface and drops off exponentially through the film following the Beer Lambert Law, while the electron beam generates most of the carriers deeper in the sample as a result of inelastic scattering.

Supplementary References

1 Tian, Y. *et al.* Mechanistic insights into perovskite photoluminescence enhancement: light curing with oxygen can boost yield thousandfold. *Phys Chem Chem Phys* **17**, 24978-24987, doi:10.1039/c5cp04410c (2015).

2 Galisteo-López, J. F., Anaya, M., Calvo, M. E. & Míguez, H. Environmental Effects on the Photophysics of Organic–Inorganic Halide Perovskites. *J. Phys. Chem. Lett.* **6**, 2200-2205, doi:10.1021/acs.jpclett.5b00785 (2015).

3 Eperon, G. E. *et al.* The Importance of Moisture in Hybrid Lead Halide Perovskite Thin Film Fabrication. *ACS Nano* **9**, 9380-9393, doi:10.1021/acsnano.5b03626 (2015).

4 Eperon, G. E., Burlakov, V. M., Docampo, P., Goriely, A. & Snaith, H. J. Morphological Control for High Performance, Solution-Processed Planar Heterojunction Perovskite Solar Cells. *Advanced Functional Materials* **24**, 151-157, doi:10.1002/adfm.201302090 (2014).

5 Stranks, S. D. *et al.* Electron-hole diffusion lengths exceeding 1 micrometer in an organometal trihalide perovskite absorber. *Science* **342**, 341-344, doi:10.1126/science.1243982 (2013).

6 Saidaminov, M. I. *et al.* High-quality bulk hybrid perovskite single crystals within minutes by inverse temperature crystallization. *Nat Commun* **6**, doi:10.1038/ncomms8586 (2015).

7 Zhang, W. *et al.* Enhanced optoelectronic quality of perovskite thin films with hypophosphorous acid for planar heterojunction solar cells. *Nat Commun* **6**, 10030, doi:10.1038/ncomms10030 (2015).

8 Pathak, S. *et al.* Atmospheric influence upon crystallization and electronic disorder and its impact on the photophysical properties of organic-inorganic perovskite solar cells. *ACS Nano* **9**, 2311-2320, doi:10.1021/nn506465n (2015).

9 Zhou, H. *et al.* Interface Engineering of Highly Efficient Perovskite Solar Cells. *Science* **345**, 542-546, doi:10.1126/science.1254050 (2014).

10 Stranks, S. D. *et al.* Recombination Kinetics in Organic-Inorganic Perovskites: Excitons, Free Charge, and Subgap States. *Phys Rev Appl* **2**, 034007, doi:10.1103/Physrevapplied.2.034007 (2014).

11 Miyata, A. *et al.* Direct measurement of the exciton binding energy and effective masses for charge carriers in organic–inorganic tri-halide perovskites. *Nature Physics* **11**, 582-587, doi:10.1038/nphys3357 (2015).

12 D'Innocenzo, V. *et al.* Excitons versus free charges in organo-lead tri-halide perovskites. *Nat. Commun.* **5**, 3586, doi:10.1038/ncomms4586 (2014).

13 Wehrenfennig, C., Liu, M. Z., Snaith, H. J., Johnston, M. B. & Herz, L. M. Charge carrier recombination channels in the low-temperature phase of organic-inorganic lead halide perovskite thin films. *Apl Mater* **2**, 081513, doi:10.1063/1.4891595 (2014).

14 Hoke, E. T. *et al.* Reversible photo-induced trap formation in mixed-halide hybrid perovskites for photovoltaics. *Chem. Sci.* **6**, 613-617, doi:10.1039/c4sc03141e (2015).

15 Eames, C. *et al.* Ionic transport in hybrid lead iodide perovskite solar cells. *Nat Commun* **6**, 7497, doi:10.1038/ncomms8497 (2015).

16 Yamada, Y., Nakamura, T., Endo, M., Wakamiya, A. & Kanemitsu, Y. Photocarrier recombination dynamics in perovskite CH3NH3PbI3 for solar cell applications. *J Am Chem Soc* **136**, 11610-11613, doi:10.1021/ja506624n (2014).

17 deQuilettes, D. W. *et al.* Impact of microstructure on local carrier lifetime in perovskite solar cells. *Science* **348**, 683-686, doi:10.1126/science.aaa5333 (2015).

18 Leijtens, T. *et al.* Electronic properties of meso-superstructured and planar organometal halide perovskite films: charge trapping, photodoping, and carrier mobility. *ACS Nano* **8**, 7147-7155, doi:10.1021/nn502115k (2014).

19 Wehrenfennig, C., Eperon, G. E., Johnston, M. B., Snaith, H. J. & Herz, L. M. High Charge Carrier Mobilities and Lifetimes in Organolead Trihalide Perovskites. *Adv. Mater.* **26**, 1584-1589, doi:10.1002/adma.201305172 (2014).

20 Hutter, E. M., Eperon, G. E., Stranks, S. D. & Savenije, T. J. Charge Carriers in Planar and Meso-Structured Organic-Inorganic Perovskites: Mobilities, Lifetimes, and Concentrations of Trap States. *J. Phys. Chem. Lett.* **6**, 3082-3090, doi:10.1021/acs.jpclett.5b01361 (2015).

21 Wetzelaer, G. J. *et al.* Trap-assisted non-radiative recombination in organic-inorganic perovskite solar cells. *Adv Mater* **27**, 1837-1841, doi:10.1002/adma.201405372 (2015).

22 D'Innocenzo, V., Srimath Kandada, A. R., De Bastiani, M., Gandini, M. & Petrozza, A. Tuning the Light Emission Properties by Band Gap Engineering in Hybrid Lead Halide Perovskite. *J. Am. Chem. Soc.*, doi:10.1021/ja511198f (2014).

23 Gottesman, R. *et al.* Extremely Slow Photoconductivity Response of CH3NH3PbI3 Perovskites Suggesting Structural Changes under Working Conditions. *J. Phys. Chem. Lett.* **5**, 2662-2669, doi:10.1021/Jz501373f (2014).

24 Kim, H. S. & Park, N. G. Parameters Affecting I-V Hysteresis of CH3NH3PbI3 Perovskite Solar Cells: Effects of Perovskite Crystal Size and Mesoporous TiO2 Layer. *J. Phys. Chem. Lett.* **5**, 2927-2934, doi:10.1021/Jz501392m (2014).

25 Muramoto, S., Brison, J. & Castner, D. G. Exploring the Surface Sensitivity of TOF-Secondary Ion Mass Spectrometry by Measuring the Implantation and Sampling Depths of Bin and C60 Ions in Organic Films. *Analytical Chemistry* **84**, 365-372, doi:10.1021/ac202713k (2012).

26 Edri, E. *et al.* Why lead methylammonium tri-iodide perovskite-based solar cells require a mesoporous electron transporting scaffold (but not necessarily a hole conductor). *Nano Lett* **14**, 1000-1004, doi:10.1021/nl404454h (2014).

27 Edri, E. *et al.* Elucidating the charge carrier separation and working mechanism of CH3NH3PbI(3-x)Cl(x) perovskite solar cells. *Nat Commun* **5**, 3461, doi:10.1038/ncomms4461 (2014).

28 Bischak, C. G., Sanehira, E. M., Precht, J. T., Luther, J. M. & Ginsberg, N. S. Heterogeneous Charge Carrier Dynamics in Organic-Inorganic Hybrid Materials: Nanoscale Lateral and Depth-Dependent Variation of Recombination Rates in Methylammonium Lead Halide Perovskite Thin Films. *Nano Lett* **15**, 4799-4807, doi:10.1021/acs.nanolett.5b01917 (2015).

29 Green, M. A., Ho-Baillie, A. & Snaith, H. J. The Emergence of Perovskite Solar Cells. *Nature Photonics* **8**, 506-514, doi:10.1038/nphoton.2014.134 (2014).

30 Bonard, J. M., Ganière, J. D., Akamatsu, B., Araújo, D. & Reinhart, F. K. Cathodoluminescence study of the spatial distribution of electron-hole pairs generated by an electron beam in Al0.4Ga0.6As. *J. Appl. Phys.* **79**, 8693-8703, doi:10.1063/1.362560 (1996).

31 Baikie, T. *et al.* Synthesis and crystal chemistry of the hybrid perovskite (CH3NH3) PbI3 for solid-state sensitised solar cell applications. *J. Mater. Chem. A* **1**, 5628-5641, doi:Doi 10.1039/C3ta10518k (2013).

32 Eperon, G. E. *et al.* Formamidinium lead trihalide: a broadly tunable perovskite for efficient planar heterojunction solar cells. *Energy Environ. Sci.* **7**, 982-988, doi:10.1039/c3ee43822h (2014).

33 Xiao, M. *et al.* A fast deposition-crystallization procedure for highly efficient lead iodide perovskite thin-film solar cells. *Angew Chem Int Ed* **53**, 9898-9903, doi:10.1002/anie.201405334 (2014).

34 Jeon, N. J. *et al.* Solvent Engineering for High-Performance Inorganic-Organic Hybrid Perovskite Solar Cells. *Nat Mater* **13**, 897-903, doi:10.1038/nmat4014 (2014).

Appendix D: Supporting Information for Chapter 5

Materials and Methods

Perovskite Precursor Preparation

$PbOAc_2$ as a Pb Source

A methylammonium iodide (MAI) stock solution was made by dissolving MAI (Dyesol, CAS:14965-49-2) in anhydrous *N*,*N*- dimethylformamide (DMF) at a concentration of 1.78 M. Then lead acetate trihydrate (99.999%, Sigma-Aldrich, CAS:6080-56-4) was added at a 3:1 molar ratio of MAI to $PbOAc_2 \cdot 3\ H_2O$ (0.59 M).[1] All solutions were made in a nitrogen filled glovebox.

$PbCl_2$ and PbI_2 as Pb Sources

Methylammonium iodide (MAI) was prepared by reacting methylamine, 33 wt% in ethanol (Sigma-Aldrich), with hydroiodic acid (HI) 57 wt% in water (Sigma-Aldrich), at room temperature. HI was added dropwise while stirring. MAI was precipitated out of solution by heating the solution at 100 °C overnight to drive off the solvent. The crude MAI was either used without further purification or recrystallized in a mixed solvent of ethanol and ether.

To form the non-stoichiometric $CH_3NH_3PbI_3(Cl)$ precursor solution, MAI and lead (II) chloride (99.999%, Sigma-Aldrich) were dissolved in DMF at a 3:1 molar ratio of MAI to $PbCl_2$, with final concentrations 0.88 M lead chloride and 2.64 M methylammonium iodide.[2] This solution was stored under a dry nitrogen atmosphere.

To form the $CH_3NH_3PbI_3$ precursor solution, MAI and PbI_2 (Sigma) were dissolved in a mixed solvent of dimethylsulfoxide and γ-butyrolactone (volume ratio of 3:7) at a 1:1 molar ratio of MAI to PbI_2, with final concentrations of 1 M and stirred at 60 ^oC for 12 h.[3]

Perovskite Deposition

First, glass substrates were cleaned sequentially in 2% Micro-90 detergent, acetone, then propan-2-ol. To form the perovskite layer for spectroscopy measurements, the precursor solutions were spin-coated on plasma-cleaned substrates in a nitrogen-filled glovebox, at 2000 rpm for 60 s.

Films prepared from the $PbOAc_2$ precursor were left to dry at room temperature in the glovebox for 10 minutes and then annealed on a hotplate at 100 °C for 5 minutes.

Films prepared from the $PbCl_2$ precursor were left at room temperature in the glovebox for 30 minutes and then annealed on a hotplate in the glovebox at 90 °C for 150 minutes.

Films prepared from the PbI_2 precursor were prepared using the "dripping" method, where the perovskite precursor was filtered through a 0.22 μm PTFE filter onto the glass substrate and spin coated at 1000 rpm for 15 s and then 4000 rpm for 45 s. During the last 15 s of the second spin-coating step, the substrate was treated with toluene drop-casting (0.7 mL). The resulting thin films were annealed at 100 ºC for 10 min.[3] All films were then encapsulated in a nitrogen atmosphere with vacuum grease and clean microscope coverslips.

Surface Treatment Deposition and Wash

All treatment solutions reported in the main article were prepared in anhydrous chlorobenzene (Sigma-Aldrich, CAS: 108-90-7) with concentration ranges from 0.005 M to 0.087 M. Other treatments not reported in the main article (Figure S1 and Table S1) were also prepared in anhydrous chlorobenzene with concentration ranges from 0.002 M to 1 M. Nearly all chemical treatments were readily solvated in CB, but a few treatments required further agitation via vortexing or sonication for ~ 10 min. Treatments were carried out by depositing ~70 μl of the treatment solution on the film then immediately spincoating at 2000 rpm for 60 s. Higher concentration treatments (> 0.025 M) can often leave a filmy residue on the surface, which can be removed with a dynamic solvent wash while still maintaining PL improvements (Figure S4) and film morphology (Figure S6). A "dynamic" wash involves depositing 40 μL of anhydrous CB or 2-propanol (IPA) onto the perovskite film while it is already rotating at 6000 rpm for 45 s, while in a "regular" wash, CB or IPA is deposited before starting the spincoating procedure at 2000 rpm for 30 s.

Characterization

Scanning Electron Microscopy (SEM)

SEM images were taken using a FEI Sirion SEM at 5 kV accelerating voltage. To prevent charging effects, samples for SEM were imaged after sputtering approximately 7 nm of Au/Pd using a SPI-Module Sputter Coater with argon flow.

X-ray Diffraction Spectroscopy

Diffractograms were collected on a Bruker D8 Discover with GADDS XRD system. The X-ray source was a Cu rotating anode operating at 5.4 kW in collimated beam geometry (Kα only) with an 800 μm beam diameter. Diffracted X-rays were collected using a Bruker Hi-Star 2D area detector, at distance of 20 cm from the sample.

Glow Discharge Optical Emission Spectroscopy (GDOES)

Depth-dependent compositional profiles were collected with a Horiba GD-Profiler-2 using a high-power radio frequency (RF) argon plasma in a 4 mm diameter anode. The plasma was operated at 30 W and a pressure of 600 Pa. Sulfur (S) and lead (Pb) were detected using the 181 nm and 406 nm atomic emission lines, respectively. Time zero was defined as the time at which the reflected plasma power stabilized. Samples were first treated with 0.087 M ODT in anhydrous CB, then dynamically washed with CB or IPA at 6000 rpm for 45 s to remove excess unreacted ligand. After the washing step,

there appeared to be no residual unreacted ODT on the surface via SEM (Figure S6), and the sample maintained a PL improvement relative to the control film (Figure S4), which showed no significant sulfur (S) content as observed via GDOES (Figure S5).

Nuclear Magnetic Resonance (NMR) Spectroscopy

1D ^{31}P solid state NMR spectra were recorded on a Bruker AV-III spectrometer at a Larmor frequency of 283.394 MHz, using a standard cross-polarization (CP) pulse sequence with ^{1}H decoupling. Both the PPh_3 control as well as perovskite samples were prepared by making fine powders that were packed densely into 3.2 mm magic angle spinning (MAS) rotors. Data were obtained using a Bruker $^{1}H\{^{13}C,^{31}P\}$ triple resonance MAS probehead with a rotor spinning rate of 10 kHz. Sample temperature was maintained at 298 K within a precision of 10 mK. The ^{31}P spectra were externally referenced to 0 ppm of ^{31}P recorded separately in H_3PO_4.

Preparation of Ligand Treated $CH_3NH_3PbI_3$ Single Crystal Powder for Solid State NMR

Lead iodide (98%) and anhydrous γ-butyrolactone (> 99%) were purchased from Sigma Aldrich and used without further purification. Methylammonium iodide (MAI) was synthesized by reacting methylamine (33 wt% in EtOH, Sigma) with equimolar hydriodic acid (57 wt%, Sigma) in an ice bath. The reaction mixture was stirred for 60 minutes and the liquid was removed with a rotary evaporator. The crude MAI solid was redissolved with EtOH (> 99.5%, Sigma), then precipitated and washed with diethyl ether (> 99%, Sigma). The MAI was dried and transferred to a nitrogen atmosphere. Our procedure for single crystal growth was based off of the inverse temperature crystallization (ITC) method of Saidaminov et al.[4] A 1.2 M solution of both PbI_2 and MAI (1:1 molar ratio) was prepared in anhydrous γ-butyrolactone. The solution, exposed to ambient conditions, was preheated to 60 °C. Approximately 2 mL of this solution was filtered using a 0.2 μm PTFE filter. The filtrate was added to a 4 mL vial which was sealed shut before submerging in an oil bath heated to 80 °C. Over the course of two days, the temperature of the oil bath was gradually increased to 110 °C. After the two days, a ~1 cm^3 $CH_3NH_3PbI_3$ single crystal was removed from the growth solution and washed with two 2 mL aliquots of acetophenone. The crystal was then dried and transferred into a N_2 filled glovebox. In the glovebox, the single crystal was ground into a very fine powder using a mortar and pestle and approximately 300 mg of the powder was transferred to a 10 mL centrifuge tube. The powder was then exposed to 1 mL of a 1 M PPh_3 solution in CB. The PPh_3/perovskite powder mixture was vortexed for ~ 20 seconds, then centrifuged for 3 minutes at 3000 rpm. The supernatant was discarded and the treated perovskite crystals were dried under N_2 flow for ~ 2 hours, the crystals were mixed with a spatula every 30 minutes to ensure uniform drying. Figure S7 shows X-ray diffraction patterns of the control and treated perovskite powders, which are consistent with previous reports.[4] The treated perovskite powder was then packed densely into the MAS rotor for solid-state NMR measurements.

External Photoluminescence Quantum Efficiency (PLQE) Measurement

PLQE measurements were acquired using an integrating sphere setup (Hamamatsu C9920-02, A10094). A 532 nm CW laser (CrystaLaser, GCL532-005-L) was used to excite the sample and neutral density filters were used to attenuate the laser for intensity dependent measurements. Data acquisition followed the protocol describe by de Mello et al.,[5] with a scattering correction.

Fluorescence Microscopy

Optical microscopy and spectroscopy were performed using a custom sample scanning confocal microscope built around a Nikon TE-2000 inverted microscope fitted with an infinity corrected 50x dry objective (Nikon L Plan, NA 0.7, CC 0-1.2). A 470 nm pulsed diode laser (PDL-800 LDH-P-C-470B, 300 ps pulse width) was used for excitation with repetition rate of 40 MHz. The emission was filtered through a 50/50 dichroic beamsplitter and a pair of 700 longpass filters. Photoluminescence from the sample was directed to a Micro Photon Devices (MPD) PDM Series single photon avalanche photodiode with a 50 μm active area for TRPL measurements or a portable charge coupled device spectrometer (USB 2000, Ocean Optics) for steady state PL measurements. The sample stage was controlled using a piezo controller (Physik Instrumente E-710). For fluorescence microscopy, the pixel size was 100 nm with a pixel dwell time (integration time) of 50 ms. Before measurements, the system was calibrated using 200 nm fluorescent microspheres (Lifetechnologies FluoSpheres® Polystyrene Microspheres, 200 nm, red fluorescent, 580/605).

Supplementary Figures and Text

S.1 Photoluminescence Improvements Using Thiol and Amine Lewis Bases

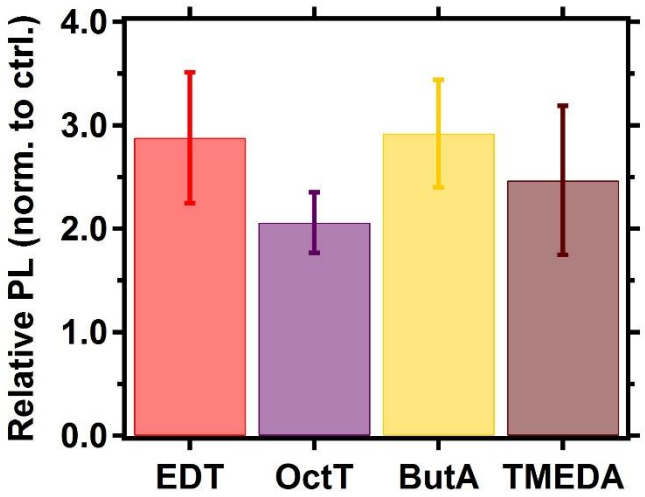

Figure S1. Integrated photoluminescence (PL) intensity enhancements for ethanedithiol (EDT), octanethiol (OctT), butylamine (ButA), and tetramethylethylenediamine (TMEDA) excited at 470 nm with fluences ranging from 15-80 nJ/cm^2 per pulse. The relative PL values on the left axis are the ratio of integrated PL intensities of treated to control samples, error bars are standard error of the mean for N=10.

Ligand	Structure	Concentration Range (M)
Ethanedithiol (EDT)	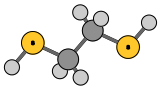	0.002 – 1
Octanethiol (OctT)	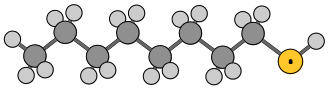	0.002 – 1
Butylamine (ButA)	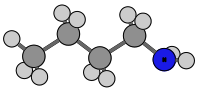	0.008 – 0.01
Tetramethyl-ethylenediamine (TMEDA)	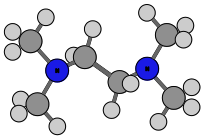	0.0008 – 0.003

Table S1. Ligand structures and concentration ranges of treatments not reported in the main text, but which also showed improvements in PL lifetime and intensity. In the structure column, yellow spheres denote sulfur atoms and purple spheres are nitrogen.

S.2 Photoluminescence Improvements for Films with $PbCl_2$ and PbI_2 as Pb Source

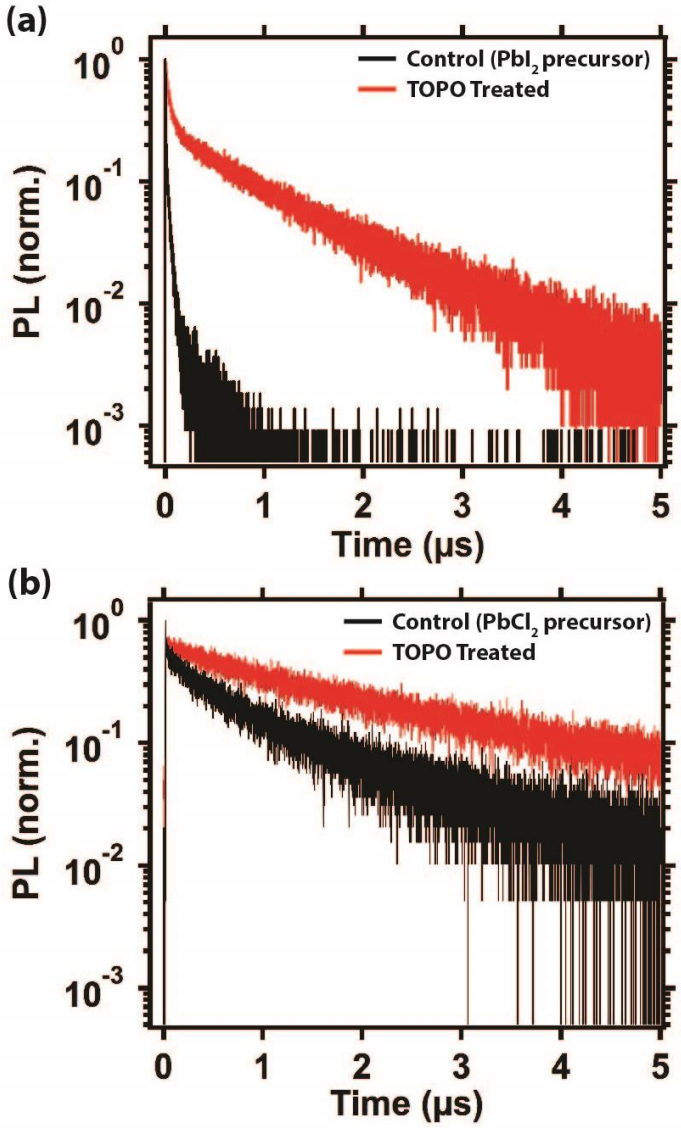

Figure S2. Bulk time-resolved photoluminescence of a (a) $CH_3NH_3PbI_3$ thin film prepared from a PbI_2 precursor and (b) $CH_3NH_3PbI_3(Cl)$ thin film prepared from a $PbCl_2$ precursor before (black) and after treatment (red) with 0.005 M trioctylphosphine oxide (TOPO) in chlorobenzene. Samples were excited at 470 nm at a fluence of 70 nJ/cm^2 per pulse.

S.3 Photoluminescence Measurements of Samples Exposed to Treatment Solvent

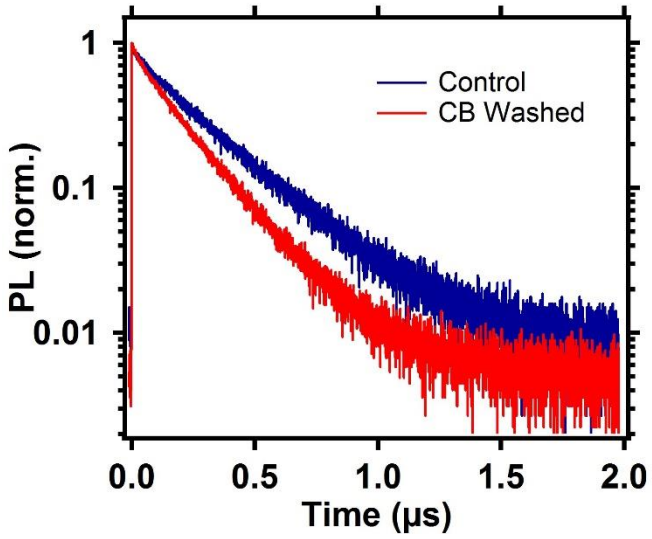

Figure S3. Bulk time-resolved photoluminescence of a control film (blue) and the same film after being washed with the treatment solvent (red), anhydrous chlorobenzene (CB), excited at 470 nm at a fluence of 30 nJ/cm^2 per pulse. PL improvements are not observed without the surface ligands in the solution.

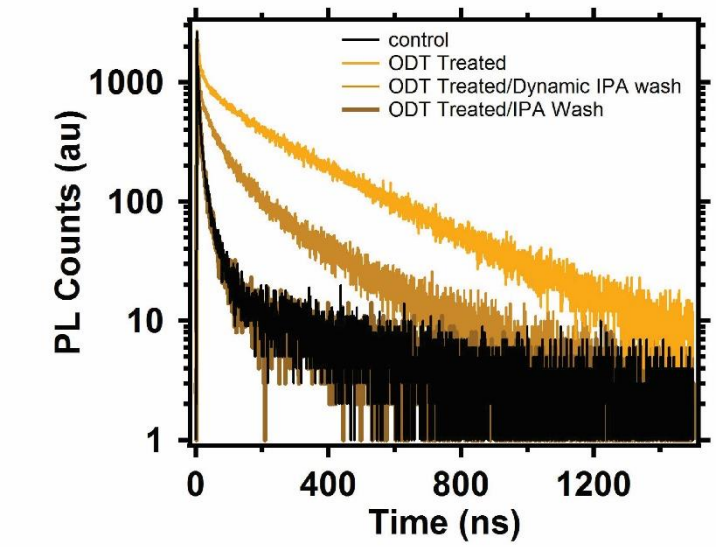

Figure S4. Time resolved photoluminescence decay traces of a control film (black) treated with octadecanethiol (ODT, bright orange), then dynamically washed with 2-propanol (IPA, orange) or regularly washed with IPA (brown). The dynamic wash retains some of the PL enhancement, whereas a regular wash removes the improvement entirely (See "Surface Treatment Deposition and Wash" in the Materials and Methods section).

S.4 GDOES, SEM, UV-Vis Spectroscopy, and XRD Characterization of Ligand Treated Films

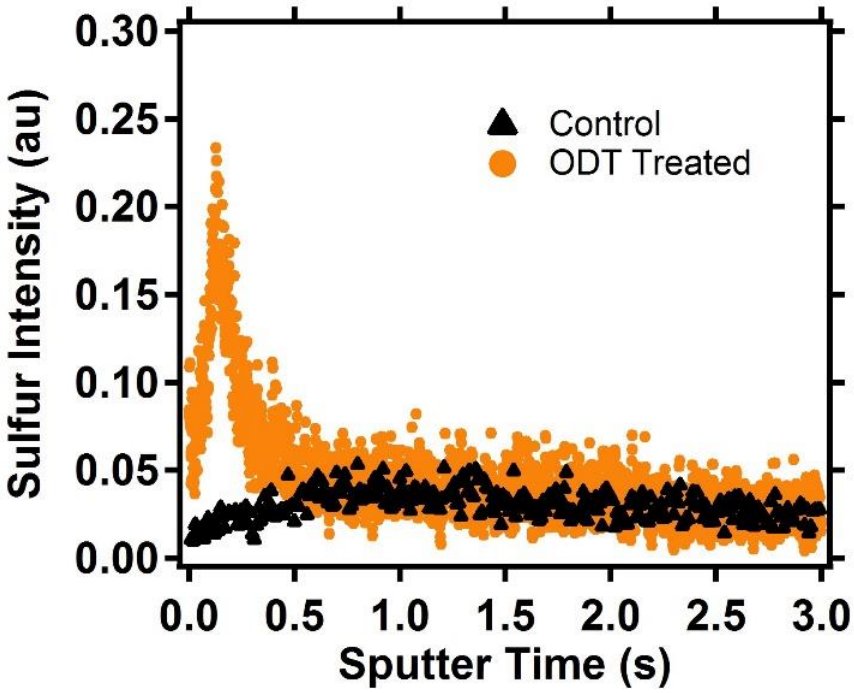

Figure S5. Glow discharge optical emission spectroscopy (GDOES) monitoring the sulfur intensity as a function of film depth of an untreated control film (black) and octadecanethiol (ODT) treated (orange) film.

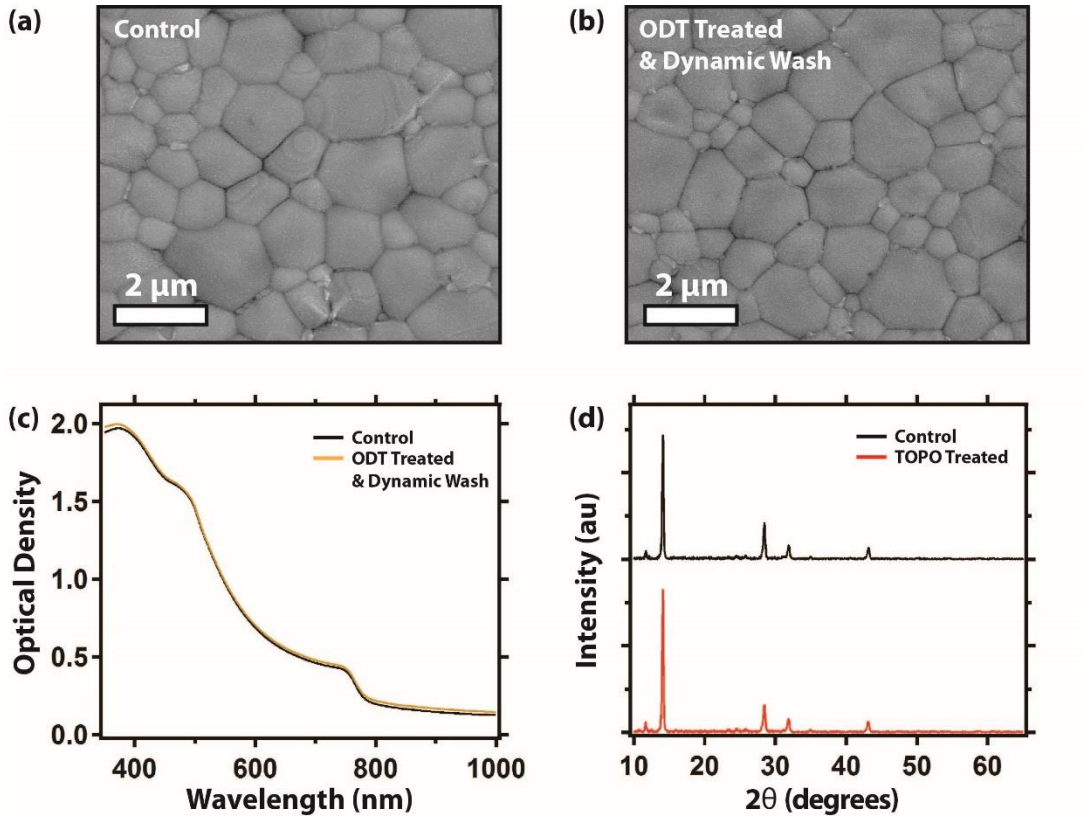

Figure S6. (a) Scanning electron microscope (SEM) images of a polycrystalline perovskite film before (a) and after (b) octadecanethiol (ODT) treatment and a subsequent dynamic wash with chlorobenzene, showing no observable restructuring of the film morphology. (c) Linear absorption spectrum of a film before and after ODT treatment which underwent a dynamic wash with IPA. (d) Background subtracted X-ray diffraction patterns of a polycrystalline film before and after treatment with trioctylphosphine oxide (TOPO), showing no significant change in phase composition or crystallinity.

S.5 XRD Characterization of Control and Ligand Treated Single Crystal Perovskite ($CH_3NH_3PbI_3$) Powders

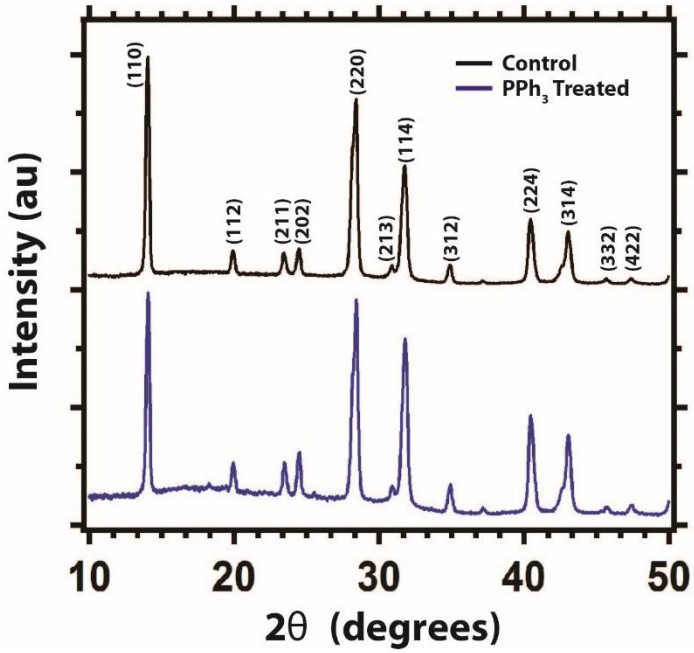

Figure S7. X-ray diffraction patterns of the single crystal powder before (black) and after treatment with triphenylphosphine (PPh_3, blue), prepared for the solid-state NMR experiment (Figure 2c in the main article), small differences in peak intensities are attributed to heterogeneity in the prepared powders. The XRD pattern is consistent with previous reports of the tetragonal phase of $CH_3NH_3PbI_3$.[4]

S.6 Calculation of Photoluminescence Decay Rate Constants

As a qualitative measure to confirm the observed changes in non-radiative decay between the control and TOPO treated samples, we model the PLQE data taking into account non-radiative and radiative monomolecular recombination, bimolecular recombination,[6,7] and Auger recombination,[8] according to equation S1:

$$PLQE = \frac{k_r N + k_b N^2}{k_{nr} N + k_r N + k_b N^2 + k_A N^3} \text{ x } 100\% \qquad \text{(S1)},$$

Where k_{nr}, k_r, k_b, and k_A are the non-radiative monomolecular (trap-assisted), radiative monomolecular, bimolecular, and Auger recombination rate constants, respectively. We simulate and fit solutions to the data using equation S1 along with the experimentally measured excitation powers to obtain the generation rates (and hence carrier densities) for the fits. Under steady-state conditions the generation rate is equal to the total recombination rate. We report small variations in the fit parameters for the treated film: $k_r = 3.8 \text{ x } 10^4 \text{ s}^{-1}$ and $k_b = 4.0 \text{ x } 10^{-11} \text{ cm}^3 \text{ s}^{-1}$, compared to the control film: $k_r = 4.1 \text{ x } 10^4 \text{ s}^{-1}$ and $k_b = 3.5 \text{ x } 10^{-11} \text{ cm}^3 \text{ s}^{-1}$ when we constrain k_A to $4 \text{ x } 10^{-28} \text{ cm}^6 \text{ s}^{-1}$, consistent with

previous reports.[9,10] Whereas we observe k_{nr} = 9.1 x 10^5 s^{-1} for the TOPO treated film and k_{nr} = 6.6 x 10^6 s^{-1} for the control film. In Figure S9 we show the simulated solutions at carrier densities higher than those achieved in the PLQE experiments, showing a decrease in PLQE as the non-radiative Auger recombination begins to dominate at higher carrier densities, consistent with previous reports.[8]

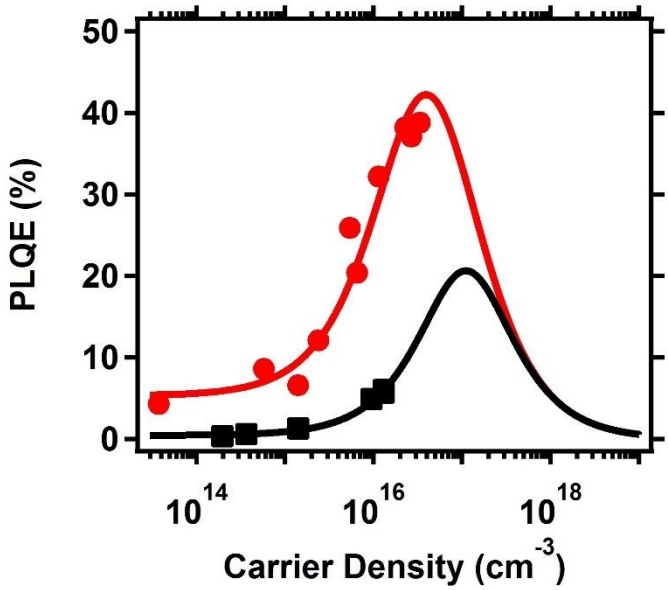

Figure S8. External PL quantum efficiency (PLQE) of the control (black) and TOPO treated films as a function of carrier density (532 nm, CW laser), reported in the main article as Figure 3c, but with x-axis as excitation power. Solid lines are fits to the data using the model described in equation S1.

S.7 Photoluminescence Spectral Shift Induced by Ligand Treatment

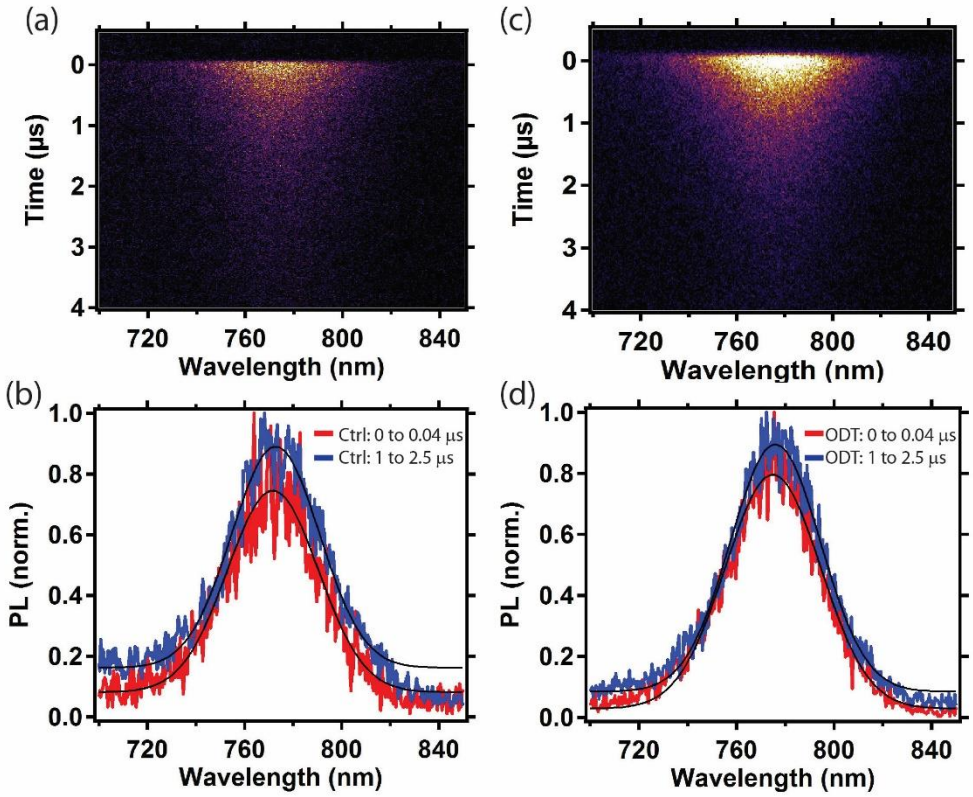

Figure S9. (a) Spectrally and temporally resolved PL emission of an untreated control film. (b) Time-integrated spectral slices from 0 to 40 ns and 1 to 2.5 μs of control in (a). Solid lines are Gaussian fits to the PL spectra, with peaks centered at ~773 nm. (c) Spectrally and temporally resolved PL emission of an octadecanethiol (ODT) treated film. (d) Time integrated spectral slices from 0 to 40 ns and 1 to 2.5 μs of the ODT treated film in (c). Solid lines are Gaussian fits to the PL spectra, with peaks centered at ~776 nm.

As briefly discussed in the main article, the spectral shift induced by ligand treatment could stem from several possibilities, including compositional changes at the grain boundaries, lattice strain, variations in crystallinity, and photon recycling.[11-15] To determine whether photon recycling contributes to the observed spectral shift, we performed temporally and spectrally resolved PL measurements with a streak camera setup. As Yamada et al. have previously reported for single crystal perovskite samples, photon recycling causes a slow spectral shift over the entire PL decay.[14] This is a result of the greater probability of higher energy photons being reabsorbed due to the greater spectral overlap with the absorption spectrum, this artificially red-shifts the observed spectrum compared to the true spectrum.[13] For single crystal samples, Yamada et al. observed a ~30 meV spectral shift over a 1 μs time window. Here, we observe little to no spectral shifts in the control and treated films for representative time slices, which

suggests that photon recycling does not significantly contribute to the ligand induced spectral changes.

S.8 Fluorescence Image Characterization: Relative PL Intensity Changes of Grain Boundaries vs. Grain Interiors and Dark, Medium, vs. Bright Regions

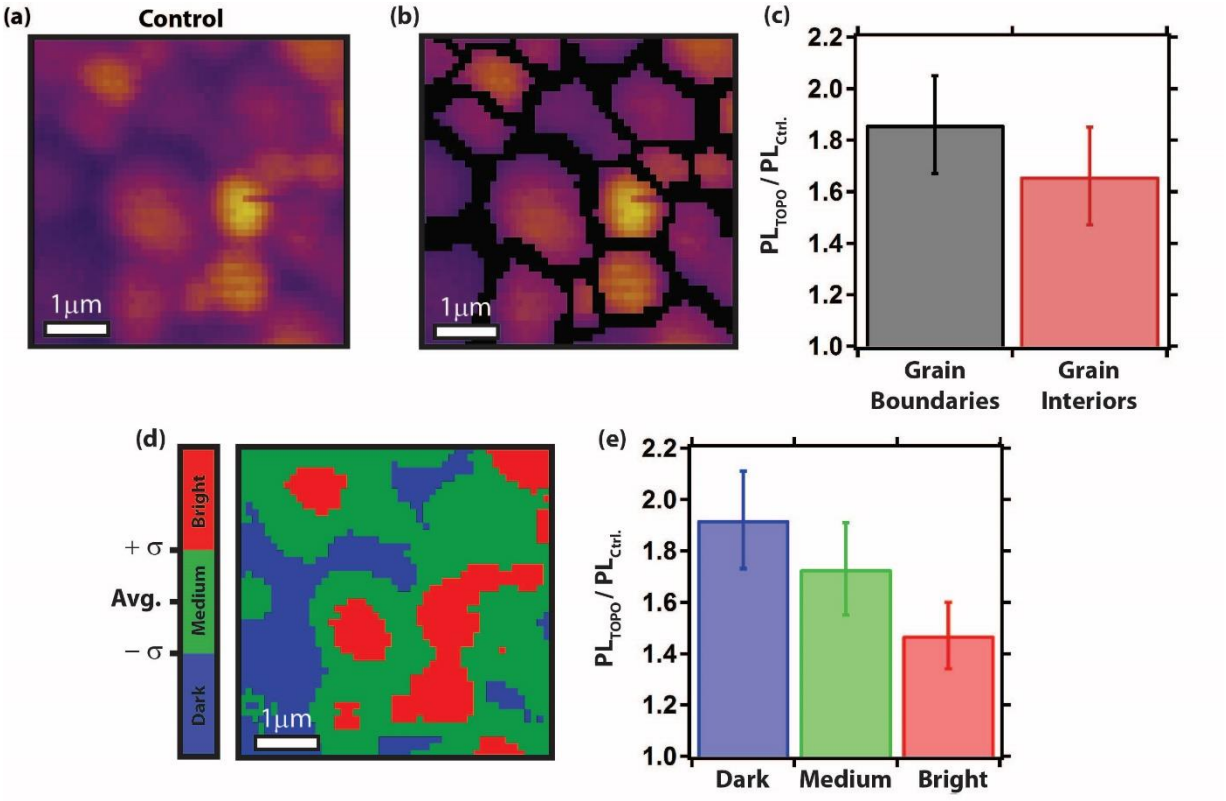

Figure S10. (a) Fluorescence image of the control film shown in Figure 4a in the main article before TOPO treatment and used as a reference to define separate grains and grain boundaries. (b) Image showing the regions that were manually defined as grain boundaries (black pixels) versus regions defined as grain interiors (colored pixels). (c) Average PL enhancements for grain boundaries (black) and grain interiors (red) using the pixel masks defined in (b) after TOPO treatment, errors bars are the standard deviations of the mean. (d) Three-color scale image showing the regions classified as dark (blue < -σ from average (avg.) PL intensity of control FI image (a)), medium (-σ from avg. ≤ green ≤ +σ from avg.) and bright (red > +σ from avg.). (e) Average PL enhancements for dark (blue), medium (green), and bright (red) regions defined in (d) after TOPO treatment, errors bars are the standard deviations of the mean. Regions that are initially dark have the largest relative improvements compared to the medium and bright regions after TOPO treatment.

In Figure S10, we analyze the relative improvements after TOPO treatment using two different definitions. In definition (1), we separate grains from grain boundaries by manually applying pixel masks to the images (Figure 10b). In Figure S10c, we report the

average PL improvements of pixels that fall under these classifications by dividing the fluorescence image after TOPO treatment (Figure 4b in the main article) by the control image (Figure S10a and 4a in the main article). Using definition (1), we report a larger improvement at the regions defined as grain boundaries as compared to grain interiors after TOPO treatment. In definition (2), we acknowledge that grain boundaries are not necessarily the regions with the lowest PL, consistent with our previous studies,[7] and therefore apply pixel masks based on the statistics of the image histogram. Following our previous study,[16] pixels which correspond to a PL intensity value that are $< -\sigma$ from the average (avg.) PL intensity of the control FI image are defined as dark regions (which could encompass grain boundaries as well as entire grains). Medium and bright regions are also defined: $-\sigma$ from the average $\leq$ medium $\leq +\sigma$ from the average, and bright $> +\sigma$ from the average. These definitions allow for an objective evaluation of the relative improvements of various regions depending on their initial PL. In Figure S10e, we report the average PL improvements of pixels that fall under these classifications by dividing the fluorescence image after TOPO treatment (Figure 4b in the main article) divided by the control image (Figure S10a and 4a in the main article). Using definition (2), we report a larger improvement at the regions defined as "dark" as compared to "bright". Interestingly, we note that many (but not all) dark pixels in Figure S10d also correspond to grain boundaries in Figure S10b.

Supplementary References:

1. Zhang, W.; Saliba, M.; Moore, D. T.; Pathak, S. K.; Horantner, M. T.; Stergiopoulos, T.; Stranks, S. D.; Eperon, G. E.; Alexander-Webber, J. A.; Abate, A. *et al.* Ultrasmooth organic-inorganic perovskite thin-film formation and crystallization for efficient planar heterojunction solar cells. *Nat. Commun.* **2015**, 6, 6142.

2. Lee, M. M.; Teuscher, J.; Miyasaka, T.; Murakami, T. N.; Snaith, H. J. Efficient hybrid solar cells based on meso-superstructured organometal halide perovskites. *Science* **2012**, 338, 643-647.

3. Jeon, N. J.; Noh, J. H.; Kim, Y. C.; Yang, W. S.; Ryu, S.; Seok, S. I. Solvent engineering for high-performance inorganic-organic hybrid perovskite solar cells. *Nat. Mater.* **2014**, 13, 897-903.

4. Saidaminov, M. I.; Abdelhady, A. L.; Murali, B.; Alarousu, E.; Burlakov, V. M.; Peng, W.; Dursun, I.; Wang, L.; He, Y.; Maculan, G. *et al.* High-quality bulk hybrid perovskite single crystals within minutes by inverse temperature crystallization. *Nat. Commun.* **2015**, 6, 7586.

5. de Mello, J. C.; Wittmann, H. F.; Friend, R. H. An improved experimental determination of external photoluminescence quantum efficiency. *Adv. Mater.* **1997**, 9, 230-232.

6. Stranks, S. D.; Burlakov, V. M.; Leijtens, T.; Ball, J. M.; Goriely, A.; Snaith, H. J. Recombination kinetics in organic-inorganic perovskites: Excitons, free charge, and subgap states. *Phys. Rev. Appl.* **2014**, 2, 034007.

7. deQuilettes, D. W.; Vorpahl, S. M.; Stranks, S. D.; Nagaoka, H.; Eperon, G. E.; Ziffer, M. E.; Snaith, H. J.; Ginger, D. S. Impact of microstructure on local carrier lifetime in perovskite solar cells. *Science* **2015**, 348, 683-686.

8. Johnston, M. B.; Herz, L. M. Hybrid perovskites for photovoltaics: Charge-carrier recombination, diffusion, and radiative efficiencies. *Acc. Chem. Res.* **2016**, 49, 146-154.

9. Trinh, M. T.; Wu, X.; Niesner, D.; Zhu, X. Y. Many-body interactions in photo-excited lead iodide perovskite. *J. Mater. Chem. A* **2015**, 3, 9285-9290.

10. Saba, M.; Cadelano, M.; Marongiu, D.; Chen, F.; Sarritzu, V.; Sestu, N.; Figus, C.; Aresti, M.; Piras, R.; Lehmann, A. G. *et al.* Correlated electron-hole plasma in organometal perovskites. *Nat. Commun.* **2014**, 5, 5049.

11. Nie, W.; Tsai, H.; Asadpour, R.; Blancon, J. C.; Neukirch, A. J.; Gupta, G.; Crochet, J. J.; Chhowalla, M.; Tretiak, S.; Alam, M. A. *et al.* High-efficiency solution-processed perovskite solar cells with millimeter-scale grains. *Science* **2015**, 347, 522-525.

12. D'Innocenzo, V.; Srimath Kandada, A. R.; De Bastiani, M.; Gandini, M.; Petrozza, A. Tuning the light emission properties by band gap engineering in hybrid lead halide perovskite. *J. Am. Chem. Soc.* **2014**, 136, 17730-17733.

13. Pazos-Outon, L. M.; Szumilo, M.; Lamboll, R.; Richter, J. M.; Crespo-Quesada, M.; Abdi-Jalebi, M.; Beeson, H. J.; Vrucinic, M.; Alsari, M.; Snaith, H. J. *et al.* Photon recycling in lead iodide perovskite solar cells. *Science* **2016**, 351, 1430-1433.

14. Yamada, Y.; Yamada, T.; Phuong, L. Q.; Maruyama, N.; Nishimura, H.; Wakamiya, A.; Murata, Y.; Kanemitsu, Y. Dynamic optical properties of ch3nh3pbi3 single crystals as revealed by one- and two-photon excited photoluminescence measurements. *J. Am. Chem. Soc.* **2015**, 137, 10456-10459.

15. Wu, B.; Nguyen, H. T.; Ku, Z.; Han, G.; Giovanni, D.; Mathews, N.; Fan, H. J.; Sum, T. C. Discerning the surface and bulk recombination kinetics of organic-inorganic halide perovskite single crystals. *Adv. Energy Mater.* **2016**, 1600551.

16. deQuilettes, D. W.; Zhang, W.; Burlakov, V. M.; Graham, D. J.; Leijtens, T.; Osherov, A.; Bulovic, V.; Snaith, H. J.; Ginger, D. S.; Stranks, S. D. Photo-induced halide redistribution in organic-inorganic perovskite films. *Nat. Commun.* **2016**, 7, 11683.

Appendix E: Supporting Information for Chapter 6

Methods

S.1: Determination of Δμ with Different Methods

Method 1: Full peak fit $\Delta\mu_{FP}$

Equation 1 in the main text relates the external spectral flux of radiative emission to the conduction band and valence band quasi-Fermi levels and the spectral absorption coefficient, which is expressed in equation S1:

$$I_{PL}(E) = \left\{\frac{2\pi E^2}{h^3c^2}\right\} \cdot \left\{\frac{1}{exp\left(\frac{E-(E_F^{CB}-E_F^{VB})}{kT}\right)-1}\right\} \cdot \{a(E, E_F^{CB}, E_F^{VB}, T)\} \quad \text{(S1)}$$

Where h is Planck's constant ($4.136\text{x}10^{-15}$ $eV{\cdot}s$), c is the speed of light ($2.998\text{x}10^{8}$ m/s), k is the Boltzmann constant ($8.617\text{x}10^{-5}$ eV/K), ε is the photon energy in eV, $a(\varepsilon, E_F^{CB}, E_F^{VB}, T)$ is the occupation and temperature dependent spectral absorptivity, and I_{PL} is the spectral photoluminescence emission flux in units of $photons/(m^2{\cdot}s{\cdot}eV)$. The first expression in brackets is the photon density of states for a blackbody surface (Lambertian emission). The second expression in brackets is the Bose-Einstein distribution describing a photon population in quasi-thermal equilibrium with both charge-carrier populations and the lattice of the semiconductor. The third expression in brackets is the dimensionless absorptivity and includes effects from reflectivity, and occupation in the conduction and valance bands given by the Fermi functions, $f_c(\varepsilon, E_F^{CB}, T)$ and $f_v(\varepsilon, E_F^{VB}, T)$, respectively. The net effect from band occupation, $(f_v - f_c)$, which includes stimulated emission, may be factored out from the density-of-states based absorption coefficient, α, and the resulting absorptivity may be expressed as:

$$a(E, E_F^{CB}, E_F^{VB}, T) = \frac{(1-R)\cdot\left(1-Exp\left(\alpha(E)\cdot d\cdot(f_v(E,E_F^{VB},T)-f_c(E,E_F^{CB},T))\right)\right)}{1-R\left(1-Exp\left(\alpha(E)\cdot d\cdot(f_v(E,E_F^{VB},T)-f_c(E,E_F^{CB},T))\right)\right)} \quad \text{(S2)}$$

Where d is the film thickness. By assuming equal effective masses for electrons and holes and an intrinsic material, the quasi-Fermi levels will split symmetrically about the middle of the bandgap, and the occupation factor may be simplified.

$$f_v(E, E_F^{VB}, T) - f_c(E, E_F^{CB}, T) = 1 - \frac{2}{Exp\left(\frac{E-\left(E_F^{CB}-E_F^{VB}\right)}{2kT}\right)+1} = 1 - \frac{2}{Exp\left(\frac{E-\Delta\mu}{2kT}\right)+1} \quad \text{(S3)}$$

In the low reflectivity limit, equations S1-S3 give an expression for the externally emitted photoluminescence flux spectrum as a function of the quasi-Fermi level splitting, density-of-states based absorption coefficient, and temperature. A further simplification may be

made by taking a partial Taylor expansion of the absorptivity and keeping the first order term.[1,2]

$$I_{PL}(E) = \left\{\frac{2\pi E^2}{h^3 c^2}\right\} \cdot \left\{\frac{1}{exp\left(\frac{E-\Delta\mu}{kT}\right)-1}\right\} \cdot \{1 - Exp(-\alpha(E)d)\} \cdot \left\{1 - \frac{2}{Exp\left(\frac{E-\Delta\mu}{2kT}\right)+1}\right\} \quad \text{(S4)}$$

Note that for the case where the lowest energy emitted photons are several units of kT greater than $\Delta\mu$, the occupation factor, (f_v- f_c), approaches unity, the Wien approximation may be made and the emission simplifies to:

$$I_{PL}(E) = \left\{\frac{2\pi E^2}{h^3 c^2}\right\} \cdot \left\{Exp\left(\frac{-(E-\Delta\mu)}{kT}\right)\right\} \cdot \{1 - Exp(-\alpha(E)d)\} \quad \text{(S5)}$$

This simplification is reasonable for the data we present in this work, however in fitting the absolute intensity peaks presented in the main text, we used the expression accounting for occupation given in equation (S4). We assume here that reflectivity has a negligible impact on the fit $\Delta\mu$. This assumption leads to a maximum $\Delta\mu$ underestimation of approximately 6 meV, determined by $\Delta\mu' - \Delta\mu = kT\ ln(1-R)$ when R is about 20%.

Method 2: Radiative limit of V_{OC} using relation derived by Ross[3] ($\Delta\mu_{\eta ext}$)

Using the radiative limit quasi Fermi-level splitting, $\Delta\mu_{rad}$, calculated in section S.3, equation (S6) is used as another method to confirm the $\Delta\mu$ reported in the main article and has now been employed by several groups to approximate V_{OC} based on the external photoluminescence quantum efficiency (η_{ext}) in perovskites.[4-6]

$$\Delta\mu_{\eta ext} = \Delta\mu_{rad} - kT\ |\ln(\eta_{ext})| \quad \text{(S6)}$$

At an above bandgap illumination intensity equivalent to 1-Sun conditions (60 mW/cm^2, see S.4), we report a η_{ext} of 0.92 ± 0.50% for the control film and 20.3 ± 5.6% for the TOPO-treated film. Using equation (S6), the radiative limit calculated in S.3, the measured η_{ext} values, and assuming a standard temperature of 298.15 K, we calculate $\Delta\mu$ to be 1.193 eV for the control and 1.276 eV for the TOPO-treated film. These values are broadly consistent with the $\Delta\mu$ values extracted from fitting with the photoluminescence model tabulated in S.3 below. Although this method is a good approximation, it requires a detailed calculation for the radiative limit $\Delta\mu$ as well as a nontrivial measurement of the sample temperature under illumination, which becomes increasingly important at low η_{ext}. For a range of realistic variations in the cell operating temperature (290-350 K) and a film with a η_{ext} of 0.65%, the calculated $\Delta\mu$ can vary by as much as 20 meV.

Method 3: High-energy tail fit ($\Delta\mu_{HT}$)

The quasi Fermi-level splitting and temperature can be abstracted from absolute intensity photoluminescence spectra by transforming the data into a logarithmic scale and performing a linear regression fit on the high-energy tail. To derive this relationship, the Wien approximation of the non-equilibrium Planck Law is given in equation (S7).

$$I_{PL}(\boldsymbol{E}) = \frac{2\pi}{h^3 c^2} \frac{\boldsymbol{E}^2 a(\boldsymbol{E})}{Exp\left(\frac{\boldsymbol{E}-\Delta\mu}{kT}\right)} \tag{S7}$$

Where I_{PL} is the spectral spontaneous emission flux, a is the absorptivity, and $\Delta\mu$ is quasi Fermi-level splitting. Considering only above-bandgap emission, the absorptivity is approximated to be a value of 1, and the equation can be rearranged as a linear expression as shown in equation (S8).

$$\boldsymbol{ln}\left(\frac{2\,\pi\,\boldsymbol{E}^2}{I_{PL}(\boldsymbol{E})h^3c^2}\right) = \frac{\boldsymbol{E}}{k\,T} - \frac{\Delta\mu_{HT}}{k\,T} \tag{S8}$$

By plotting the left-hand side of equation (S8) as a function of energy, the slope and Y-intercept of the high-energy trend are determined by the temperature and quasi Fermi-level splitting, respectively. We note that the assumption of having an absorptivity value of 1 breaks down when the peak position is red-shifted relative to the band-edge and also in the optically thin regime.

S.2: Sub-gap Absorptivity Model to Extract Band-Gap, Broadening Energy, Tail Exponent, and Temperature.

Absorption coefficient spectra have previously been modeled for GaAs, $Cu_2ZnSn(S,Se)_4$, and $Cu(In,Ga)Se_2$ by convolving a variable exponent tail distribution with a square-root density of states.[1]

$$\alpha(\boldsymbol{E}) = \alpha_0 G(\Delta\boldsymbol{E}) = \frac{\alpha_0}{\gamma\ 2\ \Gamma\left(1+\frac{1}{\theta}\right)} \int_{-\infty}^{\Delta\boldsymbol{E}} \mathrm{Exp}\left(-\left|\frac{\Delta\boldsymbol{E}'}{\gamma}\right|^{\theta}\right)\ \sqrt{\Delta\boldsymbol{E}-\Delta\boldsymbol{E}'}\ d\Delta\boldsymbol{E}' \tag{S9}$$

where α_o is a material-specific parameter related to its electronic structure; γ is a broadening energy (the Urbach energy for the case of $\theta = 1$); θ is the tail exponent, which was predicted to vary from 0.5 to 2 depending on the length scale of potential fluctuations in a material;[7] Γ is the gamma function; and $\Delta\boldsymbol{E} = \boldsymbol{E} - E_g$.

The convolution integral in equation (S9) is computation-intensive and is not amenable to iterative fitting methods. Therefore, we perform a change-of-variables for $G(\Delta\varepsilon)$ such that $G(\Delta\varepsilon/\gamma)$, and make a lookup table for a wide range of $\Delta\varepsilon/\gamma$ and θ values (ranging from 0.5 to 2). With this lookup table, we use a non-linear fit algorithm to fit absorption coefficient data – or, by extension, to fit photoluminescence peaks after modeling the absorptivity, with the absorption coefficient, using the Generalized Planck Law.

Fig. S1 shows box-and-whisker plots of the photoluminescence fitting parameter results from collecting several spectra across the area of both a control and treated film deposited on gold.

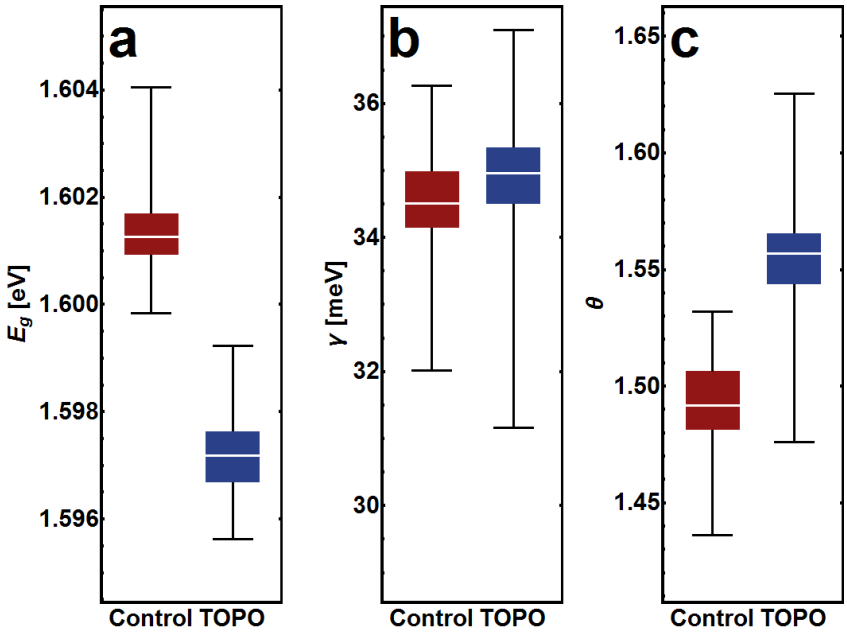

Figure S1. Subbandgap absorptivity model parameters extracted from absolute intensity photoluminescence spectra: (**a**) bandgap (E_g) , (**b**) broadening energy (γ) , and (**c**) tail exponent (θ). The sample size is 121 and the box-and-whisker statistics shown are the minimum, first quartile, median, third quartile, and maximum, respectively.

The median fit bandgap for the control and TOPO treated film were 1.601 eV and 1.597 eV, respectively. This slight red-shift of the band-edge can be recognized by observing the peak shift and broadening of the intense TOPO treated absolute intensity photoluminescence peak. The small red-shift in the bandgap energy for the TOPO treated sample could be attributed to a reduction in surface-dominated behavior and a larger contribution from the bulk (i.e. single crystal generally exhibited red-shifted optical properties)[8]. The median broadening energy for both the control and TOPO treated film was 34.4 meV. This value is closely coupled with the exponent, which were fit to be 1.49 and 1.56, for the control and TOPO treated films, respectively. Such a high fit exponent indicates potential disorder on the length scale exceeding the lattice constant. This is not surprising considering the plethora of disorder-inducing mechanisms that have been observed in these materials.[9-11]

S.3: Absolute Intensity photoluminescence Modeling, Fitting, and Radiative Limit Δμ Calculations

Calculations similar to Shockley and Queisser's derivations were carried out as described previously.[12] Here, we assume radiative losses only occur at the front surface (perfect back-reflector) and assume an illumination spectrum equivalent to the AM1.5GT solar spectrum. The radiative limit $\Delta\mu$ for the perovskite films deposited on a gold back reflector was calculated by following the general procedure summarized below:

(1) Extract the absorptivity spectrum using the absolute intensity photoluminescence spectrum.
(2) Use the absorptivity spectrum to calculate the generation rate under AM1.5GT conditions.
(3) Equate the generation rate to the total recombination rate described by photoluminescence equation and solve for $\Delta\mu$.

Detailed Description of Procedure:
(1) Absorptivity spectra were calculated from the absolute intensity photoluminescence spectra reported in Fig. 1a in the main text using the Generalized Planck Law solved for absorptivity as shown in equation (S10).

$$I_{PL}(E) = \left\{\frac{2\pi E^2}{h^3c^2}\right\} \cdot \left\{\frac{1}{exp\left(\frac{E-\Delta\mu}{kT}\right)-1}\right\} \cdot \{a(E)\} \cdot \left\{1 - \frac{2}{Exp\left(\frac{E-\Delta\mu}{2kT}\right)+1}\right\} \tag{S10}$$

Rearranged for absorptivity:

$$a(E) = I_{PL}(E) \frac{Exp\left(\frac{E-\Delta\mu}{kT}\right)-1}{E^2\frac{2\pi}{h^3c^2}\left(1-\frac{2}{Exp\left(\frac{E-\Delta\mu}{2kT}\right)+1}\right)} \tag{S11}$$

We used the $\Delta\mu$ and T extracted from fitting the photoluminescence spectrum with (S11), and the measured photoluminescence flux for each energy to calculate the absorptivity spectrum, as shown in Fig. S2a.

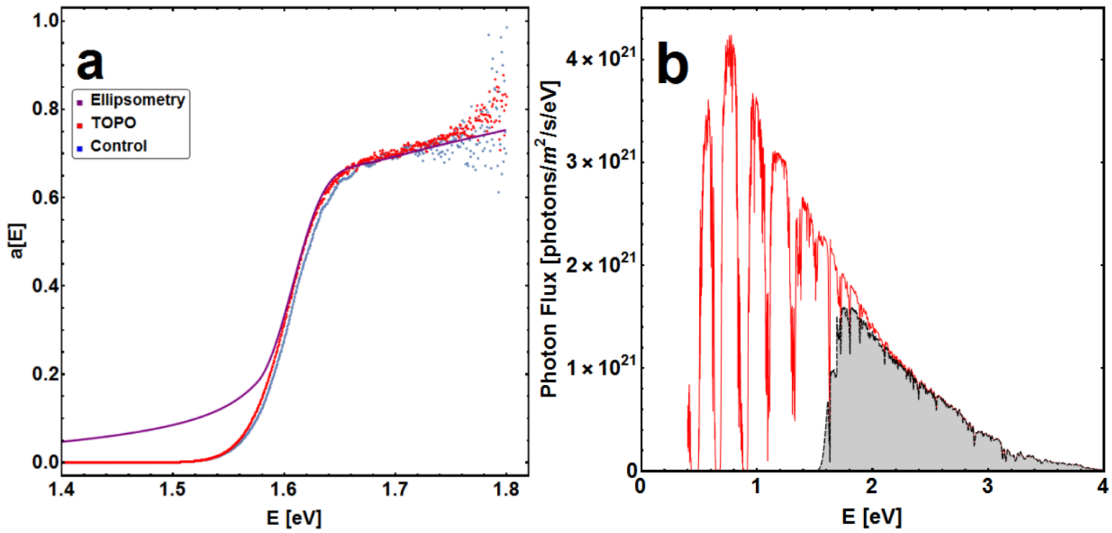

Figure S2. **a**, Absorptivity spectra calculated from TOPO and control absolute intensity photoluminescence spectra using the fit quasi-Fermi level splitting and temperature values. Absorptivity calculated from absorption coefficient spectrum determined by ellipsometry (See Fig. S13) is shown in purple as a reference. **b**, Generation rate

visualized as the integrated AM1.5 GT spectrum times the extracted hybrid perovskite absorptivity spectrum (shown as the grey area). The full AM1.5 GT spectrum is shown in red for reference.

(2) Integrate the photon flux from AM1.5GT get the total generation rate of the film (calculated here to be 1.45×10^{21} $m^{-2}s^{-1}$ and shown in Fig. S2b), which is consistent with other reports[13]. Solve for $\Delta\mu$ by setting the generation rate equal to the radiative recombination rate using the Generalized Plank Law (equation (S4)).

$$Generation\ Rate = \int I_{PL}(E, \Delta\mu) dE \tag{S12}$$

(3) The quasi Fermi-level splitting is found to be 1.319 eV when the generation rate is 1.45×10^{21} $m^{-2}s^{-1}$. Plotting the radiative limit absolute intensity photoluminescence spectrum using the Generalized Planck Law (Fig. S3) and the absorptivity spectrum of the TOPO treated sample shown in Fig. S2a. This spectrum is compared to the measured absolute intensity photoluminescence spectrum and to that of the Shockley-Queisser limit, for which $\Delta\mu$ is 1.280 and 1.326 eV, respectively.

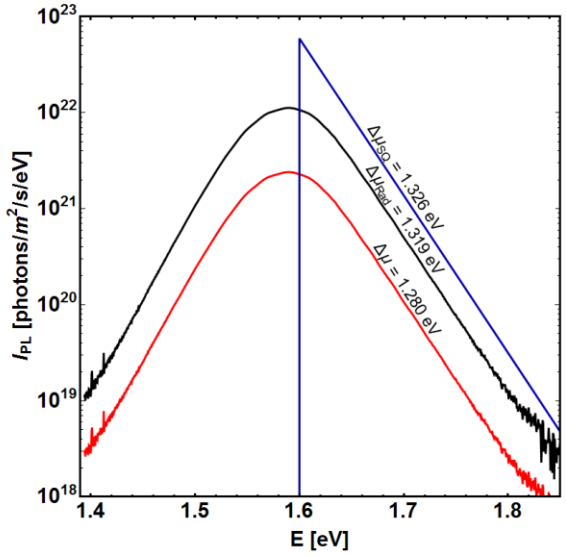

Figure S3. Measured absolute intensity photoluminescence spectrum (red line), calculated radiative limit absolute intensity photoluminescence spectrum (black line), and calculated radiative limit absolute intensity photoluminescence spectrum assuming a unit-step absorptivity (blue line).

Table S1 shows $\Delta\mu$, percent of Shockley-Queisser limit quasi Fermi-level splitting (χ), and temperature of a control and TOPO passivated film extracted using the method derived by Ross ($\Delta\mu_{n_{ext}}$)[14], a high energy tail fit ($\Delta\mu_{HT}$), and the full peak ($\Delta\mu_{FP}$) fit method reported in the main article. Here, the sample size is 121 and the errors reported are the 95% confidence intervals assuming a normal distribution.

Table S1. Material Parameters Calculated by Different Methods

Quasi Fermi-Level Splitting

	$\Delta\mu_{\eta_{ext}}$ [eV]	$\Delta\mu_{HT}$ [eV]	$\Delta\mu_{FP}$ [eV]
Control	1.193 ± 0.018	1.169 ± 0.020	1.208 ± 0.008
TOPO	1.276 ± 0.009	1.248 ± 0.103	1.280 ± 0.004

Percent of Shockley-Queisser Limit Quasi-Fermi Level Splitting

	$\chi_{\eta_{ext}}$ [%]	χ_{HT} [%]	χ_{FP} [%]
Control	89.9 ± 1.4	88.1 ± 1.5	91.1 ± 1.3
TOPO	96.2 ± 0.7	94.1 ± 0.8	96.5 ± 0.9

Film Temperature

	$T_{\eta_{ext}}$ [K]	T_{HT} [K]	T_{FP} [K]
Control	298*	303 ± 3	285*
TOPO	298*	307 ± 2	291*

*Temperature was assumed

S.4: Determination of One-Sun Equivalent Carrier Density Upon Excitation with Monochromatic Light

Photovoltaic devices are typically measured under standard AM1.5 conditions, where calculated steady state charge carrier densities are generally 1 x 10^{15} cm^{-3} for perovskite thin films.[13,15,16] Since both η_{ext} and η_{int} are strongly dependent on carrier density,[5,13] these values should be reported at an excitation power that generates a steady state charge carrier density comparable to AM1.5.

To perform this approximate calibration, we set the absorbed photon flux (ϕ) from the global tilt AM1.5 (AM1.5GT) spectrum equal the absorbed photon flux from a laser excitation source. equation (S13) can be simplified by assuming the laser is a monochromatic source (L_{λ_i}) and any differences in the bandwidths between E_λ and L_λ have been taken into account (S14). According to this definition, we calculate the excitation power to be 60 mW/cm^2 for 532 nm laser excitation and using a typical optical density spectrum for a thin film fabricated in our lab.

$$\varphi = \frac{\sum_\lambda E_\lambda \lambda \left(1-10^{-2OD_\lambda}\right)\Delta\lambda}{hc} = \frac{\sum_\lambda L_\lambda \lambda \left(1-10^{-2OD_\lambda}\right)\Delta\lambda}{hc} \quad \text{(S13)}$$

$$L_{\lambda_i} = \frac{\sum_\lambda E_\lambda \lambda \left(1-10^{-2OD_\lambda}\right)}{\lambda_i \left(1-10^{-2OD_{\lambda_i}}\right)} \quad \text{(S14)}$$

Where E_λ is the spectral irradiance value of AM1.5GT at a given wavelength (λ), L_λ is the spectral irradiance value of the laser source at a given wavelength (λ), OD_λ is the optical density at λ, $\Delta\lambda$ is the spectral bandwidth, h is Planck's constant, c is the speed of light. In this approximation, we assume that light reflects of the back reflector (see sample preparation details in the main article), and therefore passes twice ($2OD\lambda$) through the active layer with negligible optical interference.

S.5: Absolute Intensity Photoluminescence Spectra Calibration

We use a blackbody cavity at a temperature of 1050 °C to perform both the spectral shape correction and the absolute intensity spectral photon flux calibration for the confocal photoluminescence instrument used in this study. Fig. S4 shows the geometry of the blackbody source emission cone and the confocal objective collection cone.

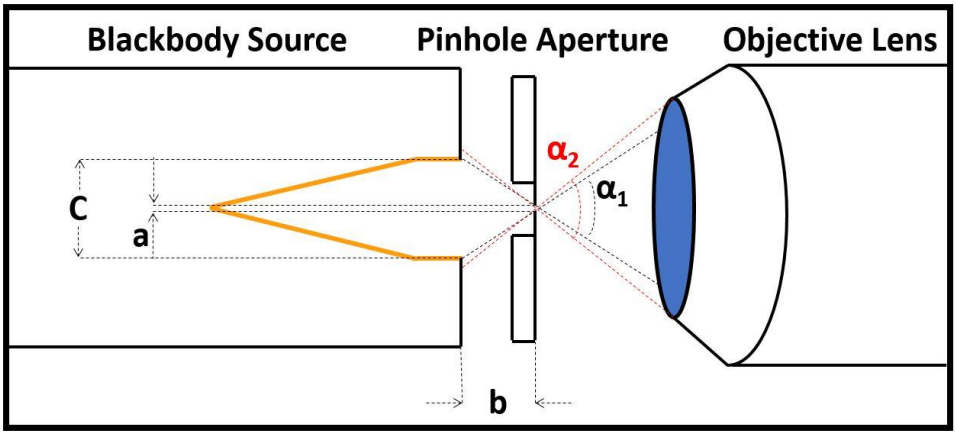

Figure S4. The blackbody calibration geometry. The blackbody source (left), having maximum cavity diameter *C*, is masked and columnated by a pinhole aperture (middle) having a diameter *a* and is offset from the blackbody cavity entrance by *b*. After the pinhole, the blackbody source is slightly collimated by the pinhole such that the intensity distribution is Lambertian from normal incidence to an angle of $\alpha_1/2$. This cone angle is compared to the collection cone angle $\alpha_2/2$, the microscope objective one-half angle aperture.

The calibration is performed by collecting a spectrum of the NIST calibrated blackbody source through a pinhole aperture of known diameter and setting the spectral photon flux collected to that determined by equation (S15).

$$I_{BB}(\boldsymbol{E}) = \left\{\frac{2\pi \boldsymbol{E}}{h^3 c^2}\right\}\left\{\frac{1}{exp\left(\frac{\boldsymbol{E}}{kT}\right)}\right\} \quad \text{(S15)}$$

Where I_{BB} is the spectral blackbody photon flux and E is the photon energy. Equation (S15) assumes a Lambertian angular distribution, which is valid so long as the microscope objective is completely filled by the blackbody emission cone. Otherwise, any underfilling of the microscope objective collection cone can be accounted by using a

geometric correction factor. To calculate this correction factor, one must first calculate the blackbody emission cone angle using equation (S16).

$$\alpha_1 = 2\,Tan^{-1}\left(\frac{a-c}{2\,b}\right) \tag{S16}$$

Where α_1 is the emission cone angle, a is the pinhole aperture diameter, c is the maximum blackbody cavity diameter, and b is the distance between the blackbody entrance and the pinhole. This emission cone angle must be compared to the collection cone angle of the microscope objective, calculated using equation (S17).

$$\alpha_2 = n\,Sin^{-1}(NA) \tag{S17}$$

Here, α_2 is the collection cone angle, n is the index of refraction of the imaging medium, and NA is the numerical aperture of the objective. These parameters are summarized in Table S2.

Table S2. Blackbody Calibration Geometry Parameters

Variable	Description	Value
C	Maximum blackbody cavity diameter	6.35 mm
b	Distance between aperture plane to blackbody cavity entrance	13 mm
a	Aperture diameter	0.01 mm
α_1	Blackbody cavity emission cone angle	27.4°
α_1	Objective lens collection cone angle	29.0°
Ω_1/ Ω_2	Solid angle correction factor	0.895
$f(\Omega_1)/f(\Omega_2)$	Cosine-corrected factor	0.898

An Olympus MPLN 10x objective is used for the confocal photoluminescence experiments, which has an NA = 0.25. The solid angle of the emission and collection cones can be found by using equation (S18) and the cone angles α_1 and α_2, respectively.

$$\Omega = 2\pi(1 - Cos[\alpha/2]) \tag{S18}$$

Where Ω is the solid angle of either the emission cone or the collection cone. Table S2 shows the blackbody emission cone fills 89.5% of the collection cone. Alternatively, the Lambertian distribution can be considered, which requires multiplying the surface integration in spherical coordinates by a factor of Cos(α). The result of this integration is shown in equation (S19).

$$f(\Omega) = \pi(1 - Cos^2[\alpha/2]) \tag{S19}$$

Where $f(\Omega)$ is the cosine weighted surface integral over the solid angle of either emission or collection. The extent to which the collection cone is underfilled by the blackbody

emission is calculated using this approach to be 89.8%, very similar to the simple fraction of the solid angles. This similarity is due to the small collection and emission angles. There would be a bigger difference between the solid angle and the Lambertian-corrected value for larger numerical apertures, since the Lambertian distribution tends to 0 as the collection angle approaches 90°. Therefore, we use a geometric correction value of 0.895 to correct the absolute intensity photoluminescence spectra.

The accuracy of the integrating sphere setup for measuring external photoluminescence quantum efficiency was verified using a known fluorescence standard. A solution of the Rhodamine 6G at a concentration of 9.91×10^{-6} M in ethanol was prepared by serial dilution. The solution was dispensed into a 10 mm path-length cuvette for placing in the center-mount position of the integrating sphere. The excitation wavelength used was 487 nm, which was obtained by filtering a halogen lamp with a monochromator. Fig. S5 shows the excitation and fluorescence spectra, and the measured photoluminescence quantum efficiency was determined to be 93.3 ± 2.0% (N = 5), which agrees with the known photoluminescence quantum efficiency of Rhodamine 6G (94%).[17]

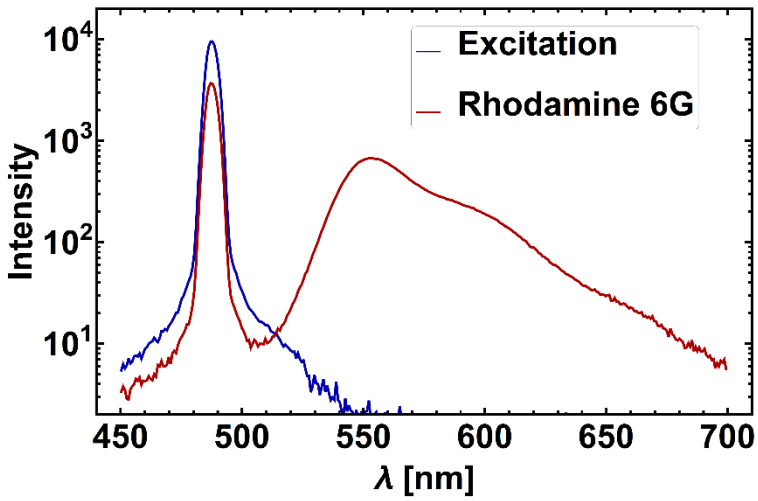

Figure S5: Spectra collected in the integrating sphere instrument of (blue) pure ethanol, and (red) Rhodamine 6G in ethanol at a concentration of 9.91×10^{-6} M.

The confidence interval spectra for the spatially varied data collected by the confocal instrument and compared it to the integrating sphere spectra of the same treated and untreated sample. These are shown in Fig. S6.

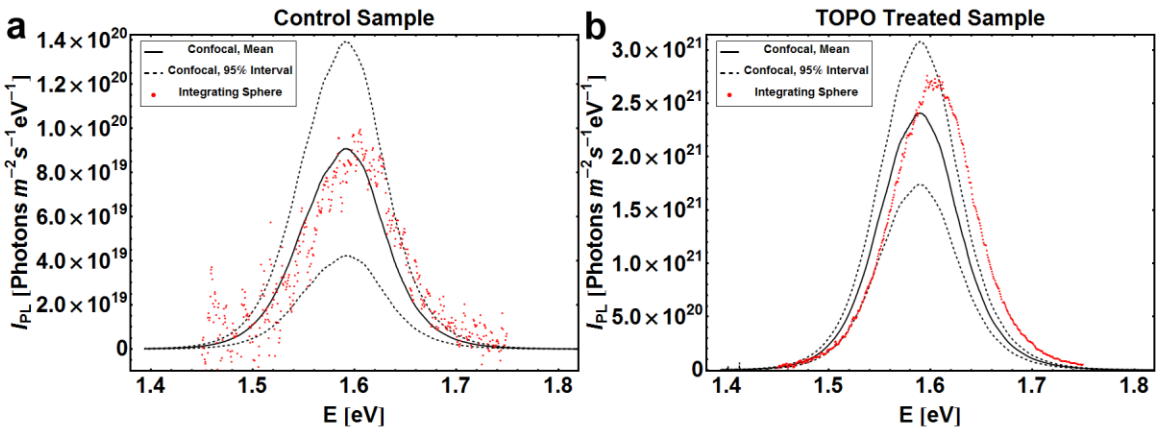

Figure S6. Comparison between the independently calibrated confocal and integrating sphere spectral photoluminescence flux data of (**a**) the untreated sample and (**b**) the TOPO treated sample. The dashed lines and solid black lines represent the 95% confidence interval and mean spectra, respectively, capturing the spatial variation within the sample. The red data represent the integrating sphere data calibrated using a power meter measurement of the incident laser light.

The integrating sphere data falls within the confidence interval of the spatial statistics collected by the confocal instrument over a majority of the peak for both the control and TOPO treated sample, including the region of maximum intensity. It is important to note that the high energy tail of the integrating sphere spectra fall outside of the 95% confidence interval of the confocal instrument spectra. This is likely due to the apparent peak shift between the spectra collected by the two instruments. For all confocal measurements, the spectrometer position is calibrated daily using a two-point calibration (the 0-order reflection of the grating and the silicon Raman peak).

The results can be further compared by looking at the integrated photoluminescence flux of the spectra collected with both the confocal instrument and the integrating sphere in Table S3.

Table S3. Total Photoluminescence Flux [photons/(s•eV•m^2)]

	Integrating Sphere	Confocal Measurement
Control	9.89×10^{18}	$9.45 \times 10^{18} \pm 5.08 \times 10^{18}$
TOPO	2.78×10^{18}	$3.35 \times 10^{20} \pm 9.3 \times 10^{19}$

Additionally, we can use the absorbed photon flux from the integrating sphere data (the absorbed photon flux was not measured using the confocal instrument and is not needed for the $\Delta\mu$ analysis) to calculate the external photoluminescence quantum efficiency as shown in Table S4.

Table S4. External Photoluminescence Quantum Efficiency [%]

	Integrating Sphere	Confocal Measurement
Control	0.96	0.92 ± 0.50
TOPO	23.5	20.3 ± 5.6

For both the total photoluminescence flux and the external photoluminescence quantum efficiency, the integrating sphere values fall within the confidence interval of the confocal instrument measured value. We note that the above integrating sphere photoluminescence quantum efficiency measurement of 23.5% is not the highest value that was measured during this study, however it is from a representative sample measured by the two instruments.

S.6 Extracted Quasi-Fermi Level Splittings ($\Delta\mu$) of Films Compared to Measured V_{OC}'s of Hybrid Perovskite Devices.

Fig. S7 shows the quasi-Fermi level splitting ($\Delta\mu$) determined in this report as well as $\Delta\mu$'s for other mixed halide formulations determined by our group[18] compared to the open circuit voltages (V_{OC}) reported in state-of-the-art devices as a function of bandgap. We first note that the method used to determine $\Delta\mu$ in this report has predicted V_{OC} values consistent with photovoltaic devices across a range of perovskite bandgaps. In particular, our previous results ($\Delta\mu$, Braly) on unpassivated films,[18] trend well with unpassivated devices, where the percent of the Shockley-Queisser limit quasi Fermi-level splitting (χ) is often constrained to values below 87.5% as previously noted by Tress (see Section S.3 for calculation of χ).[19] Some values lie above this trendline including V_{OC}'s demonstrated by Correa-Baena *et al.* at 1.23 V, where the doping concentration of the p-type hole transport layer (HTL) was optimized to control the non-radiative recombination at the perovskite/HTL interface and Saliba *et al*. at 1.24 V, where the authors incorporate rubidium into the perovskite precursor solution.[20,21] As shown in Fig. S7, these values reach approximately 92% of the Shockley-Queisser V_{OC} limit. Here the $\Delta\mu$ we extract (96.5%) is greater than the highest voltage devices, suggesting that a film with this level of quality and optimized interfaces could produce record photovoltaic devices.

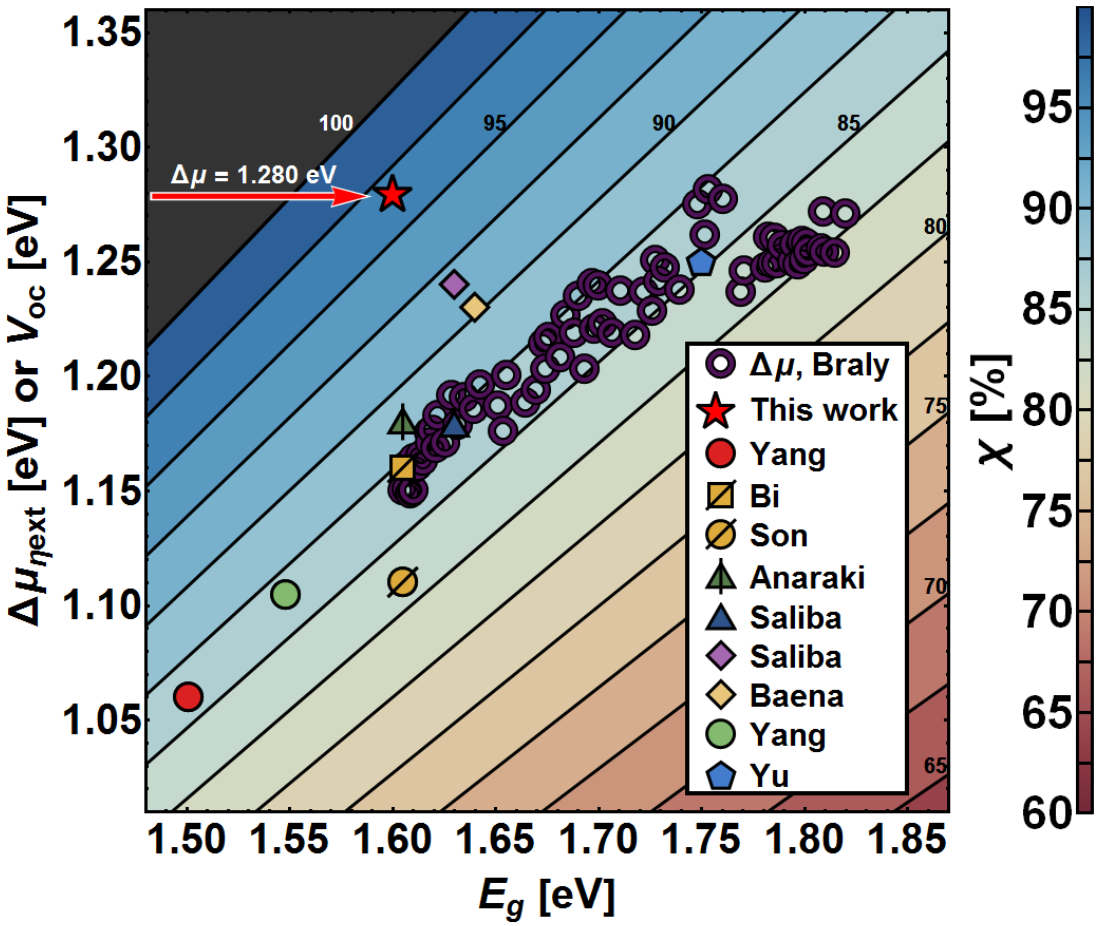

Figure S7. Comparison of $\Delta\mu_{\eta ext}$ to reported device V_{OC} values plotted against reported or EQE- or UV–vis-extracted bandgap. Contours represent constant percentages of the Shockley-Queisser limit quasi Fermi-level splitting χ [%], and the color scale for χ is shown to the right. References for the values in the chart are Braly,[18] Yang,[22] Bi,[6] Son,[23] Anaraki,[24] Saliba,[21] Baena,[20] Yang,[25] and Yu.[26]

S.7: Determination of Loss Factors of Multi-Metal Back Reflector Substrate for Calculation of Internal Photoluminescence Quantum Efficiency (η_{int})

As described in the main text, the perovskite layer is deposited on a single substrate with multiple back reflector metals having different reflectivity values, allowing us to tune the amount of parasitic absorption within the stack, while still maintaining the same quality of perovskite layer on each back reflector. To simulate the optical losses of the perovskite photoluminescence, we characterize the total loss within these substrates before perovskite deposition by measuring the angle-averaged specular reflectance from 0-14.5° using a bright-field microscope equipped with a 790 nm LED (Fig. S8) and a silicon wafer coated with bare gold for pixel value calibration (i.e. flatfield correction). We use the measured reflectivity values from imaging the multi-metal substrates with the 790 nm as a slight underestimation of the angle-averaged reflectivity, as this measured angular

distribution is close to the critical angle (~35°) subtended from the perovskite layer into the SiO_x layer (approximated using Snell's law and the index of refraction of the perovskite layer (n = 2.6) and SiO_x (n = 1.5)).[27] Based on these measurements, we report a loss factor of 2.9% for Au, 27.8% for Pd, 49.8% for Ti, and 78.5% for Si.

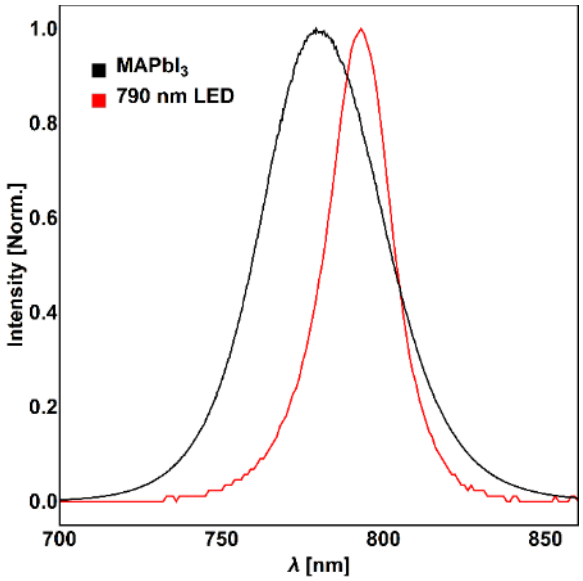

Figure S8. The normalized 790 nm LED spectrum (used to determine loss factor) versus the perovskite emission.

S.8 Determination of Internal Photoluminescence Quantum Efficiency using Multi-Metal Back Reflector Substrates

We use equation (S20) derived by Schnitzer *et al.* to fit η_{int} as a function of back reflector loss factor and η_{ext}. Here we discuss some of the assumptions made in the model and determine whether they are valid considering our samples.

$$\eta_{ext} = \frac{\eta_{int}/2n^2}{\eta_{int}/2n^2+(1-\eta_{int})+L/4\alpha_0 d_0} \quad \text{(S20)}$$

Assumptions in model:

- 100% transmission within critical angle
- Monochromatic emission
- Treat as photon gas (no depth-dependent carrier population)
  - Internal photoluminescence quantum efficiency is independent of back reflector metal
  - Perovskite/metal oxide and perovskite air interfaces are flat
  - Interference and waveguiding (i.e. thin-film effects) do not significantly change the average outcoupling efficiency/ Impact of outcoupling efficiency on extracted η_{int}.
  - The outcoupling efficiency does not significantly change after TOPO deposition

The first three assumptions are typical to simplify complex ray optics models and generally hold true for most materials.[28,29] The last four assumptions may be material-dependent, therefore we perform a set of experiments to verify if these assumptions are valid:

(S.8.1) Internal photoluminescence quantum efficiency is independent of back reflector metal.

The perovskite η_{int} is dependent on the steady-state carrier population (N) within the active layer according to equation (S21),[13]

$$\eta_{int} = \frac{k_b N^2}{k_{nr} N + k_b N^2 + k_A N^3} \quad \text{(S21)}$$

where k_{nr}, k_b, and k_A are the non-radiative monomolecular (trap-assisted), bimolecular, and Auger recombination rate constants, respectively.

Knowing this relationship, we experimentally determined whether the different back reflectors lead to different radiative recombination rates (numerator in S(20)) and total recombination rates (denominator in (20)) as function of excitation power. For a sample where these rates change, we would expect the curves to be shifted on the x-axis relative to one another, due to the different steady-state carrier densities maintained under continuous-wave illumination. Fig. S9 shows the photoluminescence intensity divided by the excitation power (where the fraction of power absorbed over the excitation power range was determined to be constant) versus the excitation power. We observe a negligible difference in the photoluminescence trends for the Au vs Si back reflector substrates at the region relevant to 1-Sun equivalent illumination intensity (60 mW/cm^2) and therefore conclude that assumption (S.8.1) is valid.

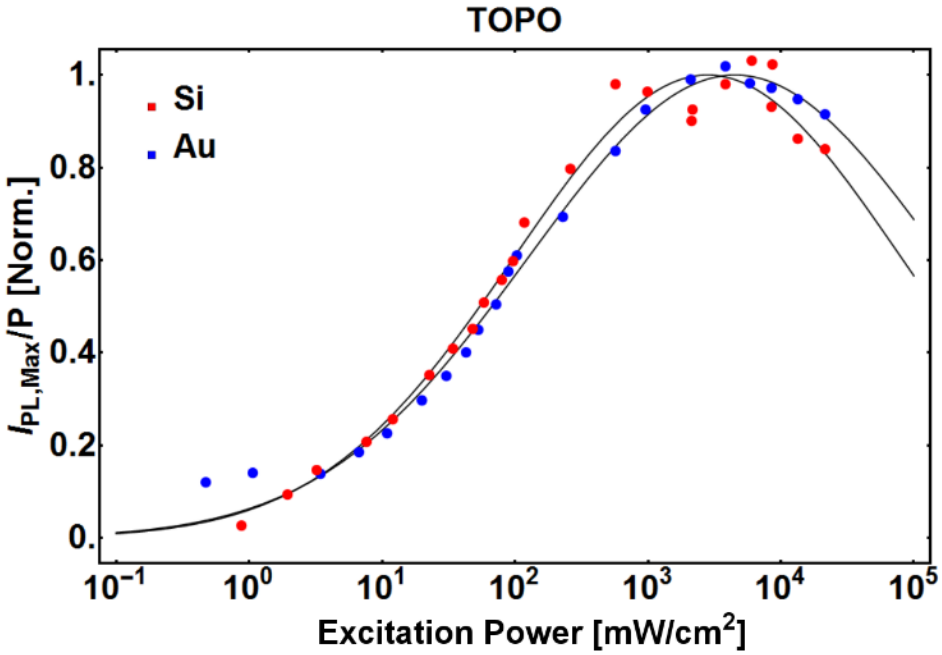

Figure S9. Plot of the photoluminescence intensity divided by the excitation power (*P*) versus excitation power for perovskite on a silicon (Si) back reflector substrate (red circles) versus a gold (Au) back reflector substrate (blue circles). Solid black lines are Gaussian fits, which were used as guides to the eye. The negligible difference in the photoluminescence trends between Au and Si back reflector substrates suggests the radiative recombination and total recombination rates are the same regardless of substrate. Samples were excited with a continuous-wave (CW) 532 nm laser and the Horiba LabRAM HR-800 upright microscope described in the main text.

(S.8.2) Perovskite/metal oxide and perovskite air interfaces are flat.

Equation (S20) assumes a smooth surface where the forward (perovskite/air) and backward (perovskite/SiO_x) escape probability can be approximated as $2 \times \frac{1}{4n^2}$ or $\frac{1}{2n^2}$ (7.4% for perovskite materials with n = 2.6) as previously done for epitaxially grown GaAs.[28] It has recently been shown by Richter *et al.* that surface texturing is an important parameter that determines the escape probability in perovskite films. In particular, by roughening the film surface (i.e. structures on the length scale of 100-1000 nm), they achieved a ~5-fold enhancement in the escape probability.[5] Here we measure both the SiO_x and perovskite layers to determine if the surface roughness is appreciable to modify the escape probability from the limiting case predicted for smooth surfaces. We note that the lead acetate fabrication protocol used in this study typically produces ultrasmooth and uniform perovskite layers, which are comparable to the best vapor-deposited films.[30] We further characterize our films by collecting topography maps using an atomic force microscope (Asylum Research MFP-3D BIO atomic force microscope, using 325 kHz silicon cantilevers from μmasch). Fig. S10a shows an AFM topography image of the SiO_x interface before perovskite deposition. We report a root mean-squared (RMS) surface roughness of 0.9 nm. Fig. S10b shows an AFM topography image of the

perovskite layer after deposition on the SiO_x layer, and report a RMS surface roughness of 16 nm. Similar surface roughness values have shown to have a negligible effect on luminance intensity for GaN LEDs when compared to untextured (smooth) surfaces,[31] and therefore we conclude assumption (S.8.2) to be valid.

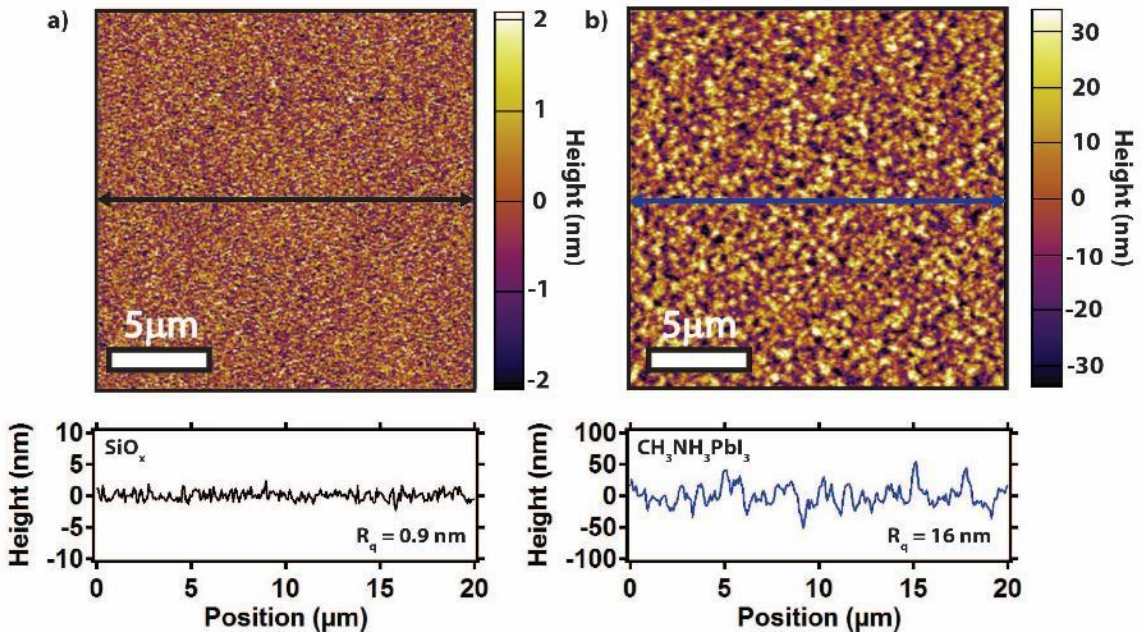

Figure S10. Atomic force microscope (AFM) topography images and line profiles of the electron-beam evaporated SiO_x layer on Au (**a**) and the spin-coated perovskite layer (**b**). (inset) root mean-squared (R_q) surface roughness values for each layer, SiO_x = 0.9 nm and $CH_3NH_3PbI_3$ = 16 nm.

(S.8.3) Interference and waveguiding (i.e. thin-film effects) do not significantly change the average outcoupling efficiency/ Impact of outcoupling efficiency on extracted η_{int}.
Interference and waveguiding are important considerations when studying the ray optics of thin film dielectric stacks[32]. We use the Stackpurcell solver from Lumerical (FDTD Solutions 2017b R2, v8.18.1298) to determine the transmitted power from a point dipole source within the active layer of the sample stack (red dot in Fig. S11a). This method uses the transfer-matrix-method (TMM) to determine the total transmission through the stack. Fig. S11b shows the integrated power density with respect the angle (0-180º) of emission and the wavelength (700-840 nm) normalized to the initial dipole power. This value is equivalent to the outcoupling efficiency and we assume that, under steady-state conditions, we can treat the photon population as a photon gas. We therefore average the depth-dependent outcoupling efficiency to obtain an average outcoupling efficiency of 6.08%, which is in close agreement with the 7.4% predicted by $1/2n^2$.

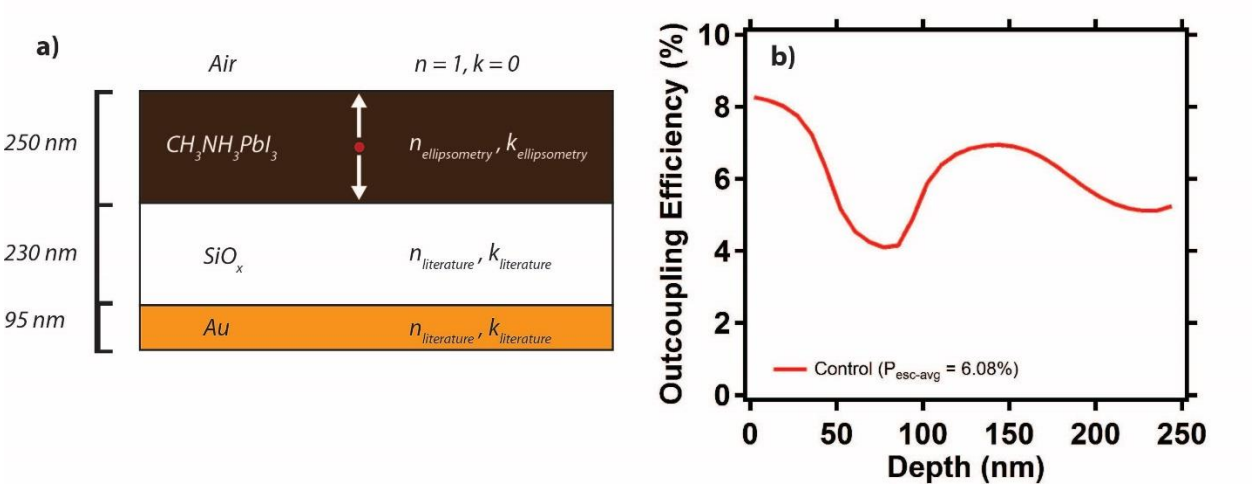

Figure S11. a, Schematic of sample stack used for thin-film simulations taking into consideration the real (n) and imaginary (k) parts of the dielectric function for each layer. **b**, Outcoupling efficiency versus depth of the perovskite emitter. The angle and spectrally integrated, depth-averaged outcoupling efficiency was determined to be 6.08%.

Next, we determine the sensitivity of equation (S20) to changes in outcoupling efficiency and how these affect the extracted η_{int} of the TOPO data set. As a lower limit of η_{int}, we assume an escape probability of $1/n^2$ and for and upper limit we assume an escape probability of $1/4n^2$.[33] Fig. S12 shows best fits to the data set and goodness of fits (R^2) for these limiting cases. Here the best fit is achieved when a $1/2n^2$ outcoupling efficiency is used, which results in the extracted η_{int} of 92% as reported in the main article. Fig. S12b shows the R^2 values for a whole range of possible outcoupling efficiencies, where the maximum R^2 value is achieved at 7.8%, which is similar to the $1/2n^2$ used in equation (S20) and equation (2) in the main article. This plot shows that equation (S20) is fairly sensitive to the outcoupling efficiency and therefore we believe that the internal η_{int} value that we report is indeed accurate.

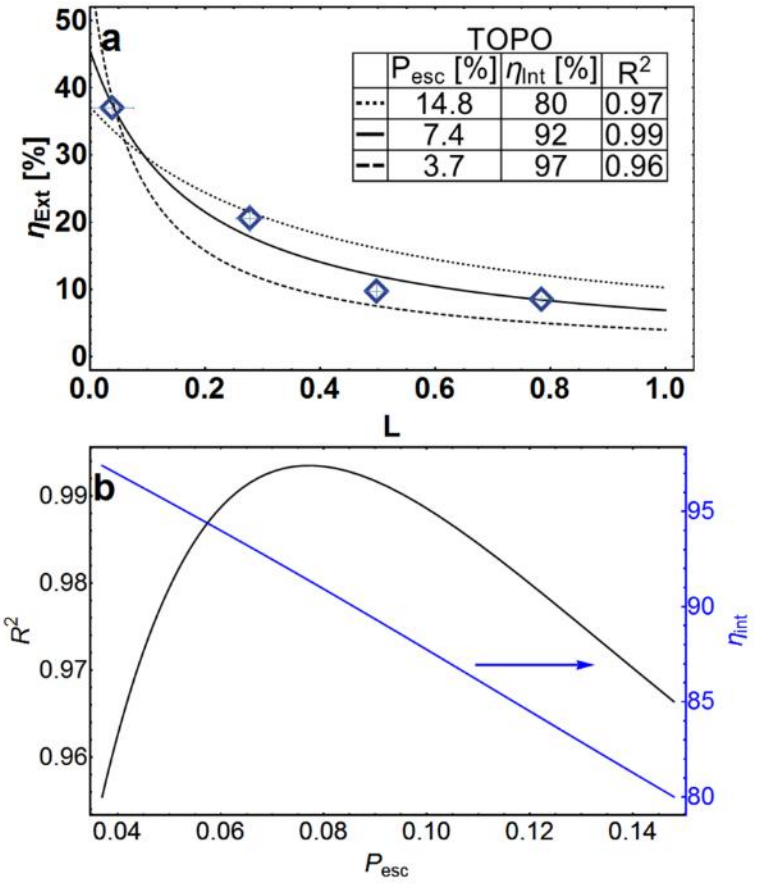

Figure S12. a, Fits to data using equation (S20) assuming the upper and lower limits of the outcoupling efficiencies. **b**, Goodness of fit (R^2) values (left axis) and the fit internal photoluminescence quantum efficiencies (right axis) for the TOPO data in a) as a function of escape probability.

(4) The outcoupling efficiency does not significantly change after TOPO deposition

The largest enhancements in photoluminescence quantum efficiency are often achieved by spincoating multiple 0.025 M TOPO surface treatments (i.e. ~3) without a solvent washing step. Washing with the ligand solvent often leads to a reduction and reinitialization of the photoluminescence, which is detrimental to maintaining high radiative efficiencies. Whether these multiple treatments result in the formation of a thin "capping layer" of unreacted TOPO on the surface which could modify the outcoupling efficiency (i.e. index matching) is an important consideration. Previously we proposed this contribution to be miniscule, considering that the improvements in photoluminescence quantum efficiency corresponded to a similar improvement factor in photoluminescence lifetime, where we note that an increase in outcoupling efficiency would actually result in the opposite trend in observed lifetime due to fewer reflections or recycling events. Here, we seek to separate these two possible contributing factors by first determining the thickness of the deposited TOPO layer and then determining how

this layer may modify the escape probability from the value $\frac{1}{2n^2}$ as described in equation (2) from the main text.

Spectroscopic ellipsometry was measured on $CH_3NH_3PbI_3$ and $CH_3NH_3PbI_3$/TOPO films on glass substrates using a J.A. Woollam M2000 ellipsometer. Measurements of the polarization state of reflected light (ψ and Δ) for three angles of incidence (55°, 65°, 75°) were taken with Scotch tape adhered to the back side of the glass substrates to scatter any backside reflections at glass/sample chuck interface. Transmittance also measured on the Woollam M2000 and was used as an additional data set to help constrain the fits for modelling the optical constants and thicknesses using the CompleteEASE software package. Fig. S13 a and b show the fits to the ψ and Δ data along with the transmittance data for the glass/$CH_3NH_3PbI_3$ sample. The n and κ values for the glass substrate were determined independently on a blank substrate and the $CH_3NH_3PbI_3$ layer was parametrized by adjusting the oscillator model reported previously by Shirayama et al.[34] The optical constants for $CH_3NH_3PbI_3$ determined from the fits are shown in Fig. S13c, and the thickness was determined to be 182.43 nm. The modelled thickness of the $CH_3NH_3PbI_3$ layer was in good agreement with the thickness measured on a Bruker Dektak profilometer (~180 nm). The ψ and Δ and transmittance data for the glass/$CH_3NH_3PbI_3$/TOPO sample were then fitted using a three layer model where the parameters for the glass/$CH_3NH_3PbI_3$ layers were fixed based on the previously determined model, and a Cauchy layer was added on top to model the TOPO. For simplicity, the data was modelled only within a transparent region of the sample (1400-1700 nm). The literature refractive index value for TOPO is reported to be ~1.45, however it is likely that this value would vary for a spin coated film of TOPO. Therefore, the data was modelled by fixing the "*A*" coefficient of the Cauchy model to different values to simulate wavelength independent refractive indices in the range of 1.3-1.6 and then allowing the thickness of the Cauchy layer to vary. Using this method, thicknesses in the range of ~18-25 nm were determined for the TOPO layer. Example fits for a refractive index of 1.45 are shown in Fig. S13 d and e.

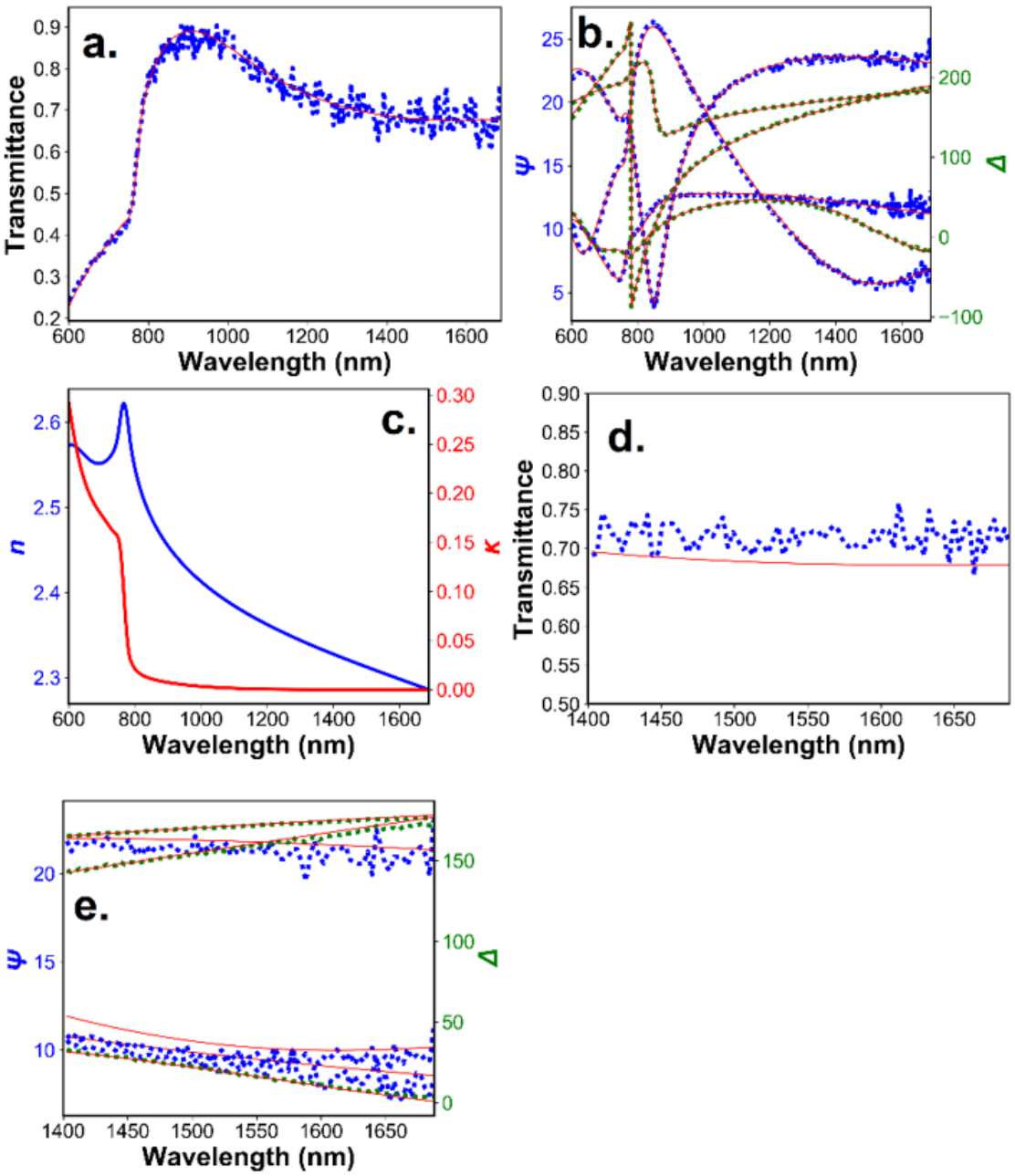

Figure S13. a and **b**, Fits to the transmittance and ψ and Δ data (ψ and Δ at 55°, 65°, 75° AOI) measured on a glass/$CH_3NH_3PbI_3$ sample (fitted model depicted by red solid lines). **c**, Optical constants of $CH_3NH_3PbI_3$ derived from the model used to fit the ellipsometry data of the glass/$CH_3NH_3PbI_3$ sample. **d** and **e**, Fits to the transmittance and ψ and Δ data (ψ and Δ at 55°, 65°, 75° AOI) measured on a glass/$CH_3NH_3PbI_3$/TOPO sample where the refractive index of the TOPO layer is fixed at a value of 1.45.

Next, we use this thickness (~20 nm) and use the transfer matrix method as described in (S.8.3) to determine how this thin layer effects the outcoupling efficiency. Fig. S14 shows the outcoupling efficiency as a function of depth with and without the thin TOPO layer. When averaged as a function of depth, the outcoupling efficiency for the sample stack with the TOPO layer is 6.32 % and without the TOPO layer is 6.08%, which is smaller than the errors in the internal photoluminescence quantum efficiency values reported in the main article and therefore we believe contributes little to the enhancements in η_{ext}.

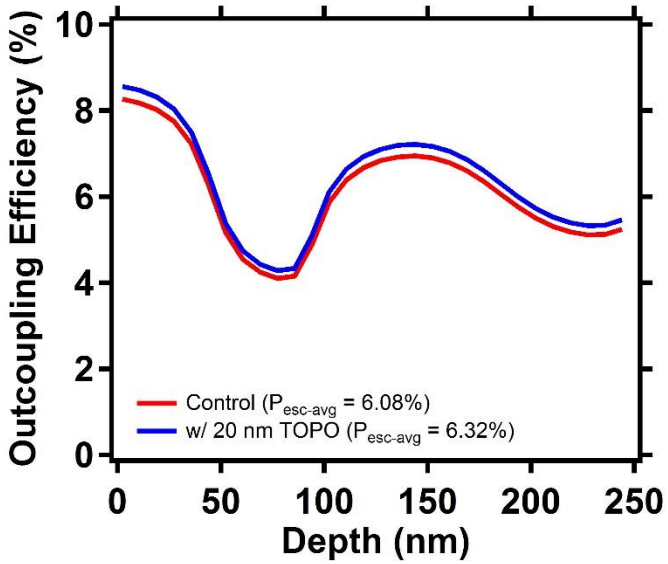

Figure S14. Outcoupling efficiency versus depth of the perovskite emitter. The angle-integrated, depth-averaged outcoupling efficiency was determined to be 6.32% for a film with a 20 nm layer of TOPO versus 6.08% without a TOPO layer.

To confirm the results from this simulation, we experimentally measure the improvements achieved without the presence of a capping layer. We submerged the perovskite film in a toluene solution with dissolved TOPO (0.025 M) and compared these improvements to those achieved when the TOPO is spincoated and a capping layer is formed. Fig. S15 shows the improvements are similar, suggesting improvements can be primarily attributed to reductions in non-radiative recombination and not changes in outcoupling.

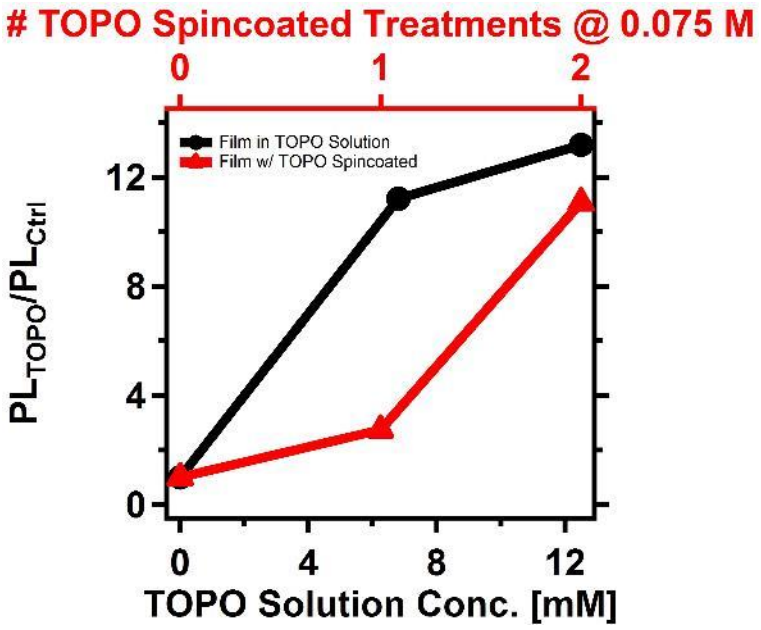

Figure S15. photoluminescence improvements of a TOPO treated film compared to a control film when the film is in a solution of TOPO in toluene at different concentrations versus the photoluminescence improvements when a TOPO solution is spincoated on top of the perovskite film.

S.9 Calculation of Photoluminescence Rate Constants from Intensity Dependent η_{ext}

We use equation (S21) for η_{int}, which takes into account non-radiative and radiative monomolecular recombination, bimolecular recombination,[15,35] and Auger recombination,[13] along with equation (S20), which defines the relationship between η_{int} and η_{ext}, to simulate and fit illumination intensity-dependent data presented in the main text. The fitting results are shown in Fig. S16, and the η_{ext} data reported in Fig. 4 in the main article is also shown in Fig. S17 on a linear scale.

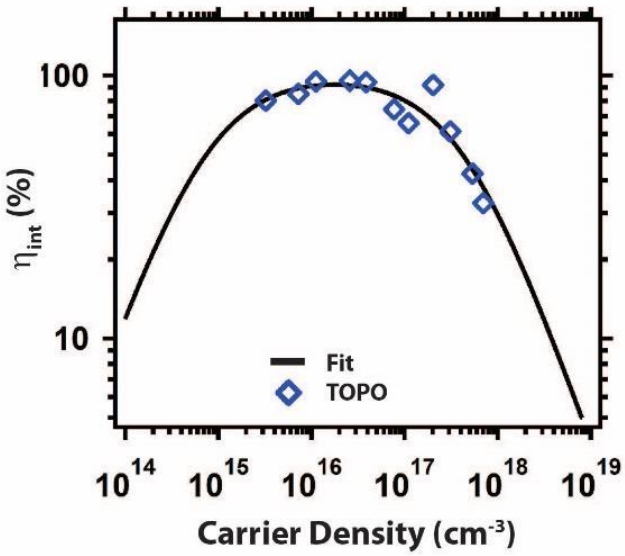

Figure S16. Internal photoluminescence quantum efficiency extracted using equation (S20) and a fit to the data using equation (S21).

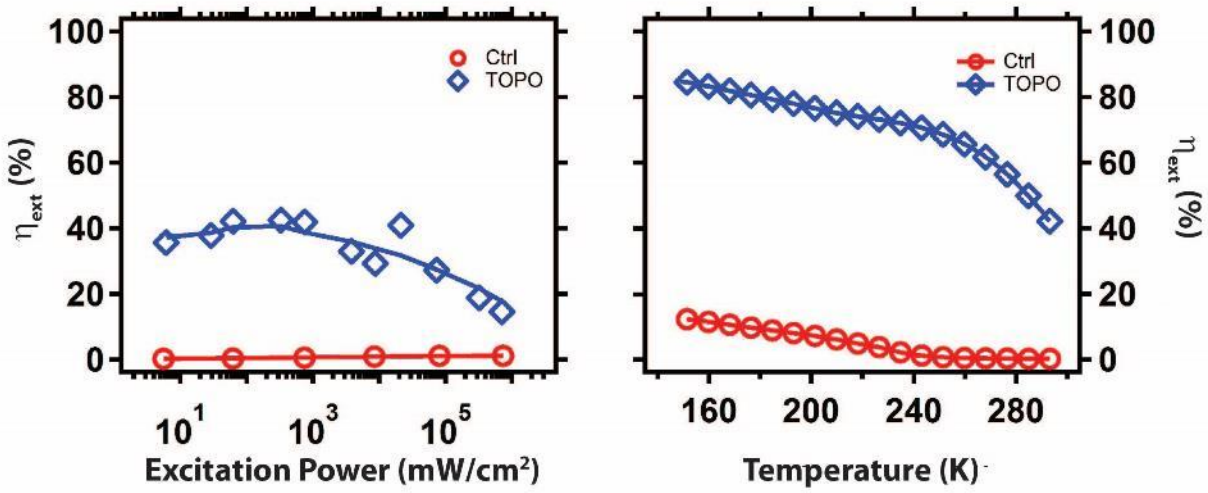

Figure S17. Photoluminescence spectroscopy measurements to determine the maximum achievable quantum efficiency under high excitation powers and low temperatures. **a**, Semi-log plot of intensity dependent η_{ext} for a control and TOPO treated film, showing a maximum η_{ext} of 1.2% and 40%, respectively. **b**, Linear plot of temperature dependent η_{ext} for the same control and TOPO treated films.

To perform the fits, we use the experimentally measured excitation powers to obtain the generation rates. We report k_{nr} = 1.7 x 10^{5} s^{-1}, k_b = 2.3 x 10^{-10} cm^3 s^{-1}, and k_A = 5.4 x 10^{-28} cm^6 s^{-1}, which are consistent with previous reports.[15,36,37] In particular, we confirm a similar monomolecular recombination rate constant from time-resolved photoluminescence as discussed in subhead S.10. We find that Auger recombination starts to dominate at carrier densities of ~4 x 10^{17} cm^{-3}, where the contribution is greater than 50 % of the total recombination rate.

S.10 Time-Resolved Photoluminescence Kinetics of Control and TOPO Treated Films

In order to verify the monomolecular rate constants we extract from fitting the intensity dependent η_{ext} data, we measured the low fluence time-resolved photoluminescence dynamics of both the control and TOPO treated films at 50 nJ/cm^2 per pulse (Fig. S18), which yield an initial carrier density (N_0) of ~ 1x10^{15} cm^{-3}.

We used a stretched exponential function to fit the decay traces at low excitation fluences, which is consistent with literature reports,[15,38,39] and indicative of a distribution of local monomolecular recombination rates resulting from heterogeneity in the local non-radiative decay rates. This decay law is typically encountered in systems with a distribution of local decay rates and the β factor can give information pertaining to a random distribution of site energies or a time dependent rate constant [40]. When $\beta = 1$ the decay function reduces to a single exponential and heterogeneity is negligible. When β is closer to 0, this represents a larger distribution (e.g. decay rates) and therefore more significant heterogeneity. We computed the average lifetime, $<\tau>$ of the stretched exponential distribution according to equation (S22):[41]

$$< t >= \frac{t_c}{b}\Gamma\left(\frac{1}{b}\right) \tag{S22}$$

where $\Gamma\left(\frac{1}{\beta}\right)$ is defined as the gamma function in equation (S23):

$$\Gamma\left(\frac{1}{b}\right) = \int_0^{\infty} x^{(1-b)/b} e^{-x}\, dx \tag{S23}$$

We obtained $<\tau>$ = 0.06 ± 0.01 µs for the control film, which improved to $<\tau>$ = 5.50 ± 0.05 µs when treated with TOPO, where error values are the propagated uncertainty in the input fit parameters.

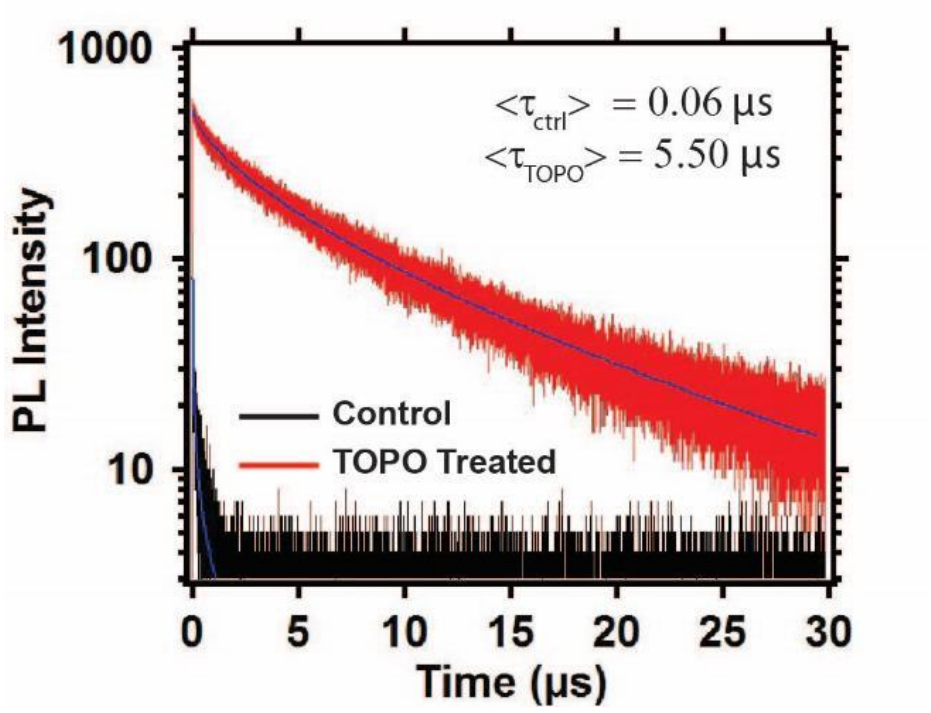

Figure S18. Time-resolved photoluminescence decay traces measured at low fluence (50 nJ/cm^2 per pulse) for a control film (black) versus a TOPO treated film (red). Blue lines are stretched exponential fits to the data, with $\langle\tau\rangle$ = 0.06 ± 0.01 µs for the control film and $\langle\tau\rangle$ = 5.50 ± 0.05 µs for the TOPO treated film.

S.11 Changes in films morphology at lower temperatures.

Previously, Osherov *et al.* have observed the fusing of crystallites upon cooling of perovskite samples, suggesting that the morphology changes at certain critical temperatures.[42] We observe morphological changes in our films starting at 235 K, as evidenced by widefield photoluminescence imaging (Fig. S19). We therefore only report internal photoluminescence quantum efficiencies down to 235 K in the main article, where the outcoupling efficiency is assumed to stay constant down to this temperature value.

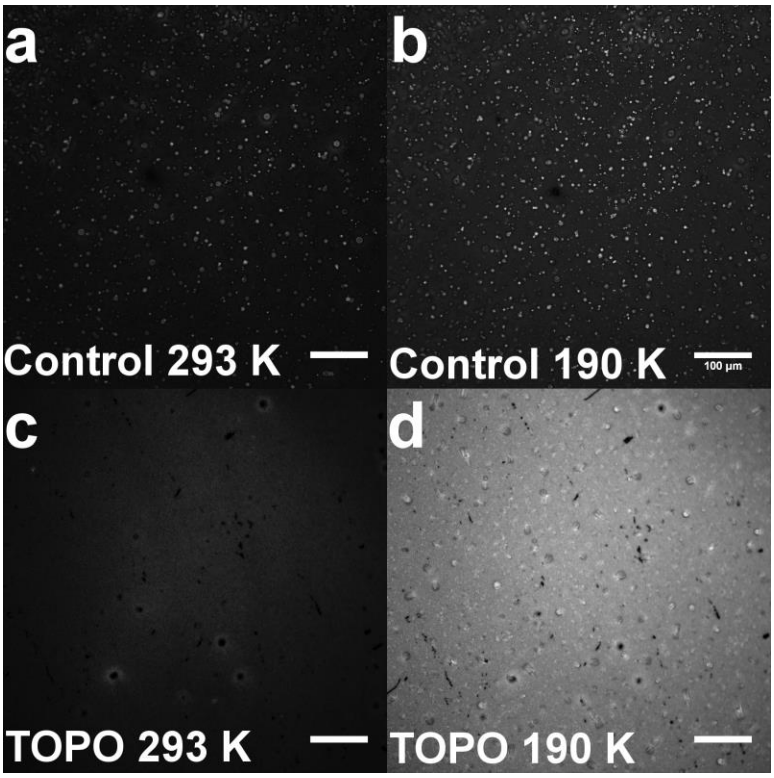

Figure S19. Widefield photoluminescence images of the (**a** and **b**) control and (**c** and **d**) TOPO treated film when measured at 293 K and 190 K, respectively. Changes in the morphology at lower temperature suggest the outcoupling efficiency is likely changing.

S.12 Qualitative determination of carrier transport length before and after TOPO treatment.

Achieving high external photoluminescence quantum efficiencies is a requirement in achieving the photovoltaic devices operating at the radiative limit. Equally important is the ability to extract charges over distances comparable to the film thickness. We recently observed an anticorrelation in photoluminescence quantum efficiency and mean lateral carrier diffusion length,[43] suggesting that both properties should be carefully assessed when determining material quality for solar cell applications. Fig. S20 shows a control

film excited with a diffraction-limited laser spot (470 nm, 0.3 μJ/cm^2 per pulse) and the widefield photoluminescence image collected with a CCD camera (Pixera, Penguin 150CLM) equipped with a 600 nm long-pass filter. Fig. S20c shows the line profiles of the images reported in Fig.s S20a and b, showing that the lateral carrier transport length (as probed via photoluminescence) is longer for the TOPO passivated film compared to the control film. We note that the control film exhibits a profile similar to that of the laser, which is consistent with the small average grain size of films prepared from lead acetate route[30] and the poor intergrain connectivity observed in perovskite thin films.[44]

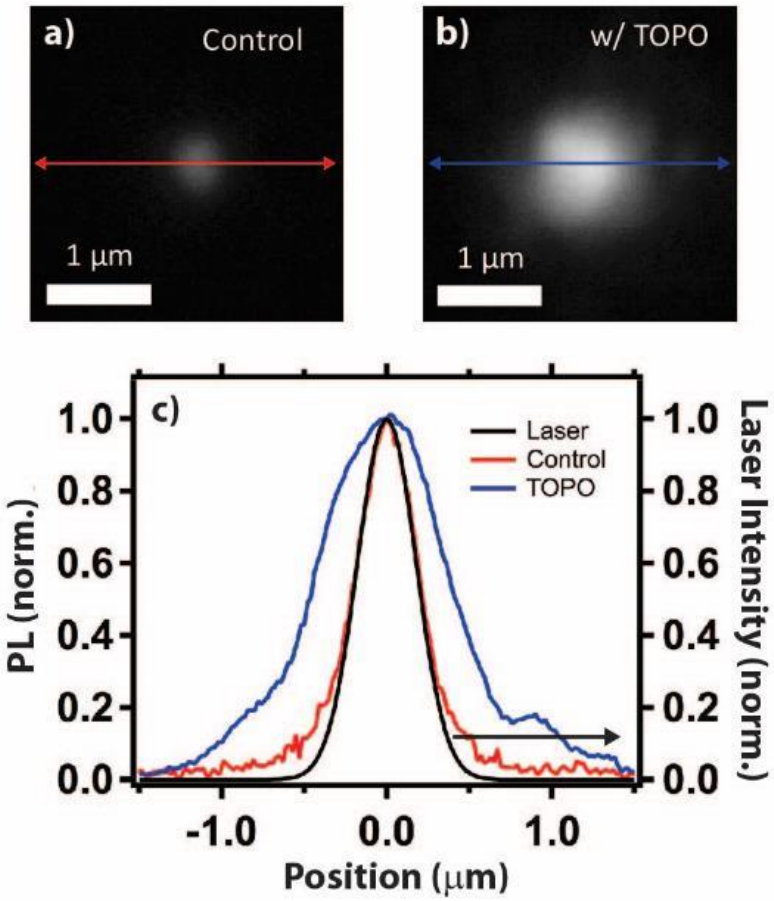

Figure S20. Local excitation and widefield photoluminescence detection of a control film (**a**) and TOPO passivated film (**b**). **c**, Line profile the laser excitation spot, the control photoluminescence image as shown in a), and the TOPO photoluminescence image as shown in b).

Supplementary References

1. Katahara, J. K. & Hillhouse, H. W. Quasi-fermi level splitting and sub-bandgap absorptivity from semiconductor photoluminescence. *J. Appl. Phys.* **116**, 173504 (2014).

2. Katahara, J. K. & Hillhouse, H. W. Erratum: "Quasi-fermi level splitting and sub-bandgap absorptivity from semiconductor photoluminescence" *J. Appl. Phys.* **119**, 239901 (2016).

3. Ross, R. T. Some thermodynamics of photochemical systems. *J. Chem. Phys.* **46**, 4590-4591 (1967).

4. Gratzel, M. The light and shade of perovskite solar cells. *Nat. Mater.* **13**, 838-842 (2014).

5. Richter, J. M. *et al.* Enhancing photoluminescence yields in lead halide perovskites by photon recycling and light out-coupling. *Nat. Commun.* **7**, 13941 (2016).

6. Bi, D. *et al.* Efficient luminescent solar cells based on tailored mixed-cation perovskites. *Sci. Adv.* **2**, e1501170 (2016).

7. Sa-yakanit, V. & Glyde, H. R. Urbach tails and disorder. *Comments Condens. Matter Phys.* **13**, 35-48 (1987).

8. Yamada, Y. *et al.* Dynamic optical properties of $CH_3NH_3PbI_3$ single crystals as revealed by one- and two-photon excited photoluminescence measurements. *J. Am. Chem. Soc.* **137**, 10456-10459 (2015).

9. Zhu, H. *et al.* Screening in crystalline liquids protects energetic carriers in hybrid perovskites. *Science* **353**, 1409 (2016).

10. Frost, J. M., Butler, K. T. & Walsh, A. Molecular ferroelectric contributions to anomalous hysteresis in hybrid perovskite solar cells. *APL Mater.* **2** 081506 (2014).

11. Eames, C. *et al.* Ionic transport in hybrid lead iodide perovskite solar cells. *Nat. Comm.* **6** (2015).

12. Shockley, W. & Queisser, H. J. Detailed balance limit of efficiency of p-n junction solar cells. *Journal of Applied Physics* **32**, 510-519 (1961).

13. Johnston, M. B. & Herz, L. M. Hybrid perovskites for photovoltaics: Charge-carrier recombination, diffusion, and radiative efficiencies. *Acc. Chem. Res.* **49**, 146-154 (2016).

14. Ross, R. T. Some thermodynamics of photochemical systems. *J. Chem. Phys.* **46**, 4590-4593 (1967).

15. deQuilettes, D. W. *et al.* Impact of microstructure on local carrier lifetime in perovskite solar cells. *Science* **348**, 683-686 (2015).

16. Pazos-Outon, L. M. *et al.* Photon recycling in lead iodide perovskite solar cells. *Science* **351**, 1430-1433 (2016).

17. Fischer, M. & Georges, J. Fluorescence quantum yield of rhodamine 6G in ethanol as a function of concentration using thermal lens spectrometry. *Chem. Phys. Lett.* **260**, 115-118 (1996).

18. Braly, I. L. & Hillhouse, H. W. Optoelectronic quality and stability of hybrid perovskites from $MAPbI_3$ to $MAPbI_2Br$ using composition spread libraries. *J. Phys. Chem. C* **120** (2016).

19. Tress, W. Perovskite solar cells on the way to their radiative efficiency limit – insights into a success story of high open-circuit voltage and low recombination. *Adv. Energy Mater.* **1602358** (2017).

20. Correa-Baena, J.-P. *et al.* Identifying and suppressing interfacial recombination to achieve high open-circuit voltage in perovskite solar cells. *Energy Environ. Sci.* (2017).

21. Saliba, M. *et al.* Incorporation of rubidium cations into perovskite solar cells improves photovoltaic performance. *Science* **354**, 206-209 (2016).

22. Yang, W. S. *et al.* Solar cells. High-performance photovoltaic perovskite layers fabricated through intramolecular exchange. *Science* **348**, 1234-1237 (2015).

23. Son, D.-Y. *et al.* Self-formed grain boundary healing layer for highly efficient $CH_3NH_3PbI_3$ perovskite solar cells. *Nat. Energy* **1**, 16081 (2016).

24. Anaraki, E. H. *et al.* Highly efficient and stable planar perovskite solar cells by solution-processed tin oxide. *Energy Environ. Sci.* **9**, 3128-3134 (2016).

25. Yang, W. S. *et al.* Iodide management in formamidinium-lead-halide-based perovskite layers for efficient solar cells. *Science* **356**, 1376-1379 (2017).

26. Yu, Y. *et al.* Synergistic Eefects of lead thiocyanate additive and solvent annealing on the performance of wide-bandgap perovskite solar cells. *ACS Energy Letters* **2**, 1177-1182 (2017).

27. Mark E. Ziffer, J. C. M., & David S. Ginger. Electroabsorption spectroscopy measurements of the exciton binding energy, electron–hole reduced effective mass, and band gap in the perovskite $CH_3NH_3PbI_3$. *ACS Photonics* **3**, 1060–1068, (2016).

28. Schnitzer, I., Yablonovitch, E., Caneau, C. & Gmitter, T.J. Ultra-high spontaneous emission quantum efficiency, 99.7% internally and 72% externally,

from AlGaAs/GaAs/AlGaAs double heterostructures. *Appl. Phys. Lett.* **62**, 131-133 (1993).

29. Steiner, M. A. *et al.* Optical enhancement of the open-circuit voltage in high quality GaAs solar cells. *J. Appl. Phys.* **113**, 123109 (2013).

30. Zhang, W. *et al.* Ultrasmooth organic-inorganic perovskite thin-film formation and crystallization for efficient planar heterojunction solar cells. *Nat. Commun.* **6**, 6142 (2015).

31. Horng, R.-H., Huang, S.-H., Yang, C.-C. & Wuu, D.-S. Efficiency improvement of GaN-based LEDs with ITO texturing window layers using natural lithography. *IEEE J. Sel. Top. Quantum Electron.* **12**, 1196-1201 (2006).

32. Murri, R. *Silicon Based Thin Film Solar Cells.* (Bentham Science Publishers, Oak Park, 2013).

33. Liu, J.-M. *Photonics Devices*. (Cambridge Univ. Press, Cambridge, 2009).

34. Shirayama, M. *et al.* Optical transitions in hybrid perovskite solar cells: Ellipsometry, density functional theory, and quantum efficiency analyses for $CH_3NH_3PbI_3$. *Phys. Rev. Appl.* **5** (2016).

35. Stranks, S. D. *et al.* Recombination kinetics in organic-inorganic perovskites: Excitons, free charge, and subgap states. *Phys. Rev. Appl.* **2**, 034007 (2014).

36. Herz, L. M. Charge-carrier dynamics in organic-inorganic metal halide perovskites. *Annu. Rev. Phys. Chem.* **67**, 65-89 (2016).

37. deQuilettes, D. W. *et al.* Photoluminescence lifetimes exceeding 8 μs and quantum yields exceeding 30% in hybrid perovskite thin films by ligand passivation. *ACS Energy Lett.* **1**, 438-444 (2016).

38. Stranks, S. D. *et al.* Electron-hole diffusion lengths exceeding 1 micrometer in an organometal trihalide perovskite absorber. *Science* **342**, 341-344 (2013).

39. Eperon, G. E. *et al.* Formamidinium lead trihalide: A broadly tunable perovskite for efficient planar heterojunction solar cells. *Energ. Environ. Sci.* **7**, 982-988 (2014).

40. Munechika, K. *et al.* Quantum dot/plasmonic nanoparticle metachromophores with quantum yields that vary with excitation wavelength. *Nano Lett.* **11**, 2725-2730 (2011).

41. Lindsey, C. P. & Patterson, G. D. Detailed comparison of the Williams–Watts and Cole–Davidson functions. *J. Chem. Phys.* **73**, 3348-3357 (1980).

42. Osherov, A. *et al.* The impact of phase retention on the structural and optoelectronic properties of metal halide perovskites. *Adv. Mater.* **28**, 10757-10763 (2016).

43. Stoddard, R. J., Eickemeyer, F. T., Katahara, J. K. & Hillhouse, H. W. Correlation between photoluminescence and carrier transport and a simple in-situ passivation method for high-bandgap hybrid perovskites. *J. Phys. Chem. Let.* (2017).

44. Tian, W. *et al.* Limiting perovskite solar cell performance by heterogeneous carrier extraction. *Angew. Chem. Int. Ed. Engl.* **55**, 13067-13071 (2016).

Dane W. deQuilettes

Department of Chemistry • University of Washington
36 Bagley Hall • Seattle, WA 98195-1700
(509) 293-0211 • dwd2@uw.edu

EDUCATION

Chemistry and Nanotechnology (dual title Ph.D.) **2012 –2017**
University of Washington **Seattle, WA**

Chemistry (B.S.) **2008 - 2012**
Pepperdine University **Malibu, CA**
Minor in Applied Mathematics
Magna Cum Laude

RESEARCH EXPERIENCE

Research Assistant **Feb. 2013 – Aug. 2017**
Department of Chemistry, University of Washington
Supervisor: Prof. David S. Ginger

- Characterization and Design Methods for Next Generation Solar Cells

Power Distribution/ Energy Storage Specialist **Jan. 2016 – Nov. 2016**
SpaceX Hyperloop Competition, University of Washington Team

- Phase Change Materials for Battery Thermal Management

Lawrence Berkeley National Lab Research Affiliate **Oct.-Nov. 2016**
Lawrence Berkeley National Lab, The Molecular Foundry
Supervisor: Dr. P. James Schuck

- 3-D Mapping of Electronic Heterogeneity in Organic-Inorganic Trihalide Perovskites Using Two-Photon Microscopy

Visiting Ph.D Student **Jan. – Feb. 2014**
Department of Condensed Matter Physics, University of Oxford, U.K.
Supervisor: Prof. Henry J. Snaith

- Organic-Inorganic Trihalide Perovskite Solar Cells

Research Assistant **2010 - 2012**
Department of Chemistry, Pepperdine University
Supervisor: Prof. Jane Ganske

- Degradation Pathways of Skin Oils in the Presence of Metal Oxides in Sunscreens and Lignin in the Presence of Air Pollutants

PUBLICATIONS (total Google Scholar citations = 856, h = 10)

*† equal contribution, * mentored undergraduate student*

(19) Jariwala, S.; **deQuilettes, D.W.;** Ginger, D.S. "Effective Removal of Traps Reveals Recombination is Dominated by Direct Band Gap Transitions in Organic-Inorganic Perovskites," **2017,** *manuscript in preparation.*

(18) **deQuilettes, D.W.;** Jariwala, S.; Ginger, D.S. "Review: Defect Control for Improved Optoelectronic Performance in Organic-Inorganic Trihalide Perovskites," Chem. Rev., **2017**, *manuscript in preparation.*

(17) **deQuilettes, D.W.;** Frohna, K.; Ginger, D.S.; Stranks, S.D. Invited Review: "Unique Recombination in Organic-Inorganic Perovskites." J. Phys. Chem. Lett., **2017,** *manuscript in preparation.*

(16) **deQuilettes, D.W**.; Jariwala, S.; *Burke, S.; Ziffer, M.E.; Wang, J.T.-W; Snaith, H.J.; Ginger, D.S. "Tracking Photoexcited Carriers in Hybrid Perovskite Semiconductors: Trap-Dominated Spatial Heterogeneity and Diffusion," **ACS Nano**, **2017,** *submitted.*

(15) Braly, I.†; **deQuilettes, D.W.**†; Pazos-Outón, L.M.; *Burke, S.; Ziffer, M.E.; Ginger, D.S.;* Hillhouse, H.W.* "Hybrid Perovskite Films Approaching the Radiative Limit with Over 90% Internal Photoluminescence Quantum Efficiency," **Nat. Photonics, 2017,** *submitted.*

(14) Quitsch, W.-A.; **deQuilettes, D.W**.; Pfingsten, O.; Schmitz, A.; Ognjanovic, S.; Winterer, M.; Ginger, D.S.; Bacher, G. "Light Induced Degradation in $CH_3NH_3PbI_3$ Perovskite Layers: The Role of Excitation Energy," **J. Phys. Chem. Lett.**, **2017,** *submitted.*

(13) Zuo, L.; Guo, H.; **deQuilettes, D.W.;** Jariwala, S.; De Marco, N.; Dong, S.; DeBlock, R.H.; Ginger, D.S.; Dunn, B.; Wang, M.; Yang, Y. "Chemically Passivated Organohalide Perovskite Films for Efficient and Stable Planar Heterojunction Solar Cells," **Sci. Adv.**, **2017,** *accepted.*

(12) Barrows, C.; Rinehart, J.; Nagaoka, H.; **deQuilettes, D.W.;** Chen, J.; Ginger, D.S.; Gamelin, D.R. "Electrical Detection of Quantum Dot Hot Carriers Generated via a Mn^{2+}-Enhanced Auger Process," ***J. Phys. Chem. Lett.,*** **2017,** 8, 126-130.

(11) **deQuilettes, D.W.; ***Koch, S.; *Burke, S. A.; Paranji, R.; *Shropshire, A.J.; Ziffer, M.E.; Ginger, D.S. "Photoluminescence Lifetimes Exceeding 8 μs and Quantum Yields Exceeding 30% in Hybrid Perovskite Thin Films by Ligand Passivation," **ACS Energy Lett**., **2016**, 1, 438-444.

(10) Wang, J.T.W.; Wang, Z.; Pathak, S.; Zhang, W.; **deQuilettes, D.W.;** Wisnivesky, F.; Huang, J.; Nayak, P.; Patel, J.; Yusof, H.; Vaynzof, Y.; Zhu, R.; Ramirez, I.; Zhang. J.; Ducati, C.; Grovenor, C.; Johnston, M.B.; Ginger, D.S.; Nicholas, R.J.; Snaith, H.J. "Efficient Perovskite Solar Cells by Metal Ion Doping," ***Energy Environ. Sci.***, **2016,** 9, 2892-2901.

(9) **deQuilettes, D.W.;** Zhang, W.; Burlakov, V. M.; Graham, D.J.; Leijtens, T.; Osherov, A. Bulovic, V.; Snaith, H.J.; Ginger, D.S.; Stranks, S.D. "Photo-induced Halide Redistribution in Organic-Inorganic Perovskite Films," ***Nat. Commun.***, **2016**, 7 (11683).

- This article in *Nature Communications* was highlighted in *Nature,* on the DOE Office of Science homepage, EurekAlert!, Phys.Org, Science Daily, MIT and UW News and other news outlets.

(8) Zhao, T.; Williams, S.T.; Chueh, C.C.; **deQuilettes, D.W.;** Liang, P.W.; Ginger, D.S.; Jen, A.K.Y. "Design Rules for the Broad Application of Fast (< 1 s) Methylamine Vapor Based, Hybrid Perovskite Post Deposition Treatments," ***RSC Adv.,*** **2016**, 6 (33), 27475-27484.

(7) Zhang, W.; Pathak, S.; Sakai, N.; Stergiopoulos, T.; Nayak, P.K.; Noel, N.K.; Haghighirad, A.A.; **deQuilettes**, **D.W.**; Sadhanala, A.; Li, W.; Wang, L.; Ginger, D.S.; Friend, R.H.; Snaith, H.J. "High-quality Perovskite Thin Film with Reduced Trap States for Efficient Planar Heterojunction Solar Cells," ***Nat. Commun*.**, **2015**, 6 (10030).

(6) Eperon, G.E.; Habisreutinger, S.; Leijtens, T.; Bruijnaers, B.; van Franeker, J.; **deQuilettes, D. W.**; Pathak, S.; Sutton, R.; Grancini, G.; Ginger, D. S.; Janssen, R.; Petrozza, A.; Snaith, H. J. "The Importance of Moisture in Hybrid Lead Halide Perovskite Thin Film Fabrication," ***ACS Nano,*** **2015**, 9 (9), 9380-9393.

(5) **deQuilettes, D.W**.; Vorpahl, S. M.; Stranks, S.D.; Nagaoka, H.; Eperon, G. E.; Ziffer, M. E.; Snaith, H. J.; Ginger, D.S. "Impact of Microstructure on Local Carrier Lifetime in Perovskite Solar Cells," ***Science,*** **2015,** 348 (6235), 683-686**.**

- This article in *Science* was highlighted in *Nature Chemistry*, Phys.Org, Science Daily, UW news and other news outlets.

(4) Nagaoka, H.; Fei, M.; **deQuilettes, D.W.,** Vorpahl, S.; Glaz, M.; Colbert, A.E.; Ziffer, M.; Ginger, D.S. "Zr-doped TiO_2 Electrodes Reduce Hysteresis and Improves Performance in Hybrid Perovskite Solar Cells while Increasing Carrier Lifetimes," ***J. Phys. Chem. Lett.*** **2015,** 6, 669-675.

(3) Yao, K.; Salvador, M.; Chueh, C.-C.; Xin, X.-K.; Xu, Y.-X.; **deQuilettes, D.W.;** Hu, T.; Chen, Y.; Ginger, D.S.; Jen, A.K.-Y., "A General Route to Enhance Polymer Solar Cell Performance with Plasmonic Nanoprisms," ***Adv. Energy Mater.,*** **2014**, 4, 1400206.

(2) Gliboff, M.; Sulas, D.; Nordlund, D.; **deQuilettes, D. W**.; Nguyen, P.; Seidler, G.T.; Li, X.; Ginger, D.S., "Direct Measurement of Acceptor Group Localization on Donor-Acceptor Polymers using Resonant Auger Spectroscopy," ***J. Phys. Chem. C.,*** **2014**, *118 (10), 5570-5578*.

(1) Strein, E.; **deQuilettes, D. W**.; Hsieh, S.; Colbert, A.; Ginger, D. S., "Hot Hole Transfer Increasing Polaron Yields in Hybrid Conjugated Polymer/PbS Blends," ***J. Phys. Chem. Lett.,*** **2014**, 5 (1), 208-211.

SELECTED AWARDS AND RECOGNITION

University of Washington (UW)

Full Scholarship, International School for Materials for Energy and Sustainability, Caltech, 2017
UW Clean Energy Institute Scientific Achievement Award, 2017
Materials Research Society (MRS) Graduate Student Gold Award, 2016
UW Clean Energy Institute Travel Grant, 2016, 2015 and 2014
UW Department of Chemistry Alma Mater Travel Award 2015
Graduate Student Merit Fellowship, Joseph Bouknight Endowed Fellowship in Chemistry, 2014
National Science Foundation Graduate Research Fellowship (NSF-GRFP), 2014-2017
National Defense Science and Engineering Fellowship (declined for NSF), 2014
Graduate School Fund for Excellence and Innovation Travel Award, 2014
Clean Energy Institute Graduate Fellowship, 2013-2014
Distinguished Energy Fellowship of the Advanced Materials for Energy (AME) Institute, 2012-2014
Kwiram/Council for Chemical Research (CCR) Fellowship, 2012-2014

Pepperdine University

Outstanding Chemistry Student Graduating Class of 2012
Natural Science Division Scholarship, 2009-2012
Faculty-Staff Scholarship, 2009-2012
Blanche E. Seaver Faculty Scholarship, 2009-2012
Resident Assistant Scholarship, 2011-2012
University Alumni Grant, 2009-2012
Pepperdine Grant, 2009-2012
Seaver Trust Grant, 2009-2012
Academic Excellence Award (Alpha Tau Omega), 2009-2012
Lewis Heidelberg Scholarship, 2011
Dean's List, 2008, 2009, 2011
Golden Key National Honor Society, 2009
Phi Eta Sigma National Honor Society, 2009

Pi Mu Epsilon National Mathematics Honor Society, 2009
Lake Chelan Valley Scholarship Fund, 2008-2011

Chelan High School
Valedictorian, Graduating Class of 2008

PRESENTATIONS (*contributed)

(16) **deQuilettes, D.W**.; Braly, I.; Ginger, D.S.; Hillhouse, H. "Hybrid Perovskite Films Approaching the Radiative Limit With >90% Internal Photoluminescence Quantum Efficiencies", Symposium: ES01: Perovskite Materials and Devices-Progress and Challenges. **Fall MRS Meeting,** Boston, MA (November 2017).

(15) **deQuilettes, D.W**. "Near Unity Radiative Efficiencies and Ultra-high Quasi-Fermi Level Splittings in Organic-Inorganic Perovskite Films by Surface Passivation", International School for Materials for Energy and Sustainability (ISMES) VI. **California Institute of Technology,** Pasadena, CA (July 2017).

(14) **deQuilettes, D.W**.; Ginger, D.S. "Photoluminescence Lifetimes Exceeding 8 μs and Quantum Yields Exceeding 30% in Hybrid Perovskite Thin Films by Ligand Passivation", Symposium: ES3: Perovskite Solar Cell Research from Material Properties to Photovoltaic Function. **Fall MRS Meeting,** Boston, MA (November 2016).

(13) **deQuilettes, D.W**.; Ginger, D.S. "Local Heterogeneity and Radiative Efficiency in Hybrid Perovskite Thin Films", Optoelectronics and Materials Seminar, invited talk. **Delft University of Technology,** Delft, Netherlands (September 2016).

(12) **deQuilettes, D.W**.; Ginger, D.S. "Local Heterogeneity and Radiative Efficiency in Hybrid Perovskite Thin Films", **International Conference on Solution Processed Innovative Solar Cells (SPINS16),** Berlin, Germany (September 2016).

(11) **deQuilettes, D.W**.; Ginger, D.S.; Stranks, S.D. "Understanding and Eliminating Non-Radiative Decay in Organic-Inorganic Perovskites", Physical Chemistry of Interfaces and Nanomaterials. **SPIE Conference,** San Diego, CA (August 2016).

(10) **deQuilettes, D.W**.; Ginger, D.S. "Pathways to a Solar Energy Future", Natural Science Division. **Pepperdine University**, Malibu, CA (January 2016).

(9) **deQuilettes, D.W**.; Ginger, D.S. "Elucidating the Complex Recombination Kinetics in Organic-Inorganic Trihalide Perovskites", Center for Excitonics, invited talk. **Massachusetts Institute of Technology**, Boston, MA (December 2015).

(8) ***deQuilettes, D.W.;** Zhang, W.; Burlakov, V.M.; Leijtens, T; Graham, D.J.; Osherov, A.; Bulović, V.; Snaith, H.J.; Ginger, D.S.; **Stranks, S.D.** "Photoinduced Halide Redistribution in Organic-Inorganic Perovskite Films", *Symposia NN/OO Special*

Rump Session—Perovskite-Based Photovoltaic and Optoelectronic Devices. **Fall MRS Meeting,** Boston, MA (November 2015).

- Also presented as a poster and received *Best Poster Award*

(7) **deQuilettes, D.W**.; Koch, S.; Shropshire, A.J.; Ginger, D.S. "Reduced Non-Radiative Recombination via Surface Passivation in $CH_3NH_3PbI_3$ Perovskite Films," *Symposium OO*: *Nanomaterials-Based Solar Energy Conversion.* **Fall MRS Meeting,** Boston, MA (November 2015).

(6) **deQuilettes, D.W**.; Vorpahl, S.; Stranks, S.D.; Nagaoka, H.; Eperon, G.; Ziffer, M.; Snaith, H.J.; Ginger, D.S. "Impact of Microstructure on Local Carrier Lifetime in Perovskite Solar Cells", *Session A8-PV Device Engineering.* **12th International Symposium on Functional π-Electron System (Fπ-12)** 2015, Seattle, WA (July 2015).

(5) ***deQuilettes, D.W.;** Harrison, J.; Karatay, D.; Vorpahl, S. M.; Ginger, D.S. "Image Correlation of Scanning Probe, Electron and Fluorescence Microscopy Images for Advanced Materials in Energy", ***Big, Deep, Smart Data Analytics in Materials Imaging,*** **Oak Ridge National Laboratory**, 2015, Oak Ridge, TN (June 2015).

(4) **deQuilettes, D.W**.; Vorpahl, S.; Stranks, S.D.; Nagaoka, H.; Eperon, G.; Ziffer, M.; Snaith, H.J.; Ginger, D.S. "Impact of Microstructure on Local Carrier Lifetime in Perovskite Solar Cells", *Symposium W*: *Perovskite-Based and Related Novel Material Solar Cells. Special Rump Session for Hybrid Organic/Inorganic and Related Perovskite-based Solar Cells.* **Fall MRS Meeting,** Boston, MA (December 2014).

(3) **deQuilettes, D.W**.; Strein, E.; Hsieh, S.; Colbert, A.; Ginger, D.S. "Hot Hole Transfer Increases Polaron Yields in Hybrid Conjugated Polymer/PbS Blends", *Symposium F: Controlling the Interaction Between Light and Semiconductor Nanostructures for Energy Applications.* F9.10, **Spring MRS Meeting**, San Francisco, CA (April 2014).

(2) **deQuilettes, D.W**.; Ganske, J.A. *Using Passive Sampling to Quantify NO_x in Library Air and SPME/GC-MS to Survey Volatile Aldehydes.* Abstract CHED 267, **241st American Chemical Society National Meeting**, Anaheim, CA (March 2011)

(1) **deQuilettes, D.W**.; Ganske, J.A. *Using Passive Sampling to Quantify NO_x in Library Air and SPME/GC-MS to Survey Volatile Aldehydes.* **Southern California Conference of Undergraduate Research**, Malibu, CA (November 2010)

RESEARCH INTERESTS/SKILL SET

Characterization of next generation thin film solar technologies, fluorescence microscopy, ultrafast spectroscopy, organic-inorganic perovskites, quantum dots, hot carrier collection, ligand and defect chemistry, scanning electron microscopy (SEM) and energy dispersive X-ray spectroscopy (EDX), time-of-flight secondary ion

mass spectrometry (ToF-SIMS), glow discharge optical emission spectroscopy (GDOES), nuclear magnetic resonance (NMR), density functional theory (DFT), Gaussian, MatLab, Python, Lumerical, Labview, Igor Pro, metal work/machine shop.

WORKSHOPS/PUBLIC OUTREACH

University of Washington

2017 Chelan Earth Day/Chelan Middle School
"Careers in Clean Energy"
2017 Pacific Science Center, Curiosity Days: Engineer it!
2016 NSF GRF Grant Writing Workshop (Chem 500), University of Washington
Past Awardee Panelist
2016 Invited Speaker, Solar Washington
"Emerging Thin Film Photovoltaic Technologies"
2016 Pacific Science Center, Paws on Science
"Racing With The Sun"
2016 University of Washington Engineering Days
"UW Hyperloop"
2016 Chelan Earth Day/Chelan High School/ Middle School
"Careers in Clean Energy"
2015 Albert Einstein Middle School
"Solar Car Derby"
2015 Invited Speaker, University of Washington, Bothell
"The Environment and Health of Populations"
2015 Pacific Science Center, Paws on Science
"Build Your Own Solar Car"
2014 NSF GRF Grant Writing Workshop (Chem 500), University of Washington
Past Awardee Panelist
2014 UW Early Engineering Institute, Clean Energy Institute
"Build Your Own Solar Panel"
2014 STEM Career Fair, Sammamish High School
Environmental Panelist
2014 Pacific Science Center, Paws on Science
"Solely Powered by Solar"
2014 Greenwood Elementary Science Fair
"The Race for Solar"
2013 Pacific Science Center, Life Sciences
"Using Small Things to Solve Big Problems- UW Nanomedicine"
2013 Highland Middle School
"Science Magic"
2013 Pacific Science Center, Paws on Science
"Solar Energy for the Future"

Pepperdine University

2012 Eaton Hall Dormitory, Resident Advisor Discussion Leader

"The Philosophy of Science- From Cosmology to Free Will", 8-week Science Convocation Series

2012 Newbury Park High School

"The Role of Chlorofluorocarbons (CFC's) in Ozone Depletion"

TEACHING EXPERIENCE/MENTORING

Rainier Scholars Internship Program **2013-2016**

UW Chemistry Program Mentor

- Rainier Scholars gives underrepresented students of color the opportunity to work in a laboratory setting and significantly contribute to a research project headed by the appointed mentor.

University of Washington Chemistry Department **2012-2014**

Chemistry Teaching Assistant

- Organic and general chemistry discussion section lecturer and lab assistant

Pacific Coast Highway (PCH) Tutors **2010-2012**

Recruiter/Tutor

- Helped build tutoring company that now has 25 tutors and supports over 80 high school and college students. Provided one on one and group academic assistance to high school and college students in chemistry, physics, and mathematics.

Pepperdine University Chemistry/Mathematics Department **2009-2012**

Chemistry/Mathematics Tutor

- Provided one on one and group academic assistance in general chemistry, probability and statistics, algebra, geometry, calculus, linear algebra, and differential equations.

PROFESSIONAL ACTIVITIES AND ORGANIZATIONS

- UW Photonics Research Center Spectroscopy Trainer **2013-2017**
- UW Chemistry Graduate Club Vice President **2013-2016**
    - *Created, implemented, and oversaw the first individual development plan (IDP) for chemistry graduate students. This document is coordinated through the UW Graduate Education Committee as well as the Chemistry Department Chair.*
        - *https://students.washington.edu/chemgrad/individual-development-plan-forms*
- UW Clean Energy Ambassador **2013-2017**
- Member AAAS/Science Program for Excellence in Science **2015-2017**
- American Chemical Society (ACS) Chemistry Ambassador **2011-2017**
- Member of the American Chemical Society **2010-2017**
- Member of Materials Research Society **2013-2017**
- Pepperdine University Resident Advisor **2011-2012**
- Pepperdine Chemistry Club Vice President **2011-2012**

REFERENCES

- David S. Ginger, Professor of Chemistry, University of Washington Chemistry Department, dginger@uw.edu, (w) 1-206-685-2331.

- Henry J. Snaith, Professor of Physics, University of Oxford Physics Department, Clarendon Laboratory, Parks Rd, Oxford, OX1 3PU, UK (e) h.snaith1@physics.ox.ac.uk, (w) +44 1865 2 72380, (f) +44 1865 2 82208.

- Daniel R. Gamelin, Professor of Chemistry, University of Washington Chemistry Department, gamelin@chem.washington.edu, (w) 1-206-685-0901 (f) 1-206-685-8665.